# Schémas compacts basés sur le résidu d'ordre élevé pour des écoulements compressibles instationnaires. Application à de la capture de fines échelles.

Karim Grimich

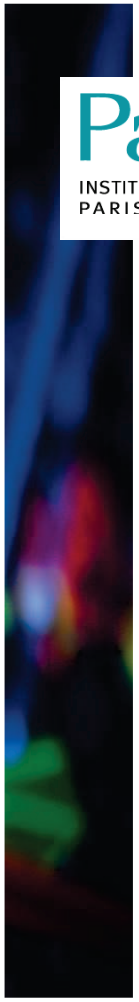

ParisTech
INSTITUT DES SCIENCES ET TECHNOLOGIES
PARIS INSTITUTE OF TECHNOLOGY

ARTS ET MÉTIERS ParisTech

2013-ENAM-0033

École doctorale n° 432 : Science des Métiers de l'ingénieur

## Doctorat ParisTech

# T H È S E

**pour obtenir le grade de docteur délivré par**

## l'École Nationale Supérieure d'Arts et Métiers

**Spécialité " Mécanique "**

*présentée et soutenue publiquement par*

**Karim GRIMICH**

le 02 octobre 2013

# Schémas compacts basés sur le résidu d'ordre élevé pour des écoulements compressibles instationnaires. Application à de la capture de fines échelles.

Directrice de thèse : **Paola CINNELLA**

**Jury**

| | |
|---|---|
| **M. Alain MERLEN**, Professeur, Branche Mécanique des Fluides, ONERA | Président |
| **M. Rémi ABGRALL**, Professeur, BACCHUS, Boredeaux 1 - INRIA | Rapporteur |
| **Mme Paola CINNELLA**, Professeur, DynFluid, Arts et Métiers ParisTech | Directrice de thèse |
| **M. Jean-Pierre CROISILLE**, Professeur, Lab. de Mathématiques, Université de Metz | Examinateur |
| **M. Charles HIRSCH**, Professeur, NUMECA, Vrije Universiteit Brussel | Rapporteur |
| **M. Alain LERAT,** Professeur émérite, DynFluid, Arts et Métiers ParisTech | Examinateur |

T H È S E

**Arts et Métiers ParisTech - Centre de Paris**
**DynFluid – Laboratoire de Dynamique des Fluides**

DynFluid
Fluid Dynamics Laboratory

*THÈSE*

*pour obtenir le grade de*

*DOCTEUR*

*de*

*L'ÉCOLE NATIONALE SUPÉRIEURE*
*D'ARTS ET MÉTIERS*

***Spécialité : Mécanique***

*par*

**Karim GRIMICH**

Directrice de thèse : **Paola CINNELLA**

# High order Residual Based Compact schemes for unsteady compressible flows. Application to scale resolving simulations.

**DynFluid - Laboratoire de Dynamique des Fluides**
**Arts et Métiers ParisTech, centre de Paris**

*Celui qui se perd dans sa passion perd moins que celui qui perd sa passion.*
Alexandre Jardin

# Remerciements

*Cette thèse de doctorat a été un grand acomplissement, autant professionnellement qu'humainement. J'ai pu notament y pratiquer et élargir mes connaissance de la mécanique des fluides numériques. Cela n'aurait pas été possible sans l'aide et le soutient de personnes compétentes que je tiens à remercier sincèrement.*

*Tout d'abord je tiens à remercier ma directrice de thèse, Paola Cinnella, qui a su me faire confiance en me recrutant dans son équipe et qui m'a permis de réaliser cette thèse. Mais aussi pour le temps qu'elle m'a consacré lors des différentes étapes de mon doctorat et des orientations qu'elle m'a conseillées. De plus, ses conseils m'ont été adressés aux moments stratégiques de ma thèse afin que je puisse dépasser mes limites, innover et produire du travail de qualité.*

*Mes remerciements vont ensuite aux membres du jury et en particulier aux deux rapporteurs, MM. Abgrall et Hirsch, qui ont accepté de lire ce manuscrit et d'y apporter leurs remarques pertinentes.*

*Également, je tiens à remercier sincèrement Alain Lerat, pour ses conseils pertinents et les échanges enrichissants que nous avons eus. C'est en partageant son expérience, sa rigueur et ses réflexions que Monsieur Lerat m'a fait grandir et murir scientifiquement.*

*J'ai également eu la chance de rencontrer Bertrand Michel. Après trois ans de travail en collaboration, je souhaite le remercier tout particulièrement pour tout le temps qu'il a investi sur ma thèse et pour l'enthousiasme qu'il a toujours réussi à me transmettre. Plus qu'un simple collègue, Bertrand a été un modèle de travail, une source de motivation et de re motivation.*

*De plus, je souhaite remercier Xavier Merle et Xavier Gloerfelt pour m'avoir aidé régulièrement. Leurs conseils techniques ou bibliographiques ainsi que leurs éclairages scientifiques ont étés des apports précieux pour la bonne réalisation de ma thèse.*

*Enfin je tiens à remercier l'ensemble des doctorants du laboratoire, qui grâce à leurs caractères chaleureux ont su donner une ambiance conviviale tout au long de ces trois ans de travail.*

*Pour finir, je tiens à remercier ces mêmes personnes et tous les membres du laboratoire pour les conseils et informations qu'ils ont pu me prodiguer et toute la sympathie dont ils ont fait preuve à mon égard.*

*Ce travail de recherche a été fait dans le cadre du projet Européen IDIHOM (Industrialization of High Order Methods) ayant pour objectif de promouvoir l'utilisation des méthodes numériques d'ordre élevé par l'industrie aéronautique Européenne. Ainsi, je remercie l'Union Européenne d'avoir financé cette thèse.*

# Contents

# Chapter I

# Introduction

Up-to-date Computational Fluid Dynamics (CFD) softwares have reached maturity in terms of solution accuracy as well as the computational efficiency. However, many progresses remain to be done, in particular for the accurate prediction of configurations with complex flow physics, or to reduce mesh refinement levels required to achieve a given tolerance on the discretization errors. This last item is particularly important in the case of unsteady simulations for laminar and, even more, turbulent viscous flows. Indeed, even if, from a theoretical viewpoint, current CFD softwares can, in the case of unsteady viscous simulations over long physical integration times, provide accurate results, this is achieved at the cost of extremely refined computational meshes that make routinary use of these kind of simulations unfeasible in the design practice, even on the most powerful machines. Mesh refinement is related, on one side, to physical constraints on the size of the physical structures to be captured but, on the other hand, this minimal resolution is generally increased by factors of 20 to 30 in each flow direction to compensate numerical errors introduced by the discretisation scheme. These stumbling block has been identified by the scientific community since quite a long time, and this has led to several research programs such that the IDIHOM FP7 STREP (Industrialization of High Order Methods), at least one ERC advanced grant, several research programs at ONERA or DLR, or industrial initiatives, at Dassault and SNECMA for instance in France, to extend high-order discretisation methods from academic, geometrically simple, configurations, to realistic flows of industrial interest. This thesis is situated within the framework of the European project IDIHOM, coordinated by DLR [3].

High-fidelity CFD (Computational Fluid Dynamics) tools, defined as simulation codes based on advanced physical models and high-order accurate numerical techniques, are not yet fully exploited in industrial design environments, mainly because of their higher computational cost and reduced robustness compared to standard approaches. Approaches currently available in virtually any industrial CFD code are based on the Reynolds-Averaged Navier-Stokes (RANS) equations, supplemented by a suitable turbulence model, and use lower-order discretisation techniques (second-order accurate at most). For essentially steady, attached flows with weak shock waves (with is generally the case for most flow systems at nominal conditions), current industrial CFD codes are able to provide useful information to within engineering accuracy criteria and with simulation turn-around times compatible with an industrial use. The increased availability of parallel computers has also contributed to the application of CFD to geometrically complex 3D configurations, and most industrial codes do possess rather good parallel scalability (also thanks to the use of small discretisation stencils). Nevertheless, CFD is now being applied to even more complex flow configurations: on the one hand, the development of highly loaded aircraft components (in view of weight reductions) may lead to the formation of separated zones and strong shock waves even at nominal conditions, on the other hand, CFD represents an attractive

tool to provide predictions about the off-design behaviour, as well as a deeper understanding of the underlying physical mechanisms (fine unsteady flow structures, shock wave/boundary layer interactions, acoustic feedback, ...). An accurate representation generally requires at least to take into account average unsteadiness (by solving , namely, the unsteady RANS, or URANS, equations), if not to consider more advanced physical models, like Large Eddy Simulation (LES) approaches or hybrid RANS/LES approaches (e.g. DES, Detached Eddy Simulation, or other). Unsteady physical models are much more sensitive than RANS approaches to numerical errors, which may be inextricably coupled to physical effects. To circumvent this problem, very fine meshes may be used, in conjunction with massive parallelisation to reduce computational costs. Nevertheless, large computational meshes lead to memory, storage and post-treatment problems; furthermore, massively parallel computer are not already commonly available in industry, require specific expertise to be used, and are highly energy consuming.
An attractive alternative to the use of large computational meshes is to increase the order of accuracy of the discretisation scheme. It has been known since a long time, in the field of Ordinary Differential Equations (ODE) that, to match a given accuracy requirement it is more computationally efficient to increase the order of accuracy of the approximation scheme than to refine the computational mesh. For many simple flows, experience shows that this is also true for space discretisation schemes used to solve systems of Partial Differential Equations (PDE). Nevertheless, some work is still required to prove the interest of higher-order methods for the numerical simulation of fluid flow of high geometrical and physical complexity, to ensure a robust behaviour of computation, and to improve their computational efficiency.
In the case of compressible flows, the development of effective high-order methods is made particularly challenging by the presence of flow discontinuities, which may interact together and with the surrounding boundary layers. A typical example is given by turbomachinery flows. On the one hand, the scheme has to be robust enough to capture flow discontinuities without generating numerical instabilities or spurious numerical artefacts and, on the other hand, it has to be accurate enough to describe accurately and with a minimal number of discretisation points smooth flow features. For instance, in the case of the interaction of a discontinuity with a smooth structure (e.g. shock/vortex interaction), the solution can be at most first-order across the discontinuity, but one may wish that the numerical dissipation is well behaved enough not to damp flow structures downstream of the shock, even for long integration times. The combination of these two features is a real challenge for current numerical schemes and, actually, for most high-order schemes, including advanced discretisation approaches like the so-called Discontinuous Galerkin schemes, Spectral Volume and Spectral Difference schemes, which cannot be used without addition of some form of artificial viscosity.
This shows that the technical challenges currently encountered by the aeronautical industry require further research effort for the development of high-order methods capable of circumventing these difficulties.

## I.1 State of the art of High-Order methods

The state-of-the-art of high-order (HO) methods cannot be separated from the general status of CFD with a perspective on its applications in the Aeronautical industry. The large majority of current industrial codes rely on the solution of the RANS equations using finite volume schemes. Significant examples of such codes are the elsA code [1] developed by Onera with some inputs from CERFACS and used by SAFRAN and Airbus among others, the TAU code [5] developed by DLR, as well as popular commercial codes as Fluent, CFX, and Fine-Hex of NUMECA. Moreover, time-accurate computations are still considered as too costly for an industrial practice so that, in the day-to-day use, unsteady simulations are often carried out with

an non physically high, often local, time step to quickly converge to a steady solution (when such a solution is physically admitted by the system under consideration). Of course, improved computer capabilities are now allowing the use of URANS simulation even in an industrial context [135]. Even more, physical limitations intrinsic to RANS modelling for the representation of unsteady flows, namely in case of separated flow [142], are pushing industry toward more advanced physical models like LES or at least hybrid RANS/LES approaches (see [136] for a review). These advanced calculations are however restricted to limited configurations and aim more to obtaining physical insight on specific phenomena characterising some aircraft components than to current design practice. Besides physical modelling improvements, considerable effort has been made to improve the handling of geometrically complex configurations, thanks to the use of hybrid grids (including structured layers close to the walls and unstructured meshing elsewhere), non-matching, sliding, and overlapping (Chimera) meshes. In spite of considerable improvement made in physical modelling and geometrical flexibility, unsteady viscous simulations remain unacceptably costly for common practice, so that these kind of simulations is still far from being routinely applicable to design purposes. In fact, currently available industrial codes require the use of discretisation meshes made by hundreds of millions of mesh points to make sure to rule out numerical errors. This not only increases CPU costs, but also memory consumption and storage requirements, which can be partly alleviated by the enormous increase in computer power. However, high-performance computers are costly and energy consuming and their use cannot be generalized. Considerable reduction in computational cost can be achieved by improving the discretization methods themselves. The need for extremely fine meshes may be relaxed considerably by choosing a discretisation scheme that maximises the resolvability for a given cost, i.e. minimise dissipation and dispersion over a wide range of scales. The other deciding factors concern the ease of implementation (parallelisation, boundary conditions, complex geometries...), and the robustness. The integration of high fidelity/high order methods in an industrial environment to support aerodynamic, aeroelastic and aeroacoustic design is expected to reduce design cycle time and cost and is then crucial for industry, as also suggested by ACARE's objectives for 2050 (Acare Vision 2050) [6].

High-order methods offer, *a priori*, the possibility to achieve a fast reduction of approximation errors with only a moderate increase in the number of unknowns. On a regular mesh, the number $N$ of degrees of freedom scales like $h^{-d}$ where $h$ is a typical size of the mesh cell or element and $d$ is the dimension of the problem ($d = 1, 2, 3$) while the formal error scales like $h^{k+1}$, with $k+1$ the scheme's convergence order. However, for a given error level, computational cost may behave very differently between different methods. This depends on several factors such as the size of the computational stencil needed to reach a given formal accuracy, the number of operations needed to update each degree of freedom (DOF), but also the type of parallelism that is implemented, as well as the characteristics of machines that is used. Higher-order methods offer the possibility to achieve a fast reduction of approximation errors with only a moderate increase in the number of unknowns. The counterpart to this quicker error reduction is that the actual cost in terms of computational time per degree of freedom increases with the order of the method, but only with a fixed factor, thus at sufficiently low error level high-order methods will be faster than low-order ones.

It is expected that, given a required accuracy level and a specific flow case it exists an optimal order in terms of computational cost. This is currently unknown, but some authors suggest orders in the range of three or four for typical CFD computations involving Euler or RANS modelling, and may be higher for unsteady simulations involving fine structures, like LES [52, 158]. In the case of high-speed compressible flows the solutions are not globally smooth and this reduces the convergence order in non-smooth regions like shocks or sharp (trailing) edges, but still high-order methods are shown to be overall more accurate [156]. Furthermore local accuracy loss close to

discontinuities can be tackled by local mesh adaptation instead of globally finer meshes. Selecting an appropriate order of the method, combined with local mesh adaptation, higher accuracy can be achieved with similar computational effort compared to classical second-order finite volume schemes. On the other hand, a given accuracy accuracy level can be achieved with reduced computational effort.
There are several ways of increasing the formal accuracy of CFD solvers. We review in this introduction their main characteristics.

### I.1.1 ENO/WENO methods

The ENO (Essentially non oscillatory) methods have been initiated in [74] and then improved into the WENO (Weighted ENO) method in [109]. These concept have been further improved by Shu and coauthors in a series of papers. The idea is to replace the polynomial reconstruction that is at the core of the van Leer MUSCL method by a higher degree one. Special care is taken to avoid oscillations near discontinuities, this leads to a hierarchical algorithm, using a large discretization stencil. In the WENO method, the regularity of the reconstruction is improved by weighting all the possible reconstructions according to the regularity of the solution. Again, the computational stencil is quite large, typically for a $k+1^{th}$ order scheme on a Cartesian mesh. Because of their complexity, very few attempts have been done to extend these methods to unstructured meshes. One may quote the early work of Abgrall [8] for ENO methods, Friedrich [56] and Hu [80]. They are also non trivial to parallelise because of the very large stencil, and then a high communication cost. However, spectacular results have been obtained, on academic configurations, by Shu and his group.

### I.1.2 Discontinuous Galerkin methods

The discontinuous Galerkin (DG) method combines features of the finite volume method as well as of the discretisation with standard (conforming) finite elements. It is especially suited for the treatment of convection-diffusion problems, in particular for the numerical simulation of compressible flows. Some of the advantages of the DG method are its flexibility with respect to the computational meshes together with a natural amenability to parallelisation and *hp*-refinement [75]. The overall order of convergence can be systematically chosen by an appropriate definition of the underlying polynomial basis. For an overview of DG methods we refer to [37]. Given a local approximation in each mesh element (hence the global approximation is discontinuous across elements in general), a DG scheme writes in three terms: an evolution term that appears as the product of a block diagonal mass matrix multiplied by the derivative of the solution variables, the sum of a surface term and a boundary term that balances the first term. In the case of viscous problems, sophisticated techniques [21] must be used for the reconstruction of the gradient across element boundaries. One advantage of the method is that the mass matrix is block diagonal, so that its inverse is easy to evaluate and can be stored. Because of this feature, explicit Runge Kutta type temporal schemes are easy to implement and very popular. In the case of stiff problems partially implicit methods, such as those known as IMEX methods, are also rather easy to implement. However, the DG methods suffer from two main drawbacks: first, because of a the local nature of the variable representation, the number of degrees of freedom grows very quickly. To fix ideas, we assume a conformal and regular mesh made of tetrahedrons: if $n_s$ is the number of vertices, the Euler formula shows that the number of element scales like $6n_s$, the number of edges like $6n_s$ also, and the number of faces as $5n_s$, so that in the case of quadratic approximation we need approximately $40n_s$ and $80n_s$ for cubic approximations. The other drawback is that the surface and boundary terms are evaluated independently. Hence, an accuracy of order $k+1$ is needed to enforce this accuracy for the surface and boundary

terms: this can be obtained via high order Gaussian like quadrature formula. Various tricks can be used to simplify the evaluation of these terms, such as quadrature free techniques (see [77] for example), and the evaluation of the integral can be made very efficient by using LAPACK type routines, but the storage is very important and the coding very tricky. We also note that the existence of a diagonal mass matrix is not always a relevant argument, in particular for viscous simulations where some form of implicitation will be needed in order to have reasonable time steps. Currently, the development of DG methods for computational aerodynamics is an active field of research. Since the pioneering work on the DG discretisation of the turbulent RANS equations by Bassi and Rebay [22, 24], many research groups have contributed to the advancement of this approach [20, 23, 28, 55, 96, 97, 125]. During the European ADIGMA and IDIHOM projects mesh refinement, local adaptation of the polynomial degree, and computational scalability were identified as key techniques for the successful application of the DG method to CFD applications. Especially worth mentioning are the results from the University of Bergamo and the DLR, who demonstrated the benefits of the DG method also for turbulent flows on three-dimensional basic configurations [92]. Still, the implementation of an accurate, computationally efficient and robust DG method for the routine simulation of steady-state three-dimensional turbulent flow remains a future challenge. Besides the numerical and computational difficulties of the DG approach, where implementations are still far from being mature, further topics have already arisen for forthcoming research. In particular, the accurate simulation of unsteady flows requires further investigation [63]. Also, shock capturing capabilities of higher-order DG methods are still unsatisfactory, and mostly rely on the addition of artificial viscosity, with subsequent loss of accuracy. Finally, since current simulations codes in the aeronautic industry rely on finite volume methods, use of DG technique requires the development of completely new codes, in terms of implementation and parallelisation techniques.

### I.1.3 Spectral Volume/Spectral Difference Schemes

In this subsection, we briefly discuss the Spectral Volume (SV) and Spectral Difference (SD) methods, two recently developed and still evolving methods for compressible flow computations. Both the SV and SD methods employ the same solution space as the DG method, *i.e.*, element-wise discontinuous polynomials. They differ on how the DOFs are updated. The SV method is similar to a FV method, while the SD method is closer to a FD method.
The SV method was developed by Wang, Liu and their collaborators for hyperbolic conservation laws, then extended to the Navier–Stokes equations (see [157] for a review). The spectral volume (SV) method is a new conservative high-order accurate numerical method developed by Wang in a series of papers [111, 143, 155, 159–161]. The SV method is a finite-volume method for unstructured grids that, unlike other FV methods, does not require information from neighbouring cells to perform reconstruction. The SV method, like other FV methods and the DG method, can be extended to discontinuous flow via the application of limiters or artificial viscosity.
The basic idea of the spectral volume method is to discretised the computational domain into N non overlapping cells $S_i$ called spectral volumes, which are the same as the usual finite volumes. The surface or line integral on each face or edge, respectively, can be performed with a $k^{th}$ order accurate Gauss quadrature. A $k^{th}$ order accurate approximation of the state variable in the SV can be obtained with a $(k+1)^{th}$ order polynomial. This approximation of the state variable is in general discontinuous across the SV boundaries and flux integration is carried out using an exact or an approximate Riemann solver like in DG methods. The weak analogy between the DG method and the SV method is that for the DG method the order of accuracy is related to the number of nodes on the element while in the SV method is determined by the number of subdivisions in control volumes.

A major obstacle for the application of the SV methods in large scale, high-Reynolds number aerodynamic simulations is time step limitation that deteriorates with the increase of the order of the method, as well as high memory requirements, especially in 3D applications.
A more recent variant of SV methods is represented by the so-called Spectral-Difference (SD) methods, proposed by Liu *et al.* [110]. The SD method is a DG-like finite element method. It is formulated using the differential form of the Navier-Stokes equation (hence its name), in contrast to the integral form used for DG. The SD method, like DG, is element-wise discontinuous. Within each element, collocated solution and flux points are used to store flow solution and flow flux information. The solution points in each dimension are chosen to be the Chebyshev points. The flux points are selected to be the zeros of the Legendre polynomial with its end points. This choice leads to a stable SD scheme. Using $N$ solution points, a degree $N-1$ solution polynomial can be constructed using Lagrange basis to represent the flow solution in the local domain span by the element. The flux polynomial is one order higher than the solution polynomial such that when it is differentiated the flux divergence is of the same order as the solution polynomial. Therefore, the number of flux points is one more than that of solution points. Because of the different reconstruction stencil used for variables and for fluxes, SD is sometimes related to staggered-grid methods. At the element interface, where two sets of local solutions meet each other, the flux across the interface is discontinuous. A method to enforce flux continuity is to use a Riemann solver at the interfaces. The SD method is presented as easier to implement than the DG and SV methods, especially for high-order curved boundaries, because it does not involve surface or volume integrals. Nevertheless, its stability may be very much dependent on partition used and small instabilities are possible [88]. Similarly to DG methods, SV and SD methods require a quite different implementation than FV methods, and cannot be easily integrated in existing industrial codes.

### I.1.4 High-order centred finite difference schemes with filtering

Although finite volume (FV), finite element (FE) and DG schemes associated to unstructured grid systems have advantages in treating complex geometries, the finite difference methods (FD) with the structured grid system are superior in boundary layer simulations, computing costs, and convenience. Thus high-order multi-block FD techniques are still attractive at present and in the future. The main drawback inherent to FD methods is the difficulty to generate a high-quality structured single-block grid system for a complex configuration. Visbal and Gaitonde [152] and other researchers use an overset grid strategy for high-order FD. Multi-block structured grid technique makes it possible to run high-order finite difference schemes on each individual block, and the information transmission between neighbouring blocks and the propagation throughout the flow field can be realised by some kind of interface conditions. Traditionally, high-order FD require smooth grids, and the smoothness of the grids shall be comparable with the order of the accuracy of the schemes. Fortunately, Visbal and Gaitonde [152] have shown that high-order schemes can be applied in low quality grids such as deforming grids and non differentiable grids if some special techniques are applied to get rid of the Geometric Conservation Law (CGL)-related errors and numerical oscillations. At low Reynolds numbers or if only low-frequency motions are of interest, the discretisation scheme should be accurate at low wave numbers, and an accurate scheme is the same as a high-order scheme in the sense of truncation of Taylor's series. On the contrary, at high Reynolds numbers, where small turbulent scales are present, a better tradeoff can be obtained with an optimisation of the coefficients in the wavenumber space. The formal order is sacrificed to preserve small scales on a given grid. For FD schemes, the choice of the number of degrees of freedom is directly linked to the size of the discretisation stencil. Too large stencils can be cumbersome for distorted grids, for the implementation of boundary conditions

or for the communication in parallelised codes. Historically this problem is clearly raised in the papers of Lele [98], who talks about quasi-spectral schemes, and Tam and Webb [146], who developed Dispersion Relation Preserving (DRP) schemes. In particular, Lele proposed to use compact schemes, i.e. spatially implicit, to improve the scheme resolvability without increasing the stencil size. The cost to pay is the solving of tri- or penta-diagonal systems, which males the implementation of compact scheme somewhat more delicate for massively parallel applications. On the other hand, DRP-type centered finite-difference exhibit an extremely large stencil which also decreases communication performance in parallel implementations. DRP schemes often lack robustness. The destabilization arises from ill-posed problems such as corner points (cavity corners, diaphragm in a duct, airfoil trailing edge). The small errors due to the singular character of those points can be amplified by the use of non centered finite-difference or filtering schemes at domain boundaries. Similar difficulties may affect compact schemes. Both kind of schemes are generally purely centered and, as such, zero dissipative, so that they cannot be used without addition of some form of artificial viscosity or filtering techniques. Tam and Webb [146] suggest the use of explicit filters optimized in the space of wave numbers. Further improvements have been suggested by Bogey and Bally [18], who also use lower order filtering to suppress spurious oscillations generated close to flow discontinuities in compressible flow [29] On the other hand, Visbal and Gaitonde use compact filters of very high order in conjunction with their compact schemes. The above-mentioned finite difference schemes have proved their interest for the LES and DNS of flows in moderately complex geometries, as well as for aeroacoustic applications, but their extension to highly compressible flows in complex geometries (e.g. transonic or supersonic turbomachines) is not straightforward.

### I.1.5 Continuous Residual-Distribution Schemes

Another promising strategy to reach higher order accuracy is the Continuous Residual-Distribution (RD) method, combining ideas from both finite elements and finite volumes. The early contributions are due to Roe [133] and Ni [119]. Afterwards several group contributions, see *e.g.* [12, 131]. Abgrall *et al.* [10, 11] RD schemes (RDS) are based on a continuous finite element representation but they also include up-winding ideas and limiting, thus allowing satisfaction of a maximum principle (borrowed from Godunov Finite Volume methods). Discrete equations are derived by splitting (distributing) in each element of the grid an approximation of the integral of the equations over the element (cell residual). This approach has two important consequences: It naturally lends itself to the use of unstructured meshes, and its accuracy is entirely determined by the accuracy with which the cell residual is evaluated, and which is ultimately determined by the choice of the degree of the finite element interpolation space of the unknowns. In order to satisfy conservation constraints, the mesh is needed to be conformal, even-though this constraint can be alleviated, see [13].
Compared to standard FV methods and their *nominal* second-order accuracy, RDS methods with linear elements have demonstrated improved accuracy [47, 48] while preserving monotone shock capturing. Moreover, the compactness of the method allows for the design of very efficient parallel solution strategies. The scheme have been extended to viscous problems, allowing a uniform accuracy whatever the Reynolds number [9]. In comparison to DG methods, and for regular conformal meshes made of tetrahedons only, RDS schemes need less DoF than DG methods. However for reasonably high approximations, RDS methods are less demanding in term of memory. Unsteady applications of RDS schemes have been studied up to now only for second accurate schemes in time and space, either using a dual time stepping or a variant of Runge-Kutta schemes [130]. Nothing has been done for higher than second order accurate schemes on triangular type meshes.

## I.2 Scientific background on RBC schemes

Residual-Based-Compact (RBC) schemes have been initially developed by Lerat and Corre [102]. They are related to Residual Distribution schemes, but are developed in a finite difference framework, *i.e.* dealing with the differential form of the governing equation, then extended to complex geometry by means of a finite volume approach. Classical methods of high-accuracy scheme construction on structured grids are non compact directional methods [137, 146] or compact methods needing the use of linear algebra through Pade approximations [79, 98, 166]. Compact schemes are more attractive since their numerical dependence domain is narrower.
The first serious discussions and analyses of compact schemes emerged during the 1970s with Kreiss. In [120], Kreiss introduced in 1974 the idea of using an implicit Pade approximation method in computational fluid dynamics. The accuracy order and the applicability of these centered scheme was verified within the next year by R.S. Hirsh [79]. Since then a considerable amount of literature has been published on implicit compact schemes with some famous schemes such as Lele's compact finite difference schemes with spectral-like resolution [98]. Compact schemes for compressible flows have been mainly developed as centered approximations in space (see [39, 98, 154, 166] for instance) relying on the use of artificial viscosities, numerical filters or limiters for shock capturing. Upwind compact schemes have also been proposed in [58, 148].
A serious weakness with the use of an implicit compact spatial discretization is the computational cost induced by the method. In 1988, Abarbanel and Kumar [7] proposed 2D and 3D compact implicit schemes solving unsteady Euler equation on a $3^d$ stencil ($d$ is the space dimension i.e. 2 or 3). The relevant contribution of these compact scheme lies in the fact that the implicitness of the schemes comes only from the time derivative approximation and not from the spatial one. The main idea remains in adding error terms that vanish by combining with other terms, and are based on the derivatives of the residual. These schemes are shown to be linearly conditionally stable in 3D. They are theoretically second order in time and fourth order in space but an artificial viscosity with a tuning parameter is needed in a view to compute a 2D shock case [7] which reduces the spatial accuracy to third order. Although it improves the computation by reducing spurious oscillations, it does not cancel them and the scheme is not shock capturing.
In the early 2000's Lerat and Corre designed a third order accurate Residual Based Compact (RBC) scheme for steady state compressible Euler equations [102, 103] in Sinumef laboratory (renamed DynFluid afterwards). This scheme is compact, needs no linear algebra and uses a numerical dissipation without any tuning parameter. As for Abarbanel and Kumar's schemes, reaching spatial high order for the centered part of the scheme is managed by adding error terms in order to express the truncation error as a linear combination of residual derivatives that vanishes at a steady-like state. The dissipation is also built on the residual and is upwinded through a characteristic time step [45, 81, 82]. This explicit method is conditionally stable but an implicit matrix-free [90] version of the scheme is also presented in the same paper [102]. RBC schemes have been reformulated in finite volume using a straightforward extension of the numerical fluxes or by maintaining the order of accuracy on irregular structured meshes [73]. They also have been extended to unsteady flow [41] in a dual time step framework. Their general design for any odd orders, up to order seven, was described in [40] for inviscid flows and in [42] for advection-diffusion problems, in 2007 and 2008 respectively. Finally an unstructured version of the third order scheme has been developed [50, 51] in the European project ADIGMA (Adaptive higher order variational methods for aerospace applications).
Second and third-order RBC schemes, RBC2 and RBC3, have been implemented in the ONERA CFD code, $elsA$, and validated on realistic and increasingly complex transonic unsteady flows [117]. Nevertheless, these schemes failed inexpectedly for some flow configurations. The reason will be made clear in the following of this manuscript. Higher-order RBC schemes, namely

RBC5 and RBC7, were mostly applied to steady or inviscid unsteady cases. The present work is a continuation of the research effort on RBC schemes in view of their application to unsteady turbulent flows.
This thesis was conducted within the framework of the European project IDIHOM, presented in the next section.

## I.3 IDIHOM project

IDIHOM is an European-Union funded project gathering 21 research groups, academic and industrial teams, from 10 European countries. The IDIHOM project aims to promote the use of high-order numerical methods by the European aerospace industry. It is motivated by the increasing need to improve the CFD-aided (Computational Fluid Dynamic-aided) design procedure and analysis, using more accurate and fast numerical methods. The project follows the European Vision-2020 [2] by supporting the purpose of *more affordable, safer, cleaner, quieter* and thus greener aircraft. The project enables transfer of these high-order methods to industry, since they will be assessed and improved by using relevant and complex industrial test cases, called application challenges. In the project, steady and unsteady turbulent aerodynamic flows are handled for external and internal (turbo-machinery) aerodynamics as well as aeroelastic and aeroacoustic applications. IDIHOM will therefore contribute to maintain and foster the leadership of the European aerospace industry by allowing accurate predictions for complex flows at an industrially acceptable computational cost.
Among the research teams involved in IDIHOM, the complete high-order methods suite is studied. Regarding numerical schemes, the two most common methods are Discontinuous Galerkin [38] and Continuous Residual-Based methods [12, 40]. The present work deals with the latter method since the numerical schemes used are Residual Based Compact schemes.

## I.4 Objectives

In line with the work done on Residual Based Compact schemes in the DynFluid laboratory and within the framework of the IDIHOM project, this thesis seeks to understand and improve the application domain of RBC schemes to unsteady compressible flows. In order to be able to use RBC schemes for complex unsteady flows several issues have to be adressed:

- to develop an improved extension to unsteady computations of RBC schemes of any order and achieve a better understanding of the dissipative and dispersive properties of these schemes
- extend unsteady RBC schemes to curvilinear grids in the more robust and accurate way possible
- apply unsteady RBC schemes to test cases of increasing complexity.

## I.5 Outline of the thesis

This thesis is divided into four main chapters:

- Chapter 2 briefly reviews the physical models for compressible flows and the litterature on RBC schemes for steady compressible flows giving the state of the art on RBC schemes before the beginning of this thesis.

- Chapter 3 presents the design of high-order RBC schems to unsteady compressible flows with a comprehensive study of their dissipation properties. It also goes further with the quantification of the dissipation and dispersion resolvability properties of RBC schemes through a detailed analysis of their Fourier spectra. Numerical applications further supports the theoretical results of this chapter.

- Chapter 4 present the FV formulation of RBC schemes and the design of a third-order finite volume Residual-Based Compact scheme, RBC$i$. This scheme is designed to take into account mesh deformations, in such a way that it is third-order on mildly distorted structured grids and second-order on highly distorted meshes. Numerical applications further supports the theoretical results of this chapter.

- Chapter 5 provides application of RBC schemes to selected unsteady compressible flows.

The manuscript is closed by a general conclusion giving also some perspectives to the present work.

# Chapter II

# General background

**Contents**



In this chapter, we briefly review the physical models for compressible flows, resolved equations and used turbulence models. Then we recall the formulations of RBC schemes for steady compressible viscous and inviscid flows.

## II.1 Physical models for compressible flows

This section gives a brief review of physical models for compressible flows computations. The models used in the present work are the system of Navier-Stokes equations and Euler equations. They are only reminded in the present document, their derivation can easily be found in any introduction to fluid mechanics [93].

### II.1.1 Navier-Stokes equations

#### II.1.1.1 General framework

Navier-Stokes equations are set under the hypothesis of continuum and assuming that the fluid stress is the sum of a diffusing viscous term and a pressure term. The system consists of three equations:

- The continuity equation (mass conservation)
- The momentum conservation equation
- The energy conservation equation

Hereafter, we consider the system of Navier Stokes equations written in conservative vector form:

$$\frac{\partial w}{\partial t} + \frac{\partial f}{\partial x} + \frac{\partial g}{\partial y} + \frac{\partial h}{\partial z} = 0 \tag{II.1}$$

where $w$ is the state vector and $f$, $g$, and $h$ are the physical fluxes in the space directions $x$, $y$, and $z$. The physical fluxes are expressed as the sum of convective fluxes and diffusive fluxes:

$$f = f^E - f^V,\ g = g^E - g^V,\ h = h^E - h^V$$

They are defined as:

$$w = \begin{pmatrix} \rho \\ \rho u \\ \rho v \\ \rho w \\ \rho E \end{pmatrix},\ f^E = \begin{pmatrix} \rho u \\ \rho u^2 + p \\ \rho uv \\ \rho uw \\ \rho H u \end{pmatrix},\ g^E = \begin{pmatrix} \rho v \\ \rho vu \\ \rho v^2 + p \\ \rho vw \\ \rho H v \end{pmatrix},\ h^E = \begin{pmatrix} \rho w \\ \rho wu \\ \rho wv \\ \rho w^2 + p \\ \rho H w \end{pmatrix},$$

$$f^V = \begin{pmatrix} 0 \\ \tau_{xx} \\ \tau_{xy} \\ \tau_{xz} \\ u\tau_{xx} + v\tau_{xy} + w\tau_{xz} + \kappa\frac{\partial T}{\partial x} \end{pmatrix},\ g^V = \begin{pmatrix} 0 \\ \tau_{yx} \\ \tau_{yy} \\ \tau_{yz} \\ u\tau_{yx} + v\tau_{yy} + w\tau_{yz} + \kappa\frac{\partial T}{\partial y} \end{pmatrix}.$$

and

$$h^V = \begin{pmatrix} 0 \\ \tau_{zx} \\ \tau_{zy} \\ \tau_{zz} \\ u\tau_{zx} + v\tau_{zy} + w\tau_{zz} + \kappa\frac{\partial T}{\partial z} \end{pmatrix}$$

where $u$, $v$, and $w$ are the components of the velocity vector $\boldsymbol{v}$ in the spatial directions $x$, $y$ and $z$, $\rho$ the fluid density, $t$ the time, $p$ the pressure, $\overline{\overline{\tau}}$ the viscous stress tensor, $E$ the specific total energy, $H$ the total enthalpy and $T$ the temperature and $\kappa$ the fluid thermal conductivity. The specific total energy and the total enthalpy expressions are:

$$E = e + \frac{1}{2}|\boldsymbol{v}|^2$$

and

$$H = E + \frac{p}{\rho}$$

where $e$ is the specific internal energy. In the preceding equations, the repeated index notation is adopted.

The system is closed by giving constitutive equations for thermodynamic properties $p$ and $e$. In this work, we restrict our considerations to perfect gases. In this case, the thermal and caloric equations of state are $p = \rho r T$ and $e = C_v T$. In addition, only Newtonian fluids flow are computed in this work. Consequently, the viscous stress tensor is related to the velocity gradient by:

$$\overline{\overline{\tau}} = \mu\left(\nabla\boldsymbol{v} + (\nabla\boldsymbol{v})^T - \frac{2}{3}\mathrm{trace}(\nabla\boldsymbol{v})\boldsymbol{I}\right) \tag{II.2}$$

where $\mu$ is the dynamic viscosity coefficient and $I$ is the identity operator. Finally, we assume that the viscosity is related to the local temperature through Sutherland's law:

$$\frac{\mu}{\mu_{ref}} = \sqrt{\frac{T}{T_{ref}}}\frac{1 + C_{ref}/T_{ref}}{1 + C_{ref}/T} \tag{II.3}$$

where $\mu_{ref}$, $T_{ref}$, and $C_{ref}$ depend on the nature of the considered gas.

#### II.1.1.2 Euler equations

The Euler equations govern inviscid flows. They are obtained from the Navier Stokes equations (*c.f.* II.1.1) in the special case of ideal fluids with no viscosity and heat transfer by setting

$$f = f^E,\ g = g^E \text{ and } h = h^E.$$

This simplified system of equations is convenient with a view to test, analyze and validate the schemes on known cases.

### II.1.2 Turbulence models

A direct approach of the computation of turbulent flows is too costly for high-Reynolds number, noted $Re$, flows. In order to have a Direct Numerical Simulation (DNS) of a flow we need a mesh fine enougth to discretize properly all the scales present in the flow. If we denote $l_k$ the highest scale present in a flow, the computational cost can be estimated by the number of mesh points needed $N$. The order of $N$ is

$$N \propto Re_{l_k}^{9/4}$$

where

$$Re_{l_k} = \frac{\rho u_k l_k}{\mu}$$

with $u_k$ is the characteristic velocity associated to the scale $l_k$, and $\mu$ and $\rho$ are respectively the dynamic viscosity coefficient and the density of the considered fluid. A realistic turbomachinery flow has a Reynolds number of the order of $10^5$ and the computational cost of a DNS of this flow is of the order of $10^{11}$. This cost is not affordable for available computational ressources.
A first viable approach is the use Reynolds-Averaged Navier-Stokes (RANS) turbulence models [17, 19, 86, 87, 115, 141, 142, 163]. This approach is by definition dedicated to steady problems but can be extended to some unsteady computations. This extension is called Unsteady RANS (URANS) [136, 142, 163] and is valid for problems involving low frequencies in the limitation of the RANS model used. The RANS/URANS models used in this thesis are the one implemented in elsA (see [1, 33, 34] for details).
We are generally interested in the large scales of a flow since these scales drive the turbulent diffusion of momentum. Large Eddy Simulation (LES) [61, 108, 126, 136] can be seen as an affordable alternative compared to DNS for the computation of time evolving flows. In this approach the wavelengths smaller than the grid mesh are filtered out and accounted for by some model. Conventional LES, where an explicit subgrid scale (SGS) model is used, have shown to be successful for the computation of several flows [61, 108, 136]. However, subgrid models seems to be too dissipative in the case of the growth of an initially small perturbation [15, 16, 108, 126, 147] because of a coupling between the SGS model and the truncation error of the numerical discretization. It has been shown that for some flows, the use of flow regularization at small scales by means of the numerical dissipation of the dicretization scheme, without the explicit addition of any sugrid scale model, have been shown to give good results [15, 31, 76, 108]. In some cases [76], the SGS model is implicitly designed in the limiting method of the numerical scheme. These computations are called Implicit LES (ILES). The LES computations in the present work are ILES where the role of the SGS model is taken by the numerical dissipation of RBC schemes.

Now that the physical models for compressible flows have been briefly introduced we review in the next section the litterature on RBC schemes for steady compressible flows.

## II.2 Residual Based Compact (RBC) schemes: *steady formulation*

Classical methods for calculating compressible flows on a structured mesh rely on a directional approach in which space derivatives are approximated independently direction by direction. In the present section, we describe compact approximations that provide high accuracy not for each space derivative treated apart but for the complete residual $r$, i.e. the sum of all of the terms in the governing equations. For steady problems solved by time marching, $r$ is the residual at steady state; it involves space derivatives only. For unsteady problems, $r$ also includes the time derivative. Schemes of this type are referred-to as Residual-Based Compact (RBC). They have been developed in the last ten years and applied to realistic flow configurations in aerodynamics and aeroacoustics (see [40–42, 101–104, 117]). This section recalls the design principles of RBC schemes for steady compressible flows.
The following discussion is based on [106].

### II.2.1 Concept of residual-based scheme

Let us consider, for simplicity, an initial-value problem for the two-dimensional hyperbolic system of conservation laws:

$$w_t + f_x + g_y = 0 \tag{II.4}$$

where $t$ is the time, $x$ and $y$ are Cartesian space coordinates, $w$ is the state vector and $f = f(w)$, $g = g(w)$ are flux components depending smoothly on $w$. The Jacobian matrices of the flux are denoted $A = \mathrm{d}f/\mathrm{d}w$ and $B = \mathrm{d}g/\mathrm{d}w$. System (II.4) is approximated in space on a uniform mesh $(x_j = j\delta x, y_k = k\delta y)$ with steps $\delta x$ and $\delta y$ of the same order of magnitude, say $\mathcal{O}(h)$, using a *residual-based* (RB) scheme. This is defined as a scheme that can be expressed only in terms of approximations of the exact residual, *i.e.* of the left-hand side of System (II.4). More precisely hereafter we consider RB schemes that present a discrete form of:

$$w_t + f_x + g_y = \frac{\delta x}{2}[\Phi_1(w_t + f_x + g_y)]_x + \frac{\delta y}{2}[\Phi_2(w_t + f_x + g_y)]_y \tag{II.5}$$

The coefficients $\Phi_1$ and $\Phi_2$ are numerical viscosity matrices that depend only on the eigensystems of the Jacobian matrices $A$ and $B$ and on the step ratio $\delta x/\delta y$. They use no tuning parameters or limiters. Their construction is presented in Section II.2.3.
In System (II.5), the exact residual

$$r = w_t + f_x + g_y$$

is everywhere approximated in a space-centered way, but not at the same location or at the same order. The discrete form of (II.5) can be written as

$$\tilde{r}_{j,k} = \tilde{d}_{j,k} \tag{II.6}$$

where $\tilde{r}_{j,k}$ is a space-centered approximation of $r$, called the *main residual* and $\tilde{d}_{j,k}$ is the *residual-based dissipation.*
Let us introduce the way we denote and handle high order approximations in the main residual. Any discrete formula can easily be expressed from combinations of a difference and an average operator over one mesh interval in each space direction, namely

$$(\delta_1 v)_{j+\frac{1}{2},k} = v_{j+1,k} - v_{j,k} \qquad (\delta_2 v)_{j,k+\frac{1}{2}} = v_{j,k+1} - v_{j,k}$$
$$(\mu_1 v)_{j+\frac{1}{2},k} = \frac{1}{2}(v_{j+1,k} + v_{j,k}) \qquad (\mu_2 v)_{j,k+\frac{1}{2}} = \frac{1}{2}(v_{j,k+1} + v_{j,k})$$

where $j$ and $k$ are integers or half integers. All these discrete operators commute. For instance:

$$\begin{aligned}\left(\frac{\delta_1\mu_1 f}{\delta x}\right)_{j,k} &= \left(\frac{\mu_1\delta_1 f}{\delta x}\right)_{j,k} = \frac{f_{j+1,k} - f_{j-1,k}}{2\delta x},\\ (\delta_1^2 f)_{j,k} &= (\delta_1(\delta_1 f))_{j,k} = f_{j+1,k} - 2f_{j,k} + f_{j-1,k}.\end{aligned} \tag{II.7}$$

Using the preceding notations, the discrete dissipation writes:

$$\tilde{d}_{j,k} = \frac{1}{2}[\delta_1(\Phi_1\tilde{r_1}) + \delta_2(\Phi_2\tilde{r_2})]_{j,k} \tag{II.8}$$

where $(\tilde{r_1})_{j+\frac{1}{2},k}$ and $(\tilde{r_2})_{j,k+\frac{1}{2}}$ are space-centered approximations of $r$, called the *mid-point residuals* - see Fig. II.1. Without the notations the dissipation expresses as

$$\tilde{d}_{j,k} = \frac{1}{2}[(\Phi_1\tilde{r_1})_{j+\frac{1}{2},k} - (\Phi_1\tilde{r_1})_{j-\frac{1}{2},k}] + \frac{1}{2}[(\Phi_2\tilde{r_2})_{j,k+\frac{1}{2}} - (\Phi_2\tilde{r_2})_{j,k-\frac{1}{2}}] \tag{II.9}$$

Despite appearance, the order of magnitude of the residual-based dissipation is not simply $\mathcal{O}(h)$ as it could seem from (II.5), but much smaller because the mid-point residuals approximate the exact residual which is everywhere null. Since centered differencing always leads to even order of accuracy, let the mid-point residuals be discretized so that

$$\begin{aligned}(\tilde{r_1})_{j+\frac{1}{2},k} &= r_{j+\frac{1}{2},k} + \mathcal{O}(h^{2p-2}) + \mathcal{O}(\Delta t^l) = \mathcal{O}(h^{2p-2}) + \mathcal{O}(\Delta t^l)\\ (\tilde{r_2})_{j,k+\frac{1}{2}} &= r_{j,k+\frac{1}{2}} + \mathcal{O}(h^{2p-2}) + \mathcal{O}(\Delta t^l) = \mathcal{O}(h^{2p-2}) + \mathcal{O}(\Delta t^l)\end{aligned}$$

where $p$ and $l$ are integers ($p \geqslant 2$, $l \geqslant 1$). Then the residual-based dissipation verifies

$$\tilde{d}_{j,k} = \mathcal{O}(h^{2p-1}) + \mathcal{O}(h\Delta t^l). \tag{II.10}$$

If in addition the main residual is such that

$$\tilde{r}_{j,k} = r_{j,k} + \mathcal{O}(h^{2p}) + \mathcal{O}(\Delta t^l) = \mathcal{O}(h^{2p}) + \mathcal{O}(\Delta t^l)$$

then the truncation error of the scheme (II.6) is

$$\begin{aligned}\varepsilon_{j,k} &= \mathcal{O}(h^{2p}) + \mathcal{O}(\Delta t^l) + \mathcal{O}(h^{2p-1}) + \mathcal{O}(h\Delta t^l)\\ &= \mathcal{O}(h^{2p-1}) + \mathcal{O}(\Delta t^l)\end{aligned} \tag{II.11}$$

and the scheme is accurate at order $2p-1$ in space. Since the spatial approximation of $\tilde{r}$, $\tilde{r_1}$ and $\tilde{r_2}$ will be made using compact formulas, the scheme (II.6) is said to be *residual-based compact* of order $2p-1$ and denoted as $\mathrm{RBC}_{2p-1}$.

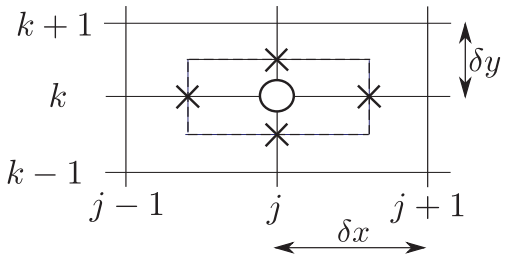


Figure II.1: Location of the discrete residuals, ∘: main residual $\tilde{r}$, ×: mid-point residual $\tilde{r_1}$ or $\tilde{r_2}$

### II.2.2 RBC schemes for steady inviscid problems

For steady flow problems the exact residual would be:

$$r^{steady} = f_x + g_y$$

and the the discrete form (II.6) is written as

$$\frac{w^{n+1} - w^n}{\Delta t} + \tilde{r}_{j,k}^{steady\ n+1} = \tilde{d}_{j,k}^{steady\ n+1} \tag{II.12}$$

where $\tilde{r}_{j,k}^{steady}$ is a space-centered approximation of $r^{steady}$, called the *main residual* and $\tilde{d}_{j,k}^{steady}$ is the residual-based dissipation defined as (II.9) by its *mid-point residuals* and numerical viscosity matrices. The time evolution being reduced to a pure numerical procedure to reach a steady-state solution, we simply use the Backward Euler approximation in time with a large time step. To complete the discretization, we need to introduce approximations for the main and midpoints residuals.

#### II.2.2.1 Approximation of the main residual

We now seek for a high-order centered approximation of the main residual. One way to do this is to use non-compact directional approximation for each derivative separately. For instance, with the preceding notations, the $8^{th}$-order centered approximation at $(j,k)$ of a first derivative of a smooth function ($f \in \mathscr{C}^9$) can be written as:

$$f_x = \left( I - \frac{1}{6}\delta_1^2 + \frac{1}{30}\delta_1^4 - \frac{1}{140}\delta_1^6 \right) \frac{\delta_1 \mu_1 f}{\delta x} + \mathcal{O}(\delta x^8) \tag{II.13}$$

where $I$ is the identity operator and the subscripts $(j,\ k)$ are omitted. This formula has a 9-point stencil (from $j-4, k$ to $j+4, k$). The advantage of the writing (II.13) is to use 3 coefficients only $\left(-\frac{1}{6}, \frac{1}{30}, -\frac{1}{140}\right)$ and to display embedded formulas of lower order: dropping the $\delta^6$ term leads to the $6^{th}$-order approximation, dropping also the $\delta^4$ term leads to the $4^{th}$-order and dropping in addition the $\delta^2$ term gives the $2^{nd}$-order formula (II.7).
Compact approximations can be described similarly by using *Pade fractions* of difference operators. For instance, a $8^{th}$-order centered approximation at $(j,k)$ of a first derivative on a 5-point stencil can be written formally as:

$$f_x = \frac{I + \frac{5}{42}\delta_1^2}{I + \frac{2}{7}\delta_1^2 + \frac{1}{70}\delta_1^4} \frac{\delta_1 \mu_1 f}{\delta x} + \mathcal{O}(\delta x^8) \tag{II.14}$$

The meaning of the above formula is

$$\left( I + \frac{2}{7}\delta_1^2 + \frac{1}{70}\delta_1^4 \right) f_x = \left( I + \frac{5}{42}\delta_1^2 \right) \frac{\delta_1 \mu_1 f}{\delta x} + \mathcal{O}(\delta x^8) \tag{II.15}$$

where both sides are defined on a 5-point stencil. In other words, the "denominator" in (II.14) denotes an operator inversion. An important point is the following one: by expanding the inverse of the denominator $(I + \varepsilon_1)^{-1}$ in terms of the operator $\varepsilon_1 = \frac{2}{7}\delta_1^2 + \frac{1}{70}\delta_1^4 = \mathcal{O}(h^2)$ and taking into account the numerator $I + \frac{5}{42}\delta_1^2$, we recover a non-compact formula which is nothing but (II.13). Conversely, this procedure is useful to determine the coefficients of a compact formula from the knowledge of a non-compact one.

In a compact formula like (II.15), the derivative is usually found by solving a linear algebraic system on each horizontal mesh line $k = cte$. In the present residual-based approach we do not follow this procedure, as we will see below. Finally, it should be emphasized that a compact formula reduces the truncation error with respect to a non-compact one of the same order of accuracy. For instance the remainder $\mathcal{O}(\delta x^8)$ in (II.13) and (II.15) can be expressed as[1]:

$$C\delta x^8 f_{9x}(x_j + \theta\delta x), \qquad \text{with } -4 \leqslant \theta \leqslant 4$$

where the constant $C$ is $-\frac{1}{630}$ for the non compact formula (II.13) and $-\frac{1}{44100}$ for the compact formula (II.15), which is precisely 70 times smaller. Fourier analysis also shows that compactness improves accuracy over the whole spectrum (see Lele [98]).
We now describe the compact treatment of the main residual $\tilde{r}_{j,k}$ in the RBC$_{2p-1}$ scheme. As we have seen in Section II.2.1, the main residual should be approximated at order $2p$. This is done by using the Pade fractions:

$$\begin{aligned}(f_x)_{j,k} &= \left(\frac{\overline{N_1}}{\overline{D_1}}\frac{\delta_1\mu_1 f}{\delta x}\right)_{j,k} + \mathcal{O}(\delta x^{2p}) \\ (g_y)_{j,k} &= \left(\frac{\overline{N_2}}{\overline{D_2}}\frac{\delta_2\mu_2 g}{\delta y}\right)_{j,k} + \mathcal{O}(\delta y^{2p})\end{aligned} \tag{II.16}$$

where $\overline{N_m}$ and $\overline{D_m}$ are formal polynomials of second difference operators:

$$\overline{N_m} = I + \overline{a}\delta_m^2, \qquad \overline{D_m} = I + \overline{b}\delta_m^2 + \overline{c}\delta_m^4, \qquad m = 1, 2, \tag{II.17}$$

The degrees of these polynomials are chosen so that the scheme stencil does not exceed 5×5 points. Both space directions are treated similarly, *i.e.* the polynomials coefficients $\overline{a}$, $\overline{b}$ and $\overline{c}$ are the same for $m = 1$ and 2.
The denominators in (II.16) are eliminated by applying the operator $\overline{D_1}\ \overline{D_2}$ to all the terms. Then, the main residual is defined as:

$$\tilde{r}_{j,k}^{steady} = \left(\overline{D_2}\ \overline{N_1}\frac{\delta_1\mu_1 f}{\delta x} + \overline{D_1}\ \overline{N_2}\frac{\delta_2\mu_2 g}{\delta y}\right)_{j,k}$$

which is really of order $2p$, since

$$\begin{aligned}\tilde{r}_{j,k}^{steady} &= (\overline{D_1}\ \overline{D_2})_{j,k}\left[f_x + g_y + \mathcal{O}(h^{2p})\right] = (\overline{D_1}\ \overline{D_2})_{j,k}\mathcal{O}(h^{2p}) \\ &= \left[I + \mathcal{O}(h^2)\right]\mathcal{O}(h^{2p}) = \mathcal{O}(h^{2p}).\end{aligned}$$

The detailed expression of the main residual is

$$\tilde{r}_{j,k}^{steady} = \left[(I + \overline{b}\delta_2^2 + \overline{c}\delta_2^4)(I + \overline{a}\delta_1^2)\frac{\delta_1\mu_1 f}{\delta x} + (I + \overline{b}\delta_1^2 + \overline{c}\delta_1^4)(I + \overline{a}\delta_2^2)\frac{\delta_2\mu_2 g}{\delta y}\right]_{j,k} \tag{II.18}$$

Several accuracy orders $2p$ can be reached with this expression.
a) Order $2p = 4$ is achievable on a 3×3-point stencil by the choice:

$$\overline{a} = 0, \quad \overline{b} = \frac{1}{6}, \quad \overline{c} = 0. \tag{II.19}$$

which reduces (II.18) to

$$\tilde{r}_{j,k}^{steady} = \left[(I + \frac{1}{6}\delta_2^2)\frac{\delta_1\mu_1 f}{\delta x} + (I + \frac{1}{6}\delta_1^2)\frac{\delta_2\mu_2 g}{\delta y}\right]_{j,k} \tag{II.20}$$

[1] In this thesis, $f_{qx}$ denotes the $q^{th}$-derivative $\frac{\partial^q f}{\partial x^q}$.

b) Order $2p = 6$ can be obtained using

$$\overline{a} = \frac{1}{30} + 6\overline{c}, \quad \overline{b} = \frac{1}{5} + 6\overline{c}$$

which gives a family of the $6^{th}$-order approximations depending on the coefficient $\overline{c}$. The choice $\overline{c} = 0$ is the simplest one, but we retain the one made in [40, 104]:

$$\overline{a} = \frac{1}{10}, \quad \overline{b} = \frac{4}{15}, \quad \overline{c} = \frac{1}{90} \tag{II.21}$$

because it is more suitable for the extension to the compressible Navier-Stokes equations.
c) Finally, order $2p = 8$ (the highest one for a 5×5-point stencil) can be obtained only with

$$\overline{a} = \frac{5}{42}, \quad \overline{b} = \frac{2}{7}, \quad \overline{c} = \frac{1}{70} \tag{II.22}$$

which corresponds to the example of Pade fractions (II.14).

#### II.2.2.2 Approximation of the mid-point residuals

We now consider the dissipation term (II.9). Using the discrete operators introduced in the previous section, it can be rewritten as:

$$\tilde{d}^{steady}_{j,k} = \frac{1}{2}[\delta_1(\Phi_1 \tilde{r}^{steady}_1) + \delta_2(\Phi_2 \tilde{r}^{steady}_2)]_{j,k} \tag{II.23}$$

In theory, the mid-point residuals $(\tilde{r}^{steady}_1)_{j+\frac{1}{2},k}$ and $(\tilde{r}^{steady}_2)_{j,k+\frac{1}{2}}$ are constructed similarly as the main residual. In practice, the treatment is a bit more intricate. First, to define a mid-point residual, say $(\tilde{r}^{steady}_1)_{j+\frac{1}{2},k}$, we have to approximate $f_x$ and to average $g_y$ at the mid location $x = (j + \frac{1}{2})\delta x$, using new types of Pade fractions based on the 2-point difference and average operators $\delta_1$ and $\mu_1$. As mentioned in Section II.2.1, the mid-point residuals are discretized at a lower order than the main residual ($2p - 2$ instead of $2p$). So we introduce:

$$\begin{aligned}
(f_x)_{j+\frac{1}{2},k} &= \left(\frac{N^\delta_1}{D^\delta_1}\frac{\delta_1 f}{\delta x}\right)_{j+\frac{1}{2},k} + \mathcal{O}(\delta x^{2p-2}) \\
(g_y)_{j,k+\frac{1}{2}} &= \left(\frac{N^\delta_2}{D^\delta_2}\frac{\delta_2 g}{\delta y}\right)_{j,k+\frac{1}{2}} + \mathcal{O}(\delta y^{2p-2})
\end{aligned} \tag{II.24}$$

and for any mesh function $v$:

$$\begin{aligned}
(v)_{j+\frac{1}{2},k} &= \left(\frac{N^\mu_1}{D^\mu_1}\mu_1 v\right)_{j+\frac{1}{2},k} + \mathcal{O}(\delta x^{2p-2}) \\
(v)_{j,k+\frac{1}{2}} &= \left(\frac{N^\mu_2}{D^\mu_2}\mu_2 v\right)_{j,k+\frac{1}{2}} + \mathcal{O}(\delta y^{2p-2})
\end{aligned} \tag{II.25}$$

where $N^\delta_m$, $D^\delta_m$, $N^\mu_m$ and $D^\mu_m$ for $m = 1, 2$ are formal polynomials of second difference operators:

$$\begin{aligned}
N^\delta_m &= I + a^\delta \delta^2_m, \quad N^\mu_m = I + a^\mu \delta^2_m \\
D^\delta_m &= I + b^\delta \delta^2_m + c^\delta \delta^4_m, \quad D^\mu_m = I + b^\mu \delta^2_m + c^\mu \delta^4_m.
\end{aligned} \tag{II.26}$$

Another point is that the dissipation has to be defined on a 5×5-point stencil as the main residual. Therefore, the formula (II.23) shows that the mid-point residuals should have smaller stencils.

Namely, $(\tilde{r}_1)_{j+\frac{1}{2},k}$ and $(\tilde{r}_2)_{j,k+\frac{1}{2}}$ should only use 4×5 and 5×4 points, respectively. Fortunately, this is possible because orders $2p-2=2$, 4 and 6 can be achieved with Pade fractions (II.24) having the same denominators, more precisely:

$$D_1^\delta = D_1^\mu \qquad D_2^\delta = D_2^\mu \tag{II.27}$$

Finally, for the approximations of $g_y$ at $j+\frac{1}{2},k$ in $\tilde{r}_1^{steady}$ (respectively of $f_x$ at $j,k+\frac{1}{2}$ in $\tilde{r}_2^{steady}$), we need the average (II.25) in the $x$-direction (resp. in the $y$-direction), but also the classical Pade fractions for a derivative in the $y$-direction (resp. in the $x$-direction). These Pade fractions are analogous to the formulas (II.16) used in the main residual, but they have different coefficients because they require a lower accuracy order ($2p-2$ instead of $2p$). So we introduce new formal polynomials $N_m$, $D_m$ and define:

$$\begin{aligned}(f_x)_{j,k} &= \left(\frac{N_1}{D_1}\frac{\delta_1\mu_1 f}{\delta x}\right)_{j,k} + \mathcal{O}(\delta x^{2p-2}) \\ (g_y)_{j,k} &= \left(\frac{N_2}{D_2}\frac{\delta_2\mu_2 g}{\delta y}\right)_{j,k} + \mathcal{O}(\delta y^{2p-2})\end{aligned} \tag{II.28}$$

where

$$N_m = I + a\delta_m^2, \quad D_m = I + b\delta_m^2 + c\delta_m^4, \;\; m=1,\,2. \tag{II.29}$$

Here the denominators are compatible with the stencils of the mid-point residuals (5 points allowed in the $y$-direction for $\tilde{r}_1$ and in the $x$-direction for $\tilde{r}_2$).
A direct discretization of the exact residual at $j+\frac{1}{2},k$ gives:

$$(f_x+g_y)_{j+\frac{1}{2},k} = \left[\frac{N_1^\mu}{D_1^\mu}\frac{N_2}{D_2}\frac{\mu_1\delta_2\mu_2 g}{\delta y} + \frac{N_1^\delta}{D_1^\delta}\frac{\delta_1 f}{\delta x}\right]_{j+\frac{1}{2},k} + \mathcal{O}(h^{2p-2})$$

By applying the operator $D_1^\mu D_2 = D_1^\delta D_2$ to all the terms, we obtain the first mid-point residual:

$$(\tilde{r}_1^{steady})_{j+\frac{1}{2},k} = \left[N_1^\mu N_2\frac{\mu_1\delta_2\mu_2 g}{\delta y} + N_1^\delta D_2\frac{\delta_1 f}{\delta x}\right]_{j+\frac{1}{2},k} \tag{II.30}$$

Similarly, we get the second mid-point residual:

$$(\tilde{r}_2^{steady})_{j,k+\frac{1}{2}} = \left[N_2^\mu N_1\frac{\mu_2\delta_1\mu_1 f}{\delta x} + N_2^\delta D_1\frac{\delta_2 g}{\delta y}\right]_{j,k+\frac{1}{2}}. \tag{II.31}$$

These residuals are respectively defined on a 4×5 and a 5×4-point stencil. Both can be $\mathcal{O}(h^{2p-2})$ for $p=2$, 3, 4. Their detailed expressions can be written as:

$$\begin{aligned}\tilde{r}_1^{steady} =& (I+b\delta_2^2+c\delta_2^4)(I+a^\delta\delta_1^2)\frac{\delta_1 f}{\delta x} + (I+a^\mu\delta_1^2)(I+a\delta_2^2)\frac{\delta_2\mu_2\mu_1 g}{\delta y} \\ \tilde{r}_2^{steady} =& (I+b\delta_1^2+c\delta_1^4)(I+a^\delta\delta_2^2)\frac{\delta_2 g}{\delta y} + (I+a^\mu\delta_2^2)(I+a\delta_1^2)\frac{\delta_1\mu_1\mu_2 f}{\delta x}.\end{aligned} \tag{II.32}$$

They depend on the five coefficients $a^\mu$, $a^\delta$, $a$, $b$ and $c$, the values of which will be given in Section III.3 and III.4. Note that all sets of possible coefficients are given in [40] for steady flow problems.

### II.2.3 Dissipation matrices

The numerical viscosity matrices $\Phi_1$ and $\Phi_2$ in the residual-based dissipation were designed for the solution of steady flow problems. For these problems, the scheme becomes a discrete form of

$$w_t + f_x + g_y = d^{steady} \tag{II.33}$$

where

$$d^{steady} = \frac{\delta x}{2}[\Phi_1(f_x + g_y)]_x + \frac{\delta y}{2}[\Phi_2(f_x + g_y)]_y \tag{II.34}$$

The time evolution being reduced to a numerical procedure to reach a steady-state solution, we simply use the Backward Euler approximation in time with a large time step. During the convergence to the steady-state, note that the residual-based scheme is also first-order in space because of the lack of $w_t$ in (II.34). This ensures robustness to the scheme in the convergence process. At steady-state, the scheme recovers the high accuracy order of the spatial approximation.
It is clear that some conditions should be satisfied by $\Phi_1$ and $\Phi_2$ in order that (II.34) be actually dissipative. The term $d^{steady}$ can be rewritten as:

$$d^{steady} = \frac{\delta x}{2}(\Phi_1 A w_x + \Phi_1 B w_y)_x + \frac{\delta y}{2}(\Phi_2 A w_x + \Phi_2 B w_y)_y \tag{II.35}$$

Consider the case where $A$, $B$, $\Phi_1$ and $\Phi_2$ are scalar constants. Then (II.35) reduces to

$$d^{steady} = \mathscr{D}^{steady} w$$

with the linear partial differential operator of second order:

$$\mathscr{D}^{steady} = \frac{\delta x}{2}\Phi_1 A\frac{\partial^2}{\partial x^2} + \frac{1}{2}(\delta x \Phi_1 B + \delta y \Phi_2 A)\frac{\partial^2}{\partial x \partial y} + \frac{\delta y}{2}\Phi_2 B\frac{\partial^2}{\partial y^2}$$

which contains the highest derivatives of (II.35). The Fourier symbol of $\mathscr{D}^{steady}$ is:

$$\hat{\mathscr{D}}^{steady} = -\frac{1}{2}\left[\delta x \Phi_1 A\xi^2 + (\delta x \Phi_1 B + \delta y \Phi_2 A)\xi\eta + \delta y \Phi_2 B\eta^2\right] \tag{II.36}$$

where $\xi$ and $\eta$ are the wave numbers (Fourier variables).
By dissipation (in the broad sense), we mean:

$$\forall \xi \in \mathbb{R},\ \forall \eta \in \mathbb{R}, \qquad \hat{\mathscr{D}}^{steady}(\xi, \eta) \leqslant 0,$$

that is $d^{steady}$ damps any Fourier mode.
For $\xi = 0$, the above dissipation condition leads to $\Phi_2 B \geqslant 0$. For $\xi \neq 0$, we can rewrite (II.36) as:

$$\hat{\mathscr{D}}^{steady}(\xi, \eta) = -\frac{\xi^2}{2}\mathcal{D}(\xi, \eta)$$

with

$$\mathcal{D}(\xi, \eta) = \delta x \Phi_1 A + (\delta x \Phi_1 B + \delta y \Phi_2 A)\left(\frac{\eta}{\xi}\right) + \delta y \Phi_2 B\left(\frac{\eta}{\xi}\right)^2$$

Clearly, $\mathcal{D}$ is always positive if and only if

$$\Phi_2 B \geqslant 0 \text{ and } \Delta \leqslant 0$$

where

$$\Delta = (\delta x \Phi_1 B + \delta y \Phi_2 A)^2 - 4\delta x \Phi_1 A \delta y \Phi_2 B = (\delta x \Phi_1 B - \delta y \Phi_2 A)^2.$$

Thus, the necessary and sufficient conditions to get dissipation are $\Phi_2 B \geqslant 0$ and $\Delta = 0$, which can also be expressed as:

$$\begin{gathered} \Phi_1 A \geqslant 0, \quad \Phi_2 B \geqslant 0 \\ \delta x \Phi_1 B = \delta y \Phi_2 A \end{gathered} \tag{II.37}$$

Introducing the notations

$$\begin{gathered} \Phi_1 = \mathrm{sgn}(A)\Phi,\ \Phi_2 = \mathrm{sgn}(B)\Psi \\ \alpha = \frac{\delta x |B|}{\delta y |A|}, \end{gathered} \tag{II.38}$$

the dissipation conditions (II.37) become:

$$\Phi \geqslant 0,\ \Psi = \alpha \Phi. \tag{II.39}$$

Note that the parameter $\alpha$ characterizes the local advection direction with respect to the mesh. For $\alpha = 1$, the advection takes place along the mesh diagonal. For $\alpha < 1$, it takes place between the $x$-direction and a mesh diagonal and for $\alpha > 1$ between the $y$-direction and a mesh diagonal. Various choices of $\Phi$ satisfying (II.39) are possible. An optimal one proposed in [102] is:

$$\Phi = \min\left(1, \frac{1}{\alpha}\right),\ \Psi = \alpha\Phi = \min(1, \alpha). \tag{II.40}$$

These functions make use of no tuning parameter and only depend on the local advection direction $\alpha$. For hyperbolic systems of conservation laws, the matrix functions $\Phi_1$ and $\Phi_2$ are defined through a direct extension of the scalar case: the eigenvectors of $\Phi_1$ are those of the Jacobian matrix $A$ – evaluated at some suitable intermediate state–, the eigenvectors of $\Phi_2$ are those of $B$ and the eigenvalues of $\Phi_1$ and $\Phi_2$ are deduced from the above scalar definitions. More precisely, let $T_A$ (respectively $T_B$) be a matrix the columns of which are the right eigenvectors of $A$ (resp. $B$) and let $a^{(i)}$ (resp. $b^{(i)}$) be the eigenvalues of $A$ (resp. $B$). Matrices $\Phi_1$ and $\Phi_2$ are then defined as

$$\Phi_1 = T_A \mathrm{Diag}[\phi_1^{(i)}] T_A^{-1},\ \Phi_2 = T_B \mathrm{Diag}[\phi_2^{(i)}] T_B^{-1}$$

with

$$\begin{gathered} \phi_1^{(i)} = \mathrm{sgn}(a^{(i)})\phi^{(i)},\ \phi_2^{(i)} = \mathrm{sgn}(b^{(i)})\psi^{(i)} \\ \phi^{(i)} = \min\left(1, \frac{\delta y |a^{(i)}|}{\delta x\ \mathrm{m}(B)}\right),\ \psi^{(i)} = \min\left(1, \frac{\delta x |b^{(i)}|}{\delta y\ \mathrm{m}(A)}\right) \end{gathered}$$

where $\mathrm{Diag}[d^{(i)}]$ denotes a diagonal matrix with diagonal entries $d^{(i)}$ and $\mathrm{m}(A) = \min_i |a^{(i)}|$, $\mathrm{m}(B) = \min_i |b^{(i)}|$.

### II.2.4 Extension to the Navier Stokes equations

We now consider the steady Navier-Stokes equation introduced in Section II.1.1:

$$(f^E - f^V)_x + (g^E - g^V)_x = 0 \text{ on } \Omega_t = \mathbb{R}^2 \times \mathbb{R}^+ \tag{II.41}$$

Viscous RBC schemes are defined by (II.6). Only the definition of the main and mid-points residuals are modified. The exact residual is:

$$r = (f^E - f^V)_x + (g^E - g^V)_x \tag{II.42}$$

For the discretisation of viscous terms, both a second-order and a high-order approximation formula can be constructed [104]. In the present work, we restrict our analysis to a standard second-order approximation of the viscous fluxes for the main residual and the mid-point residuals.

#### II.2.4.1 Approximation of the main residual

The compact treatment of Euler fluxes is the one detailed in Section II.2.2. We now describe the compact treatment of the viscous terms at order 2. This is done by using the Pade fractions:

$$\begin{aligned}(f_x^V)_{j,k} &= \left(\frac{I}{\overline{D_1}\ \overline{D_2}}\frac{\delta_1 f^V}{\delta x}\right)_{j,k} + \mathcal{O}(\delta x^2)\\ (g_y^V)_{j,k} &= \left(\frac{I}{\overline{D_1}\ \overline{D_2}}\frac{\delta_2 g^V}{\delta y}\right)_{j,k} + \mathcal{O}(\delta y^2)\end{aligned} \tag{II.43}$$

where $\overline{D_m}$ are the formal polynomials introduced in Section II.2.2, $f^V$ and $g^V$ are the viscous fluxes approximated at cell faces through with mean and difference operators. Consequently, the main residual $\tilde{r_0}$ is approximated through a difference operator of the form:

$$(\tilde{r_0})_{j,k} = \left[\frac{\delta_1}{\delta x}\left(\overline{D_2}\ \overline{N_1}\mu_1 f^E - f^V\right) + \frac{\delta_2}{\delta y}\left(\overline{D_1}\ \overline{N_2}\mu_2 g^E - g^V\right)\right]_{j,k} \tag{II.44}$$

and errors introduced by $\tilde{r_0}$ are an error of order $2p-1$ for $\mathrm{RBC}_{2p-1}$ only dependent of Euler fluxes and an error of order two function only of the viscous terms. The truncation error of (II.44) is indeed

$$\varepsilon_{j,k} = \left[I + \mathcal{O}(h^2)\right]\left[r_{j,k} + \mathcal{O}(h^{2p})\mathcal{L}^E(f^E, g^E) + \mathcal{O}(h^2)\mathcal{L}^V(f^V, g^V)\right] \tag{II.45}$$

where $\mathcal{L}^E(.,.)$ and $\mathcal{L}^V(.,.)$ are linear differential operators since $\overline{D_1}\ \overline{D_2} = [I + \mathcal{O}(h^2)]$.

#### II.2.4.2 Approximation of the mid-point residuals

The dissipation operator $\tilde{d}_{j,k}$ is given again by Eq. (II.9). The Pade fractions (II.43) are used here for the discretization of viscous terms in the mid-point residuals residuals. Precisely, the following difference operators define the mid-point residuals:

$$\begin{aligned}(\tilde{r_1})_{j+\frac{1}{2},k} &= \left[\frac{\delta_2}{\delta y}\left(N_1^\mu N_2\mu_1\mu_2 g^E - \mu_2 g^{V_1}\right) + \frac{\delta_1}{\delta x}\left(N_1^\delta D_2 f^E - \mu_1 f^{V_1}\right)\right]_{j+\frac{1}{2},k}\\ (\tilde{r_2})_{j,k+\frac{1}{2}} &= \left[\frac{\delta_1}{\delta x}\left(N_2^\mu N_1\mu_2\mu_1 f^E - \mu_1 f^{V_2}\right) + \frac{\delta_2}{\delta y}\left(N_2^\delta D_1 g^E - \mu_2 g^{V_2}\right)\right]_{j,k+\frac{1}{2}}\end{aligned} \tag{II.46}$$

where $f^{V_d}$ and $g^{V_d}$ are viscous fluxes $f^V$ and $g^V$ evaluated at the center of a cell face in the $d^{th}$-direction of the mesh. The notations are based again on the use of formal polynomials introduced in Section II.2.2. Here, the error introduced by viscous terms is of order three and the error introduced by Euler terms is of order $2p-1$ for $\mathrm{RBC}_{2p-1}$.
Finally, the use of complex Pade fractions to discretize the viscous terms at order two leads us to a very simple extension of RBC schemes to Navier-Stokes equations.

## II.3 Chapter summary

In this Chapter, we have layed out a brief overview of the physical models for compressible flows used in the present work. Then we have presented the formulations of RBC schemes for steady compressible inviscid and viscous flows. RBC schemes are compact approximations that provide high accuracy not for each space derivative treated apart but for the complete residual $r$. RBC schemes are defined by a space-centered approximation $\tilde{r_0}$ called the *main residual* and a residual-based dissipation term $\tilde{d}$. They are both built on derivatives of the residual $r$ that becomes high-order accurate as $r$ tends to 0. We have denoted RBC$q$ the RBC scheme of order $q$ ($q = 3, 5, 7$). With this notations, RBC3 scheme can be constructed with $3 \times 3$ points only and RBC5 and RBC7 schemes with $5 \times 5$ points.
Difficulties arise when these formulations of RBC schemes are extended to unsteady problem in a straightforward manner, apparently because a weak instability may appear for some flow conditions. In the next Chapter, we present the design of high-order RBC schemes for unsteady compressible flows, along with a comprehensive study of their dissipation properties. We then go further with the investigation of the dissipation and dispersion resolvability properties of RBC schemes through a detailed analysis of their Fourier spectra. Numerical exemples will further illustrate the theoretical results.

# Chapter III

# Design of high order RBC schemes for unsteady compressible flows

**Contents**

## III.1 Introduction

A special feature of RBC schemes is the use of a numerical dissipation term also constructed from the complete residual $r$. This unusual dissipation gives to RBC schemes special properties that have not been fully analyzed so far. In practice, the RBC schemes are robust for steady flow computations (*cf.* Section II.2.2.2), but some of them may have difficulties for unsteady problems, apparently due to a weak instability. In this chapter, we present a comprehensive study of the residual-based dissipation term of high-order RBC schemes for the unsteady Euler equations. The study provides a deeper insight of the dissipation mechanism, provides a mathematical criterion (called $\chi$-criterion) characterizing the dissipation for 2-D and 3-D problems and restores the stability of RBC schemes for unsteady problems. Given the importance of numerical dissipation in Computational Fluid Dynamics, it is also hoped that the present work could help the development of other classes of high-order schemes.
A peculiarity of the present RBC schemes is to use three independent compact approximations of the residual (four in 3-D). One applies to the usual residual at the current location $j, k$ (main residual). The two others are involved in the dissipation and defined at location $j+\frac{1}{2}, k$ or $j, k+\frac{1}{2}$ (mid-point residuals). A correct choice of the discretization of the mid-point residuals is essential to ensure dissipation for all flow conditions. This is why we try here to identify the effective dissipation operator, which is not obvious for a RBC scheme since the dissipation operator comes from high order expansions of the mid-point residuals. Then we move a further step toward the understanding of the numerical properties of high-order RBC discretizations by looking into their spectral behaviorn and the introduced dispersion and diffusion errors. The dissipation analysis of RBC schemes is done in two stages, in Section III.3 and III.4 respectively, for RBC schemes of order $2p-1 = 3$, 5 and 7. In Section III.5, the dissipation operator is cast into a general form (2-D partial differential operator of degree $2p$) and a necessary and sufficient condition, the $\chi$-criterion, is found for this operator be always dissipative. Application of this criterion to the RBC schemes gives the correct coefficients to use in the high-order approximations of the mid-point residuals. A complete extension of the analysis to three space-dimension is presented in Section III.6. In Section III.7, the $\chi$-criterion is confirmed through a Von Neumann stability analysis then interpreted in Section III.8. In section III.9.2 we derive the spectral counterparts of the RBC schemes and discuss their dissipation and dispersion properties. Finally, numerical experiments are presented in Section III.10 to confirm the relevance of the $\chi$-criterion and supporting the theoretical analysis on spectral properties of RBC schemes.
The material presented in this chapter has been published in two refered international journal articles [68, 106].

## III.2 Straightforward extension to unsteady problem

Consider the initial-value problem for the hyperbolic system of conservation laws:

$$w_t + f_x + g_y = 0$$

The exact residual is:

$$r = w_t + f_x + g_y$$

A straightforward extension of steady RBC schemes to unsteady problems is to solve the above unsteady equation as a steady one with a residual vanishing at steady state in a dual time framework as proposed in [40, 41]. To enable this resolution the evolution problem is modified by adding a derivative with respect to a dual time framework $\tau$:

$$w_\tau + w_t + f_x + g_y = 0. \tag{III.1}$$

As seen in Section II.2.1 in the truncation error (II.11) of a general RBC scheme the error due to the spatial and temporal derivative can be uncoupled in the truncation error. Thus, at this stage, we treat time derivatives exactly, i.e. we focus on semi-discrete approximations in space. Using the Pade fraction presented in II.2.2 the main residual and mid-point residuals approximations expresses as:

$$\begin{aligned}
(\tilde{r_0})_{j,k} &= \left[\overline{D_1}\ \overline{D_2} w_t + \overline{D_2}\ \overline{N_1}\frac{\delta_1\mu_1 f}{\delta x} + \overline{D_1}\ \overline{N_2}\frac{\delta_2\mu_2 g}{\delta y}\right]_{j,k} \\
(\tilde{r_1})_{j+\frac{1}{2},k} &= \left[D_2 N_1^{\mu}\mu_1 w_t + N_1^{\mu} N_2\frac{\mu_1\delta_2\mu_2 g}{\delta y} + N_1^{\delta} D_2\frac{\delta_1 f}{\delta x}\right]_{j+\frac{1}{2},k} \\
(\tilde{r_2})_{j,k+\frac{1}{2}} &= \left[D_1 N_2^{\mu}\mu_2 w_t + N_2^{\mu} N_1\frac{\mu_2\delta_1\mu_1 f}{\delta x} + N_2^{\delta} D_1\frac{\delta_2 g}{\delta y}\right]_{j,k+\frac{1}{2}}
\end{aligned} \tag{III.2}$$

In a first approach one can use the formal polynomials used for steady RBC schemes as in [40, 101].
For steady flow problems, it is clear that the operator $d^{steady}$ in (II.34) with the numerical viscosity matrices $\Phi_1$ and $\Phi_2$ ensures dissipation. As a matter of fact, its use has led to successful calculations of various steady flow problems (see [101, 103] for instance).
For unsteady simulations, the time derivative is included in the dissipation operator as in (II.5) and the viscosity matrices are kept unchanged. This has allowed the solution of the Euler equations using RBC schemes of order 5 and 7 for shock-vortex interaction [40], the computation of some turbomachinery flows using RBC3 [117] and a 3D propagation of spinning acoustic modes in an aeroengine inlet using RBC7 [101]. However for the later case, a $10^{th}$-order azimuthal filtering was necessary. Other unsteady applications to turbomachinery flows were difficult, even with the RBC scheme of order 3, so that a weak instability of the unsteady scheme can be suspected. This is the reason why a deeper insight of the dissipation mechanism is needed.
For the unsteady scheme, the discrete operator $\tilde{d}_{j,k}$ represents the differential operator:

$$d = \frac{\delta x}{2}[\Phi_1(w_t + f_x + g_y)]_x + \frac{\delta y}{2}[\Phi_2(w_t + f_x + g_y)]_y \tag{III.3}$$

which cannot be viewed as the real dissipation since it is identically null! So the effect of $\tilde{d}_{j,k}$ must be identified by expanding it further in space and time. For a $\mathrm{RBC}_{2p-1}$ scheme, the dissipation $\tilde{d}_{j,k}$ is of order $h^{2p-1}$ in space -see (II.10)-. To identify it, the centered term $\tilde{d}_{j,k}$ must be expanded up to a remainder $\mathcal{O}(h^{2p+1})$. Concerning the expansion in time, the expression (II.11) of the truncation error of the global scheme shows that the leading term in space comes from the dissipation and the leading term in time from the main residual. Therefore, the dissipation operator can finally be studied by expanding $\tilde{d}_{j,k}$ in space only, that is by keeping the time derivative continuous in the dissipation. In other words, a semi-discrete analysis of the dissipation (based on the expression (II.32) of the mid-point residuals) is sufficient for studying its effect on the scheme. For a better understanding of the role of the different contributions in the dissipation, this semi-discrete analysis will be done in two stages: in the following section, we restrict our attention to the role of the $x$-discretization in $\tilde{r}_1$ and of the role of the $y$-discretization in $\tilde{r}_2$ and, in the section after, we complete the analysis by adding the effect of the remaining spatial discrete terms.

## III.3 Partial analysis of the RBC dissipation

### III.3.1 Partial residual $\tilde{r_1}^x$

Here, we discretize at $(j+\frac{1}{2},k)$ the $x$-derivative as in (II.24) and the $x$-average as in (II.25), but we keep the $y$-derivative continuous (we do not use (II.28)). Then the mid-point residual $\tilde{r}_1$ defined in (II.30) takes the partial form:

$$\begin{aligned}(\tilde{r_1}^x)_{j+\frac{1}{2},k} &= \left[N_1^\mu \mu_1(w_t+g_y) + N_1^\delta \frac{\delta_1 f}{\delta x}\right]_{j+\frac{1}{2},k} \\ &= \left[(I+a^\mu\delta_1^2)\mu_1(w_t+g_y) + (I+a^\delta\delta_1^2)\frac{\delta_1 f}{\delta x}\right]_{j+\frac{1}{2},k}\end{aligned} \tag{III.4}$$

We now carry out a Taylor expansion of $\tilde{r_1}^x$ around $(j+\frac{1}{2})\delta x$. Provided the exact residual is sufficiently smooth, we obtain after some algebra:

$$N_1^\mu \mu_1 v = v + \frac{\delta x^2}{8}(1+8a^\mu)v_{xx} + \frac{\delta x^4}{384}(1+80a^\mu)v_{4x} + \frac{\delta x^6}{46080}(1+728a^\mu)v_{6x} + \mathcal{O}(\delta x^8), \tag{III.5}$$

where $v = w_t + g_y$ and,

$$N_1^\delta \frac{\delta_1 f}{\delta x} = f_x + \frac{\delta x^2}{24}(1+24a^\delta)f_{xxx} + \frac{\delta x^4}{1920}(1+240a^\delta)f_{5x} + \frac{\delta x^6}{322560}(1+2184a^\delta)f_{7x} + \mathcal{O}(\delta x^8). \tag{III.6}$$

For brevity, the subscript $(j+\frac{1}{2},k)$ has been omitted. Summing (III.5) and (III.6) gives:

$$\begin{aligned}\tilde{r_1}^x = r &+ \frac{\delta x^2}{8}(1+8a^\mu)r_{xx} + \delta x^2\left(a^\delta - a^\mu - \frac{1}{12}\right)f_{xxx} \\ &+ \frac{\delta x^4}{384}(1+80a^\mu)r_{4x} + \frac{\delta x^4}{24}\left(3a^\delta - 5a^\mu - \frac{1}{20}\right)f_{5x} \\ &+ \frac{\delta x^6}{46080}(1+728a^\mu)r_{6x} + \frac{\delta x^6}{5760}\left(39a^\delta - 91a^\mu - \frac{3}{28}\right)f_{7x} + \mathcal{O}(\delta x^8)\end{aligned} \tag{III.7}$$

with the exact residual $r = w_t + f_x + g_y = v + f_x$. Since $r$ is null everywhere for an exact unsteady solution, $\tilde{r_1}^x$ at $(j+\frac{1}{2},k)$ reduces to:

$$\tilde{r_1}^x = \delta x^2\left(a^\delta - a^\mu - \frac{1}{12}\right)f_{xxx} + \frac{\delta x^4}{24}\left(3a^\delta - 5a^\mu - \frac{1}{20}\right)f_{5x} + \frac{\delta x^6}{5760}\left(39a^\delta - 91a^\mu - \frac{3}{28}\right)f_{7x} + \mathcal{O}(\delta x^8) \tag{III.8}$$

which no longer contains $t$ and $y$-derivatives.

### III.3.2 Partial residual $\tilde{r_2}^y$

Similarly, we restrict the mid-point residual $\tilde{r}_2$ to the partial form:

$$\begin{aligned}(\tilde{r_2}^y)_{j,k+\frac{1}{2}} &= \left[N_2^\mu \mu_2(w_t+f_x) + N_2^\delta \frac{\delta_2 g}{\delta y}\right]_{j,k+\frac{1}{2}} \\ &= \left[(I+a^\mu\delta_2^2)\mu_2(w_t+f_x) + (I+a^\delta\delta_2^2)\frac{\delta_2 g}{\delta y}\right]_{j,k+\frac{1}{2}}\end{aligned} \tag{III.9}$$

Carrying out similar Taylor expansions at $(j,k+\frac{1}{2})$ as above, we obtain

$$\tilde{r_2}^y = \delta y^2\left(a^\delta - a^\mu - \frac{1}{12}\right)g_{yyy} + \frac{\delta y^4}{24}\left(3a^\delta - 5a^\mu - \frac{1}{20}\right)g_{5y} + \frac{\delta y^6}{5760}\left(39a^\delta - 91a^\mu - \frac{3}{28}\right)g_{7y} + \mathcal{O}(\delta y^8) \tag{III.10}$$

### III.3.3 Partial dissipation $\tilde{d}^{x,y}$

Inserting the partial residuals (III.4) and (III.69) in the dissipation (II.23) gives the partial dissipation term:

$$\tilde{d}^{x,y}_{j,k} = \frac{1}{2}[\delta_1(\Phi_1 \tilde{r_1}^x) + \delta_2(\Phi_2 \tilde{r_2}^y)]_{j,k} \tag{III.11}$$

a) For $a^\delta - a^\mu \neq \frac{1}{12}$, the partial mid-point residuals are $\mathcal{O}(h^2)$.
If

$$a^\delta = a^\mu = 0 \tag{III.12}$$

then these residuals reduce to 2-point formulas and from the expansions (III.68) and (III.72), we obtain:

$$\tilde{r_1}^x = -\frac{\delta x^2}{12} f_{xxx} + \mathcal{O}(\delta x^4), \quad \tilde{r_2}^y = -\frac{\delta y^2}{12} g_{yyy} + \mathcal{O}(\delta y^4) \tag{III.13}$$

Therefore the partial dissipation involves only $3 \times 3$-points and expands as:

$$\tilde{d}^{x,y} = -\frac{1}{24}[\delta x^3 (\Phi_1 f_{xxx})_x + \delta y^3 (\Phi_2 g_{yyy})_y] + \mathcal{O}(h^5) \tag{III.14}$$

b) For

$$a^\delta - a^\mu = \frac{1}{12} \text{ and } a^\mu \neq \frac{1}{10} \tag{III.15}$$

the mid-point residuals are $\mathcal{O}(h^4)$ and expand as:

$$\tilde{r_1}^x = \frac{\delta x^4}{12}\left(\frac{1}{10} - a^\mu\right) f_{5x} + \mathcal{O}(\delta x^6), \; \tilde{r_2}^y = \frac{\delta y^4}{12}\left(\frac{1}{10} - a^\mu\right) g_{5y} + \mathcal{O}(\delta y^6) \tag{III.16}$$

so that the partial dissipation is represented by:

$$\tilde{d}^{x,y} = \frac{1}{24}\left(\frac{1}{10} - a^\mu\right)[\delta x^5 (\Phi_1 f_{5x})_x + \delta y^5 (\Phi_2 g_{5y})_y] + \mathcal{O}(h^7) \tag{III.17}$$

c) Finally, for

$$a^\mu = \frac{1}{10} \text{ and } a^\delta = \frac{11}{60} \tag{III.18}$$

we obtain:

$$\tilde{r_1}^x = -\frac{\delta x^6}{2800} f_{7x} + \mathcal{O}(\delta x^8), \qquad \tilde{r_2}^y = -\frac{\delta y^6}{2800} g_{7y} + \mathcal{O}(\delta y^8) \tag{III.19}$$

and

$$\tilde{d}^{x,y} = -\frac{1}{5600}[\delta x^7 (\Phi_1 f_{7x})_x + \delta y^7 (\Phi_2 g_{7y})_y] + \mathcal{O}(h^9) \tag{III.20}$$

In this first stage of the analysis, we have obtained the dissipation contribution due to the approximation in the main direction of each mid-point residual. This intermediate result is useful to simplify the global analysis, but above all it will be important for the interpretation of the $\chi$-criterion for dissipation in Section III.5.

## III.4 Full analysis of the RBC dissipation

### III.4.1 Residuals $\tilde{r}_1$ and $\tilde{r}_2$

We consider the complete mid-point residuals (II.30), (II.31). A Taylor expansion of $\tilde{r}_1$ can easily be obtained from the one of $\tilde{r}_1^x$ by noting that (II.28) yields

$$N_2 \frac{\delta_2 \mu_2 g}{\delta y} = D_2(g_y + \varepsilon_2), \quad \varepsilon_2 = \mathcal{O}(\delta y^{2p-2}) \tag{III.21}$$

so that $\tilde{r}_1$ can be related to $\tilde{r}_1^x$ as

$$\tilde{r}_1 = D_2(\tilde{r}_1^x + N_1^\mu \mu_1 \varepsilon_2).$$

Since $N_1^\mu$ and $D_2$ are consistent with the identity plus second order terms, whereas $\tilde{r}_1^x$ and $\varepsilon_2$ are $\mathcal{O}(h^{2p-2})$ for $p \geqslant 2$, we get

$$\tilde{r}_1 = \tilde{r}_1^x + \mu_1 \varepsilon_2 + \mathcal{O}(h^{2p}). \tag{III.22}$$

Similarly, using

$$N_1 \frac{\delta_1 \mu_1 f}{\delta x} = D_1(f_x + \varepsilon_1), \quad \varepsilon_1 = \mathcal{O}(\delta x^{2p-2}) \tag{III.23}$$

we get

$$\tilde{r}_2 = \tilde{r}_2^y + \mu_2 \varepsilon_1 + \mathcal{O}(h^{2p}). \tag{III.24}$$

The simple relations (III.22) and (III.24) are used below to obtain the full dissipation term $\tilde{d}$ of the $\text{RBC}_{2p-1}$ schemes, for $p = 2$, 3 and 4.

### III.4.2 Dissipation for RBC3

The RBC3 scheme is constructed on a 3×3-point stencil from the $4^{th}$-order main residual (II.20) and from a $3^{rd}$-order dissipation based on $2^{nd}$-order mid-point residuals defined by (II.32) with

$$a^\delta = a^\mu = a = c = 0, \tag{III.25}$$

that is

$$\begin{aligned} \tilde{r}_1 =& (I + b\delta_2^2)\left(\mu_1 w_t + \frac{\delta_1 f}{\delta x}\right) + \frac{\delta_2 \mu_2 \mu_1 g}{\delta y} \\ \tilde{r}_2 =& (I + b\delta_1^2)\left(\mu_2 w_t + \frac{\delta_2 g}{\delta y}\right) + \frac{\delta_1 \mu_1 \mu_2 f}{\delta x} \end{aligned} \tag{III.26}$$

the stencils of which use 2×3 and 3×2-points, respectively. Thus, the RBC3 dissipation depends on the parameter $b$ only. Its simplest form corresponds to $b = 0$. This choice was made in the first paper on residual-based schemes [102], focussed on the calculation of steady compressible flows. As we discussed in Section II.2.2.2, any consistent approximation of $d^{steady}$ is dissipative with the numerical viscosity matrices given in Section II.2.3. However for unsteady problems, the RBC3 dissipation with $b = 0$ is not always dissipative as we will prove through the study of the dissipation for any $b$.

Let us now complete the expansion of the mid-point residuals (III.26) using the relations (III.22), (III.24) and the expansions (III.75) of $\tilde{r}_1^x$ and $\tilde{r}_2^y$ for $a^\delta = a^\mu = 0$. A classical expansion of the Pade approximations (III.21), (III.23) with $a = c = 0$ gives the error terms:

$$\varepsilon_1 = \left(\frac{1}{6} - b\right)\delta x^2 f_{xxx} + \mathcal{O}(\delta x^4),\ \varepsilon_2 = \left(\frac{1}{6} - b\right)\delta y^2 g_{yyy} + \mathcal{O}(\delta y^4),$$

so that we obtain:

$$\tilde{r_1} = -\frac{\delta x^2}{12} f_{xxx} + \left(\frac{1}{6} - b\right) \delta y^2 g_{yyy} + \mathcal{O}(h^4)$$
$$\tilde{r_2} = -\frac{\delta y^2}{12} g_{yyy} + \left(\frac{1}{6} - b\right) \delta x^2 f_{xxx} + \mathcal{O}(h^4).$$

Inserting these expansions in the definition (II.23) of $\tilde{d}$, we find the effective RBC3 dissipation term for unsteady problems:

$$\tilde{d} = -\kappa[\Phi_1(\delta x^3 f_{xxx} + \chi \delta x \delta y^2 g_{yyy})]_x - \kappa[\Phi_2(\delta y^3 g_{yyy} + \chi \delta y \delta x^2 f_{xxx})]_y + \mathcal{O}(h^5) \tag{III.27}$$

with the coefficients

$$\kappa = \frac{1}{24}, \quad \chi = 2(6b - 1).$$

The dissipative nature of this term depends on the parameter $b$ and will be studied in the general framework of Section III.5.

### III.4.3 Dissipation for RBC5

The RBC5 scheme is constructed on a 5×5-point stencil from the $6^{th}$-order main residual (II.18) with (II.21) and a $5^{th}$-order dissipation based on $4^{th}$-order mid-point residuals defined by (II.32) with $a^\delta$ and $a^\mu$ related by (III.78). For the error terms $\varepsilon_1$ and $\varepsilon_2$ in (III.21), (III.23) be $\mathcal{O}(h^4)$, we prescribe

$$b - a = \frac{1}{6} \tag{III.28}$$

which precisely gives:

$$\varepsilon_1 = \left(\frac{b}{6} - c - \frac{1}{30}\right) \delta x^4 f_{5x} + \mathcal{O}(\delta x^6)$$

and a similar expression for $\varepsilon_2$. By plugging these results in Eqs (III.22), (III.24) and by using the expansions (III.79), we obtain:

$$\begin{aligned} \tilde{r_1} =& \frac{1}{12}(\frac{1}{10} - a^\mu)\delta x^4 f_{5x} + \left(\frac{b}{6} - c - \frac{1}{30}\right) \delta y^4 g_{5y} + \mathcal{O}(h^6) \\ \tilde{r_2} =& \frac{1}{12}(\frac{1}{10} - a^\mu)\delta y^4 g_{5y} + \left(\frac{b}{6} - c - \frac{1}{30}\right) \delta x^4 f_{5x} + \mathcal{O}(h^6) \end{aligned} \tag{III.29}$$

Inserting (III.29) in (II.23), we get the effective RBC5 dissipation term for unsteady problems:

$$\tilde{d} = \kappa[\Phi_1(\delta x^5 f_{5x} + \chi \delta x \delta y^4 g_{5y})]_x + \kappa[\Phi_2(\delta y^5 g_{5y} + \chi \delta y \delta x^4 f_{5x})]_y + \mathcal{O}(h^7) \tag{III.30}$$

with the coefficients

$$\kappa = \frac{1}{24}(\frac{1}{10} - a^\mu), \quad \chi = \frac{1}{2\kappa}\left(\frac{b}{6} - c - \frac{1}{30}\right).$$

and $a^\mu < 1/10$.

### III.4.4 Dissipation for RBC7

The RBC7 scheme is constructed on a 5×5-point stencil from the $8^{th}$-order main residual (II.18) with (II.22) and a $7^{th}$-order dissipation based on $6^{th}$-order mid-point residuals defined by (II.32) with $a^{\delta}$ and $a^{\mu}$ given by (III.80). For the error terms $\varepsilon_1$ and $\varepsilon_2$ in (III.21), (III.23) be $\mathcal{O}(h^6)$, we impose

$$b - a = \frac{1}{6}, \quad \frac{b}{6} - c = \frac{1}{30} \tag{III.31}$$

so that

$$\varepsilon_1 = \frac{1}{30}\left(\frac{1}{70} - c\right)\delta x^6 f_{7x} + \mathcal{O}(\delta x^8)$$

and similarly for $\varepsilon_2$. By using the relations (III.22), (III.24) and the expansion (III.19), we obtain:

$$\begin{aligned} \tilde{r_1} &= -\frac{\delta x^6}{2800} f_{7x} + \frac{1}{30}\left(\frac{1}{70} - c\right)\delta y^6 g_{7y} + \mathcal{O}(h^8) \\ \tilde{r_2} &= -\frac{\delta y^6}{2800} g_{7y} + \frac{1}{30}\left(\frac{1}{70} - c\right)\delta x^6 f_{7x} + \mathcal{O}(h^8) \end{aligned} \tag{III.32}$$

Inserting (III.32) in (II.23), we get the effective RBC7 dissipation term for unsteady problems:

$$\tilde{d} = -\kappa[\Phi_1(\delta x^7 f_{7x} + \chi \delta x \delta y^6 g_{7y})]_x - \kappa[\Phi_2(\delta y^7 g_{7y} + \chi \delta y \delta x^6 f_{7x})]_y + \mathcal{O}(h^9) \tag{III.33}$$

with the coefficients

$$\kappa = \frac{1}{5600}, \quad \chi = \frac{280}{3}\left(c - \frac{1}{70}\right).$$

## III.5 The $\chi$-criterion for dissipation

### III.5.1 Dissipation criterion

The effective dissipation term $\tilde{d}$ induced by the discretization of the second-order partial differential operator (III.3) has been identified through the above expressions (III.27) for RBC3, (III.30) for RBC5 and (III.33) for RBC7. Owing to the residual-based structure of the dissipation, these expressions contain no time derivative. In some sense, the time derivatives have been replaced by space derivatives because the exact residual $r$ and its derivatives are null everywhere.
The dissipation expressions (III.27), (III.30) and (III.33) can be cast in a general form. Consider a $\mathrm{RBC}_{2p-1}$ scheme and denote partial derivatives as

$$f_{qx} = \frac{\partial^q f}{\partial x^q}, \quad g_{qy} = \frac{\partial^q g}{\partial y^q}, \quad q = 2p - 1,$$

the dissipation term is of the form:

$$\tilde{d} = d_q + \mathcal{O}(h^{q+2}) \tag{III.34}$$

with

$$d_q = (-1)^{p-1}\kappa\left\{\delta x[\Phi_1(\delta x^{q-1} f_{qx} + \chi \delta y^{q-1} g_{qy})]_x + \delta y[\Phi_2(\delta y^{q-1} g_{qy} + \chi \delta x^{q-1} f_{qx})]_y\right\} \tag{III.35}$$

where $\kappa > 0$ and $\chi$ are two constant coefficients depending on the order $q$ of the scheme.
To determine whether the multidimensional operator (III.35) is really dissipative or not, we

proceed as in Section II.2.3 for the operator $d^{steady}$. Considering the linear scalar case, (III.35) reduces to

$$d_q = \mathscr{D}_q w$$

with the linear partial differential operator:

$$\mathscr{D}_q = (-1)^{p-1}\kappa\,(\,\delta x^{2p-1}\Phi_1 A\frac{\partial^{2p}}{\partial x^{2p}} + \chi\delta x\delta y^{2p-2}\Phi_1 B\frac{\partial^{2p}}{\partial x\partial y^{2p-1}} + \delta y^{2p-1}\Phi_2 B\frac{\partial^{2p}}{\partial y^{2p}} + \chi\delta y\delta x^{2p-2}\Phi_2 A\frac{\partial^{2p}}{\partial y\partial x^{2p-1}}\Big)$$

which contains the highest derivatives in (III.35).
All the derivatives in $\mathscr{D}_q$ being even, its Fourier symbol is real. It is denoted by $\hat{\mathscr{D}}_q(\xi,\eta)$, where $\xi$ and $\eta$ are the wave numbers (Fourier variables).
Again, by dissipation (in the broad sense), we mean:

$$\forall\xi\in\mathbb{R},\ \forall\eta\in\mathbb{R},\qquad \hat{\mathscr{D}}_q(\xi,\eta)\leqslant 0. \tag{III.36}$$

**Theorem III.5.1 ($\chi$-criterion)** *The operator* (III.35) *is dissipative for any order $q=2p-1$ ($p\geqslant 2$), any advection direction ($A$, $B$) and any functions $\Phi_1$, $\Phi_2$ satisfying the conditions* (II.37) *if and only if $\chi=0$.*

**Proof.** Since the Fourier symbol of a derivative like $\partial^{2p}/\partial x\partial y^{2p-1}$ is $(-1)^p\xi\eta^{2p-1}$, we get:

$$\hat{\mathscr{D}}_q = -\kappa\delta x^{2p-1}\left[\Phi_1 A\xi^{2p} + \chi\left(\frac{\delta y}{\delta x}\right)^{2p-2}\Phi_1 B\xi\eta^{2p-1} + \chi\left(\frac{\delta y}{\delta x}\right)\Phi_2 A\xi^{2p-1}\eta + \left(\frac{\delta y}{\delta x}\right)^{2p-1}\Phi_2 B\eta^{2p}\right].$$

- For $A=B=0$ (no advection), then $\hat{\mathscr{D}}_q=0$.
- For $A=0$ and $B\neq 0$ (1-D advection), then from (II.23) $\Phi_1=0$, $\Phi_2 B\geqslant 0$ and
$$\hat{\mathscr{D}}_q = -\kappa\delta y^{2p-1}\Phi_2 B\eta^{2p}\leqslant 0.$$
- Now for $A\neq 0$, $\hat{\mathscr{D}}_q$ can be written as:
$$\hat{\mathscr{D}}_q = -\kappa\delta x^{2p-1}\Phi_1 A\xi^{2p}\mathcal{D}$$
with
$$\mathcal{D} = 1+\chi\left(\frac{\delta x}{\delta y}\frac{B}{A}\lambda^{2p-1}+\frac{\Phi_2}{\Phi_1}\lambda\right)+\frac{\delta x}{\delta y}\frac{\Phi_2 B}{\Phi_1 A}\lambda^{2p}$$
where $\lambda=\dfrac{\delta y}{\delta x}\dfrac{\eta}{\xi}$.
Using the conditions (II.37) with the definition (II.38) of $\alpha$, we have
$$\frac{\delta x B}{\delta y A}=\frac{\Phi_2}{\Phi_1}=\mathrm{sgn}(AB)\alpha=\breve{\alpha}$$
so that
$$\mathcal{D}(\lambda,\breve{\alpha}) = 1+\chi\breve{\alpha}\lambda(\lambda^{2p-2}+1)+\breve{\alpha}^2\lambda^{2p}$$
Since $\Phi_1 A$ is always positive, $\hat{\mathscr{D}}_q$ is negative if and only if
$$\forall\breve{\alpha}\in\mathbb{R},\quad\forall\lambda\in\mathbb{R},\qquad \mathcal{D}(\lambda,\breve{\alpha})\geqslant 0.$$

Note that $\lambda$ is a reduced wave number ratio and $\breve{\alpha}$ characterizes the advection direction with respect to the mesh. It is not easy to discuss the sign of $\mathcal{D}$ viewed as a polynomial of degree $2p$ in $\lambda$. It is better to begin with the dependency on $\breve{\alpha}$. Considering $\mathcal{D}$ as a polynomial of degree 2 in $\breve{\alpha}$, we compute its discriminant

$$\begin{aligned}\Delta &= \chi^2\lambda^2(\lambda^{2p-2}+1)^2 - 4\lambda^{2p} \\ &= \lambda^2[\chi(\lambda^{2p-2}+1) + 2\lambda^{p-1}][\chi(\lambda^{2p-2}+1) - 2\lambda^{p-1}]\end{aligned}$$

$\mathcal{D}$ is positive if and only if $\Delta \leqslant 0$. For $\lambda = 0$, $\Delta = 0$. For $\lambda \neq 0$, $\Delta \leqslant 0$ is tantamount to:

$$-\frac{2|\lambda|^{p-1}}{1+\lambda^{2p-2}} \leqslant \chi \leqslant \frac{2|\lambda|^{p-1}}{1+\lambda^{2p-2}}$$

Since the lower and upper bounds of $\chi$ tend to zero as $\lambda$ tends to infinity, the above condition can be satisfied for all real numbers $\lambda$ if and only if $\chi = 0$.

### III.5.2 Application of the $\chi$-criterion to RBC3

The mid-point residuals of the RBC3 scheme are defined by (III.26) and depend on the parameter $b$. Since $\chi = 2(6b-1)$ for RBC3, the condition $\chi = 0$ for dissipation requires

$$b = \frac{1}{6} \tag{III.37}$$

For this value of $b$, $g_y$ in $\tilde{r_1}$ and $f_x$ in $\tilde{r_2}$ are approximated at order 4. Thus, the simplest choice $b = 0$ should not be used for unsteady problems. However, the correct choice (III.37) does not extend the scheme stencil.

### III.5.3 Application of the $\chi$-criterion to RBC5 and RBC7

The mid-point residuals of the RBC5 and RBC7 schemes are defined by (II.32) with

$$a^\delta = a^\mu + \frac{1}{12} \tag{III.38}$$

and

$$b - a = \frac{1}{6}.$$

For RBC5, $a^\mu \neq 1/10$. In addition, the condition $\chi = 0$ for dissipation gives

$$\frac{b}{6} - c = \frac{1}{30},$$

that is

$$a = \frac{1}{30} + 6c, \qquad b = \frac{1}{5} + 6c. \tag{III.39}$$

When (III.39) holds, $g_y$ in $\tilde{r_1}$ and $f_x$ in $\tilde{r_2}$ are approximated at order 6. Note that the correct dissipation depends on two parameters ($a^\mu$ and $c$), but the dissipation coefficient $\kappa$ in (III.30) depends only on $a^\mu$ (that should be strictly lower than $1/10$).
In the previous works [40, 104], the following coefficients were used:

$$a^\mu = \frac{1}{12}, \qquad a^\delta = \frac{1}{6}, \qquad a = \frac{1}{10}, \qquad b = \frac{4}{15}, \qquad c = \frac{1}{90}. \tag{III.40}$$

They happen to satisfy (III.38) and (III.39).
Another correct choice satisfying the same conditions and producing the same dissipation (same $a^\mu$) for RBC5 is:

$$a^\mu = \frac{1}{12}, \qquad a^\delta = \frac{1}{6}, \qquad a = \frac{1}{30}, \qquad b = \frac{1}{5}, \qquad c = 0. \tag{III.41}$$

It is simpler because the operators $\delta_1^4$ and $\delta_2^4$ vanish in $\tilde{r_1}$ and $\tilde{r_2}$. Finally for RBC7, the coefficients

are given by (III.38) and (III.39) along with $a^\mu = 1/10$. Here the condition $\chi = 0$ for dissipation gives $c = 1/70$, and a unique set of coefficients is found, leading to a dissipative RBC7 scheme. This is:

$$a^\mu = \frac{1}{10}, \qquad a^\delta = \frac{11}{60}, \qquad a = \frac{5}{42}, \qquad b = \frac{2}{7}, \qquad c = \frac{1}{70}. \tag{III.42}$$

Here, $g_y$ in $\tilde{r_1}$ and $f_x$ in $\tilde{r_2}$ are approximated at order 8. Note that the coefficients are different from those used in [40, 104] for RBC7, that were:

$$a^\mu = \frac{1}{10}, \qquad a^\delta = \frac{11}{60}, \qquad a = \frac{1}{30}, \qquad b = \frac{1}{5}, \qquad c = 0. \tag{III.43}$$

Actually, the coefficients (III.43) do not ensure dissipation to RBC7 for all flow conditions.

## III.6 Extension to 3-D

### III.6.1 Dissipation criterion in 3-D

Consider now the three-dimensional hyperbolic system

$$w_t + f_x + g_y + e_z = 0 \tag{III.44}$$

where $e = e(w)$ is the flux component in the $z$-direction and $C = \mathrm{d}e/\mathrm{d}w$. Using difference and average operators $\delta_3$ and $\mu_3$ on the discrete axis $z_l = l\delta z$, the residual-based scheme reads:

$$\tilde{r}_{j,k,l} = \tilde{d}_{j,k,l} \tag{III.45}$$

where the main residual $\tilde{r}$ is a space-centered approximation of the exact residual $r$ (the left-hand side of (III.44)) and $\tilde{d}$ is the dissipation term

$$\tilde{d}_{j,k,l} = \frac{1}{2}[\delta_1(\phi_1\tilde{r_1}) + \delta_2(\phi_2\tilde{r_2}) + \delta_3(\phi_3\tilde{r_3})]_{j,k,l} \tag{III.46}$$

which approximates:

$$d = \frac{\delta x}{2}(\phi_1 r)_x + \frac{\delta y}{2}(\phi_2 r)_y + \frac{\delta z}{2}(\phi_3 r)_z \tag{III.47}$$

For steady problems, the time derivative is cancelled into (III.46) and $\tilde{d}$ is consistent with $d^{steady}$ defined from (III.47) after replacing $r$ by

$$r^{steady} = f_x + g_y + e_z$$

Conditions on $\Phi_1$, $\Phi_2$ and $\Phi_3$ should be satisfied for the operator $d^{steady}$ be actually dissipative in the broad sense. For a scalar problem, these conditions are found to be

$$\begin{gathered} \Phi_1 A \geqslant 0, \qquad \Phi_2 B \geqslant 0, \qquad \Phi_3 C \geqslant 0, \\ \delta x \Phi_1 B = \delta y \Phi_2 A, \qquad \delta x \Phi_1 C = \delta z \Phi_3 A. \end{gathered} \tag{III.48}$$

With the following notations:

$$\Phi_1 = \mathrm{sgn}(A)\phi, \qquad \Phi_2 = \mathrm{sgn}(B)\psi, \qquad \Phi_3 = \mathrm{sgn}(C)\zeta,$$
$$\alpha = \frac{\delta x|B|}{\delta y|A|}, \qquad \beta = \frac{\delta x|C|}{\delta z|A|},$$

the dissipation conditions (III.48) for $d^{steady}$ become

$$\phi \geqslant 0, \qquad \psi = \alpha\phi, \qquad \zeta = \beta\phi. \tag{III.49}$$

An optimal choice is

$$\begin{aligned}
\phi &= \min\left(1, \frac{1}{\alpha}, \frac{1}{\beta}\right) = \min\left(1, \frac{\delta y|A|}{\delta x|B|}, \frac{\delta z|A|}{\delta x|C|}\right), \\
\psi &= \min\left(1, \alpha, \frac{\alpha}{\beta}\right) = \min\left(1, \frac{\delta x|B|}{\delta y|A|}, \frac{\delta z|B|}{\delta y|C|}\right), \\
\zeta &= \min\left(1, \beta, \frac{\beta}{\alpha}\right) = \min\left(1, \frac{\delta x|C|}{\delta z|A|}, \frac{\delta y|C|}{\delta z|B|}\right).
\end{aligned} \tag{III.50}$$

For hyperbolic systems, $\Phi_1$, $\Phi_2$ and $\Phi_3$ are matrix functions defined from the above relations by following a process perfectly similar to the one described in Section II.2.3 for the bidimensional case.

To construct and analyse the dissipation term (III.46), we discretize the mid-point residuals $\tilde{r_1}$, $\tilde{r_2}$ and $\tilde{r_3}$ in two stages as in the 2-D case. First, we discretize $\tilde{r_p}$ in the $p^{th}$-direction only. For instance for $\tilde{r_1}$, this leads to the partially discrete residual

$$(\tilde{r_1}^x)_{j+\frac{1}{2},k,l} = \left[N_1^\mu \mu_1(w_t + g_y + e_z) + N_1^\delta \frac{\delta_1 f}{\delta x}\right]_{j+\frac{1}{2},k,l}$$

where the operator polynomials $N_1^\mu$ and $N_1^\delta$ are still defined by (II.26) with $m = 1$. Clearly, the expansions made in Section III.3.1 remains valid with the new definition of $v$:

$$v = w_t + g_y + e_z.$$

As a result the expansions of $\tilde{r_1}^x$ and $\tilde{r_2}^y$ are unchanged in 3-D and we just have to introduce a similar expansion for $\tilde{r_3}^z$.

Then in the second stage, we proceed as in Section III.4 to complete the space discretization, which requires to introduce a Pade approximation for $e_z$:

$$N_3 \frac{\delta_3 \mu_3 e}{\delta z} = D_3(e_z + \varepsilon_3), \qquad \varepsilon_3 = \mathcal{O}(\delta z^{2p-2}) \tag{III.51}$$

where $N_3$ and $D_3$ are defined by (II.29) for $m = 3$ and $\varepsilon_3$ is the error term.

After applying the operator product $D_2D_3$ to all the terms involved in $\tilde{r_1}$, we define:

$$(\tilde{r_1})_{j+\frac{1}{2},k,l} = \left[N_1^\mu \mu_1 \left(D_2D_3 w_t + D_3N_2 \frac{\delta_2\mu_2 g}{\delta y} + D_2N_3 \frac{\delta_3\mu_3 e}{\delta z}\right) + N_1^\delta D_2D_3 \frac{\delta_1 f}{\delta x}\right]_{j+\frac{1}{2},k,l} \tag{III.52}$$

and similarly:

$$(\tilde{r_2})_{j,k+\frac{1}{2},l} = \left[N_2^\mu \mu_2 \left(D_3D_1 w_t + D_3N_1 \frac{\delta_1\mu_1 f}{\delta x} + D_1N_3 \frac{\delta_3\mu_3 e}{\delta z}\right) + N_2^\delta D_3D_1 \frac{\delta_2 g}{\delta y}\right]_{j,k+\frac{1}{2},l} \tag{III.53}$$

$$(\tilde{r_3})_{j,k,l+\frac{1}{2}} = \left[N_3^\mu \mu_3 \left(D_1D_2 w_t + D_2N_1 \frac{\delta_1\mu_1 f}{\delta x} + D_1N_2 \frac{\delta_2\mu_2 g}{\delta y}\right) + N_3^\delta D_1D_2 \frac{\delta_3 e}{\delta z}\right]_{j,k,l+\frac{1}{2}} \tag{III.54}$$

A Taylor expansion of $\tilde{r_1}$ can be easily obtained by noting that the formulas (III.21) and (III.51) yield

$$D_3 N_2 \frac{\delta_2 \mu_2 g}{\delta y} = D_2 D_3 (g_y + \varepsilon_2), \qquad D_2 N_3 \frac{\delta_3 \mu_3 e}{\delta z} = D_2 D_3 (e_z + \varepsilon_3)$$

so that $\tilde{r_1}$ is related to $\tilde{r_1}^x$ by

$$\tilde{r_1} = D_2 D_3 [\tilde{r_1}^x + N_1^\mu \mu_1 (\varepsilon_2 + \varepsilon_3)].$$

With the same arguments as in the 2-D case, we can reduce this relation to

$$\tilde{r_1} = \tilde{r_1}^x + \mu_1 (\varepsilon_2 + \varepsilon_3) + \mathcal{O}(h^{2p})$$

and similar expressions for $\tilde{r_2}$ and $\tilde{r_3}$, the error $\varepsilon_3$ being quite similar to the error $\varepsilon_1$ and $\varepsilon_2$.
Finally, we easily find the general form of the dissipation in 3-D. With the same notations as in Section III.5.1, the dissipation of a RBC$q$ scheme ($q = 2p-1$) is given by (III.34) with

$$\begin{aligned} d_q = (-1)^{p-1} \kappa \{ & \delta x [\Phi_1 (\delta x^{q-1} f_{qx} + \chi \delta y^{q-1} g_{qy} + \chi \delta z^{q-1} e_{qz})]_x \\ & + \delta y [\Phi_2 (\delta y^{q-1} g_{qy} + \chi \delta z^{q-1} e_{qz} + \chi \delta x^{q-1} f_{qx})]_y \\ & + \delta z [\Phi_3 (\delta z^{q-1} e_{qz} + \chi \delta x^{q-1} f_{qx} + \chi \delta y^{q-1} g_{qy})]_z \} \end{aligned} \tag{III.55}$$

and exactly the same coefficients $\kappa$ and $\chi$ as in 2-D (these coefficients depend only of the order $q$ of the RBC$q$ scheme).
The definition (III.36) of dissipation is unchanged except by the adding of a third wave number.

**Theorem III.6.1 ($\chi$-criterion)** *The operator* (III.55) *is dissipative for any order $q = 2p-1$ ($p \geqslant 2$), any advection direction (A, B, C) and any functions $\Phi_1$, $\Phi_2$, $\Phi_3$ satisfying the conditions* (III.48) *if and only if $\chi = 0$.*

**Proof.** The condition $\chi = 0$ is sufficient for dissipation since when it holds, the operator $d_q$ has no crossed derivatives and reads

$$d_q = (-1)^{p-1} \kappa \{ \delta x^q (\Phi_1 f_{qx})_x + \delta y^q (\Phi_2 g_{qy})_y + \delta z^q (\Phi_3 e_{qz})_z \} \tag{III.56}$$

which is always dissipative provided $\Phi_1 A \geqslant 0$, $\Phi_2 B \geqslant 0$ and $\Phi_3 C \geqslant 0$.
The condition $\chi = 0$ is also necessary since it does in a 2-D situation as we have shown in Section III.5.

The above $\chi$-criterion can be interpreted similarly as in 2-D: a RBC$q$ scheme ($q = 2p-1$) satisfying this condition has a mid-point residual $\tilde{r_1}$ (resp. $\tilde{r_2}$, $\tilde{r_3}$) in which the derivative $f_x$ (resp. $g_y$, $e_z$) is approximated at order $2p-2$ and the two other derivatives are approximated at order $2p$.

### III.6.2 Application of the $\chi$-criterion to RBC3 in 3-D

In 3-D, the RBC3 dissipation involves $3 \times 3 \times 3$-points and is given by (III.46) with a $2 \times 3 \times 3$-point residual $(\tilde{r_1})_{j+\frac{1}{2},k,l}$ defined as:

$$\tilde{r_1} = (I + b\delta_2^2)(I + b\delta_3^2) \left( \mu_1 w_t + \frac{\delta_1 f}{\delta x} \right) + (I + b\delta_3^2) \frac{\delta_2 \mu_2 g}{\delta y} + (I + b\delta_2^2) \frac{\delta_3 \mu_3 e}{\delta z} \tag{III.57}$$

along with a $3 \times 2 \times 3$-point residual $(\tilde{r_2})_{j,k+\frac{1}{2},l}$ and a $3 \times 3 \times 2$-point residual $(\tilde{r_3})_{j,k,l+\frac{1}{2}}$ deduced from (III.57) by circular permutations of the subscripts 1,2,3, of the flux components f, g, e and of the space steps $\delta x$, $\delta y$, $\delta z$.
Since the coefficient $\chi$ is the same in 3-D as in 2-D, the dissipation condition is again (III.37), which sets the only parameter $b$.

### III.6.3 Application of the $\chi$-criterion to RBC5 and RBC7 in 3-D

The $5 \times 5 \times 5$-point RBC5 and RBC7 schemes are defined by (III.46) with

$$\begin{aligned}\tilde{r_1} =&(I + b\delta_2^2 + c\delta_2^4)(I + b\delta_3^2 + c\delta_3^4)\left[(I + a^\mu\delta_1^2)\mu_1 w_t + (I + a^\delta\delta_1^2)\frac{\delta_1 f}{\delta x}\right] \\ &+ (I + a^\mu\delta_1^2)\mu_1\left[(I + b\delta_3^2 + c\delta_3^4)(I + a\delta_2^2)\frac{\delta_2\mu_2 g}{\delta y} + (I + b\delta_2^2 + c\delta_2^4)(I + a\delta_3^2)\frac{\delta_3\mu_3 e}{\delta z}\right]\end{aligned} \tag{III.58}$$

and similar expressions for $\tilde{r_2}$ and $\tilde{r_3}$ deduced by circular permutations of the subscripts, the flux components and the space steps.
The coefficients corresponding to the RBC5 dissipation satisfying the condition $\chi = 0$ are given by (III.38) and (III.39). They still depend on the two parameters $a^\mu$ and $c$. The analogous coefficients for RBC7 are uniquely set by (III.42).

## III.7 Numerical verification of the $\chi$-criterion

Up to now, we restricted our considerations to space approximation schemes. The time approximation is treated independently so that various choices can be made. In the present work, we use a Linear Multistep Method (LMM). In this implicit method, the residual is taken at the new time level $(n+1)\Delta t$ and

$$(w_t)^{n+1} = \frac{1}{\Delta t}\left(\Delta w + \frac{1}{2}\Delta^2 w + \frac{1}{3}\Delta^3 w + ... + \frac{1}{l}\Delta^l w\right)^{n+1} + \mathcal{O}(\Delta t^l) \tag{III.59}$$

where

$$(\Delta w)^{n+1} = w^{n+1} - w^n,\ \Delta^2 w = \Delta(\Delta w),\ \Delta^3 w = \Delta(\Delta^2 w),\ ...$$

For $l = 2$, we get the popular approximation

$$(w_t)^{n+1} = \frac{1}{2\Delta t}\left(3w^{n+1} - 4w^n + w^{n-1}\right) + \mathcal{O}(\Delta t^2). \tag{III.60}$$

LMM methods are A-stable at order $l = 1$ and 2 and A($\alpha$)-stable at higher orders (see [44, 95, 164]). A-stable methods are unconditionally stable when the spatial approximation is dissipative. Given the complexity of RBC schemes we first confirm numerically the $\chi$-criterion through a Von Neumann stability analysis of schemes satisfying or not this criterion. The time-discretization chosen for this numerical investigation is the second-order A-stable LMM method. To study these properties, we consider the linear problem

$$w_t + Aw_x + Bw_y + Cw_z = 0 \tag{III.61}$$

where $A$,$B$ and $C$ are scalar constants. Thereby, the physical fluxes are: $f = Aw$, $g = Bw$ and $e = Cw$. This equation serves as a model for the reduced hyperbolic part of the Navier-Stokes equations.
The Fourier symbol of the difference and average operators are:

$$\widehat{\delta_1\mu_1} = i\sin(\xi),\ \widehat{\delta_2\mu_2} = i\sin(\eta),\ \widehat{\delta_3\mu_3} = i\sin(\zeta),$$

$$\widehat{\delta_1^2} = 2(\cos(\xi) - 1),\ \widehat{\delta_2^2} = 2(\cos(\eta) - 1) \text{ and } \widehat{\delta_3^2} = 2(\cos(\zeta) - 1)$$

where $i^2 = -1$ and $\xi$, $\eta$ and $\zeta$ are the reduced wave numbers in the $x$-, $y$- and $z$-direction respectively. For a three step, second-order accurate LMM method, the time derivative is approximated as

$$\mathcal{T}(w) = \frac{1}{2\Delta t}\left(3w^{n+1} - 4w^n + w^{n-1}\right)$$

and its Fourier symbol is

$$\widehat{\mathcal{T}(w)} = \frac{1}{2\Delta t}\left(3G - 4 + \frac{1}{G}\right)\hat{w}^n$$

where $G = \hat{w}^{n+1}/\hat{w}^n = \hat{w}^n/\hat{w}^{n-1}$ is the amplification factor. We denote $\dot{A}$, $\dot{B}$ and $\dot{C}$ the CFL (Courant–Friedrichs–Lewy) numbers $\dot{A} = A\Delta t/\delta x$, $\dot{B} = B\Delta t/\delta y$ and $\dot{C} = C\Delta t/\delta z$. In order to carry out the Von Neumann stability analysis of RBC schemes, the Fourier symbols of the schemes are written in the form:

$$\alpha\Delta t\widehat{\mathcal{T}(w)} = -\beta\hat{w}^{n+1}$$

where $\alpha$ and $\beta$ are functions of $\dot{A}$, $\dot{B}$, $\dot{C}$, $\xi$, $\eta$ and $\zeta$. With the preceding notations, this can be re-written as

$$\frac{\alpha}{2}\left(3G - 4 + \frac{1}{G}\right) = -\beta G.$$

Finally, by reordering with respect to $G$; we obtain:

$$P(G) = 0$$

where $P(G) = \left(\frac{3\alpha}{2} + \beta\right)G^2 - 2\alpha G + \frac{\alpha}{2}$ is a second order polynomial in $G$. The amplification factor is one of the two roots, $G_1$ and $G_2$, of $P$. $|G|$ is chosen to be $\max(|G_1|, |G_2|)$ which is the more conservative choice for a stability analysis.
The values of $\alpha$ and $\beta$ are:

$$\begin{aligned}
\alpha =& \overline{D}(Z_1)\overline{D}(Z_2)\overline{D}(Z_3) - \frac{i}{2}[\Phi_1\sin(\xi)N^\mu(Z_1)D(Z_2)D(Z_3) \\
&+ \Phi_2\sin(\eta)N^\mu(Z_2)D(Z_1)D(Z_3) + \Phi_3\sin(\zeta)N^\mu(Z_3)D(Z_1)D(Z_2)] \\
\beta =& \frac{\Phi_1}{2}[-\dot{A}Z_1D(Z_2)D(Z_3)N^\delta(Z_1) + N(Z_2)N^\mu(Z_1)D(Z_3)\dot{B}\sin(\xi)\sin(\eta) \\
&+ N(Z_3)N^\mu(Z_1)D(Z_2)\dot{C}\sin(\xi)\sin(\zeta)] + \frac{\Phi_2}{2}[-\dot{B}Z_2D(Z_1)D(Z_3)N^\delta(Z_2) \\
&+ N(Z_1)N^\mu(Z_2)D(Z_3)\dot{A}\sin(\eta)\sin(\xi) + N(Z_3)N^\mu(Z_2)D(Z_1)\dot{C}\sin(\eta)\sin(\zeta)] \\
&+ \frac{\Phi_3}{2}[-\dot{C}Z_3D(Z_1)D(Z_2)N^\delta(Z_3) + N(Z_1)N^\mu(Z_3)D(Z_2)\dot{A}\sin(\zeta)\sin(\xi) \\
&+ N(Z_2)N^\mu(Z_3)D(Z_1)\dot{B}\sin(\zeta)\sin(\eta)] + i[\dot{A}\sin(\xi)\overline{N}(Z_1)\overline{D}(Z_2)\overline{D}(Z_3) \\
&+ \dot{B}\sin(\eta)\overline{N}(Z_2)\overline{D}(Z_1)\overline{D}(Z_3) + \dot{C}\sin(\zeta)\overline{N}(Z_3)\overline{D}(Z_1)\overline{D}(Z_2)]
\end{aligned} \tag{III.62}$$

where $Z_1 = 2(\cos\xi - 1)$, $Z_2 = 2(\cos\eta - 1)$, $Z_3 = 2(\cos\zeta - 1)$ and where $N$, $\overline{N}$, $D$, $\overline{D}$, $N^\mu$, $N^\delta$ are the polynomials introduced previously.

We consider now the specific case of the RBC3 scheme with a dissipation operator corresponding to $b = 0$ or $b = 1/6$. According to the preceding analysis, the former choice does not allow to satisfy the $\chi$-criterion, whereas the latter does. Additionnally, we also consider the case of the RBC7 scheme with the coefficients (III.43) associated to $c = 0$ ($\chi \neq 0$) or the coefficients (III.42) associated to $c = 1/70$ ($\chi = 0$). Given the complexity of the analytical expression of $\alpha$ and $\beta$ a computer code has been written to study the Von Neumann stability of these schemes. The analysis is carried out in 2D and 3D. In the 3D analysis (respectively in 2D), for every triplet (respectively couple) of CFL numbers the maximum value of the amplification factor modulus $|G|$ in the wave numbers space, called $|G|_{max}$, is determined.

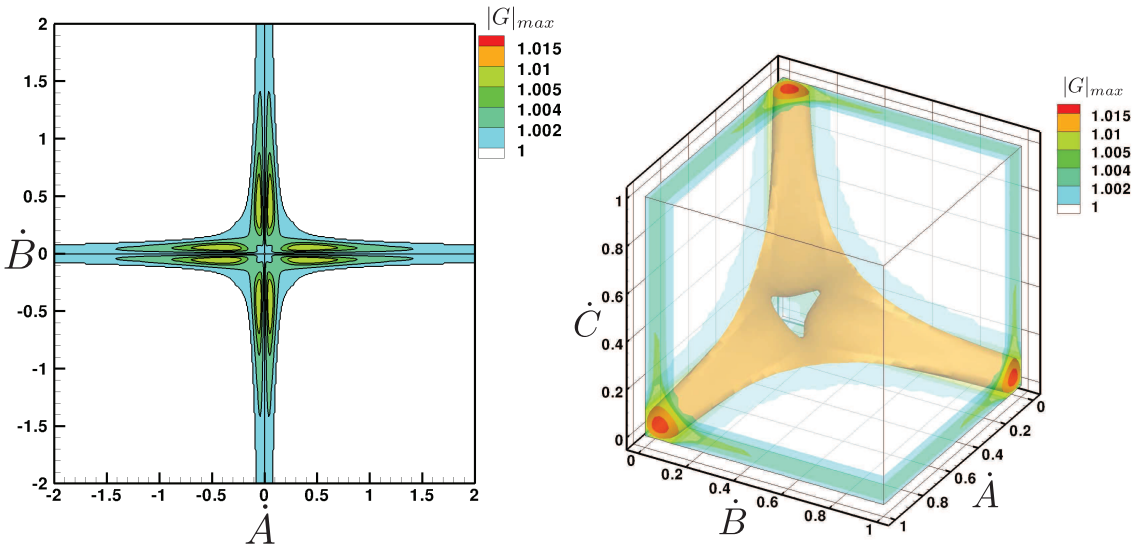


Figure III.1: 2D and 3D Von Neumann stability analysis of RBC3 ($b = 0$ *i.e.* $\chi \neq 0$).

In the 2D analysis, the reduced wave numbers $(\xi, \eta)$ vary in $[-\pi; \pi] \times [0; \pi]$ with a step $\Delta\xi = \Delta\eta = \pi/50$ and the CFL numbers in the range $[-2; 2]$ with a step $\Delta\dot{A} = \Delta\dot{B} = 1/100$. In the 3D analysis, the triplet $(\xi, \eta, \zeta)$ varies in $[-\pi; \pi]^2 \times [0; \pi]$ with a step $\Delta\xi = \Delta\eta = \Delta\zeta = \pi/50$, and the CFL numbers in $[-1; 1]^3$ with a step $\Delta\dot{A} = \Delta\dot{B} = \Delta\dot{C} = 1/50$. The ranges of variation of the parameters take into account symmetries of $|G|$. The discretizations have been tested so as to have a sufficient resolution for the analysis.

Fig. III.1 shows that RBC3 with $b = 0$ ($\chi$-criterion violated) is not linearly stable in 2D and 3D since the maximum modulus of the amplification factor is greater than one for some waves number. The maximum value of $|G|_{max}$ is 1.006 for the 2D scheme and 1.019 for the 3D configuration. It has to be stressed that several complex unsteady computations have been successfully carried out with this scheme despite this slight linear instability [40, 101, 117]. It seems likely that this is due to the fact that high values of $|G|_{max}$ are restricted to a small range of CFL numbers, and for these values of CFL numbers, $|G|$ is higher than one only in a small range of reduced wave numbers. Moreover, $|G|_{max}$ is always close to one for this fully discretized scheme. Thereby in the computation of a viscous case, the fact that the linear advection scheme is unstable might not be an issue in most of the cases thanks to the stabilizing effect of the viscous terms. Similarly Fig. III.2 provides the results of the Von Neumann analysis in 2D and 3D for RBC7 with $c = 0$ ($\chi \neq 0$). They reveal that this scheme is also slightly linearly unstable. The maximum values of $|G|_{max}$ are 1.00079 in 2D and 1.00184 in 3D, which is very close to 1, but may lead to computational break-up for some configurations.

On the other, the Von Neumann stability analysis of RBC schemes of third-, fifth- and seventh-order of accuracy satisfying the $\chi$-criterion, respectively defined by the set of coefficients (III.37), (III.38) and (III.42), shows these schemes to be unconditionally linearly stable for both 2D and 3D configurations, which confirms the relevance of the $\chi$-criterion.

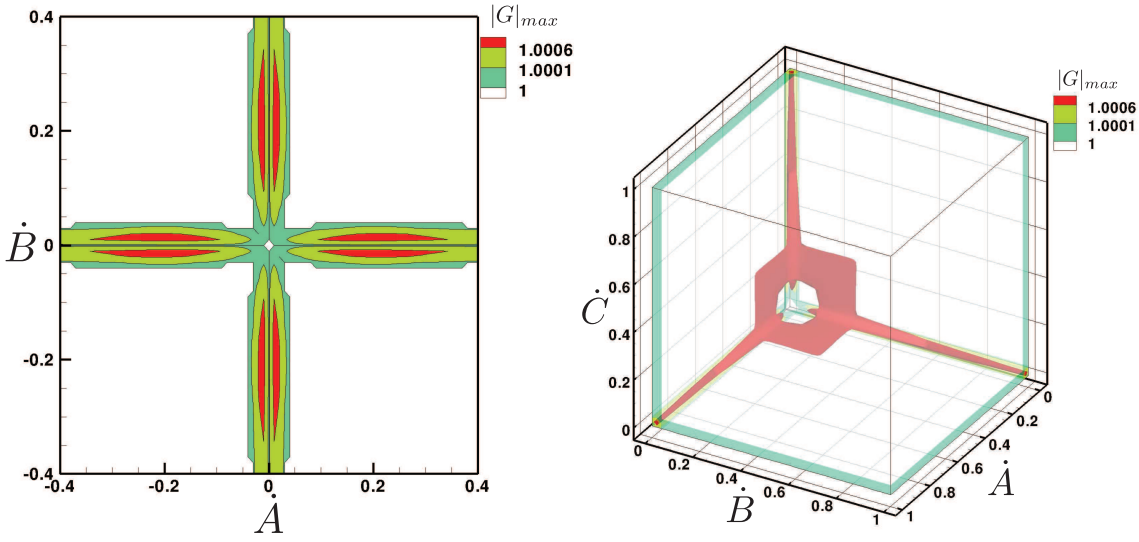


Figure III.2: 2D and 3D Von Neumann stability analysis of RBC7 ($c = 0$ *i.e.* $\chi \neq 0$).

## III.8 Interpretation of the $\chi$-criterion

We now try to understand the meaning of the dissipation condition $\chi = 0$. When it holds, the mixed derivatives vanish and the dissipation operator reduces to

$$d_q = (-1)^{p-1}\kappa[\delta x^q(\Phi_1 f_{qx})_x + \delta y^q(\Phi_2 g_{qy})_y], \quad q = 2p-1 \tag{III.63}$$

which is precisely the result obtained in the partial analysis of Section III.3 where we only took into account the $x$-discretization in $\tilde{r_1}$ and the $y$-discretization in in $\tilde{r_2}$. This means that the effect of the complementary discretization comes at a higher order in the expansion of $\tilde{d}$. To ensure dissipation, the derivative $g_y$ in the mid-point residual $\tilde{r_1}$ (resp. $f_x$ in $\tilde{r_2}$) should be approximated at a higher order than necessary to get the accuracy required for the mid-point residual. Practically, the mid-point residual $\tilde{r_1}$ of RBC$q$ scheme ($q = 2p-1$) uses approximations of order $2p-2$ for $f_x$ and of order $2p$ for $g_y$. The latter is nothing but the one used in the main residual $\tilde{r}$. For the mid-point residual $\tilde{r_2}$, the roles of $f_x$ and $g_y$ are exchanged.
Fortunately, this extra accuracy for half of the dissipation terms is achieved without extending the scheme stencil.

In this section we try to show why ensuring dissipation means that the derivative $g_y$ in the mid-point residual $\tilde{r}_1$ (resp. $f_x$ in $\tilde{r}_2$) has to be approximated at a higher order than necessary to get the accuracy required for the mid-point residual. We do it by computing the truncation error of RBC schemes using only the Taylor expansions of the Pade fraction used.
This expansions could be done in the general framework of RBC schemes. However, in order to fix ideas and to simplify this interpretation we only take the example of RBC7. The main residual Taylor expansion is:

$$\tilde{r_0} = (\overline{D_1}\ \overline{D_2})\left[r + \mathcal{O}(h^8)\right] = \left[I + \mathcal{O}(h^2)\right]\mathcal{O}(h^8) = \mathcal{O}(h^8)$$

Now, we consider the Taylor expansion of one of the mid-point residual, $\tilde{r}_1$ for instance. For RBC7, the approximations have to be at least at sixth order in the dissipation. Thus, the Taylor

expansion of the Pade fraction used are:

$$\frac{N_1^\delta}{D_1^\delta}\frac{\delta_1 f}{\delta x} = f_x - \frac{223}{4838400}\delta x^6 f_{7x} + \mathcal{O}(\delta x^7)$$

$$\frac{N_1^\mu}{D_1^\mu}\mu_1 f = f + \frac{\delta x^6}{5120} f_{6x} + \mathcal{O}(\delta x^8)$$

and

$$\frac{N_2}{D_2}\frac{\delta_2\mu_2 g}{\delta y} = g_y + \left(\frac{1}{140} - \frac{b}{30} + \frac{c}{6}\right)\delta y^6 g_{7y} + \mathcal{O}(\delta y^8) = g_y + \alpha\delta y^6 g_{7y} + \mathcal{O}(\delta y^8)$$

where $\alpha = \dfrac{1}{140} - \dfrac{b}{30} + \dfrac{c}{6}$. Besides $D_1^\delta = D_1^\mu$ for reason of compactness. Consequently, the expansion of $\tilde{r}_1$ writes:

$$\begin{aligned}
\tilde{r}_1 &= D_2 D_1^\delta\left[\frac{N_1^\mu}{D_1^\mu}\mu_1\left(w_t + \frac{N_2}{D_2}\frac{\delta_2\mu_2 g}{\delta y}\right) + \frac{N_1^\delta}{D_1^\delta}\frac{\delta_1 f}{\delta x}\right] \\
&= D_2 D_1^\delta\left[r + \frac{\delta x^6}{5120}(w_t + f_x + g_y)_{6x} + \alpha\delta y^6 g_{7y} - \left(\frac{223}{4838400} + \frac{1}{5120}\right)\delta x^6 f_{7x}\right] + \mathcal{O}(h^8) \\
&= D_2 D_1^\delta\left[r + \frac{\delta x^6}{5120} r_{6x} + \alpha\delta y^6 g_{7y} - \frac{73}{302400}\delta x^6 f_{7x}\right] + \mathcal{O}(h^8)
\end{aligned}$$

The exact residual $r$ is null and consequently

$$\begin{aligned}
\tilde{r}_1 &= D_2 D_1^\delta\left[\alpha\delta y^6 g_{7y} - \frac{73}{302400}\delta x^6 f_{7x}\right] + \mathcal{O}(h^8) \\
&= \left[I + \mathcal{O}(h^2)\right]\left[\alpha\delta y^6 g_{7y} - \frac{73}{302400}\delta x^6 f_{7x}\right] + \mathcal{O}(h^8) \\
&= \alpha\delta y^6 g_{7y} - \frac{73}{302400}\delta x^6 f_{7x} + \mathcal{O}(h^8)
\end{aligned}$$

Finally, in the case of the linear scalar advection, the truncation error of RBC7 is

$$\begin{aligned}
\epsilon &= \frac{\Phi_1}{2}\left[\alpha\delta x\delta y^6 g_{x7y} - \frac{73}{302400}\delta x^7 f_{8x}\right] + \frac{\Phi_2}{2}\left[\alpha\delta y\delta x^6 f_{y7x} - \frac{73}{302400}\delta y^7 g_{8y}\right] + \mathcal{O}(h^8) \\
&= \mathscr{D}_7 w + \mathcal{O}(h^8)
\end{aligned}$$

and the Fourier transform of $\mathscr{D}_7$ is

$$\hat{\mathscr{D}}_7 = -\frac{\Phi_1}{2}\left[\alpha\delta x\delta y^6 B\xi\eta^7 - \frac{73}{302400}\delta x^7 A\xi^8\right] - \frac{\Phi_2}{2}\left[\alpha\delta y\delta x^6 A\eta\xi^7 - \frac{73}{302400}\delta y^7 B\eta^8\right] \qquad \text{(III.64)}$$

The only terms that could be non-dissipative in the sens of (III.36) are terms with the coefficient $\alpha$. Thus, the dissipation prperties of RBC7 depends only on the choice of the Pade fraction $N_1/D_1$ and $N_2/D_2$. When the $\chi$-criterion ($\chi = 0$) is satisfied $\alpha$ is null and when the $\chi$-criterion is not satisfied ($c = 0$) $\alpha$ is equal to 1/2100. If $\chi \neq 0$ the sign of $-\dfrac{\Phi_1\alpha}{2}\delta x\delta y^6 B\xi\eta^7$ depends on the configuration of the flow. In the 2D scalar advection case the sign of this contribution is negative when:

- $\dot{A}$ and $\dot{B}$ have contrary signs, and $\xi$ and $\eta$ have contrary signs

- $\dot{A}$ and $\dot{B}$ have the same sign, and $\xi$ and $\eta$ have the same sign

The present result is consistent with a Von Neumann analysis; the amplification factor is indeed greater than one in the Fourier space only for configurations described above ($cf.$ Figure III.3).

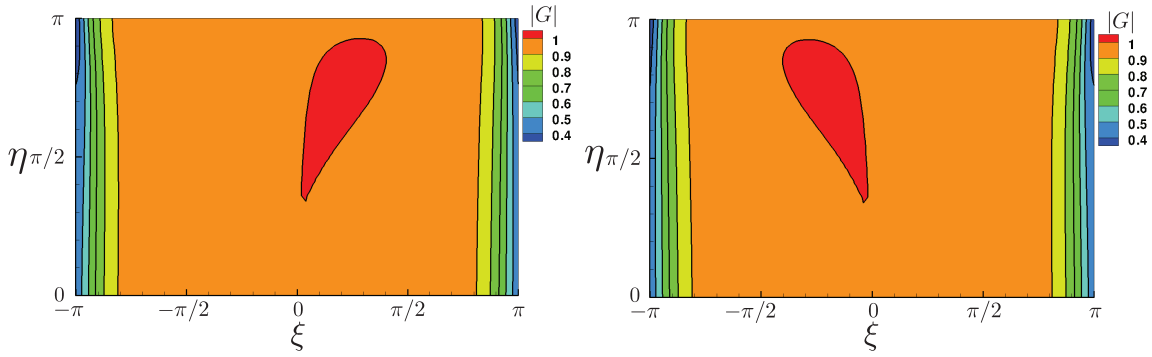


Figure III.3: $|G|$ for unsteady RBC7 with $(\dot{A}, \dot{B}) = (0.19, 0.01)$ on the left and $(\dot{A}, \dot{B}) = (0.19, -0.01)$ on the right

Note that the cross derivatives in the proof of the $\chi$-criterion are multiplied by the coefficient $-\kappa\chi$ which is equal to $-\dfrac{1}{4200} = -\dfrac{\alpha}{2}$ for RBC7 with $c = 0$.
In summary, we have interpreted the $\chi$-criterion for dissipation. To ensure the validity of $\chi$-criterion and thus dissipation, the derivative $g_y$ in the mid-point residual $\tilde{r_1}$ (resp. $f_x$ in $\tilde{r_2}$) should be approximated at a higher order than necessary to get the accuracy required for the mid-point residual. Moreover we have shown the flow condition leading to this numerical instability when the $\chi$-criterion is not satisfied.

## III.9 Spectral properties of RBC schemes

### III.9.1 General framework

The aim of the present section is to move a further step toward the understanding of the numerical properties of high-order RBC discretizations, and precisely of the internal representation of solution modes provided by these schemes. Truncation error analysis provides information about the asymptotic behavior of numerical schemes in the limit of vanishing mesh size. Namely, for stable methods and for smooth flow problems, it allows to conclude on the convergence rate of the global error. Furthermore, it may be used to establish, as done in the present chapter, the dominant (dissipative or dispersive) nature of the numerical scheme, according to the kind of derivatives (even or odd) of the unknown field featuring in the leading error term. Nevertheless, this type of analysis does not provide all possible information on the actual error introduced by the scheme on finite computational grids, and precisely on the cutoff frequencies associated to the numerical representation of the solution. For this purpose, the wave propagation (spectral) properties of the scheme can be studied to obtain information on the evolution of the Fourier modes of the computed field that are supported on a given grid of finite size. The spectral behavior of high order schemes has been extensively investigated in the past, namely in view of their application to aeroacoustics [18, 146] and Large-Eddy Simulation [18, 54]. Specifically, a careful analysis of the approximation of convective terms in the governing equations is in order for the numerical simulation of high-Reynolds compressible flows, since it is likely to introduce dispersion and diffusion errors that affect the numerical representation of a given solution mode.

For directional schemes, spectral analysis is often applied to a single space derivative taken apart [18, 54, 146]. Morover, since many high-order schemes have a purely centered nature, only the dispersion errors are taken into account, numerical damping being introduced *a posteriori* via the addition of some form of artificial dissipation or explicit filtering, whose transfer function (rate of damping associated to a given wave number) is investigated separately.
This kind of disjoint analysis is not applicable to RBC schemes because of their genuinely multi-dimensional and intrinsically dissipative nature. For these schemes, an analysis of the properties of the multidimensional spatial discretization operator as a whole is required. In this case, the dispersive and dissipative behavior depends on a multidimensional wave number (or on the local advection direction). Since our main goal is to investigate the spectral properties of numerical approximations for the convective terms, in the following we restrict our analysis to inviscid compressible flow problems.

### III.9.2 Spectral analysis of the RBC spatial operator

Omitting the subscript $j,k$, the RBC$q$ spatial discretization scheme of order $q = 3, 5, 7$ can be expressed as:

$$\tilde{r_0}(w, w_t) = \tilde{d}(w, w_t) \tag{III.65}$$

where $\tilde{r_0}$ is the centered residual operator and $\tilde{d}$ is the numerical dissipation operator. They can both be split in a part dependent on the state vector $w$ only and another one that involves $w_t$. Precisely, calling:

$$\mathfrak{I}_{\tilde{r}_0} = \overline{D_1}\ \overline{D_2}, \qquad \mathfrak{I}_{\tilde{d}} = \frac{1}{2}\left(\delta_1\Phi_1 N_1^{\mu}\mu_1 D_2 + \delta_2\Phi_2 N_2^{\mu}\mu_2 D_1\right) \tag{III.66}$$

the difference operators that apply to $w_t$ and:

$$\begin{aligned} \mathfrak{R}_{\tilde{r}_0} &= \overline{D_2}\ \overline{N_1}\frac{\delta_1\mu_1 f}{\delta x} + \overline{D_1}\ \overline{N_2}\frac{\delta_2\mu_2 g}{\delta y}, \\ \mathfrak{R}_{\tilde{d}} &= \frac{1}{2}\left[\delta_1\Phi_1\left(N_1^{\delta}D_2\frac{\delta_1 f}{\delta x} + N_1^{\mu}\mu_1 N_2\frac{\delta_2\mu_2 g}{\delta y}\right) + \delta_2\Phi_2\left(N_2^{\delta}D_1\frac{\delta_2 g}{\delta y} + N_2^{\mu}\mu_2 N_1\frac{\delta_1\mu_1 f}{\delta x}\right)\right] \end{aligned} \tag{III.67}$$

the operators depending on $w$ only, Eq. (III.65) can be rewritten as;

$$(\mathfrak{I}_{\tilde{r}_0} - \mathfrak{I}_{\tilde{d}})w_t = -\mathfrak{R}_{\tilde{r}_0} + \mathfrak{R}_{\tilde{d}}$$

or, in a more compact way:

$$w_t = -\mathfrak{I}^{-1}\mathfrak{R}, \text{ with } \mathfrak{I} = \mathfrak{I}_{\tilde{r}_0} - \mathfrak{I}_{\tilde{d}} \text{ and } \mathfrak{R} = \mathfrak{R}_{\tilde{r}_0} - \mathfrak{R}_{\tilde{d}} \tag{III.68}$$

Finally, we can formally set:

$$w_t = \mathcal{S}(w), \text{ with } \mathcal{S} = -\mathfrak{I}^{-1}\mathfrak{R} \tag{III.69}$$

Eq. (III.69) represents now a system of ordinary differential equations and, completed by initial conditions $w(.,0) = w_0(.)$, it defines a Cauchy problem. Thus, the spectral properties of the semi-discrete scheme depend only on those of the operator $\mathcal{S}$.
To study these properties, we consider the linear problem

$$w_t + Aw_x + Bw_y = 0 \tag{III.70}$$

where $A$ and $B$ are scalar constants. The Fourier transform of Eq. (III.70) is:

$$\widehat{w}_t = -i(Ak_x + Bk_y)\widehat{w} = -i\mathbf{A}.\mathbf{k}\widehat{w} \tag{III.71}$$

where $\mathbf{A} = (A, B)$ is the advection velocity vector and $\mathbf{k} = (k_x, k_y)$ a 2D wave vector. Denoting $\dot{\mathbf{A}} = (\dot{A}, \dot{B})$ a vector whose components are the CFL numbers in the $x$ and $y$ directions, respectively:

$$\dot{A} = A\Delta t/\delta x, \qquad \dot{B} = B\Delta t/\delta y$$

and introducing the reduced wave number in the $\dot{\mathbf{A}}$-direction:

$$\xi_\theta = \frac{\dot{\mathbf{A}}}{|\dot{\mathbf{A}}|}.\boldsymbol{\xi}$$

with $\boldsymbol{\xi} = (\xi, \eta) = (k_x\delta x, k_y\delta y)$ the reduced wave vector, Eq. (III.71) can be rewritten as:

$$\widehat{w}_t = -i|\dot{\mathbf{A}}|\xi_\theta \frac{\widehat{w}}{\Delta t} \tag{III.72}$$

The notation $\xi_\theta$ refers to the local advection direction with respect to the mesh, where $\cos(\theta) = \dot{A}/|\dot{\mathbf{A}}|$, $\sin(\theta) = \dot{B}/|\dot{\mathbf{A}}|$, and $|\dot{\mathbf{A}}|$ is the global CFL number. The right-hand side of Eq. (III.72) represents the exact transport operator, a pure imaginary number, and $\xi_\theta$ is a pure real number. We now consider the semi-discrete counterpart to Eq. (III.72). Taking the spatial Fourier transform of the semi-discrete system (III.69) applied to the linear problem (III.70), we obtain:

$$\widehat{w}_t = \widehat{\mathcal{S}}(\boldsymbol{\xi}, \dot{\mathbf{A}}) \frac{\widehat{w}}{\Delta t} \tag{III.73}$$

with $\widehat{\mathcal{S}}$ the Fourier symbol of the spatial operator. Introducing the modified wave number:

$$\xi_\theta^* = i\frac{\widehat{\mathcal{S}}(\boldsymbol{\xi}, \dot{\mathbf{A}})}{|\dot{\mathbf{A}}|} \tag{III.74}$$

Eq. (III.73) can be rewritten as:

$$\widehat{w}_t = -i|\dot{\mathbf{A}}|\xi_\theta^* \frac{\widehat{w}}{\Delta t} \tag{III.75}$$

which represents the numerical counterpart of the exact operator (III.72). Eq. (III.74) is called the approximate dispersion relation of the semi-discrete scheme and relates a given reduced wave number $\xi_\theta$ to its numerical representation $\xi_\theta^*$. Contrary to the exact wave number, the modified wave number $\xi_\theta^*$ is a complex, since it has a non-zero imaginary part in general. Inspection of Eq. (III.75) shows that, according to its positive or negative sign, this imaginary part contributes to the amplification or damping of $\widehat{w}$ in time. If the imaginary part is positive, then any Fourier mode set as an initial condition to the ordinary differential equation (III.69) will grow without bound.

As a consequence, a necessary condition for the Cauchy-stability of the semi-discrete system of equations is that:

$$\forall \dot{\mathbf{A}} \in \mathbb{R}^2, \sup_{\boldsymbol{\xi} \in [-\pi,\pi]^2} \mathfrak{Im}(\xi_\theta^*) \leqslant 0 \tag{III.76}$$

This comes to require that the Fourier symbol of the spatial discretization $\widehat{\mathcal{S}}$ always lies in the left-hand side of the complex plane. Any spatial discretization satisfying the stability condition (III.76) leads to an unconditionally stable fully discrete scheme whenever it is combined to an A-stable time integration method.

In addition to stability analysis, the modified wave number may be used as an indicator of how accurately a given wave number is represented by the difference operator. Specifically, we define the error with respect to the exact wave number:

$$\mathcal{E} = \xi_\theta^* - \xi_\theta = (\mathfrak{Re}(\xi_\theta^*) - \xi_\theta) + i\mathfrak{Im}(\xi_\theta^*) \tag{III.77}$$

More precisely, following previous works [18, 57, 98, 146, 149] for 1-D problems, we consider the multidimensional counterparts of the scheme normalised phase error and damping function:

$$\mathcal{P}_{\xi_\theta} = \frac{|\mathfrak{Re}(\xi_\theta^*) - \xi_\theta|}{\pi}, \; \mathcal{D}_{\xi_\theta} = 1 - \exp[\mathfrak{Im}(\xi_\theta^*)] \tag{III.78}$$

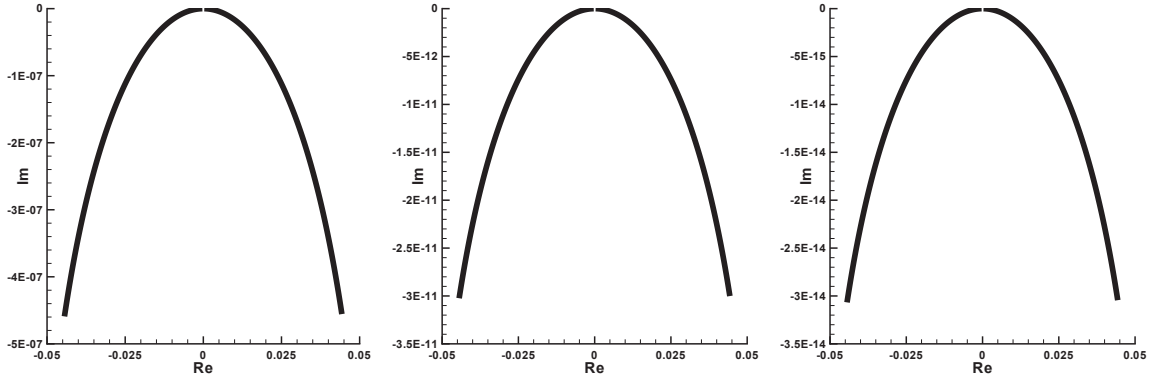


(a) RBC3: $(a, b, c) = (0, \frac{1}{6}, 0)$. (b) RBC5: $(a, b, c) = (\frac{1}{10}, \frac{4}{15}, \frac{1}{90})$. (c) RBC7: $(a, b, c) = (\frac{5}{42}, \frac{2}{7}, \frac{1}{70})$.

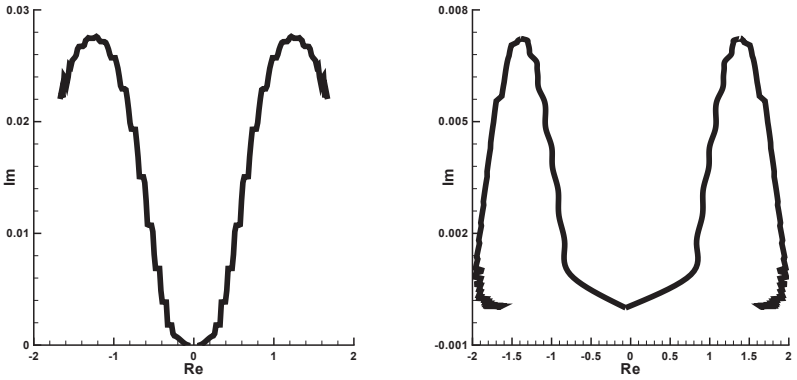


(d) RBC3: $(a, b, c) = (0, 0, 0)$. (e) RBC7: $(a, b, c) = (\frac{1}{30}, \frac{1}{5}, 0)$.

Figure III.4: Representation in the complex plane of the Cauchy-stability criterion (III.76) for RBC schemes with different choices of the Pade coefficients used in the numerical dissipation term.

For an infinitely accurate scheme, $\mathcal{P}_{\xi_\theta} = 0$ and $\mathcal{D}_{\xi_\theta} = 0$. In the following, we apply the preceding measures to the RBC schemes presented in Section III. To this purpose, we first establish the approximate dispersion relation for a RBC scheme. We start by taking the Fourier transform of Eq. (III.68), which gives:

$$\widehat{w}_t = -\widehat{\mathfrak{I}}^{-1}\widehat{\mathfrak{R}}\widehat{w}, \text{ with } \widehat{\mathfrak{I}} = \widehat{\mathfrak{I}}(\boldsymbol{\xi}, \dot{\mathbf{A}}) \text{ and } \widehat{\mathfrak{R}} = \widehat{\mathfrak{R}}(\boldsymbol{\xi}, \dot{\mathbf{A}})$$

As a consequence:

$$\xi_\theta^* = -i\Delta t \frac{\widehat{\mathfrak{I}}^{-1}\widehat{\mathfrak{R}}}{|\dot{\mathbf{A}}|} \tag{III.79}$$

Taking the Fourier transform of Eqs. (III.66) and (III.67), we finally obtain:

$$\begin{aligned}\Delta t\widehat{\mathfrak{R}} = \quad & \frac{\Phi_1}{2}\Big(N(Z_2)N^{\mu}(Z_1)\dot{B}\sin(\xi)\sin(\eta) - \dot{A}Z_1D(Z_2)N^{\delta}(Z_1)\Big) \\ & + \frac{\Phi_2}{2}\Big(N(Z_1)N^{\mu}(Z_2)\dot{A}\sin(\eta)\sin(\xi) - \dot{B}Z_2D(Z_1)N^{\delta}(Z_2)\Big) \\ & + i\Big(\dot{A}\sin(\xi)\overline{N}(Z_1)\overline{D}(Z_2) + \dot{B}\sin(\eta)\overline{N}(Z_2)\overline{D}(Z_1)\Big) \\ \widehat{\mathfrak{I}}^{-1} = & \left\{\overline{D}(Z_1)\overline{D}(Z_2) - \frac{i}{2}\left(\Phi_1\sin(\xi)N^{\mu}(Z_1)D(Z_2) + \Phi_2\sin(\eta)N^{\mu}(Z_2)D(Z_1)\right)\right\}^{-1}\end{aligned} \tag{III.80}$$

where $Z_1 = 2(\cos\xi - 1)$, $Z_2 = 2(\cos\eta - 1)$ and where $N$, $\overline{N}$, $D$, $\overline{D}$, $N^{\mu}$, $N^{\delta}$ are the polynomials introduced previously, with coefficients given by Eq. (II.14) and (III.42), (II.15) and (III.32), and (II.16) and (III.34) for RBC3, RBC5, and RBC7 respectively.
Given the complexity for the analytical expression of the modified wave number for an RBC$q$ scheme, a computer code has been written to study its mathematical properties. First of all, we numerically check that RBC$q$ schemes using coefficients given by Eq. (III.42) to (III.34) are Cauchy stable. To this purpose, the imaginary part of $\xi_\theta^*$ is computed for CFL numbers $\dot{A}$ and $\dot{B}$ ranging in $[-2, 2]$ with a step $\Delta\dot{A} = \Delta\dot{B} = 1/100$ and the wave vector $\boldsymbol{\xi}$ ranging in $[-\pi, \pi] \times [0, \pi]$ with steps $\Delta\xi = \Delta\eta = \pi/50$. Fig. III.4 displays criterion (III.76) for several RBC schemes. Precisely, Fig. III.4(a) to III.4(c) show that RBC schemes with coefficients satisfying the dissipation criterion of Thm. III.6.1 verify condition (III.76) for any CFL and any wave number, whereas the third- and seventh-order RBC schemes with coefficients given in [40] violate the stability criterion over a range of wave numbers, which may lead to stability problems for some flow configurations.

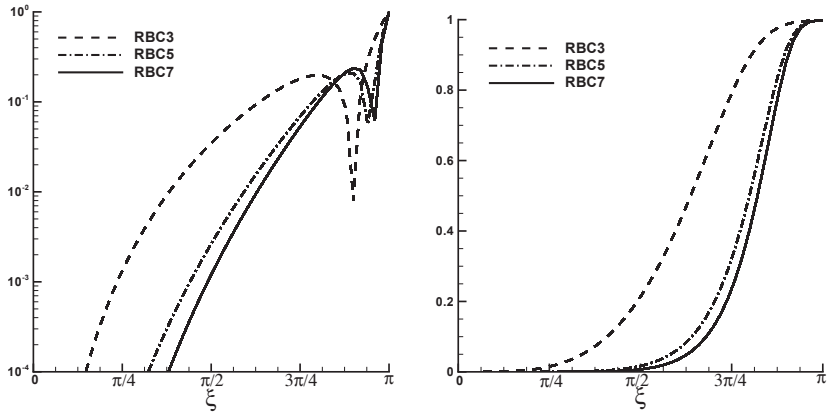


(a) $\mathcal{P}_{\xi_0^*}$. (b) $\mathcal{D}_{\xi_0^*}$.

Figure III.5: 1D behavior of $\mathcal{P}_{\xi_0^*}$ and $\mathcal{D}_{\xi_0^*}$ for RBC schemes.

| | $\xi_c$ | $\lambda_c/\delta x$ |
|---|---|---|
| RBC3 | 0.74 | 8.47 |
| RBC5 | 1.39 | 4.53 |
| RBC7 | 1.54 | 4.07 |

Table III.1: Resolvability limit due to dispersion of RBC schemes.

| | $\xi_c$ | $\lambda_c/\delta x$ |
|---|---|---|
| RBC3 | 0.40 | 15.56 |
| RBC5 | 1.03 | 6.08 |
| RBC7 | 1.24 | 5.06 |

Table III.2: Resolvability limit due to dissipation of RBC schemes.

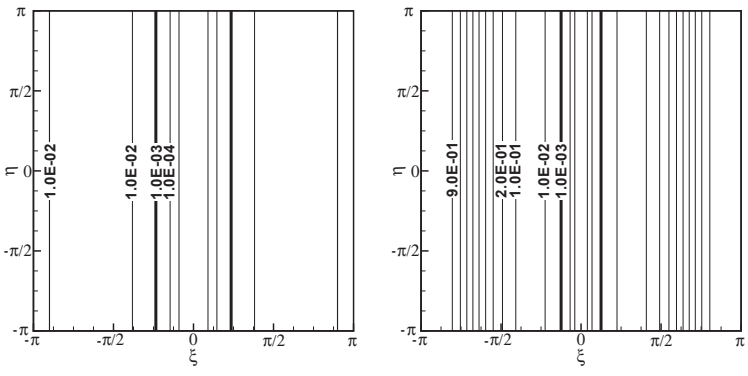


(a) $\mathcal{P}_{\xi_0^*}$, RBC3. (b) $\mathcal{D}_{\xi_0^*}$, RBC3.

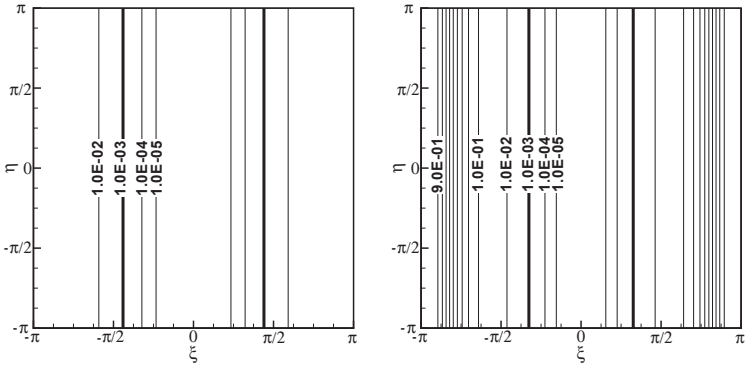


(c) $\mathcal{P}_{\xi_0^*}$, RBC5. (d) $\mathcal{D}_{\xi_0^*}$, RBC5.

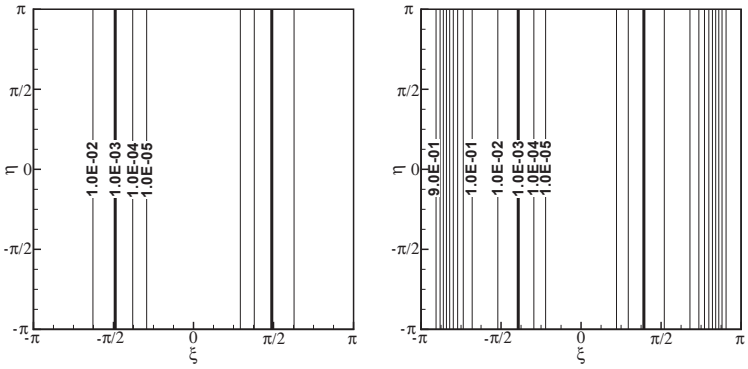


(e) $\mathcal{P}_{\xi_0^*}$, RBC7. (f) $\mathcal{D}_{\xi_0^*}$, RBC7.

Figure III.6: Contours of the phase error $\mathcal{P}_{\xi_0^*}$ (left) and damping function $\mathcal{D}_{\xi_0^*}$ (right) for pure advection in the $x$ direction, $\dot{\mathbf{A}} = (\dot{A}, 0)$, *i.e.* $\theta = 0$. Bold black lines correspond to a threshold error of $10^{-3}$.

Then, we proceed to the analysis of the dispersion error and damping function for dissipative RBC schemes of different orders. Fig. III.6 shows contour levels of the dispersion error and damping function for different combinations of the reduced wave numbers and an advection velocity aligned with one grid direction, i.e. $\theta = 0$. Specifically, we choose $\dot{\mathbf{A}} = (\dot{A}, 0)$. In these figures, the bold black lines correspond to a threshold error of $10^{-3}$. It can be seen that, when the order of accuracy increases, the threshold moves towards higher wave numbers. For this 1D configuration, the error does not depend on $\eta$ even if the schemes are formulated in 2D. Thus,

for a deeper analysis, we take a 1D cut of figures III.6 for all of the schemes under investigation, and represent the errors on the same graph for comparison purposes. Fig. III.5(a) shows the 1D phase errors (in log scale), for RBC schemes of different orders.

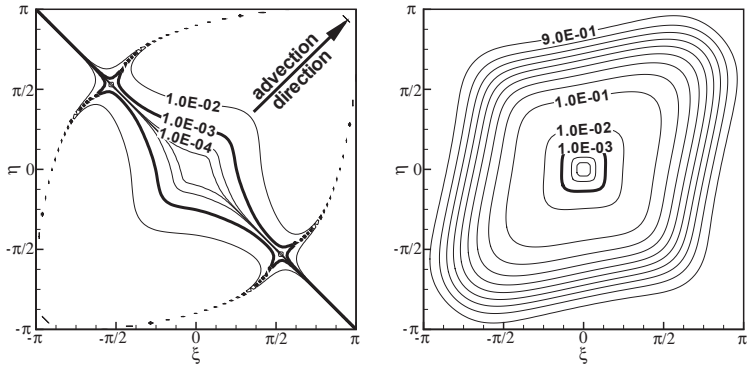


(a) $\mathcal{P}_{\xi^*_{\pi/4}}$, RBC3. (b) $\mathcal{D}_{\xi^*_{\pi/4}}$, RBC3.

(c) $\mathcal{P}_{\xi^*_{\pi/4}}$, RBC5. (d) $\mathcal{D}_{\xi^*_{\pi/4}}$, RBC5.

(e) $\mathcal{P}_{\xi^*_{\pi/4}}$, RBC7. (f) $\mathcal{D}_{\xi^*_{\pi/4}}$, RBC7.

Figure III.7: Contours of the phase error $\mathcal{P}_{\xi^*_{\pi/4}}$ (left) and damping function $\mathcal{D}_{\xi^*_{\pi/4}}$ (right) for pure advection in the diagonal direction, $\dot{\mathbf{A}} = (\dot{A}, \dot{A})$, *i.e.* $\theta = \pi/4$. Bold black lines correspond to a threshold error of $10^{-3}$.

Tab. III.3 provides the wave number corresponding to an error of $10^{-3}$. RBC$q$ schemes of fifth- and seventh-order accuracy exhibit a cut-off wave number $\xi_c$ very close to $\pi/2$, the

smallest resolvable wave number being close to $2\pi/5$ according to Nyquist criterion. Similarly, Fig. III.5(b) displays 1D cuts of the damping function $\mathcal{D}_{\xi_0^*}$. As it can be seen in Tabs. III.2, RBC5 and RBC7 exhibit a damping function of less than $10^{-3}$ up to cut-off wave numbers of 1.03 and 1.24, respectively, which raises sharply at higher wave numbers.

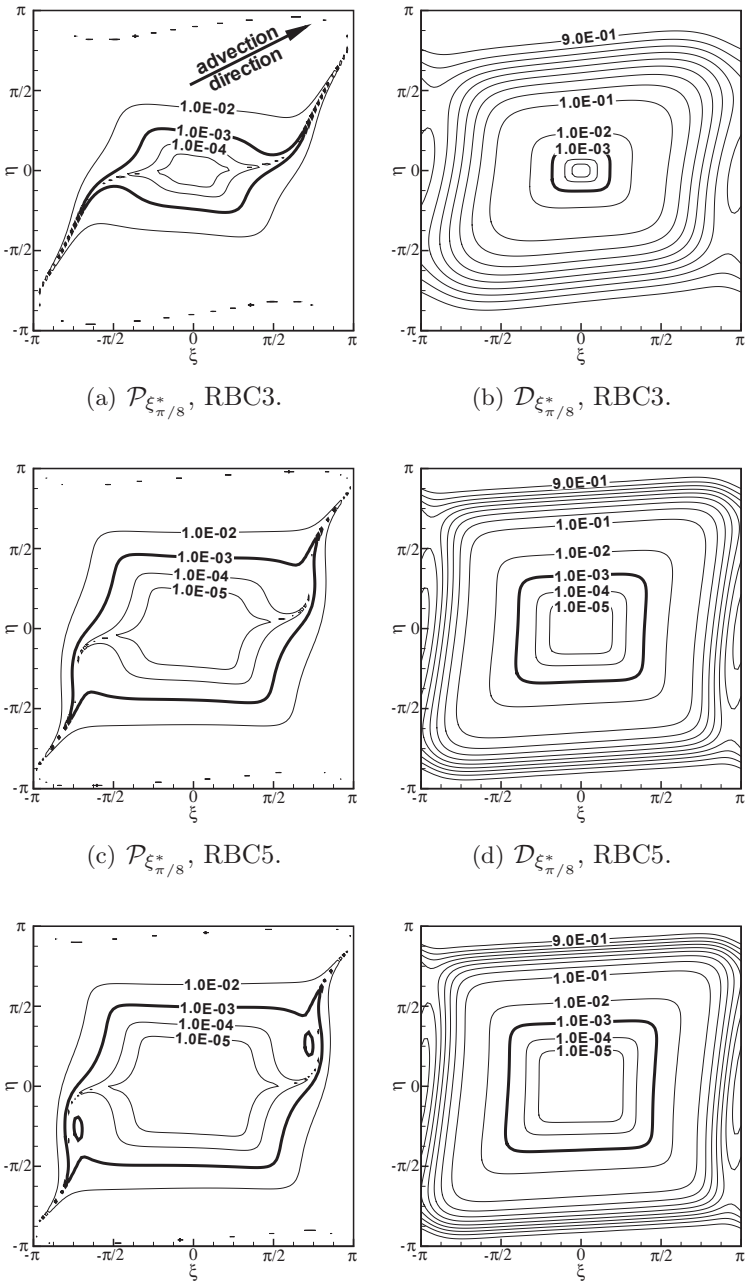


(a) $\mathcal{P}_{\xi^*_{\pi/8}}$, RBC3. (b) $\mathcal{D}_{\xi^*_{\pi/8}}$, RBC3.

(c) $\mathcal{P}_{\xi^*_{\pi/8}}$, RBC5. (d) $\mathcal{D}_{\xi^*_{\pi/8}}$, RBC5.

(e) $\mathcal{P}_{\xi^*_{\pi/8}}$, RBC7. (f) $\mathcal{D}_{\xi^*_{\pi/8}}$, RBC7.

Figure III.8: Contours of the phase error $\mathcal{P}_{\xi^*_{\pi/8}}$ (top) and damping function $\mathcal{D}_{\xi^*_{\pi/8}}$ (bottom) for pure advection in the direction, $\dot{\mathbf{A}} = (\dot{A}, \dot{A}/2)$, *i.e.* $\theta = \pi/8$. Bold black lines correspond to a threshold error of $10^{-3}$.

This shows that the intrinsic numerical dissipation of high-order RBC$q$ schemes acts as a

selective filter with a sharp cut-off at high frequency: it efficiently damps out grid-to-grid oscillations that can lead to numerical instabilities without affecting the resolved wave numbers.
Also note that, coherently with the truncation error analysis, the resolvability limit of RBC schemes is essentially ruled by the dissipation and not by the dispersion error, their leading-order error term being of dissipative nature. The results summarized in Tab. III.3 and III.2 prove that RBC schemes of order 5 and 7 can accurately resolve a given wavelength by means of less than 7 or 6 mesh cells respectively, whereas RBC3 requires approximately 9 mesh cells to meet the prescribed accuracy requirements on dispersion errors and 16 mesh points for dissipation errors. Nevertheless, these requirements are still lower than those e.g. of the third-order upwind scheme, for which 10 and 20 mesh cells per wavelength are required to meet the accuracy criteria on dispersion and dissipation, respectively.
Then, we investigate the spectrum of RBC$q$ schemes in the case of multidimensional advection, and namely for $\dot{\mathbf{A}} = (\dot{A}, \dot{A})$ or $\theta = \pi/4$. This corresponds to an advection velocity aligned with a mesh diagonal. Fig. III.7 shows the phase error and damping function contours for this case, which illustrate well the multidimensional nature of RBC$q$ schemes. The bold black contour corresponds to the error criterion $10^{-3}$. RBC$q$ schemes display very low dissipation and dispersion errors up to small reduced wave numbers in the diagonal direction. Precisely, inspection of the damping function contours displayed in Fig. III.7(b)-III.7(d)-III.7(f) shows that the multidimensional nature of RBC$q$ schemes allows minimising numerical dissipation along the advection direction. Moreover, the dispersion error is almost zero in the transverse direction (see Fig. III.7(a)-III.7(c)-III.7(e)). This effect is more evident for higher order RBC5 and RBC7 schemes compared to RBC3.

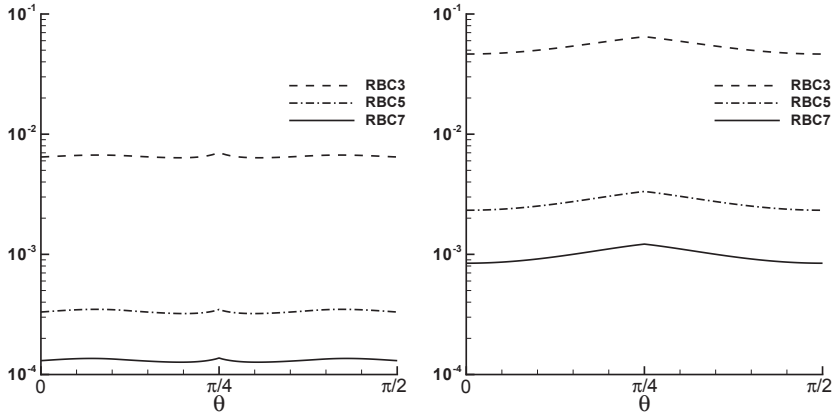


(a) $\underset{\boldsymbol{\xi}\in[-\pi/2,\pi/2]^2}{\text{mean}}(\mathcal{P}_{\xi^*_\theta})$. (b) $\underset{\boldsymbol{\xi}\in[-\pi/2,\pi/2]^2}{\text{mean}}(\mathcal{D}_{\xi^*_\theta})$.

Figure III.9: Average of $\mathcal{P}_{\xi^*_\theta}$ and $\mathcal{D}_{\xi^*_\theta}$ over the interval $\boldsymbol{\xi} \in [-\pi/2, \pi/2]^2$ as a function of the advection direction $\theta$.

We also investigate the spectrum of RBC$q$ schemes in case of multidimensional advection in which no symmetry is present, namely for $\dot{\mathbf{A}} = (\dot{A}, \dot{A}/2)$ (*i.e.* $\theta = \pi/8$). Fig. III.8 shows the phase error and damping function contours for this case. It illustrates well the multidimensional nature of RBC$q$ schemes for any flow conditions. It also shows very low dissipation and dispersion errors up to small reduced wavelengths in the advection direction.
Finally, we give an overview of the phase and damping error for the range of advection directions, $\theta \in [0, \pi/2]$. Specifically Fig. III.9 shows the average value of $\mathcal{P}_{\xi^*_\theta}$ and $\mathcal{D}_{\xi^*_\theta}$ for $\boldsymbol{\xi} \in [-\pi/2, \pi/2]^2$. The present plots show that thanks to their genuinlly multi-dimensional formulation RBC pro-

vides an almost constant error level over the whole range of advection direction, with a maximum at $\theta = \pi/4$ and a minimum at $\theta = 0$ and $\theta = \pi/2$. It also confirms that error levels decrease quickly with the order of accuracy, and that dissipation errors dominate over dispersion errors for a given order of accuracy.

## III.10 Numerical tests

In the following, we carry out some numerical tests to check the effect of satisfying or not the $\chi$-criterion. We consider the RBC3 scheme with a dissipation operator corresponding to $b = 0$ ($\chi$-criterion violated) or $b = 1/6$ ($\chi$-criterion satisfied) and the RBC7 scheme with the coefficients (III.43) associated to $c = 0$ ($\chi$-criterion violated) or the coefficients (III.42) associated to $c = 1/70$ ($\chi$-criterion satisfied). Then, numerical applications are considered in order to illustrate the accuracy and resolvability properties of RBC$q$ schemes ($q = 3, 5, 7$). Initially, we consider a simple linear problem, namely the advection of a sine wave, to numerically check the theoretical results of the preceding Section. Only RBC$q$ schemes satisfying the $\chi$-criterion are considered for the last computations.

For the following computations, the time derivative in the main residual and in the mid-point residuals is approximated by second-order accurate Backward Linear Multistep Method, which is A-stable (see Equ. (III.60)). Such a choice leads to an unconditionally stable fully discrete scheme when coupled to a dissipative spatial approximation. The time-discretization being fully implicit, the resulting system of equations is solved at each time step by using a dual-time stepping approach. Newton subiterations are also a valid alternative. For more details on the time integration scheme, we refer the reader to Refs [41, 117].

### III.10.1 Advection of a sine wave: *numerical proof of the $\chi$-criterion*

In the proof of Theorem III.5.1, we have found that the multidimensional dissipation property is equivalent to the positivity of the function $\mathcal{D}(\lambda, \breve{\alpha})$. Consider the simple case of an advection directed in the first mesh diagonal, that is $\breve{\alpha} = 1$ and consider any sinusoïdal wave propagating along this diagonal, that is $\delta y\, \eta = \delta x \xi$, or $\lambda = 1$. Then

$$\mathcal{D}(1, 1) = 2(1 + \chi)$$

for any order of the RBC scheme.
Clearly $\mathcal{D}(1, 1)$ is positive for $\chi = 0$, but it is negative for the values corresponding to RBC3 ($b = 0$) and RBC7 ($c = 0$) as summarized in Table III.3. So this diagonal advection is an interesting situation to investigate numerically.

| | $\kappa$ | $\chi$ | $\mathcal{D}(1,1)$ |
|---|---|---|---|
| RBC3 ($b = 0$) | $\frac{1}{24}$ | $-2$ | $-2$ |
| RBC3 ($b = \frac{1}{6}$) | $\frac{1}{24}$ | 0 | 2 |
| RBC7 ($c = 0$) | $\frac{1}{5600}$ | $-\frac{4}{3}$ | $-\frac{2}{3}$ |
| RBC7 ($c = \frac{1}{70}$) | $\frac{1}{5600}$ | 0 | 2 |

Table III.3: Dissipation characteristics for a diagonal advection

We thus consider the initial-value problem:

$$\begin{cases} w_t + w_x + w_y = 0 \\ w(x,y,0) = \sin(2\pi(x+y)), \ -1 \leqslant x \leqslant 1, \ -1 \leqslant y \leqslant 1, \end{cases}$$

with periodic boundary conditions. The initial condition is shown on Fig. III.10. In the diagonal direction, the wavelength is $\sqrt{2}/2$ and the advection speed is $\sqrt{2}$. The computational domain $[-1,1]^2$ is discretized by 25×25 square cells ($\delta x = \delta y = 0.08$), which corresponds to 12.5 points per wavelength. The time step is rather small: $\Delta t/\delta x = 0.05$. The time evolution of the amplitude is notably amplified when the $\chi$-criterion is violated as shown in Fig. III.11. This amplification is faster with RBC7 than with RBC3. On the contrary the sine wave is damped out when the $\chi$-criterion is satisfied. The damping is very small for RBC7: 1.6% after 5000 time-iterations ($t = 20$), corresponding to a diagonal advection over a distance of 40 wavelengths.

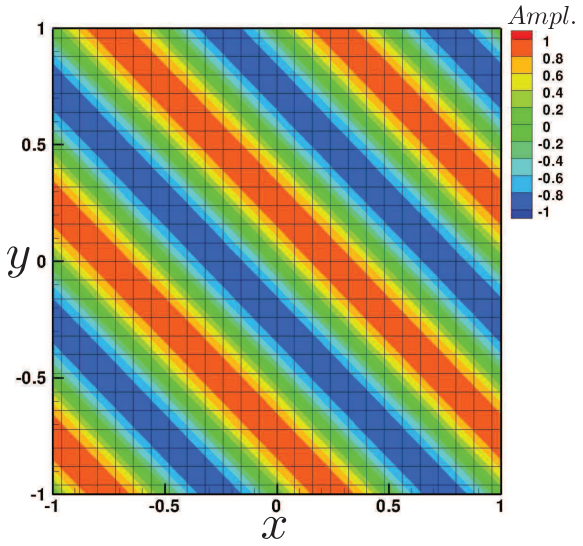


Figure III.10: Initial wave on the 25×25 mesh.

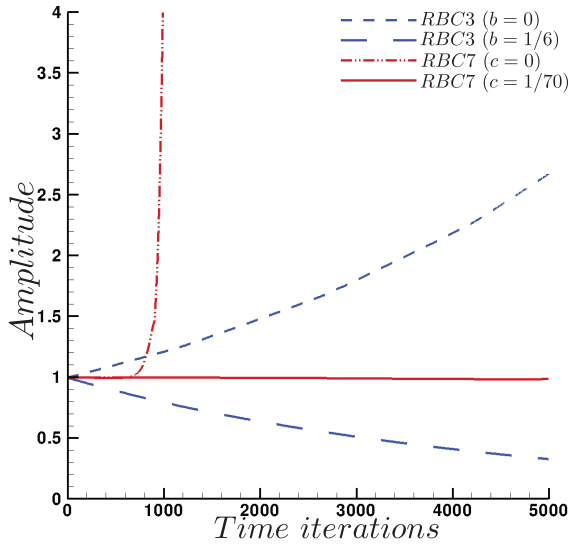


Figure III.11: Wave amplitude versus time-iterations.

### III.10.2 Advection of a sine wave: *assesment of the spectral properties*

The accuracy of RBC schemes has been quantified in Section III.9.2 through the study of dissipation and dispersion errors in the Fourier space, and their resolvability limits have been stated in term of minimum number of points per wavelength. To assess those results, we study linear advection of a sine wave for different choices of the number of points per wavelength used to represent it in both directions. The computational domain $[-1,1]^2$ is discretised by $48 \times 48$ cells and periodicity conditions are applied at the four boundaries. A very small time step ($\Delta t = 0.002$) is used to rule out errors due to the time integration scheme.
Precisely, we consider the initial-value problem:

$$\begin{cases} w_t + Aw_x + Bw_y = 0 \\ w(x,y,0) = \sin\left[2\pi\left(\dfrac{x}{\delta x\ n_x} + \dfrac{\beta\, y}{\delta y\ n_y}\right)\right], \ -1 \leqslant x \leqslant 1, \ -1 \leqslant y \leqslant 1, \end{cases}$$

where $w$ is a scalar quantity, $\mathbf{A} = (A, B)$ is the advection velocity vector, $n_x$ and $n_y$ are the number of points per wavelength in the $x$- and $y$-direction and $\beta$ is a parameter governing the

inclination of the wave front with respect to the $x$-axis: for $\beta = 0$, the wave front is perpendicular to $x$ and the initial condition does not depend on $y$. In the following, we choose $A$ and $B$ in order to reproduce the flow situations studied theoretically in Section 3. Namely, by choosing $\mathbf{A} = (1, 0)$, $\mathbf{A} = (1, 1)$ and $\mathbf{A} = (1, 0.5)$ we get the cases $\theta = 0$ (horizontal advection), $\theta = \pi/4$ (diagonal advection), $\theta = \pi/8$. Note that the first choices introduce some symmetry in the discretization, whereas the last one does not. For each situation, we investigate the impact of the number of points per wavelength used in each direction on the numerical solution.

#### III.10.2.1 Case $\theta = 0$

For $\theta = 0$, damping of the sine wave only depends on the number of mesh points along this direction. Fig. III.12 illustrates two cases using different wavelengths in the direction orthogonal to the advection direction and thus different values of the reduced wavenumber in the $y$ direction, but the same number of points per wavelength (and thus the same reduced wavenumber) in the $x$ direction. Numerical computations using any RBC scheme give the same damping of the sine wave for both cases. This behaviour is due to the structure of the dissipation matrices $\Phi_i$ $(i = 1, 2)$ which adapt numerical dissipation to the local advection direction with respect to the mesh [82].

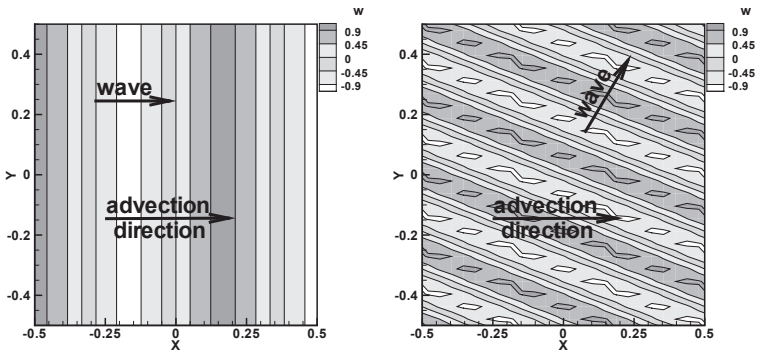


(a) $n_x = 16$, $n_y = 0$, $\beta = 0$. (b) $n_x = 16$, $n_y = 6$, $\beta \neq 0$.

Figure III.12: Case $\theta = 0$. Initial conditions leading to the same dissipation and dispersion error for $\mathrm{RBC}_q$ schemes

For this reason, we only consider a wave aligned with $y$, i.e. we choose $\beta = 0$. Simulations are carried out with a number of points per wavelentgh equal to 6, 8 and 16, respectively. The choice 6 or 8 points per wavelength gives a rather rough representation of the wave. The amplitude of the numerical solution versus the number of wavelengths traveled by the sine wave in the $x$-direction is displayed in Fig. III.13 for the three values of $n_x$ and several RBC schemes. The simulations are carried out over a very long integration time, namely, 150 wavelengths. Even after such a long time, only approximately 20% of the initial amplitude has been lost by using RBC7 and only 6 points per wavelength, against 65% for RBC5. For RBC3, the sine wave is completely damped out after less than 30 travelled wave lengths. If grid resolution is increased to 8 points per wavelength, RBC7 and RBC5 lose about 5% and 20% of the initial amplitude, respectively, whereas again RBC3 totally damps it out. Finally, for a well discretised initial condition (16 points per wavelength), the amplitude is almost conserved by RBC7 and RBC5, whereas RBC3 still loses about 90% of the initial amplitude after 150 travelled wavelengths.
Fig. III.14 illustrates phase lag effects on the numerical solution after 48 traveled wavelentghs.

For any scheme and any number of mesh points used to discretize the wave, dispersion errors are almost negligible. This proves numerically the theoretical results, i.e. the fact that RBC$q$ schemes are dissipative dominant and not dispersive.

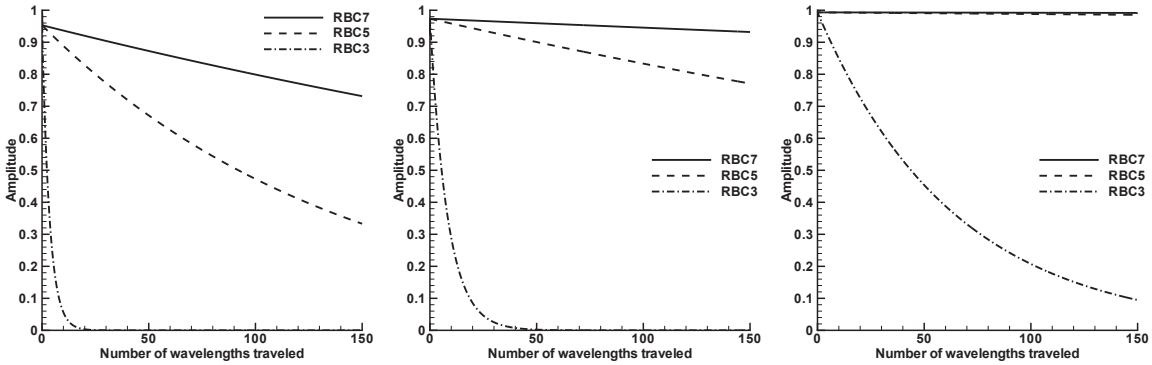


(a) $n_x = 6$. (b) $n_x = 8$. (c) $n_x = 16$.

Figure III.13: Wave amplitude versus number of wavelengths traveled in the case of $\mathbf{A} = (1, 0)$ *i.e.* $\theta = 0$.

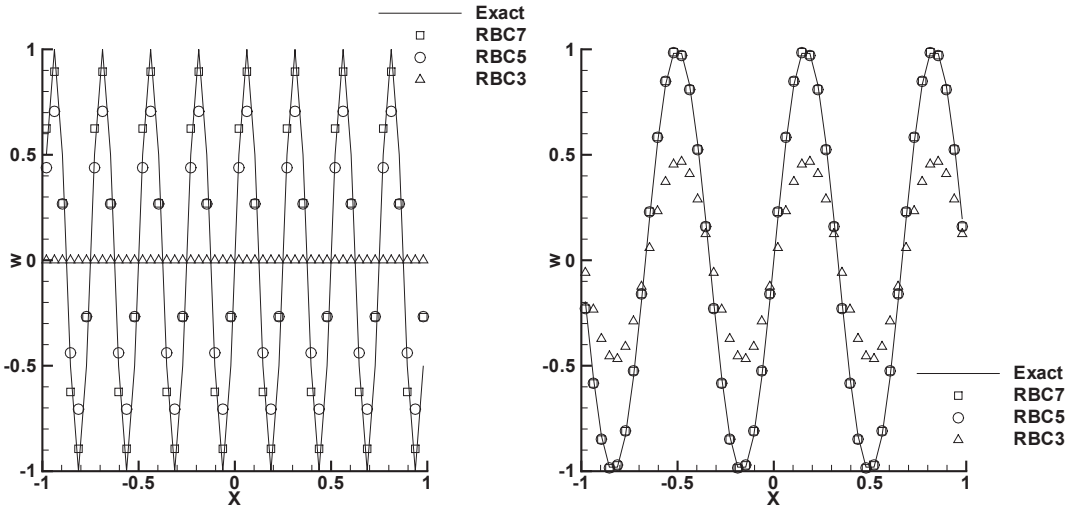


(a) $n_x = 6$. (b) $n_x = 16$.

Figure III.14: Sine wave after an advection over 48 wavelengths in the case of $\theta = 0$ with $n_x$ equal 6 and 16.

### III.10.2.2 Case $\theta = \pi/4$

For the case $\theta = \pi/4$, we study the advection along a mesh diagonal of a sine wave aligned with the mesh and another one aligned with the diagonal. The two cases are represented in Fig. III.15. In the first case, the initial condition does not depend on $y$ and the sine wave is represented by 6 points per wavelength in the $x$-direction (see the case with $n_x = 6$ and $\beta = 0$ of Fig. III.15(a)). In the second case, the sine wave direction is aligned with the second mesh diagonal and progagates along the first diagonal. It is represented by $8/\sqrt{2} \approx 5.6$ points per wavelength

in the advection direction (see the case with $n_x = 8$, $n_y = 8$ and $\beta = 1$ in Fig. III.15(b)).
Fig. III.16 shows that RBC7 resolves the wave equally accurately in both cases: namely, the sine wave is damped only by approximately 20% of the initial amplitude after travelling 150 wavelengths. Moreover, results given by RBC7 for diagonal advection are similar to those obtained for $\theta = 0$.
RBC5 also provides similar results to case $\theta = 0$ for the case of a wave aligned with a mesh direction: the sine wave loses 65% of its amplitude after 150 travelled wavelenths; in the case of a diagonal wave, the results are even better and amplitude is damped by approximately 40%. As in the previous case, RBC3 is not able to preserve the wave over long integration times when using such coarse grid resolution levels. These results confirm the theoretical analysis of Section III.9.2 and prove that, thanks to their genuine multidimensionality, RBC schemes ensure high resolvability even for structures that are not aligned with the mesh. This would not have been the case if a directional scheme had been used: for instance, the study presented in ref. [138] for a class of purely centered schemes shows that directional schemes provide higher dispersion error levels than multidimensional ones for advection direction that are not aligned with the grid.

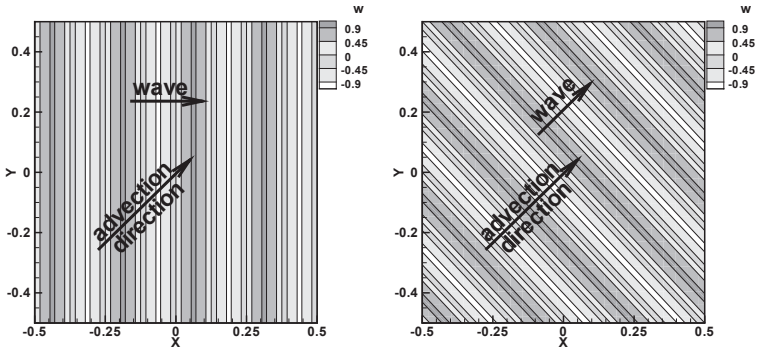


(a) $n_x = 6$, $\beta = 0$. (b) $n_x = 8$, $n_y = 8$, $\beta = 1$.

Figure III.15: Wave amplitude versus number of wavelengths traveled in the case of $\theta = \pi/4$.

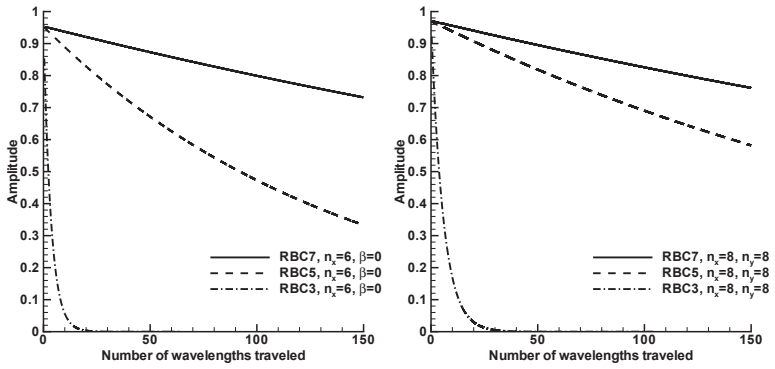


(a) $n_x = 6$, $\beta = 0$. (b) $n_x = 8$, $n_y = 8$, $\beta = 1$.

Figure III.16: Wave amplitude versus number of wavelengths traveled in the case of $\mathbf{A} = (1, 1)$ *i.e.* $\theta = \pi/4$.

### III.10.2.3 Case $\theta = \pi/8$

This last example (see Fig. III.17) allows to further illustrate the accuracy of RBC schemes in multidimensional settings, namely for an advection problem that does not exhibit any flow symmetry with respect to the computational mesh. The results, shown in Fig. III.18, are very similar to those of the preceding cases, further demonstrating that the resolvability properties of RBC schemes are essentially insensitive to the advection direction.

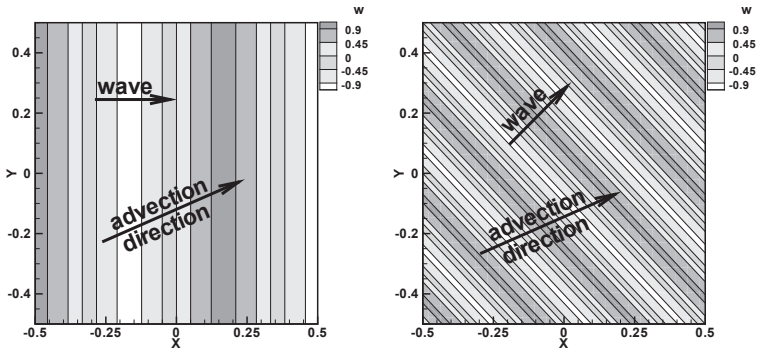


(a) $n_x = 6$, $\beta = 0$. (b) $n_x = 8$, $n_y = 8$, $\beta = 1$.

Figure III.17: Wave amplitude versus number of wavelengths traveled in the case of $\theta = \pi/8$.

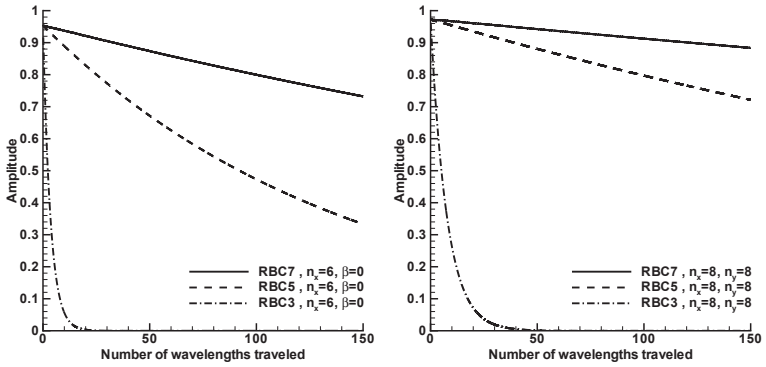


(a) $n_x = 6$, $\beta = 0$. (b) $n_x = 8$, $n_y = 8$, $\beta = 1$.

Figure III.18: Wave amplitude versus number of wavelengths traveled in the case of $\mathbf{A} = (1, 1/2)$ *i.e.* $\theta = \pi/8$.

## III.10.3 A multidimensional flow problem: *the converging cylindrical shock*

When the $\chi$-criterion is violated in an RBC scheme, the lack of dissipation occurs in some oblique flow directions. So, we consider a test case involving all the flow directions and a large range of wave numbers, that is a 2-D simulation of a converging cylindrical shock on a uniform Cartesian mesh. Of course, this axisymmetric problem could be solved more easily as a 1-D problem in polar coordinates. Here, the 2-D Euler equations, for a perfect gas with a specific heat ratio $\gamma = 1.4$, are solved in a square domain $[-0.5, 0.5]^2$.
At time $t = 0$, a cylindrical shock (satisfying the Rankine-Hugoniot relations) lies on a circle of

center $(x, y) = (0, 0)$ and radius $r_0 = 0.25$. Inside the cylindrical shock (state 0), the fluid is at rest and at pressure $p_0$. The pressure just behind the shock is $p_1 = 2.4\ p_0$ at $t = 0$. Outside the cylindrical shock, the initial state corresponds to a steady converging flow, *i.e.* the flow at a radius $r > r_0$ is related to the state 1 just behind the shock by the conservation of mass ($\rho V r = \rho_1 V_1 r_0$ where $\rho$ is the density and $V$ the radial velocity), the conservation of total enthalpy and of the entropy. For improving the initial representation of the shock on the Cartesian mesh, the vector $w$ of conservative variables is defined as follows in the mesh cells intersecting the shock:

$$w_* = (1 - \theta)w_0 + \theta w_1, \quad 0 \leqslant \theta \leqslant 1$$

where $\theta \delta x \delta y$ is the cell area fraction in state 1.

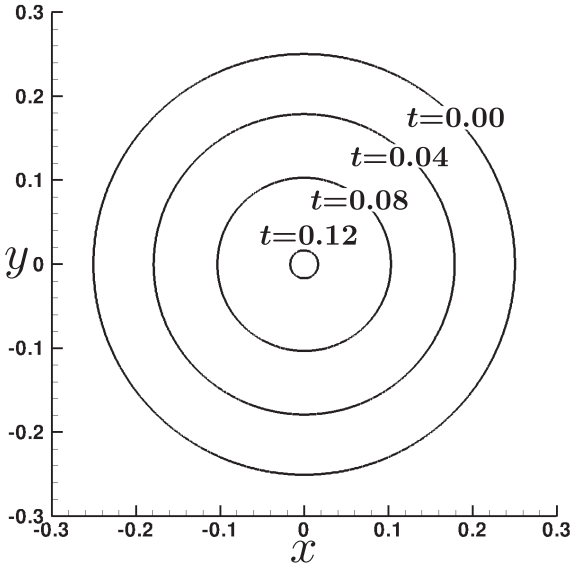


Figure III.19: Shape of the converging shock at different times computed by RBC7.

During the evolution, the cylindrical shock increases in strength as it converges towards the axis. When the shock reaches the axis, it is reflected as a divergent shock. At the very instant of reflection, the pressure at the axis becomes infinite in the Euler model. To avoid a numerical difficulty, the Cartesian mesh is set so that the axis corresponds to a cell vertex and not to a cell center. This prevents the computation of any unphysical quantity on the axis. Note also that the outside boundary is not affected by the perturbations coming from the shock motion in the duration of the present simulation.

Chisnell [36] gave in 1957 an analytical estimation of the pressure behind a moving cylindrical shock, the theoretical arguments of which were improved by Whitham [162]. According to this theory, the Mach number $M$ of the shock wave (relative to the fluid at rest) at radius $r$ is solution of the differential equation:

$$\frac{dM}{dr} = -\frac{1}{r}\frac{(M^2 - 1).K(M)}{2M} \tag{III.81}$$

where

$$K(M) = 2\left[\left(1 + \frac{2}{\gamma + 1}\frac{1 - \mu^2}{\mu}\right)\left(2\mu + 1 + \frac{1}{M^2}\right)\right]^{-1}$$

$$\mu = \left[\frac{(\gamma - 1)M^2 + 2}{2\gamma M^2 - (\gamma - 1)}\right]^{\frac{1}{2}}.$$

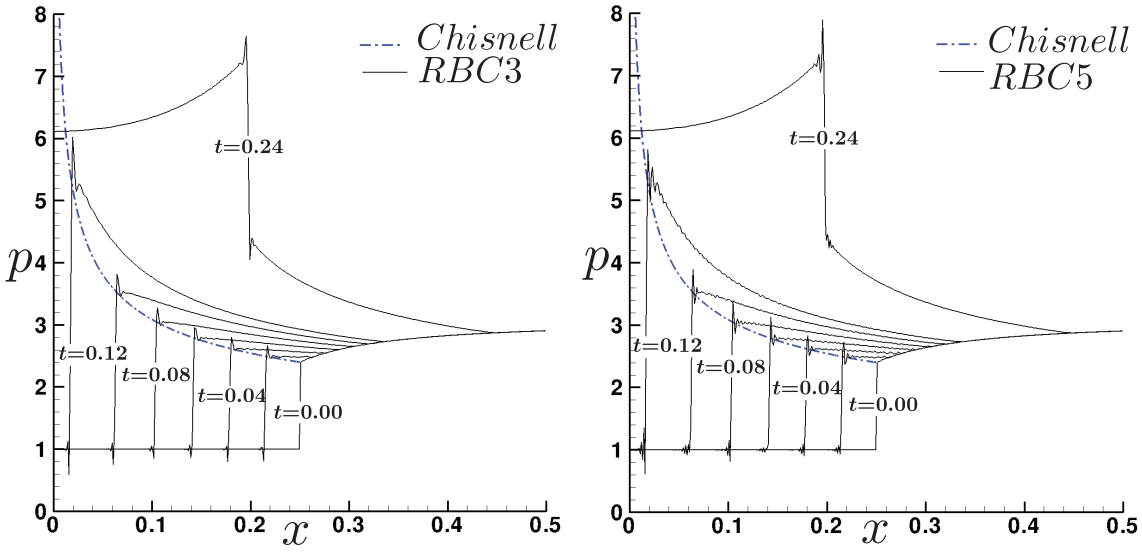


(a) RBC3.




(b) RBC5.

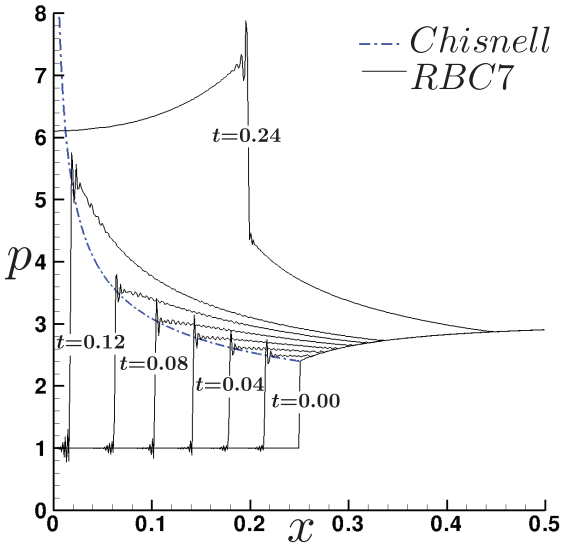


(c) RBC7.

Figure III.20: Pressure along the x-axis at different times for RBC schemes satisfying the $\chi$-criterion.

For $\gamma = 1.4$, the function $K(M)$ decreases slowly from 0.5 for $M = 1$ to $14/(17+7\sqrt{7}) \approx 0.394$ for $M \to \infty$. Starting from the initial condition $M_0 = M(r_0)$, the equation (III.81) can easily be solved numerically with a high accuracy. An exact solution is also available [36], but its expression is very complicated and defined in the form $r = r(M)$.
The pressure behind the shock in motion is deduced from $M = M(r)$ using the Rankine-Hugoniot relations:

$$p_1 = \frac{2\gamma M^2 - (\gamma - 1)}{\gamma + 1} p_0 \tag{III.82}$$

The converging cylindrical shock problem is solved by the RBC schemes on a 800×800 Cartesian mesh with $\Delta t/\delta x = 0.21$. When the $\chi$-criterion is violated, the computation fails after a few time iterations (one iteration for RBC3 with $b = 0$ and 26 for RBC7 with $c = 0$). When the $\chi$-criterion is satisfied, the computation succeeds, even after the shock reflection on the axis. In

this case, the pressure profiles along the $x$-axis are shown on Fig. III.20 for the RBC3, RBC5 and RBC7 schemes at different times, together with the analytical pressure behind the shock deduced from (III.81)-(III.82). The agreement between the numerical solution and the Chisnell theory is very good. The shape of the converging shock computed by the RBC7 scheme at different times is shown on Fig. III.19 . This shape has been defined as the isobar lines of level $\frac{1}{2}(p_1 + p_0)$ at each time. The converging shock appears to be perfectly circular on the Cartesian mesh. Clearly, Fig. III.20 reveals the oscillatory nature of the shock profiles computed by the present high order schemes, specially by RBC5 and RBC7. It should be noted that the computations have been achieved by a strict use of the method described in the present paper: there is no limiter, no entropy correction, no filtering or other additive. In these conditions, it appears that a good design of the dissipative operator allows the calculation of a difficult test case, even if the discrete shock is oscillatory and could be improved.

## III.11 Chapter summary

In this chapter, a comprehensive study of the dissipation properties of a family of Residual-Based Compact schemes has been presented for 2-D and 3-D hyperbolic systems of conservation laws. The residual-based numerical dissipation operator has been shown to be the counterpart of a high-order differential operator based on pure and mixed derivatives of even order. A general criterion (Thm. III.5.1 and III.6.1) has been established for this operator to be dissipative. This criterion has also been confirmed and interpreted. The dissipation and resolvability properties of RBC schemes of several orders have been quantified through a detailed analysis of their Fourier spectra for a multidimensional linear problem. The analysis of the modified wave number $\xi_\theta^*$ associated to RBC schemes of different orders proves that, for RBC schemes which coefficients have been selected according to a sufficient and necessary dissipation condition –the $\chi$-criterion–, $\xi_\theta^*$ exhibit a negative imaginary part for any wave number and any choice of the CFL numbers associated to space directions. As a consequence, no solution mode can be amplified spuriously by the schemes. The modified wave number is also used to define damping and phase errors with respect to an exact transport operator. Present results confirm former studies based on truncation error analysis and show that odd-order RBC schemes are eminently dissipative and not dispersive. For RBC schemes of higher orders (5 and 7), both dissipation and dispersion errors take very low values (less than $10^{-3}$) up to reduced wave numbers close to $\pi/2$, i.e. to the grid resolvability limit. Then, dissipation increases sharply so that higher frequencies are efficiently damped out. Moreover, thanks to their genuinely multidimensional formulation, RBC schemes conserve good dissipation and dispersion properties even for flow modes that are not aligned with the computational grid.

Numerical tests confirm the theoretical results and demonstrate the importance of a well-designed dissipation operator for numerical simulations in gas dynamics. Specifically, the present residual-based formulation ensures controlled damping of sine waves propagating along any direction with respect to the computational mesh and with any advection speed. It also allows the computation of unsteady multidimensional flows with strong shocks without any treatment for shock capturing. Moreover, numerical tests for a linear advection problem confirm the theoretical results on the spectral properties of RBC schemes.

In this chapter, RBC schemes have been introduced only for Cartesian regular meshes. However, with a view of computing *realistic* fluid flows their is a need of a formulation of these schemes on curvilinear meshes. The next chapter deals with this issue describing the extension of RBC schemes to curvilinear meshes.

# Chapter IV

# Extension to curvilinear meshes

**Contents**



## IV.1 Introduction

For the numerical simulation of fluid flows in complex geometries using body-fitted meshes, finite difference schemes require exact or approximate coordinate coordinate transformation techniques to map the physical domain into a Cartesian computational domain (see e.g. [60, 114, 150–152]). Special care is required to evaluate the metrics on non-smooth meshes because of numerical errors in the determination of the transformation Jacobian [60]. Suitable treatement is also required to preserve uniform flow on 3D curvilinear meshes [150, 151]. Finally, the conservation property is not automatically guaranteed in the Finite Difference framework.

An alternative to coordinate transformation, widely used in Computational Fluid Dynamics for its ability to handle complex geometries while ensuring conservation, is represented by the

finite-volume (FV) method. This consists in discretizing a system of conservation laws written in integral form over a mesh composed of small volumes or cells. For compressible flows, the first developements of the method have been made in the early seventies at NASA Ames [112, 113, 132], but the concept can also be found in the pioneering work by Godunov [66]. FV schemes are classified according to the kind of mesh used (structured or unstructured) and to the place where the discrete unknown are assigned (cell centers, cell vertices, ...). Once the system of conservation laws has been discretized on every mesh cell, the main issue for lower order FV methods (i.e. methods of second-order accuracy at most) is to define the numerical flux at the interfaces from the unknowns. For higher-order methods (third-order and more), it is essential to distinguish whether the unknowns represent cell-averaged properties or pointwise values of the field variables in the control volume (e.g. values at cell centroids). The use of cell-averaged values and fluxes as main unknowns is quite a natural choice in FV methods, since it avoids introducing quadrature formulae to evaluate volume and surface integrals. Nevertheless, an implicit deconvolution step is required to relate cell-averaged values to face values [59, 91, 94, 123]: this procedure is restricted to uniform Cartesian meshes, and its application to non-uniform grids leads to a loss of accuracy. A more general procedure valid for non-uniform structured grids has been proposed in [94], with focus on compact schemes: thanks to this, it was possible to construct a compact scheme of fourth-order accuracy on Cartesian meshes and 3rd-order accuracy on distorted meshes. The implicit deconvolution step requires the solution of a linear system for each cell face, which may increase the computational cost considerably. In [72], a high-order piecewise polynomial reconstruction is used to increase the accuracy of MUSCL schemes on arbitrary unstructured grids. Face values are computed from cell-averaged quantities via a recursive correction technique involving approximations of the solution derivatives. Nevertheless, this approach requires to store additional connectivity information about the reconstruction stencil and to store or recompute at each time step reconstruction matrices. Since we are mainly interested into FV schemes on structured meshes, and in an effort to minimize storage and computational cost requirements, in this work we adopt a point-wise cell-centered FV formulation, according to the general framework presented in [128, 129].

Point-wise cell-centered FV RBC schemes of third-order accuracy have been developed in the case of both structured [73, 105] and unstructured meshes [51, 101], and applied mainly to steady flow problems. In this case, the numerical dissipation does not contain time derivatives, which simplifies the accuracy and stability analysis. For unsteady problems, this kind of analysis is no longer sufficient, and straightforward extensions of the steady schemes to unsteady flows may lead to numerical instabilities for some flow conditions, as shown in the preceding Chapter for finite-difference RBC schemes ( see also [106]). For this reason, in the following we design a dissipative third-order FV RBC scheme for unsteady compressible flows of second order on highly deformed structured meshes and third order on slightly distorted meshes. We call this scheme RBC$i$ where the $i$ stands for *irregular*, since it is designed for irregular meshes. Because we are essentially interested into spatial accuracy properties, in the following of this paper we restrict our discussion to semi-discrete schemes. The Cauchy-stability and spectral properties of RBC$i$ are then investigated for regular meshes. The scheme is implemented within the flow solver elsA [1, 33, 34], developed by the Numerical Simulation and Aeroacoustics Department (DSNA) of ONERA, and applied to the computation of a variety of unsteady flow problems governed by the Euler or Reynolds-Averaged Navier–Stokes equations.
At this stage, no attempt is made to generalize the proposed procedure to high-order since it leads to a very cumbersome formulation at orders higher then three. Alternative approaches represented by finite element-like reconstructions, coordinate transformations and Cartesian grids with immersed boundary techniques [35, 139, 144, 145, 153].

The present chapter is organised as follows. In Section IV.2 we briefly recall some important definitions and measures of accuracy for finite volume schemes. Section IV.3 gives the general definition of a Residual-Based Compact scheme in the finite volume framework. Section IV.4 describes two different finite volume extensions of the third-order accurate RBC scheme: the first one is a straightforward extension of the finite-difference scheme, whereas the second one takes into account the effective mesh geometry in order to satisfy accuracy conditions in the finite-volume sense on general meshes. When applied to regular Cartesian grids, such a scheme degenerates to an approximation of the spatial derivatives that differs from the finite-difference RBC approximation. In Section IV.6, we study the Cauchy-stability and the spectral properties of this approximation. Finally, Section IV.7 is devoted to numerical applications.
Material presented in this Chapter makes the object of an article submitted to an international journal [70].

## IV.2 Finite volume framework

Consider the integral form of a hyperbolic system of conservation laws:

$$\frac{d}{dt}\int_{\Omega} w \; d\Omega + \oint_{\partial\Omega} \boldsymbol{\phi}.\boldsymbol{n} \; d\Gamma = 0 \tag{IV.1}$$

with initial conditions

$$w(x,y,z,0) = w_0(x,y,z)$$

where $t$ is the time, $x$, $y$ and $z$ are Cartesian space coordinates, $w$ is the vector of conservative variables, $\Omega$ is a closed control volume which boundary is $\partial\Omega$, $\boldsymbol{\phi}$ is the physical flux density $\boldsymbol{\phi} = [f, g, e]$ depending smoothly on $w$, and $\boldsymbol{n}$ is the unit outward normal. The Jacobian matrices of the flux are denoted $A = \mathrm{d}f/\mathrm{d}w$, $B = \mathrm{d}g/\mathrm{d}w$ and $C = \mathrm{d}e/\mathrm{d}w$.
Define a structured mesh composed of hexaedral cells $\Omega_{j,k,l}$ and denote the cell centers by $C_{j,k,l}$, the cell vertices by $M_{j+\frac{1}{2},k+\frac{1}{2},l+\frac{1}{2}}$ and the cell faces by $\Gamma_{j+\frac{1}{2},k,l}$, $\Gamma_{j,k+\frac{1}{2},l}$ or $\Gamma_{j,k,l+\frac{1}{2}}$:

$$\begin{aligned}\partial\Omega_{j,k,l} =& \Gamma_{j+\frac{1}{2},k,l} \cup \Gamma_{j,k+\frac{1}{2},l} \cup \Gamma_{j,k,l+\frac{1}{2}} \\ & \cup \Gamma_{j-\frac{1}{2},k,l} \cup \Gamma_{j,k-\frac{1}{2},l} \cup \Gamma_{j,k,l-\frac{1}{2}}\end{aligned}$$

The cell volume is denoted by $|\Omega_{j,k,l}|$ and an edge surface by $|\Gamma_{j+\frac{1}{2},k,l}|$. For each cell face $\Gamma_{j+\frac{1}{2},k,l}$ we denote $\boldsymbol{\Gamma}_{j+\frac{1}{2},k,l} = (\Gamma_x, \Gamma_y, \Gamma_z)_{j+\frac{1}{2},k,l}$ the oriented surface directed in the sense of increasing mesh indeces, with module equal to $|\Gamma_{j+\frac{1}{2},k,l}|$. For each cell $\Omega_{j,k,l}$ we identify the cell center by its coordinates $(x_{j,k,l}, y_{j,k,l}, z_{j,k,l})$ calculated as the mean of the cell node coordinates, and we denote its maximum dimension in each direction as $\delta x_{j,k,l}, \delta y_{j,k,l}$, and $\delta z_{j,k,l}$, respectively. As mentioned in the Introduction, we choose to locate the unknown vector $w$ at cell centers. Finally, we define a characteristic mesh size by $h = \max(\max_{j,k,l} \delta x_{j,k,l}, \max_{j,k,l} \delta y_{j,k,l}, \max_{j,k,l} \delta z_{j,k,l})$.

Applied to the cell $\Omega_{j,k,l}$, the conservation law (IV.1) reads:

$$\frac{d}{dt}\int_{\Omega_{j,k,l}} w \; d\Omega + \sum_{\Gamma\in\partial\Omega_{j,k,l}} \int_{\Gamma} \boldsymbol{\phi}.\boldsymbol{n} \; d\Gamma = 0 \tag{IV.2}$$

We define a FV exact residual $R$ as:

$$R_{j,k,l} := \mathcal{V}_{j,k,l} + \mathcal{S}_{j,k,l} \tag{IV.3}$$

with

$$\mathcal{V}_{j,k,l} = \frac{d}{dt} \int_{\Omega_{j,k,l}} w \; d\Omega \tag{IV.4}$$

and

$$\mathcal{S}_{j,k,l} = \sum_{\Gamma \in \partial\Omega_{j,k,l}} \int_{\Gamma} \boldsymbol{\phi}.\boldsymbol{n} \; d\Gamma. \tag{IV.5}$$

A FV approximation of (IV.3) can be written:

$$\tilde{R}_{j,k,l} = \tilde{\mathcal{V}}_{j,k,l} + \tilde{\mathcal{S}}_{j,k,l} \tag{IV.6}$$

where $\tilde{\mathcal{V}}_{j,k,l}$ approximates the volume integral

$$\frac{1}{|\Omega_{j,k,l}|}\tilde{\mathcal{V}}_{j,k,l} = \frac{1}{|\Omega_{j,k,l}|}\mathcal{V}_{j,k,l} + \mathcal{O}(h^p) \tag{IV.7}$$

and $\tilde{\mathcal{S}}_{j,k,l}$ approximate the surface integral

$$\frac{1}{|\Gamma|}\tilde{\mathcal{S}}_{j,k,l} = \frac{1}{|\Gamma|}\mathcal{S}_{j,k,l} + \mathcal{O}(h^p) \tag{IV.8}$$

for any edge $\Gamma$ of the cell $\Omega_{j,k,l}$. If Equations (IV.6) and (IV.7) are satisfied simultaneously, the FV approximation (IV.6) is said to be accurate at order $p$ in the FV sense [128, 129].

## IV.3 Finite Volume RBC schemes

Let us introduce for further convenience the difference and average operators for any mesh function $v$:

$$\begin{aligned}
(\delta_1 v)_{j+\frac{1}{2},k,l} &= v_{j+1,k,l} - v_{j,k,l} \\
(\delta_2 v)_{j,k+\frac{1}{2},l} &= v_{j,k+1,l} - v_{j,k,l} \\
(\delta_3 v)_{j,k,l+\frac{1}{2}} &= v_{j,k,l+1} - v_{j,k,l} \\
(\mu_1 v)_{j+\frac{1}{2},k,l} &= \frac{1}{2}(v_{j+1,k,l} + v_{j,k,l}) \\
(\mu_2 v)_{j,k+\frac{1}{2},l} &= \frac{1}{2}(v_{j,k+1,l} + v_{j,k,l}) \\
(\mu_3 v)_{j,k,l+\frac{1}{2}} &= \frac{1}{2}(v_{j,k,l+1} + v_{j,k,l})
\end{aligned}$$

where $j$, $k$ and $l$ are integers or half integers.

A *residual-based* scheme can be expressed in terms of approximations of the exact residual $R$. More precisely, such a scheme is of the following form:

$$(\tilde{R}_0)_{j,k,l} = \tilde{d}_{j,k,l} \tag{IV.9}$$

where $\tilde{R}_0$ is a space-centered approximation of $R$ called the *main residual* and $\tilde{d}$ is a residual-based dissipation term, introduced to ensure numerical stabiliy, defined in terms of first-order differences of the residual as:

$$\tilde{d}_{j,k,l} = \frac{1}{2}[\delta_1(\Phi_1\tilde{R}_1) + \delta_2(\Phi_2\tilde{R}_2) + \delta_3(\Phi_3\tilde{R}_3)]_{j,k,l} \tag{IV.10}$$

where $\tilde{R}_1$, $\tilde{R}_2$ and $\tilde{R}_3$, respectively defined at $j+\frac{1}{2},k,l$, $j,k+\frac{1}{2},l$ and $j,k,l+\frac{1}{2}$ (*cf.* Fig. IV.1), are also space-centered approximations of $R$ on a suitably chosen shifted control volume, are called the *mid-point residuals*, and $\Phi_1$, $\Phi_2$, $\Phi_3$ are numerical viscosity matrices (defined at the same location as the corresponding mid-point residuals).

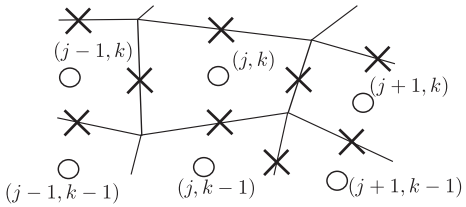


Figure IV.1: Location of the discrete residuals, $\circ$: main residual $\tilde{R}$, $\times$: mid-point residual $\tilde{R}_1$ or $\tilde{R}_2$

These matrices depend only on the eigensystems of the Jacobian matrices $A$, $B$ and $C$ and on the geometry of the current cell $\Omega_{j,k,l}$. They are designed once for all [73, 104, 116] and use no tuning parameters nor limiters. Since the matrices $\Phi_1$, $\Phi_2$ and $\Phi_3$ remain $\mathcal{O}(1)$ as $h$ tend to zero, the dissipation $\tilde{d}$ represents, to the leading order, a numerical approximation of the partial differential term:

$$d = \left[\frac{\delta x}{2}(\Phi_1 R)_x + \frac{\delta y}{2}(\Phi_2 R)_y + \frac{\delta z}{2}(\Phi_3 R)_z\right] \tag{IV.11}$$

This leading term of the expansion, that is only first order accurate, vanishes for an exact solution ($R=0$), so that $\tilde{d}$ is actually consistent with a higher-order dissipation term when the mesh is Cartesian uniform. For FD RBC schemes, the accuracy and spectral properties of the RBC dissipation operator have been discussed in [106] and [67, 68], respectively. Its properties in the case of FV extensions of RBC schemes are discussed later in this paper.

In the following of the discussion, we introduce a direct extension of RBC schemes to Finite Volume. Then, we develop approximations of the main and midpoint residuals that are fourth-order and second-order accurate on uniform Cartesian grids, respectively, and that are as accurate as possible on general curvilinear grids. These approximations will use a stencil made of $3^3$ grid points at most. The resulting scheme is expected to be third-order accurate on uniform Cartesian grids; on the other hand, according to the specific approximation that is adopted, the scheme accuracy will be preserved to a more or less great extent on general curvilinear grids.

## IV.4 Direct FV extension of RBC schemes

As a first step, we describe a straightforward FV extension of the finite difference RBC scheme of nominal third, fifth or seventh order of accuracy for unsteady flows, referred-to as RBC$q$ ($q=3,5,7$) in the following. These *non-weighted* versions of the schemes are shown to degenerate on the corresponding finite difference described in the previous section and in [106], when applied to regular Cartesian grids.

### IV.4.1 Approximation of the main residual

The main residual approximation $\tilde{R}_0$ can be splitted into a volume integral and a surface integral approximation

$$(\tilde{R}_0)_{j,k,l} = (\tilde{\mathcal{V}}_0)_{j,k,l} + (\tilde{\mathcal{S}}_0)_{j,k,l} \tag{IV.12}$$

where $\tilde{\mathcal{V}}_0$ is a centered approximation of $\mathcal{V}$ and $\tilde{\mathcal{S}}_0$ is a centered approximation of $\mathcal{S}$, $\mathcal{V}$ and $\mathcal{S}$ being defined by Eqs. (IV.4) and (IV.5), respectively. Precisely, $\tilde{\mathcal{V}}_0$ and $\tilde{\mathcal{S}}_0$ are given by the following compact approximation operators:

$$(\tilde{\mathcal{V}}_0)_{j,k,l} = \left[\mathcal{FD}^{w_0}_{RBCq}(w_t)\right]_{j,k,l} |\Omega_{j,k,l}| \tag{IV.13}$$

$$(\tilde{\mathcal{S}}_0)_{j,k,l} = [\delta_1 F_1 + \delta_2 F_2 + \delta_3 F_3]_{j,k,l} \tag{IV.14}$$

whith

$$(F_1)_{j+\frac{1}{2},k,l} = \left[\mathcal{FD}^{F_{01}}_{RBCq}(\boldsymbol{\phi})\right]_{j+\frac{1}{2},k,l} . \boldsymbol{\Gamma}_{j+\frac{1}{2},k,l}, \tag{IV.15}$$

where $\mathcal{FD}^{w_0}_{RBCq}$ and $\mathcal{FD}^{F_{01}}_{RBCq}$ are FD operators applied to the time derivative and to the flux in the first direction defined in the previous sections for an RBC$q$ scheme. For instance, for RBC3 we have:

$$\mathcal{FD}^{w_0}_{RBC3} = \left(I + \frac{1}{6}\delta_1^2\right)\left(I + \frac{1}{6}\delta_2^2\right)\left(I + \frac{1}{6}\delta_3^2\right) \tag{IV.16}$$

$$\mathcal{FD}^{F_{01}}_{RBC3} = \left(I + \frac{1}{6}\delta_2^2\right)\left(I + \frac{1}{6}\delta_3^2\right)\mu_1 \tag{IV.17}$$

Similar expressions are used for $(F_2)_{j,k+\frac{1}{2},l}$ and $(F_3)_{j,k,l+\frac{1}{2}}$. For RBC3, approximations (IV.13), (IV.14) and (IV.15) can be seen as multidimensional Simpson formulae for the numerical approximation of volume and surface integrals, where local mesh irregularities are neglected. Because of this simplification, the formulae are not expected to be high-accurate on general grids, as confirmed by numerical experiments presented in the following. Nevertheless, Ref. [128] shows, in the framework of non compact schemes, that nominal accuracy can still be preserved if the mesh satisfies suitable regularity conditions. The higher the scheme accuracy, the more stringent grid regularity requirements, so that nominal accuracy is generally lost for most cases of practical interest.

For RBC3, in the case of a uniform Cartesian mesh, $\Omega_{j,k,l} = \delta x \delta y \delta z$, the main residual $\tilde{R}_0$ reduces to the fourth-order accurate operator seen in the previous section:

$$\begin{aligned}(\tilde{R}_0)_{j,k,l} = \Bigg[&\left(I + \frac{1}{6}\delta_1^2\right)\left(I + \frac{1}{6}\delta_2^2\right)\left(I + \frac{1}{6}\delta_3^2\right) w_t + \left(I + \frac{1}{6}\delta_2^2\right)\left(I + \frac{1}{6}\delta_3^2\right)\frac{\delta_1\mu_1 f}{\delta x} \\ &+ \left(I + \frac{1}{6}\delta_1^2\right)\left(I + \frac{1}{6}\delta_3^2\right)\frac{\delta_2\mu_2 g}{\delta y} + \left(I + \frac{1}{6}\delta_1^2\right)\left(I + \frac{1}{6}\delta_2^2\right)\frac{\delta_3\mu_3 e}{\delta z}\Bigg]_{j,k,l} |\Omega|_{j,k,l}.\end{aligned} \tag{IV.18}$$

### IV.4.2 Residual-based dissipation operator

To complete the scheme formulation we still have to approximate the dissipation operator $\tilde{d}_{j,k,l}$, defined by Eq.(IV.10). This requires approximations of the mid-point residuals. To this end, we define shifted control volumes around cell faces; for instance, a shifted volume denoted $\Omega_{j+\frac{1}{2},k,l}$ will be used to approximate $(\tilde{R}_1)_{j+\frac{1}{2},k,l}$. We associate to this shifted cell the oriented surfaces $\boldsymbol{\Gamma}^1_{j,k,l}$, $\boldsymbol{\Gamma}^2_{j+\frac{1}{2},k+\frac{1}{2},l}$ and $\boldsymbol{\Gamma}^3_{j+\frac{1}{2},k,l+\frac{1}{2}}$ respectively in the directions 1, 2 and 3 (*c.f.* Fig. IV.2) approximated by:

$$\begin{aligned}\boldsymbol{\Gamma}^1_{j,k,l} &= \frac{1}{2}(\boldsymbol{\Gamma}_{j+\frac{1}{2},k,l} + \boldsymbol{\Gamma}_{j-\frac{1}{2},k,l}) \\ \boldsymbol{\Gamma}^2_{j+\frac{1}{2},k+\frac{1}{2},l} &= \frac{1}{2}(\boldsymbol{\Gamma}_{j,k+\frac{1}{2},l} + \boldsymbol{\Gamma}_{j+1,k+\frac{1}{2},l}) \\ \boldsymbol{\Gamma}^3_{j+\frac{1}{2},k,l+\frac{1}{2}} &= \frac{1}{2}(\boldsymbol{\Gamma}_{j,k,l+\frac{1}{2}} + \boldsymbol{\Gamma}_{j+1,k,l+\frac{1}{2}})\end{aligned}$$

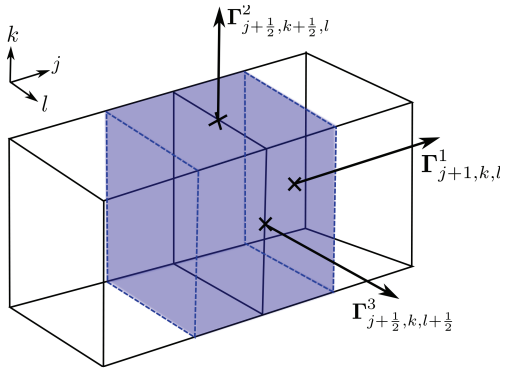


Figure IV.2: Shifted cell

The mid-point residuals can also be splitted into a mid-point volume integral and a mid-point surface integral approximation. For instance, the mid-point residual in the first direction writes:

$$(\tilde{R}_1)_{j+\frac{1}{2},k,l} = (\tilde{\mathcal{V}}_1)_{j+\frac{1}{2},k,l} + (\tilde{\mathcal{S}}_1)_{j+\frac{1}{2},k,l} \tag{IV.19}$$

where $\tilde{\mathcal{V}}_1$ and $\tilde{\mathcal{S}}_1$ are given by the following approximation operators:

$$\begin{aligned}
(\tilde{\mathcal{V}}_1)_{j+\frac{1}{2},k,l} &= \left[\mathcal{FD}^{w_1}_{RBCq}(w_t)\right]_{j+\frac{1}{2},k,l} |\Omega_{j+\frac{1}{2},k,l}| \\
(\tilde{\mathcal{S}}_1)_{j+\frac{1}{2},k,l} &= \left[\mathcal{FD}^{F_{11}}_{RBCq}(\boldsymbol{\phi}).\mathbf{\Gamma}^1 + \mathcal{FD}^{F_{12}}_{RBCq}(\boldsymbol{\phi}).\mathbf{\Gamma}^2 + \mathcal{FD}^{F_{13}}_{RBCq}(\boldsymbol{\phi}).\mathbf{\Gamma}^3\right]_{j+\frac{1}{2},k,l}
\end{aligned} \tag{IV.20}$$

where $|\Omega|_{j+\frac{1}{2},k,l} = \frac{1}{2}(|\Omega|_{j,k,l} + |\Omega|_{j+1,k,l})$ and $\mathcal{FD}^{w_1}_{RBCq}$, $\mathcal{FD}^{F_{11}}_{RBCq}$, $\mathcal{FD}^{F_{12}}_{RBCq}$ and $\mathcal{FD}^{F_{13}}_{RBCq}$ are the FD operators used in the FD definition of RBC$q$ scheme. As an illustration, for RBC3:

$$\begin{aligned}
\mathcal{FD}^{w_1}_{RBC3} &= \left(I + \frac{1}{6}\delta_2^2\right)\left(I + \frac{1}{6}\delta_3^2\right)\mu_1 \\
\mathcal{FD}^{F_{11}}_{RBC3} &= \left(I + \frac{1}{6}\delta_2^2\right)\left(I + \frac{1}{6}\delta_3^2\right)\delta_1 \\
\mathcal{FD}^{F_{12}}_{RBC3} &= \left(I + \frac{1}{6}\delta_3^2\right)\delta_2\mu_2\mu_1 \\
\mathcal{FD}^{F_{13}}_{RBC3} &= \left(I + \frac{1}{6}\delta_2^2\right)\delta_3\mu_3\mu_1
\end{aligned} \tag{IV.21}$$

$\tilde{R}_2$ and $\tilde{R}_3$ use similar approximations in the other directions of the mesh.
For RBC3, in the case of a Cartesian uniform mesh, the mid-point residual $\tilde{R}_1$ can be written in the following form:

$$\begin{aligned}
(\tilde{R}_1)_{j+\frac{1}{2},k,l} = \Bigg[&\left(I + \frac{1}{6}\delta_2^2\right)\left(I + \frac{1}{6}\delta_3^2\right)\left(\mu_1 w_t + \frac{\delta_1 f}{\delta x}\right) \\
&+ \left(I + \frac{1}{6}\delta_3^2\right)\frac{\delta_2\mu_2\mu_1 g}{\delta y} \\
&+ \left(I + \frac{1}{6}\delta_2^2\right)\frac{\delta_3\mu_3\mu_1 e}{\delta z}\Bigg]_{j+\frac{1}{2},k,l} |\Omega|_{j+\frac{1}{2},k,l}
\end{aligned} \tag{IV.22}$$

and similar expressions are obtained for $\tilde{R}_2$ and $\tilde{R}_3$, so that the dissipation operator becomes identical to the dissipation operator of the corresponding finite difference scheme [106]. The same results is straightforward for RBC5 and RBC7.

### IV.4.3 Limitations

The preceding straightforward FV extension of RBC3 is third-order accurate on Cartesian uniform meshes but its order of accuracy is not preserved on non-uniform curvilinear meshes. For instance, by applying (IV.13) and (IV.14) in the simple case of a 1D problem we show that the order of accuracy of the scheme is equal to one for the discretization of the main residual.
Consider a non-uniform 1D mesh as illustrated in Fig. IV.3, with cell centers of coordinates $x_j$, $\delta x_j$ being the size of the $j$th-cell. Also, let be $\alpha = (x_j - x_{j-1})/\delta x_j$ and $\theta = (x_{j+1} - x_j)/\delta x_j$.

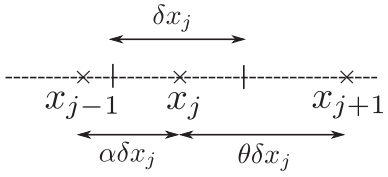


Figure IV.3: 1D configuration

For such a 1D configuration, the FV formulation of the hyperbolic system is:

$$\int_{x_{j-1/2}}^{x_{j+1/2}} w_t \, dx + [\delta_1 f]_j = 0,$$

and the main residual approximation writes:

$$(\tilde{R}_0)_j = \left[ \left( I + \frac{1}{6}\delta_1^2 \right) w_t \right]_j \delta x_j + [\delta_1 \mu_1 f]_j \tag{IV.23}$$

Thus, in the main residual, the volume integral is approximated by:

$$(\tilde{\mathcal{V}}_0)_j = \delta x_j \left[ \left( I + \frac{1}{6}\delta_1^2 \right) w_t \right]_j \tag{IV.24}$$

and the surface integral by:

$$(\tilde{\mathcal{S}}_0)_j = [\delta_1 \mu_1 f]_j = \frac{1}{2}\left(f_{j+1} - f_{j-1}\right) \tag{IV.25}$$

By carrying out a Taylor series expansion of the preceding formulae for an exact solution of the conservation law, we obtain:

$$\begin{aligned} \frac{1}{\delta x_j}(\tilde{\mathcal{V}}_0)_j &= (w_t)_j + \frac{(\theta - \alpha)\delta x_j}{6}(w_{tx})_j + \mathcal{O}(h^2) \\ (\tilde{\mathcal{S}}_0)_j &= \frac{(\alpha + \theta)\delta x_j}{2}(f_x)_j + \mathcal{O}(h^2). \end{aligned} \tag{IV.26}$$

as a consequence:

$$\frac{1}{\delta x_j}(\tilde{\mathcal{V}}_0)_j = \frac{1}{\delta x_j}\int_{x_{j-1/2}}^{x_{j+1/2}} w_t \; dx + \frac{(\theta - \alpha)\delta x_j}{6}(w_{tx})_j + \mathcal{O}(h^2)$$

where the first order term is in general non zero for a non uniform mesh ($\theta \neq \alpha$), thus

$$\frac{1}{\delta x_j}(\tilde{\mathcal{V}}_0)_j = \frac{1}{\delta x_j}\int_{x_{j-1/2}}^{x_{j+1/2}} w_t \; dx + \mathcal{O}(h).$$

Similarly:

$$(\tilde{\mathcal{S}}_0)_j = [\delta_1 f]_j + \left(\frac{\alpha+\theta}{2} - 1\right) \delta x_j (f_x)_j + \mathcal{O}(h^2)$$

where the first-order term is equal to zero if and only if $\theta + \alpha = 2$. Thus, according to the definition (IV.7) and (IV.8), the straightforward extension of RBC3 to FV is of order one in the FV sense for non uniform meshes ($\theta \neq 1$ or $\alpha \neq 1$) in the case of one-dimensional configurations. Similar or worst accuracy losses are encountered for multi-dimensional irregular grids, as it will be made clear from numerical experiments shown in the following.

We described a straightforward FV extension of the finite difference RBC schemes. In the following, this simple extension is referred-to as RBC$r$ for RBC scheme of nominal third order of accuracy (the $r$ stands for regular) , the *non-weighted* version of the scheme. In the next Section, we introduce a finite volume extension of RBC3, called RBC$i$, which is at least second-order accurate on any structured mesh and third-order on meshes with smooth irregularities.

## IV.5 Finite volume third-order RBC scheme

The RBC$i$ scheme is also expressed through the general formula (IV.9) where the numerical dissipation is of the form (IV.10) and the residual is defined in (IV.3). The main difference with respect to RBC$r$ scheme described above is that the main and mid-point residual are now approximated by means of weighted discretization operators that take into account mesh deformations. The procedure used to approximate the volume and surface integrals involved in the residuals is described hereafter. The dissipation matrices $\Phi_i$ do not affect the order of accuracy of the scheme and they are consequently not modified.

### IV.5.1 Approximation of the main residual

Once again, we express the main residual as the sum of a volume integral and a surface integral. For the sake of simplicity and to avoid complex reconstruction procedures we do not try to ensure third-order accuracy on any irregular mesh. Instead, we look for approximations of the integrals that are second order accurate on highly irregular grids and third order accurate on sufficiently smooth grids. Grid regularity criteria were introduced in [128] based on grid stretching, parallelism and orthonormality criteria.
Let us start with the approximation of the volume integral in the main residual $\mathcal{V}_0$. The standard second-order accurate approximation for $\mathcal{V}_0$ at point $(j,k,l)$ is just given by:

$$(\tilde{\mathcal{V}}_0)^{std} = w_{tP}|\Omega_{j,k,l}| = (\mathcal{V}_0)_{j,k,l} + \mathcal{O}(|\Omega_{j,k,l}|h^2), \tag{IV.27}$$

where $P$ is any point in $\Omega_{j,k,l}$. Hereafter, we choose instead to approximate $(\mathcal{V}_0)_{j,k,l}$ as a linear combination of the standard volume integral referred to the cell-center and of integrals evaluated at cell vertices $A$, $B$, $C$, $D$, $E$, $F$, $G$ and $H$ (see Fig. IV.4):

$$\begin{aligned} \tilde{\mathcal{V}}_0 =& \alpha T_{C_1} + \beta(T_A + T_B + T_C + T_D + T_E + T_F + T_G + T_H) \\ =& \mathcal{V}_0 + \mathcal{O}(|\Omega_{j,k,l}|h^2) \end{aligned} \tag{IV.28}$$

where we set $T_P = w_{tP}|\Omega_{j,k,l}|$, and where the values of $w_t$ at the cell vertices are obtained by linear interpolation from the surrounding cell centers [25, 65], which is second-order accurate. By consistency, the coefficients of Eq. (IV.28) should satisfy the relation $\alpha + 8\beta = 1$. Moreover, since $T_P$ is a second-order accurate approximation of $\mathcal{V}_0$, Eq. (IV.28) is also second-order accurate for general irregular grids (no hypothesis on mesh regularity or symmetry). An additional relation is

required to complete the choice of coefficients $\alpha$ and $\beta$. To this purpose, we develop Eq. (IV.28) in the case of a uniform Cartesian grid. In this case, the interpolated values of $w_t$ at cell vertices are just given by 1/8 of the sum of the surrounding cell-center values, which results in:

$$\begin{aligned}\frac{1}{|\Omega_{j,k,l}|}\tilde{\mathcal{V}}_0^{Cart} =& \alpha w_{tj,k,l} + \frac{\beta}{8}[8w_{tj,k,l} + 4(w_{tj+1,k,l} + w_{tj-1,k,l} + w_{tj,k+1,l} + w_{tj,k-1,l} \\ &+ w_{tj,k,l+1} + w_{tj,k,l-1}) + 2(w_{tj+1,k+1,l} + w_{tj-1,k+1,l} + w_{tj,k+1,l+1} + w_{tj,k-1,l+1} \\ &+ w_{tj+1,k,l+1} + w_{tj+1,k,l-1} + w_{tj+1,k-1,l} + w_{tj-1,k-1,l} + w_{tj,k+1,l-1} + w_{tj,k-1,l-1} \\ &+ w_{tj-1,k,l+1} + w_{tj-1,k,l-1}) + (w_{tj+1,k+1,l+1} + w_{tj-1,k+1,l+1} + w_{tj+1,k-1,l+1} \\ &+ w_{tj+1,k+1,l-1} + w_{tj+1,k-1,l-1} + w_{tj-1,k+1,l-1} + w_{tj-1,k-1,l+1} + w_{tj-1,k-1,l-1})]\end{aligned} \tag{IV.29}$$

The preceding expression is now rewritten under the form:

$$\begin{aligned}\frac{1}{|\Omega_{j,k,l}|}\tilde{\mathcal{V}}_0^{Cart} =& \left[\left(I + \frac{1}{6}\delta_1^2\right)\left(I + \frac{1}{6}\delta_2^2\right)\left(I + \frac{1}{6}\delta_3^2\right) w_t\right]_{j,k,l} \\ &+ (\gamma_1[\delta_1^2\delta_2^2 + \delta_1^2\delta_3^2 + \delta_2^2\delta_3^2]w_t + \gamma_2\delta_1^2\delta_2^2\delta_3^2 w_t)_{j,k,l}\end{aligned} \tag{IV.30}$$

where $\gamma_1$ and $\gamma_2$ are free coefficients introduced for convenience. Equation (IV.30) can be seen as the non-weighted approximation of the main volume integral (IV.13) plus some higher order terms resulting from the general formulation (IV.28) that allow preserving second-order of accuracy on irregular grids. By identification between Eqs. (IV.29) and (IV.30), we get the following relations for coefficients $\alpha$, $\beta$, $\gamma_1$ and $\gamma_2$:

$$\begin{cases} \frac{8}{27} &= \alpha + \beta - 12\gamma_1 + 8\gamma_2 \\ \frac{2}{27} &= \frac{1}{2}\beta + 4\gamma_1 - 4\gamma_2 \\ \frac{1}{54} &= \frac{1}{4}\beta - \gamma_1 + 2\gamma_2 \\ \frac{1}{216} &= \frac{1}{8}\beta - \gamma_2 \end{cases} \tag{IV.31}$$

The preceding relations satisfy the consistency condition $\alpha + 8\beta = 1$ and lead finally to the unique solution

$$\begin{cases} \alpha = \frac{1}{3} \\ \beta = \frac{1}{12} \\ \gamma_1 = \frac{1}{72} \\ \gamma_2 = \frac{5}{864} \end{cases} \tag{IV.32}$$

In practice, the approximation for the volume integral on a general grid used in the RBC$i$ formulation is given by relation (IV.28), with $\alpha = 1/3$ and $\beta = 1/12$.

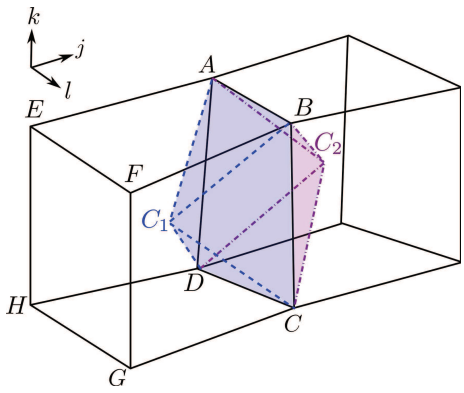


Figure IV.4: Shifted cell $\Omega_{j+1/2,k,l}$

We now look for an approximation of the surface integral $(\mathcal{S}_0)_{j,k,l}$. This requires the evaluation of flux integrals over each cell face. To ensure high accuracy on highly distorted grids, one important point is to account for possible skewness of the faces.
To this purpose, let us consider the auxiliary shifted control volume represented in Fig. IV.4. For any main cell face identified through its vertices $A$, $B$, $C$ and $D$, this shifted control volume is represented by an irregular octahedron with vertices coincident with the face vertices plus the adjacent cell centers $C_1$ and $C_2$.
To fix ideas, we consider the approximation of the surface integral over face $\Gamma_{j+\frac{1}{2},k,l}$, so that the vertices $A$, $B$, $C$ and $D$ correspond to points $(j+\frac{1}{2},k+\frac{1}{2},l+\frac{1}{2})$, $(j+\frac{1}{2},k-\frac{1}{2},l+\frac{1}{2})$, $(j+\frac{1}{2},k-\frac{1}{2},l-\frac{1}{2})$ and $(j+\frac{1}{2},k+\frac{1}{2},l-\frac{1}{2})$. Integrals on the other faces are approximated in a similar way.
The surface integral over face $\Gamma_{j+\frac{1}{2},k,l}$ is approximated as follows:

$$\int_{\Gamma_{j+\frac{1}{2},k,l}} \boldsymbol{\phi}.\boldsymbol{n} d\Gamma = \frac{1}{2}(I_L - I_R) \tag{IV.33}$$

where

$$I_L = \int_{\Gamma_{j+\frac{1}{2},k,l}} \boldsymbol{\phi}.\boldsymbol{n}_{P_1} d\Gamma,\ I_R = \int_{\Gamma_{j+\frac{1}{2},k,l}} \boldsymbol{\phi}.\boldsymbol{n}_{P_2} d\Gamma$$

and $\boldsymbol{n}_{P_1}$ and $\boldsymbol{n}_{P_2}$ are the outward normals to the pyramids $ABCDC_1$ and $ABCDC_2$, respectively. On face $\Gamma_{j+\frac{1}{2},k,l} = ABCD$ we have $\boldsymbol{n}_{P_1} = \boldsymbol{n}$ and $\boldsymbol{n}_{P_2} = -\boldsymbol{n}$. Instead of calculating these integrals on face $\Gamma_{j+\frac{1}{2},k,l}$, which can be non planar for a general irregular mesh, we express them as a combination of integrals on the other faces of the pyramids, which are triangular and then belong to a plane. To this purpose, we remark that, for steady flows, application of the conservation laws to pyramids $ABCDC_1$ and $ABCDC_2$, respectively, leads to:

$$I_L = -\int_{AC_1B} \boldsymbol{\phi}.\boldsymbol{n}_{P_1} d\Gamma - \int_{BC_1C} \boldsymbol{\phi}.\boldsymbol{n}_{P_1} d\Gamma - \int_{CC_1D} \boldsymbol{\phi}.\boldsymbol{n}_{P_1} d\Gamma - \int_{DC_1A} \boldsymbol{\phi}.\boldsymbol{n}_{P_1} d\Gamma \tag{IV.34}$$

$$I_R = -\int_{BC_2A} \boldsymbol{\phi}.\boldsymbol{n}_{P_2} d\Gamma - \int_{CC_2B} \boldsymbol{\phi}.\boldsymbol{n}_{P_2} d\Gamma - \int_{DC_2C} \boldsymbol{\phi}.\boldsymbol{n}_{P_2} d\Gamma - \int_{AC_2D} \boldsymbol{\phi}.\boldsymbol{n}_{P_2} d\Gamma \tag{IV.35}$$

Relations (IV.34) and (IV.35) are exact for steady flows and $I_L$ is strictly equal to $-I_R$ for an exact solution.

For unsteady flows, formulae (IV.34) and (IV.35) should be modified as follows:

$$I_L = -\int_{AC_1B} \boldsymbol{\phi}.\boldsymbol{n}_{P_1} d\Gamma - \int_{BC_1C} \boldsymbol{\phi}.\boldsymbol{n}_{P_1} d\Gamma - \int_{CC_1D} \boldsymbol{\phi}.\boldsymbol{n}_{P_1} d\Gamma - \int_{DC_1A} \boldsymbol{\phi}.\boldsymbol{n}_{P_1} d\Gamma - \int_{ABCDC_1} w_t d\Omega, \tag{IV.36}$$

$$I_R = -\int_{BC_2A} \boldsymbol{\phi}.\boldsymbol{n}_{P_2} d\Gamma - \int_{CC_2B} \boldsymbol{\phi}.\boldsymbol{n}_{P_2} d\Gamma - \int_{DC_2C} \boldsymbol{\phi}.\boldsymbol{n}_{P_2} d\Gamma - \int_{AC_2D} \boldsymbol{\phi}.\boldsymbol{n}_{P_2} d\Gamma - \int_{ABCDC_2} w_t d\Omega, \tag{IV.37}$$

which would lead to the appearence of the following extra term in Eq. (IV.33):

$$-\frac{1}{2}\left[\int_{ABCDC_1} w_t d\Omega - \int_{ABCDC_2} w_t d\Omega\right] = -\frac{1}{2}\Delta_{Pyr} \ . \tag{IV.38}$$

Note however that:

$$\Delta_{Pyr} = w_{t\Gamma_{j+\frac{1}{2},k,l}} |\Gamma_{j+\frac{1}{2},k,l}| \frac{h_1}{3}\left(1 - \frac{h_2}{h_1}\right) + \mathcal{O}(|\Gamma_{j+\frac{1}{2},k,l}| h^2) \tag{IV.39}$$

where $h_1$ and $h_2$ are the heights of pyramids $ABCDC_1$ and $ABCDC_2$, respectively. The ratio $h_2/h_1$ is a measure of grid streching in the $j$-th direction. For highly irregular meshes, the streching ratio can be written under the form:

$$\left(1 - \frac{h_2}{h_1}\right) = \mathcal{O}(h) \tag{IV.40}$$

and $\Delta_{Pyr} = \mathcal{O}(|\Gamma_{j+\frac{1}{2},k,l}| h^2)$ represents a second-order error. Condition (IV.40) includes quite extreme situations; for instance, it allows for doubling or tripling mesh height is direction $j$. Taking into account (IV.40) in (IV.39), we conclude that for highly irregular grids the extra term (IV.38) can be simply estimated as:

$$-\frac{1}{2}\left[\int_{ABCDC_1} w_t d\Omega - \int_{ABCDC_2} w_t d\Omega\right] = |\Gamma_{j+\frac{1}{2},k,l}| \mathcal{O}(h^2) \tag{IV.41}$$

and, consequently, it can be neglected while keeping an overall second-order accuracy. For sufficiently smooth irregular grids, e.g. such that $(1 - h_2/h_1) = \mathcal{O}(h^2)$ the extra term is $\mathcal{O}(h^3)$ or higher and it can, a fortiori, be neglected. On the other hand, for regular Cartesian grids $h_1 = h_2$, the pyramids are symmetric with respect to $\Gamma_{j+\frac{1}{2},k,l}$, and the extra term (IV.38) is exactly equal to zero.

In summary, the preceding reasoning shows that relations (IV.33), (IV.34) and (IV.35) can be used to estimate surface integrals in the main residual exactly for steady flows and to the second order on highly irregular grids.

We still need to approximate the surface integrals on triangles used in relations (IV.34) and (IV.35). To this purpose, we first interpolate linearly the fluxes at cell vertices $A$, $B$, $C$ and $D$, and then approximate the integrals as:

$$\int_{AC_1B} \boldsymbol{\phi}.\boldsymbol{n}_{P_1} d\Gamma = \frac{1}{3}(\boldsymbol{\phi}_A + \boldsymbol{\phi}_{C_1} + \boldsymbol{\phi}_B).\boldsymbol{n}_{AC_1B}, \tag{IV.42}$$

which is second-order accurate. Similar approximations as (IV.42) are used for the other triangles. The advantage of the proposed approach is that triangular surfaces allow to compute a unique

normal vector to that surface, which greatly inhances the scheme accuracy on highly skewed grids. Finally, we note that, thank to the choice of 1/3 in (IV.42), the final expression for $\tilde{\mathcal{S}}_0$ degenerates to Eq. (IV.14) with

$$(F_1)_{j+\frac{1}{2},k,l} = \left[\left(I+\frac{1}{6}\delta_2^2\right)\left(I+\frac{1}{6}\delta_3^2\right)\mu_1\boldsymbol{\phi} + \frac{1}{72}\delta_2^2\delta_3^2\mu_1\boldsymbol{\phi}\right]_{j+\frac{1}{2},k,l}.\boldsymbol{\Gamma}_{j+\frac{1}{2},k,l}, \tag{IV.43}$$

on a regular Cartesian grid. In other terms, we recover a formulation that is similar to that of the non-weighted approximation of RBC3 augmented with a high-order corrective term. In summary the final approximation of the main residual used for RBC$i$ is:

$$\tilde{R}_0 = \tilde{\mathcal{V}}_0 + \tilde{\mathcal{S}}_0 \tag{IV.44}$$

with $\tilde{\mathcal{V}}_0$ given by (IV.28) with coefficients (IV.32) and $\tilde{\mathcal{S}}_0$ given by a sum of integrals of the form (IV.33). Since the approximations used for $\tilde{\mathcal{V}}_0$ and $\tilde{\mathcal{S}}_0$ are second-order accurate on general grids, then $\tilde{R}_0$ is at least second-order accurate in a FV sense.

### IV.5.2 Approximation of the mid-point residuals

To fix ideas, we consider the approximation of mid-point residual $R_1$ at point $(j+\frac{1}{2},k,l)$, the other residuals being approximated in a similar way. To evaluate $R_1$ at $(j+\frac{1}{2},k,l)$, we consider again the shifted octahedral control volume of Fig. IV.4, and look for an approximation $\tilde{R}_1$ of the form:

$$(\tilde{R}_1)_{j+\frac{1}{2},k,l} = \left(\tilde{\mathcal{V}}_1 + \tilde{\mathcal{S}}_1\right)_{j+\frac{1}{2},k,l} \tag{IV.45}$$

with $\tilde{\mathcal{V}}_1$ an approximation of

$$\begin{aligned}\mathcal{V}_1 =& 3\int_{\Omega^{Oct}_{j+\frac{1}{2},k,l}} w_t\ d\Omega \\ =& 3\left(\int_{C_1ABCD} w_t\ d\Omega + \int_{C_2ABCD} w_t\ d\Omega\right),\end{aligned} \tag{IV.46}$$

where we denote $\Omega^{Oct}_{j+\frac{1}{2},k,l}$ the shifted control volume and we split the volume integral on the shifted cell in two integrals over the pyramids on both sides. We denote $\tilde{\mathcal{S}}_1$ an approximation of:

$$\mathcal{S}_1 = 3\left(\oint_{ABCDC_1} \boldsymbol{\phi}.\boldsymbol{n}_{P_1} d\Gamma + \oint_{ABCDC_2} \boldsymbol{\phi}.\boldsymbol{n}_{P_2} d\Gamma\right) \tag{IV.47}$$

The factor 3 in (IV.46) and (IV.47) accounts for the fact that the volume of an octahedron is one third that of a parallelepiped with the same height $C_1C_2$ (see Fig. IV.5), *i.e.* the shifted cell used for the FV RBC$r$ scheme.

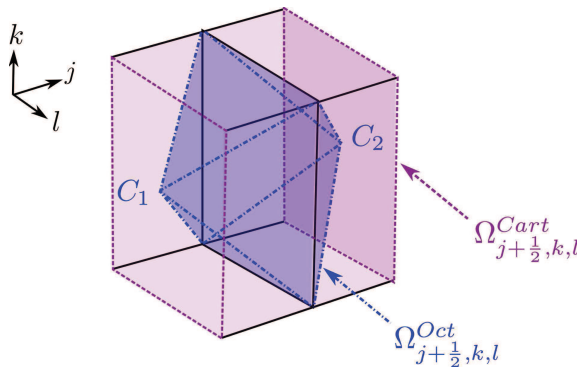


Figure IV.5: $\Omega^{Oct}_{j+\frac{1}{2},k,l}$ and $\Omega^{Cart}_{j+\frac{1}{2},k,l}$

To find $\mathcal{V}_1$, we look for an approximation of the volume integrals on $ABCDC_1$ and $ABCDC_2$ under the form:

$$\begin{aligned}\int_{C_1ABCD} w_t \, d\Omega =& |\Omega_{P_1}|[\alpha^\star w_{tC_1} + \beta^\star(w_{tA} + w_{tB} + w_{tC} + w_{tD}) + \mathcal{O}(h^2)] \\ \int_{C_2ABCD} w_t \, d\Omega =& |\Omega_{P_2}|[\alpha^\star w_{tC_2} + \beta^\star(w_{tA} + w_{tB} + w_{tC} + w_{tD}) + \mathcal{O}(h^2)]\end{aligned} \tag{IV.48}$$

where $\alpha^\star$ and $\beta^\star$ are real coefficients and $|\Omega_{P_1}|$ and $|\Omega_{P_2}|$ are the volumes of pyramids $ABCDC_1$ and $ABCDC_2$, respectively. By plugging relations (IV.48) in (IV.46) we finally obtain:

$$\tilde{\mathcal{V}}_1 = \mathcal{V}_1 + \mathcal{O}(|\Omega_{j+\frac{1}{2},k,l}|h^2) \tag{IV.49}$$

with

$$\tilde{\mathcal{V}}_1 = 3\alpha^\star(|\Omega_{P_1}|w_{tC_1} + |\Omega_{P_2}|w_{tC_2}) + 3\beta^\star(|\Omega_{P_1}| + |\Omega_{P_2}|)(w_{tA} + w_{tB} + w_{tC} + w_{tD}) \tag{IV.50}$$

We still need to choose the weighting coefficients $\alpha^\star$ and $\beta^\star$. Consistency requires that $\alpha^\star + 4\beta^\star = 1$. To this end we follow a procedure similar to that used to construct $\tilde{\mathcal{V}}_0$, and we look for a set of coefficients such that $\tilde{\mathcal{V}}_1$ can be reduced to the following writing in the case of a regular Cartesian grid:

$$\tilde{\mathcal{V}}_1 = \left[\left(I + \frac{1}{6}\delta_2^2\right)\left(I + \frac{1}{6}\delta_3^2\right) + \gamma^\star\delta_2^2\delta_3^2\right](\mu_1 w_t)_{j+\frac{1}{2},k,l}|\Omega^{Cart}_{j+\frac{1}{2},k,l}| \tag{IV.51}$$

where $\gamma^\star$ is a supplementary coefficient introduced for convenience and $|\Omega^{Cart}_{j+\frac{1}{2},k,l}|$ is the volume of the Cartesian shifted cell represented in Figs. IV.2 and IV.5. Similarly to the approximation of $\tilde{\mathcal{V}}_0$, relation (IV.51) is the sum of a term formally identical to the non weighted approximation used in RBC$r$, plus an additional higher-order term with coefficient $\gamma^\star$, required to match the general second-order formulation of the scheme given by (IV.50). By developing relations (IV.50) and (IV.51) in the case of a uniform Cartesian grid, by identification of analogous terms we get the following set of relations for $\alpha^\star$, $\beta^\star$ and $\gamma^\star$, which automatically satisy the consistency condition:

$$\begin{cases} \frac{4}{9} & = \alpha^\star + \beta^\star - 4\gamma^\star \\ \frac{1}{9} & = \frac{1}{2}\beta^\star + 2\gamma^\star \\ \frac{1}{36} & = \frac{1}{4}\beta^\star - \gamma^\star \end{cases} \tag{IV.52}$$

which leads to the unique choice:

$$\begin{cases} \alpha^\star &= \frac{1}{3} \\ \beta^\star &= \frac{1}{6} \\ \gamma^\star &= \frac{1}{72} \end{cases} \tag{IV.53}$$

The approximation of $\mathcal{V}_1$ is then given by Eq. (IV.50) with the coefficients (IV.53).
Finally, we turn to the approximation of $\mathcal{S}_1$. Note that:

$$\begin{aligned} \mathcal{S}_1 &= 3\left(\oint_{ABCDC_1} \boldsymbol{\phi}.\boldsymbol{n}_{P_1} d\Gamma + \oint_{ABCDC_2} \boldsymbol{\phi}.\boldsymbol{n}_{P_2} d\Gamma\right) \\ &= 3(I_L + I_R) \end{aligned} \tag{IV.54}$$

where $I_L$ and $I_R$ are given by Eqs. (IV.34) and (IV.35) and are computed by following the procedure described in Section IV.5.1, which leads to a second order-accurate approximation. For a regular Cartesian grid, Eq. (IV.54) reduces to:

$$\begin{aligned} (\tilde{\mathcal{S}}_1)_{j+\frac{1}{2},k,l} =& |\Omega^{Cart}_{j+\frac{1}{2},k,l}| \left[\frac{\delta_1 f}{\delta x} + \left(I + \frac{1}{6}\delta_3^2\right)\frac{\delta_2\mu_2\mu_1 g}{\delta y} + \left(I + \frac{1}{6}\delta_2^2\right)\frac{\delta_3\mu_3\mu_1 e}{\delta z}\right. \\ &\left. + \frac{1}{12}\left(\delta_3^2\frac{\delta_2\mu_2\mu_1 g}{\delta y} + \delta_2^2\frac{\delta_3\mu_3\mu_1 e}{\delta z}\right)\right]_{j+\frac{1}{2},k,l} \end{aligned} \tag{IV.55}$$

This corresponds to the RBC$r$ formulation, augmented with higher-order terms specific to the second-order formulation on irregular grids. The mid-point residual $\tilde{R}_1$ writes as (IV.45) with (IV.54) and (IV.50) defined by the coefficients (IV.53). Similar expressions are used in the second and third direction to construct $\tilde{R}_2$ and $\tilde{R}_3$ with the same choice of coefficients $\alpha^\star$ and $\beta^\star$.

### IV.5.3 Comments on the extension to curvilinear meshes of high-order RBC schemes

No attempt is made to generalize the proposed procedure to high-order since it leads to a very cumbersome formulation at orders higher then three. In order to increase the accuracy on curvilinear meshes we have multiple choices. We can use a high-order piecewise polynomial reconstruction [72] or coordinate transformations [145, 153] for instance. However, all these choices implies a non negligible increase of the computational cost since we have to approximate the Jacobian, the Hessian and higher order derivatives of the metrics or the numerical fluxes in these procedures.
The strategy that is the most likely to be chosen for high-order computations with RBC schemes is the use of multiblock computation with overset grids [35, 139, 144]. The computational domain can be decomposed into body-fitted curvilinear meshes and Cartesian meshes. This way the body-fitted meshes could be computed with RBC$i$ and the Cartesian meshes with higher-order finite-difference RBC schemes. Besides, Cartesian grids can aesily be generated through automatic techniques [124]. This strategy is being developed within the framework of the Ph.D. thesis of P.Y. Outtier and implemented in DynoLab [122], the C.F.D. code of the DynFluid Laboratory. Such a choice could be coupled in the future with mesh adaptation techniques [26, 124].

## IV.6 Stability properties of RBC$i$

Stability properties of FV RBC schemes depend on mesh regularity properties and may hardly be studied in the general case. In [128] the energy method was used to show —for a simple case and a purely centered scheme —that weighted discretization operators may be favorable or not

to stability depending on grid properties. For regular Cartesian meshes, stability and spectral properties of FV schemes may be studied using analysis tools typical of the finite difference (FD) framework. Since RBC$r$ degenerates to its FD equivalent when written on Cartesian grids, results discussed in [106] for finite-difference RBC schemes remain also valid for RBC$r$. Specifically, RBC$r$ leads to a Cauchy-stable spatial approximation, like its finite-difference equivalent. On the other hand, it has been shown in the preceding Section that the RBC$i$ FV formulation introduces, even on Cartesian grids, additional terms with respect to RBC$r$. It is then necessary to investigate the impact of these additional terms on the dissipation and stability properties of RBC$i$.

### IV.6.1 Dissipation properties of RBC$i$

Similarly to all RBC schemes, RBC$i$ is the sum of a purely centered, non dissipative, approximation of the residual, $\tilde{R}_0$, and a dissipation term $\tilde{d}$. Since $\tilde{R}_0$ does not introduce any form of dissipation, we investigate the dissipation properties of RBC$i$ by studying the discrete operator $\tilde{d}_{j,k,l}$.

Precisely, the dissipation operator of RBC$i$ follows the general definition (IV.10) where, according to Eqs (IV.51) and (IV.55), the midpoint residuals written for a regular Cartesian grid (and denoted hereafter with the superscript $i$) are:

$$\frac{1}{|\Omega|}(\tilde{R}_1^i)_{j+\frac{1}{2},k,l} = \left\{ \left[ \left( I + \frac{1}{6}\delta_2^2 \right) \left( I + \frac{1}{6}\delta_3^2 \right) + \frac{1}{72}\delta_2^2\delta_3^2 \right] \mu_1 w_t + \frac{\delta_1 f}{\delta x} + \left( I + \frac{1}{6}\delta_3^2 \right) \frac{\delta_2\mu_2\mu_1 g}{\delta y} + \left( I + \frac{1}{6}\delta_2^2 \right) \frac{\delta_3\mu_3\mu_1 e}{\delta z} + \frac{1}{12}\left( \delta_3^2 \frac{\delta_2\mu_2\mu_1 g}{\delta y} + \delta_2^2 \frac{\delta_3\mu_3\mu_1 e}{\delta z} \right) \right\}_{j+\frac{1}{2},k,l} \tag{IV.56}$$

and similar relations hold for $\tilde{R}_2^i$ and $\tilde{R}_3^i$. In the above, $|\Omega| = |\Omega|_{j,k,l} = (|\Omega|_{j,k,l} + |\Omega|_{j+1,k,l})/2$ since the mesh is Cartesian regular.

On the other hand, the dissipation operator of RBC$r$, noted hereafter $\tilde{d}^r$, also satisfies and expression similar to Eq. (IV.10), with the midpoint residuals (now denoted with the superscript $r$):

$$\frac{1}{|\Omega|}(\tilde{R}_1^r)_{j+\frac{1}{2},k,l} = \left[ \left( I + \frac{1}{6}\delta_2^2 \right) \left( I + \frac{1}{6}\delta_3^2 \right) \left( \mu_1 w_t + \frac{\delta_1 f}{\delta x} \right) \left( I + \frac{1}{6}\delta_3^2 \right) \frac{\delta_2\mu_2\mu_1 g}{\delta y} + \left( I + \frac{1}{6}\delta_2^2 \right) \frac{\delta_3\mu_3\mu_1 e}{\delta z} \right]_{j+\frac{1}{2},k,l} \tag{IV.57}$$

and similarly for $\tilde{R}_2^r$ and $\tilde{R}_3^r$.

According to the general study carried out for finite difference RBC schemes of order $2p-1$ [106], the operator (IV.10) with the mid-point residual (IV.57) is always dissipative. We prove hereafter that, *a fortiori*, the same is true when relation (IV.56) is used, since this choice introduces an additional dissipation with respect to (IV.57).

To this purpose, we apply RBC$r$ and RBC$i$ to the linear scalar problem:

$$w_t + Aw_x + Bw_y + Cw_z = 0 \qquad A,\, B,\, C \in \mathbb{R} \tag{IV.58}$$

In this case the dissipation matrices $\Phi_1$, $\Phi_2$, $\Phi_3$, designed in [102, 104] in order to introduce some form of upwinding of the numerical scheme with respect to the local advection direction, satisfy the conditions

$$\begin{aligned} &\Phi_1 A \geqslant 0, \qquad \Phi_2 B \geqslant 0, \qquad \Phi_3 C \geqslant 0, \\ &\delta x \Phi_1 B = \delta y \Phi_2 A, \qquad \delta x \Phi_1 C = \delta z \Phi_3 A. \end{aligned} \tag{IV.59}$$

with

$$\Phi_1 = \mathrm{sgn}(A)\phi, \qquad \Phi_2 = \mathrm{sgn}(B)\psi, \qquad \Phi_3 = \mathrm{sgn}(C)\zeta,$$
$$\phi = \min\left(1, \frac{1}{\alpha}, \frac{1}{\beta}\right), \ \psi = \min\left(1, \alpha, \frac{\alpha}{\beta}\right), \ \zeta = \min\left(1, \beta, \frac{\beta}{\alpha}\right)$$
$$\text{with } \alpha = \frac{\delta x|B|}{\delta y|A|} \text{ and } \beta = \frac{\delta x|C|}{\delta z|A|}. \tag{IV.60}$$

The interested reader is referred to [102–104, 106, 116] for more details about the dissipation matrices $\Phi_1$, $\Phi_2$, $\Phi_3$ and their extension to systems of conservation laws.

On the other hand, the Taylor-series expansion of $\tilde{d^r}$ (see [106] for details) writes as:

$$\frac{1}{|\Omega|}(\tilde{d^r}) = D^r + \mathcal{O}(h^4) \tag{IV.61}$$

with

$$D^r = -\frac{1}{24}\left[\delta x(\Phi_1 \delta x^2 f_{xxx})x + \delta y(\Phi_2 \delta y^2 g_{yyy})_y + \delta z(\Phi_3 \delta z^2 e_{zzz})_z\right] \tag{IV.62}$$

For problem (IV.58), $\Phi_1$, $\Phi_2$ and $\Phi_3$ become scalar constants, and the operator (IV.61) reduces to

$$D^r = \mathscr{D}^r w$$

with $\mathscr{D}^r$ a linear partial differential operator of fourth-order. The Fourier symbol of $\mathscr{D}^r$ is:

$$\hat{\mathscr{D}}^r = -\frac{1}{24}\left[\delta x(\Phi_1 A \delta x^2 \xi^4) + \delta y(\Phi_2 B \delta y^2 \eta^4) + \delta z(\Phi_3 C \delta z^2 \zeta^4)\right] \tag{IV.63}$$

where $\xi$, $\eta$ and $\zeta$ are the reduced wave numbers in the $x$, $y$, and $z$ direction, respectively. All the derivatives in $\mathscr{D}^r$ being even, $\hat{\mathscr{D}}^r(\xi, \eta, \zeta)$ is real.
It is easy to check that operator $D^r$ is dissipative, in the sense that [106]:

$$\forall \xi \in \mathbb{R}, \forall \eta \in \mathbb{R}, \forall \zeta \in \mathbb{R}, \qquad \hat{\mathscr{D}}^r(\xi, \eta, \zeta) \leqslant 0. \tag{IV.64}$$

In other terms, $D^r$ satisfies the following

**Dissipation property.** *The operator* (IV.62) *is dissipative for any advection direction (A,B,C) and any functions* $\Phi_1$, $\Phi_2$ *and* $\Phi_3$ *satisfying the conditions* (IV.59).

We now turn to RBC*i*. In this case, the dissipation operator $\tilde{d^i}$ can be written in a way similar to Eq. (IV.61), with:

$$\begin{aligned} D^i = D^r &+ \delta x[\Phi_1(2\delta y^2 f_{yyx} + 2\delta z^2 f_{zzx} - 2\delta z^2 g_{zzy} - 2\delta y^2 e_{yyz})]_x \\ &+ \delta y[\Phi_2(2\delta x^2 g_{xxy} + 2\delta z^2 g_{zzy} - 2\delta z^2 f_{zzx} - 2\delta x^2 e_{xxz})]_y \\ &+ \delta z[\Phi_3(2\delta x^2 e_{xxz} + 2\delta y^2 e_{yyz} - 2\delta y^2 f_{yyz} - 2\delta x^2 g_{xxy})]_z \end{aligned} \tag{IV.65}$$

The preceding equation clearly shows the supplementary error terms, based on fourth-order cross derivatives, introduced by RBC*i* with respect to Eq. (IV.62). We need to investigate if these terms contribute to dissipate or amplify solution modes. To this aim, we consider the Fourier symbol:

$$\hat{\mathscr{D}}^i = \hat{\mathscr{D}}^r - \frac{\delta x^3}{12}\Phi_1 A \xi^4 \mathcal{D}' \tag{IV.66}$$

where

$$\mathcal{D}' = \sigma^2 + \omega^2 + \varphi^2\sigma^2 + \varphi^2\sigma^2\omega^2 + \psi^2\omega^2 + \psi^2\sigma^2\omega^2 - 2\left(\varphi\sigma\omega^2 + \psi\sigma^2\omega + \varphi\psi\sigma\omega\right)$$

where $\sigma = \dfrac{\delta y\ \eta}{\delta x\ \xi}$, $\omega = \dfrac{\delta z\ \zeta}{\delta x\ \xi}$, $\varphi = \dfrac{\Phi_2}{\Phi_1} = \dfrac{\delta x B}{\delta y A}$ and $\psi = \dfrac{\Phi_3}{\Phi_1} = \dfrac{\delta x C}{\delta z A}$. Since:

$$\mathcal{D}' = \sigma^2(1-\psi\omega)^2 + \omega^2(1-\varphi\sigma)^2 + (\varphi\sigma - \psi\omega)^2 \geq 0$$

it is clear that corrective terms in RBC$i$ always introduce an additional dissipation with respect to RBC$r$, so that the preceding dissipation property is *a fortiori* valid for RBC$i$.

### IV.6.2 Cauchy stability of RBC$i$

We now prove that, thanks to the fact that RBC$i$ involves a purely centered approximation of the residual $R_0$, supplemented by the dissipative operator $\tilde{d}$, it leads to a Cauchy-stable semi discrete scheme. Hereafter, we recall the Cauchy stability condition in the case of a linear scalar problem of the form (IV.58).
The Fourier transform of (IV.58) is

$$\widehat{w}_t = -i(Ak_x + Bk_y + Ck_z)\widehat{w} = -i\mathbf{A}.\mathbf{k}\widehat{w} \tag{IV.67}$$

where $\mathbf{A} = (A, B, C)$ is the advection velocity vector and $\mathbf{k} = (k_x, k_y, k_z)$ a 3D wave vector. Denoting $\dot{\mathbf{A}} = (\dot{A}, \dot{B}, \dot{C})$ a vector whose components are the CFL numbers in the $x$, $y$ and $z$ directions, respectively:

$$\dot{A} = A\Delta t/\delta x, \qquad \dot{B} = B\Delta t/\delta y, \qquad \dot{C} = C\Delta t/\delta z$$

and introducing the reduced wave number in the $\dot{\mathbf{A}}$-direction:

$$\xi_{\theta,\phi} = \frac{\dot{\mathbf{A}}}{|\dot{\mathbf{A}}|}.\boldsymbol{\xi}$$

with $\boldsymbol{\xi} = (\xi, \eta, \zeta) = (k_x\delta x, k_y\delta y, k_z\delta z)$ the reduced wave vector, Eq. (IV.67) can be rewritten as:

$$\widehat{w}_t = -i|\dot{\mathbf{A}}|\xi_{\theta,\phi}\frac{\widehat{w}}{\Delta t} \tag{IV.68}$$

The notation $\xi_{\theta,\phi}$ refers to the local advection direction with respect to the mesh, where $\cos(\phi) = \dot{C}/|\dot{\mathbf{A}}|$, $\tan(\theta) = \dot{B}/\dot{A}$, and $|\dot{\mathbf{A}}|$ is the global CFL number. The right-hand side of Eq. (IV.68) represents the exact transport operator, a pure imaginary number, and $\xi_{\theta,\phi}$ is a pure real number. We now consider the semi-discrete counterpart to Eq. (IV.68). Taking the spatial Fourier transform of the semi-discrete system (IV.75) applied to the linear problem (IV.58), we obtain:

$$\widehat{w}_t = \widehat{\mathcal{C}}(\boldsymbol{\xi}, \dot{\mathbf{A}})\frac{\widehat{w}}{\Delta t} \tag{IV.69}$$

with $\widehat{\mathcal{C}}$ the Fourier symbol of the spatial operator. Introducing the modified wave number:

$$\xi^*_{\theta,\phi} = i\frac{\widehat{\mathcal{C}}(\boldsymbol{\xi}, \dot{\mathbf{A}})}{|\dot{\mathbf{A}}|} \tag{IV.70}$$

Eq. (IV.69) can be rewritten as:

$$\widehat{w}_t = -i|\dot{\mathbf{A}}|\xi^*_{\theta,\phi}\frac{\widehat{w}}{\Delta t} \tag{IV.71}$$

which represents the numerical counterpart of the exact operator (IV.68). Eq. (IV.70) is called the approximate dispersion relation of the semi-discrete scheme, and relates a given reduced wave number $\xi_{\theta,\phi}$ to its numerical representation $\xi^*_{\theta,\phi}$. Unlike the exact wave number, the modified wave number $\xi^*_{\theta,\phi}$ is a complex, since it has a non-zero imaginary part in general. Inspection of Eq. (IV.71) shows that, according to its positive or negative sign, this imaginary part contributes to the amplification or damping of $\widehat{w}$ in time. If the imaginary part is positive, then any Fourier mode set as an initial condition to the ordinary differential equation (IV.75) will grow without bound.
The spatial discretization operator $\mathcal{C}$ is Cauchy-stable if:

$$\forall \dot{\mathbf{A}} \in \mathbb{R}^3, \quad \sup_{\boldsymbol{\xi} \in [-\pi,\pi]^3} \mathfrak{Im}(\xi^*_{\theta,\phi}) \leqslant 0 \tag{IV.72}$$

This comes to require that the Fourier symbol of the spatial discretization $\widehat{\mathcal{C}}$ always lies in the left-hand side of the complex plane. Any spatial discretization satisfying the stability condition (IV.72) leads to an unconditionally stable fully discrete scheme whenever it is combined to an A-stable time integration method.

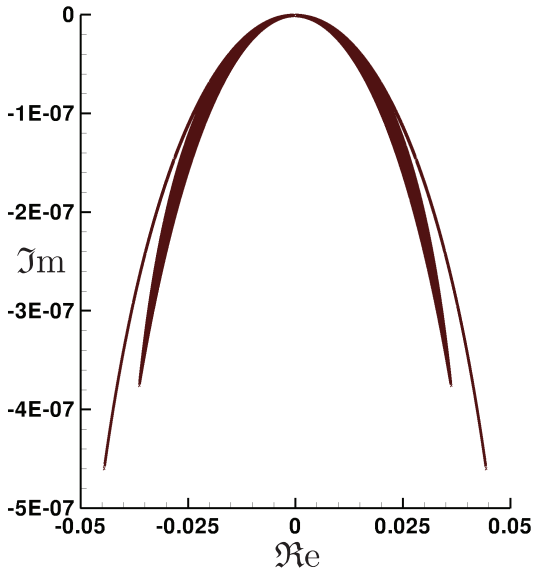


Figure IV.6: Representation in the complex plane of the Cauchy-stability criterion (IV.72) for RBC$i$

We determine now the expression of $\mathcal{C}$ in the case of RBC$i$ discretization. Omitting the subscript $j, k, l$, the RBC$i$ spatial discretization scheme can be expressed as:

$$\tilde{R}_0(w, w_t) = \tilde{d}(w, w_t) \tag{IV.73}$$

where $\tilde{R}_0$ is the main residual discretization operator and $\tilde{d}$ is the numerical dissipation operator. They can both be split in a part dependent on the state vector $w$ only and another one that involves $w_t$. Precisely, calling $\mathfrak{I}$ the difference operator that applies to $w_t$ and $\mathfrak{R}$ the operator depending on $w$ only, Eq. (IV.73) can be rewritten as;

$$w_t = -\left[\mathfrak{I}^{-1}\mathfrak{R}\right](w) \tag{IV.74}$$

Finally, we can formally set:

$$w_t = \mathcal{C}(w), \text{ with } \mathcal{C} = -\mathfrak{I}^{-1}\mathfrak{R} \tag{IV.75}$$

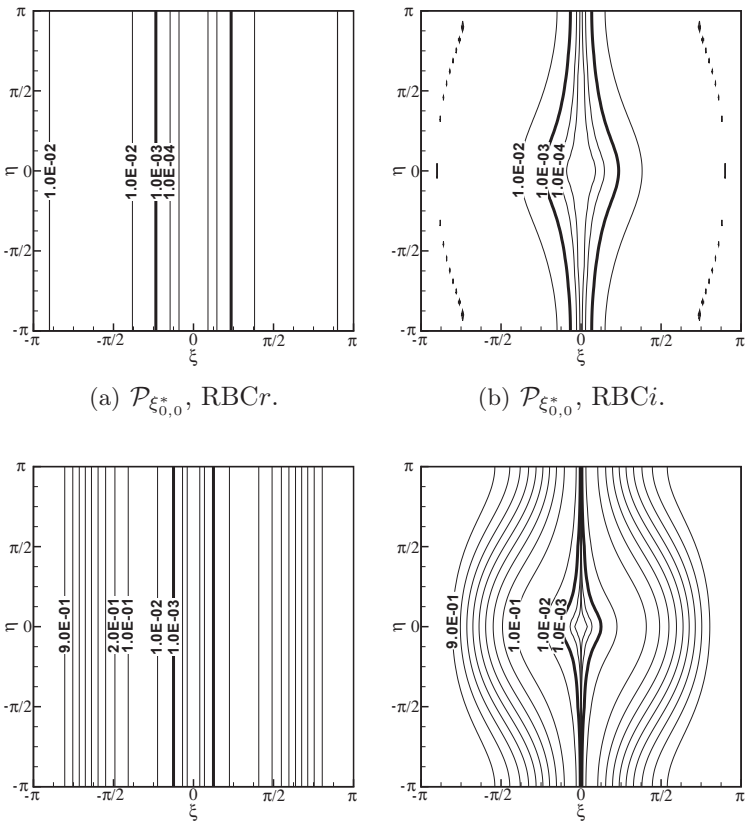


(a) $\mathcal{P}_{\xi^*_{0,0}}$, RBC$r$. (b) $\mathcal{P}_{\xi^*_{0,0}}$, RBC$i$.

(c) $\mathcal{D}_{\xi^*_{0,0}}$, RBC$r$. (d) $\mathcal{D}_{\xi^*_{0,0}}$, RBC$i$.

Figure IV.7: Contours of the phase error $\mathcal{P}_{\xi^*_{0,0}}$ (top) and damping function $\mathcal{D}_{\xi^*_{0,0}}$ (bottom) for pure advection in the $x$ direction, $\dot{\mathbf{A}} = (\dot{A}, 0, 0)$, *i.e.* $(\theta, \phi) = (0, 0)$. Bold black lines correspond to a threshold error of $10^{-3}$.

Eq. (IV.75) represents now a system of ordinary differential equations and, completed by initial conditions $w(.,0) = w_0(.)$, it defines a Cauchy problem. For this problem to be well-posed, operator $\mathcal{C}$ has to be Cauchy-stable, *i.e.* it has to satisfy Eq. (IV.72). To this purpose, we compute $\widehat{\mathcal{C}}$ as:

$$\widehat{\mathcal{C}} = -\Delta t \widehat{\mathfrak{R}} \widehat{\mathfrak{I}}^{-1}$$

By taking the Fourier transform of (IV.73) and after some algebra, we obtain:

$$\begin{aligned}
\Delta t\widehat{\mathfrak{R}} =& \frac{\Phi_1}{2}[D_i(Z_3)\dot{B}\sin(\xi)\sin(\eta) + D_i(Z_2)\dot{C}\sin(\xi)\sin(\zeta) - \dot{A}Z_1] \\
&+\frac{\Phi_2}{2}[D_i(Z_3)\dot{A}\sin(\eta)\sin(\xi) - \dot{B}Z_2 + D_i(Z_1)\dot{C}\sin(\eta)\sin(\zeta)] \\
&+\frac{\Phi_3}{2}[D_i(Z_2)\dot{A}\sin(\zeta)\sin(\xi) + D_i(Z_1)\dot{B}\sin(\zeta)\sin(\eta) - \dot{C}Z_3] \\
&+i[\dot{A}\sin(\xi)N(Z_2,Z_3) + \dot{B}\sin(\eta)N(Z_1,Z_3) + \dot{C}\sin(\zeta)N(Z_1,Z_3)] \\
\widehat{\mathfrak{I}}^{-1} =& \left\{ D(Z_1)D(Z_2)D(Z_3) + \frac{1}{72}(Z_1Z_2 + Z_2Z_3 + Z_3Z_1) + \frac{5}{864}Z_1Z_2Z_3 \right. \\
&\left. -\frac{i}{2}[\Phi_1\sin(\xi)N(Z_2,Z_3) + \Phi_2\sin(\eta)N(Z_1,Z_3) + \Phi_3\sin(\zeta)N(Z_1,Z_2)] \right\}^{-1}
\end{aligned} \tag{IV.76}$$

where $Z_1 = 2(\cos\xi - 1)$, $Z_2 = 2(\cos\eta - 1)$, $Z_3 = 2(\cos\zeta - 1)$, $D_i(Z) = 1 + Z/4$, $D(Z) = 1 + Z/6$ and $N(Y, Z) = D(Y)D(Z) + YZ/72$.

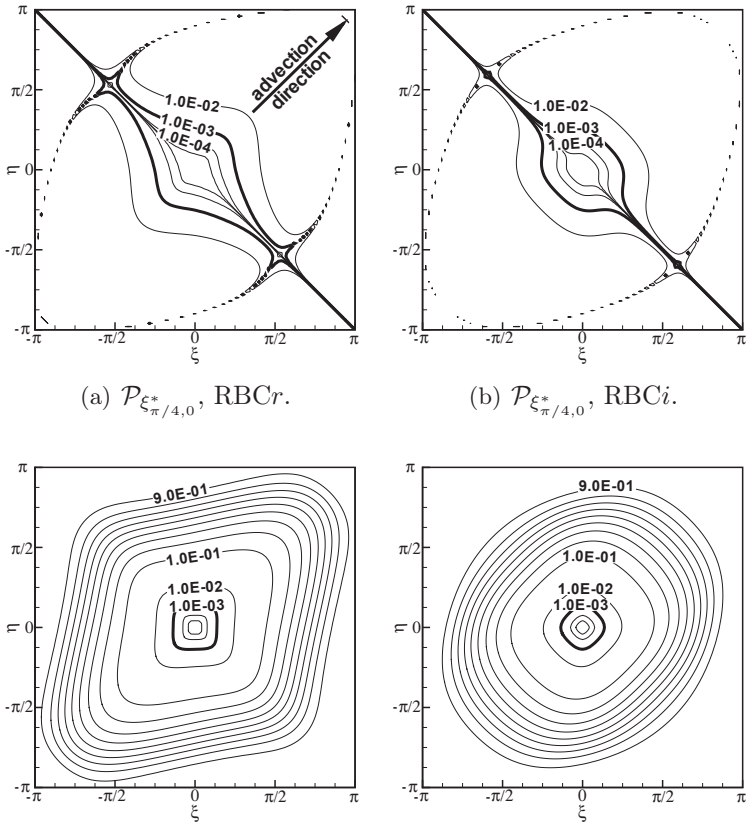


(a) $\mathcal{P}_{\xi^*_{\pi/4,0}}$, RBC$r$. (b) $\mathcal{P}_{\xi^*_{\pi/4,0}}$, RBC$i$.

(c) $\mathcal{D}_{\xi^*_{\pi/4,0}}$, RBC$r$. (d) $\mathcal{D}_{\xi^*_{\pi/4,0}}$, RBC$i$.

Figure IV.8: Contours of the phase error $\mathcal{P}_{\xi^*_{\pi/4,0}}$ (top) and damping function $\mathcal{D}_{\xi^*_{\pi/4,0}}$ (bottom) for pure advection in the diagonal direction, $\dot{\mathbf{A}} = (\dot{A}, \dot{A}, 0)$, *i.e.* $(\theta, \phi) = (\pi/4, 0)$. Bold black lines correspond to a threshold error of $10^{-3}$.

Given the complexity of the analytical expression of the modified wave number for RBC$i$ scheme, a computer code has been written to study its mathematical properties. We numerically check that RBC$i$ is Cauchy stable. To this purpose, the imaginary part of $\xi^*_{\theta,\phi}$ is computed for CFL numbers $\dot{A}$, $\dot{B}$ and $\dot{C}$ ranging in $[-2, 2]$ with a step $\Delta\dot{A} = \Delta\dot{B} = \Delta\dot{C} = 1/100$ and the wave vector $\boldsymbol{\xi}$ ranging in $[-\pi, \pi]^2 \times [0, \pi]$ with steps $\Delta\xi = \Delta\eta = \Delta\zeta = \pi/50$. Fig. IV.6 displays criterion (IV.72) for RBC$i$. Precisely, it shows that RBC$i$ verifies condition (IV.72) for any CFL and any wave number, which confirms that RBC$i$ is a dissipative, and thus Cauchy-stable approximation.

In addition to stability analysis, the modified wave number may be used as an indicator of how accurately a given wave number is represented by the difference operator. Specifically, we define the error with respect to the exact wave number:

$$\mathcal{E} = \xi^*_{\theta,\phi} - \xi_{\theta,\phi} = \big(\mathfrak{Re}(\xi^*_{\theta,\phi}) - \xi_{\theta,\phi}\big) + i\mathfrak{Im}(\xi^*_{\theta,\phi}) \tag{IV.77}$$

More precisely, following previous works [18, 57, 98, 146, 149] for 1-D problems, we consider the

multidimensional counterparts of the scheme normalised phase error and damping function:

$$\mathcal{P}_{\xi_{\theta,\phi}} = \frac{|\Re\mathrm{e}(\xi^*_{\theta,\phi}) - \xi_{\theta,\phi}|}{\pi},\ \mathcal{D}_{\xi_{\theta,\phi}} = 1 - \exp[\Im\mathrm{m}(\xi^*_{\theta,\phi})] \tag{IV.78}$$

For an infinitely accurate scheme, $\mathcal{P}_{\xi_{\theta,\phi}} = 0$ and $\mathcal{D}_{\xi_{\theta,\phi}} = 0$.
We investigate the dispersion error and damping function for dissipative RBC$r$ and RBC$i$ schemes in 2D. Figs. IV.7 and IV.8 shows contour levels of the dispersion error and damping function for different combinations of the reduced wave numbers with an advection velocity aligned with one grid direction and a multidimensional advection respectively, i.e. $(\theta, \phi) = (0, 0)$ and $(\theta, \phi) = (\pi/4, 0)$ respectively. Specifically, we choose $\dot{\mathbf{A}} = (\dot{A}, 0, 0)$ and $\dot{\mathbf{A}} = (\dot{A}, \dot{A}, 0)$. In these figures, the bold black lines correspond to a threshold error of $10^{-3}$.
Figs. IV.7 and IV.8 shows that RBC$i$ is more dissipative and dispersive than RBC$r$ on a Cartesian mesh. Dissipation and dispersion errors increase especially for situations such that the transverse flow direction with respect to the advection speed is ill-resolved. However, numerical tests presented in the following will demonstrate that this loss of accuracy on Cartesian meshes is the price to pay to ensure high accuracy and robustness on general deformed grids.

## IV.7 Numerical tests

For the following computations, the time derivative in the main residual and in the mid-point residuals is approximated by second-order accurate Backward Linear Multistep Method [44, 95, 164], which is A-stable. Such a choice leads to an unconditionally stable fully discrete scheme when coupled to a dissipative spatial approximation. The time-discretization being fully implicit, the resulting large system of equations is solved at each time step by using a dual-time stepping approach. Newton subiterations are also a valid alternative. For more details on the time integration scheme, we refer the reader to Refs [41, 117].
For viscous flow simulations, a second-order discretization of the viscous terms that does not alter the discretization operator applied to inviscid terms is adopted. The interest reader may refer to reference [101] for details.

### IV.7.1 Advection of an inviscid vortex

The convergence order of FV RBC schemes is investigated for an inviscid flow problem, namely the advection of an inviscid vortex. In this test case, an isentropic vortex is added to a uniform freestream flow. The free stream density and pressure are given by $\rho_\infty = 1$, $p_\infty = 1/\gamma$ with $\gamma = 1.4$ the ratio of specific heats. The freestream flow velocity components are chosen such that $u_\infty = v_\infty = \sqrt{2}$ in order to yield an advection at supersonic speed along the grid diagonal.The problem is therefore fully multidimensional.
The perturbation values of the vortex are those given in [167]:

$$(\delta u, \delta v) = \frac{\Gamma}{2\pi}\mathrm{e}^{\frac{1-r^2}{2}}(-\overline{y}, \overline{x}) \qquad \delta T = -\frac{(\gamma-1)\Gamma^2}{8\gamma\pi^2}\mathrm{e}^{1-r^2}$$

where $\Gamma$ is the vortex strength set equal to 5, $T$ is the temperature equal to $p/\rho$ through the non-dimensional perfect gas equation of state, $(x_{c0}, y_{c0})$ is the initial position of the vortex, $(\overline{x}, \overline{y}) = (x - x_{c0}, x - y_{c0})$ is the relative position and $r = \overline{x}^2 + \overline{y}^2$. Thereby, the initial primitive

variables are:

$$\begin{aligned}
\rho^0 &= \left[\frac{1}{S_\infty}\left(T_\infty - \frac{(\gamma-1)\Gamma^2}{8\gamma\pi^2}\mathrm{e}^{1-r^2}\right)\right]^{\frac{1}{\gamma-1}} \\
u^0 &= u_\infty - \frac{\Gamma}{2\pi}\mathrm{e}^{\frac{1-r^2}{2}}\overline{y} \\
v^0 &= v_\infty + \frac{\Gamma}{2\pi}\mathrm{e}^{\frac{1-r^2}{2}}\overline{x} \\
p^0 &= S_\infty(\rho^0)^\gamma
\end{aligned}$$

with $S_\infty = p/\rho^\gamma = p_\infty/\rho_\infty^\gamma$. The exact solution of this problem consists in the passive advection of the vortex at freestream velocity. The vortex evolution is computed up to $t_f = 14$. The computational domain extends from $-15$ to $+15$ in both directions in space with periodic boundary conditions. The initial position of the core vortex is $(x_{c0}, y_{c0}) = (-10, -10)$.

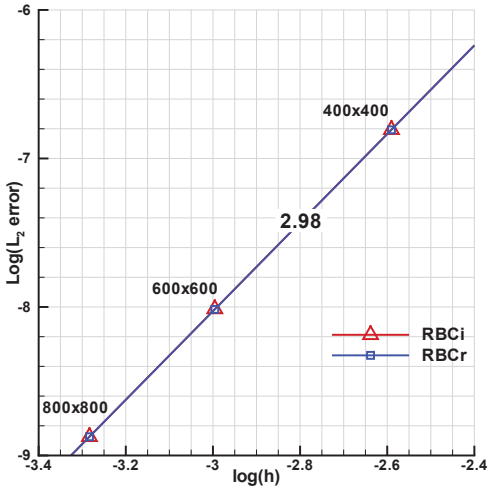


Figure IV.9: $L_2$ error on $\rho$ for Cartesian meshes.

The convergence study is first done on a series of Cartesian regular grids with 400×400, 600×600 and 800×800 cells. We want to check if the spatial schemes RBC$r$ and RBC$i$ are third order accurate.
Since the time approximation is second-order accurate, we choose the time step such that $\Delta t \propto h^{\frac{p}{2}}$, where $p \geqslant 2$ is the spatial order of accuracy and $h$ the spatial mesh size, in order to recover a global order of accuracy equal to $p$.
Fig. IV.9 plots the $L_2$ norm of the error with respect to the exact solution (for the density field) as a function of the mesh size, in a double-log scale. A slope almost equal to 3 is recovered both for RBC$r$ and RBC$i$, which confirms the preceding theoretical results.
In order to introduce mesh irregularities we randomly shake the meshes by an amount $\sigma$. In practice, each cell node is randomly moved within a circle centered on its initial position and of radius $\sigma h$ where $h$ is the mesh size for a regular Cartesian mesh with the same number of nodes. Fig. IV.10 shows the aspect of shaken meshes with random amounts $\sigma$ equal to 0.05 and 0.1.

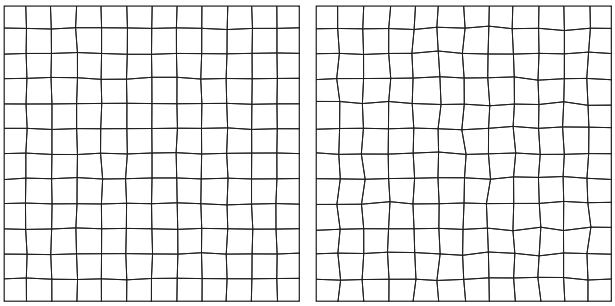

(a) $\sigma = 0.05$ (b) $\sigma = 0.1$

Figure IV.10: Aspect of the shaken meshes.

Fig. IV.11 shows that for mildly deformed grids ($\sigma = 0.05$) RBC$i$ remains third order accurate, unlike RBC$r$, for which a lower slope (2.85) is found.

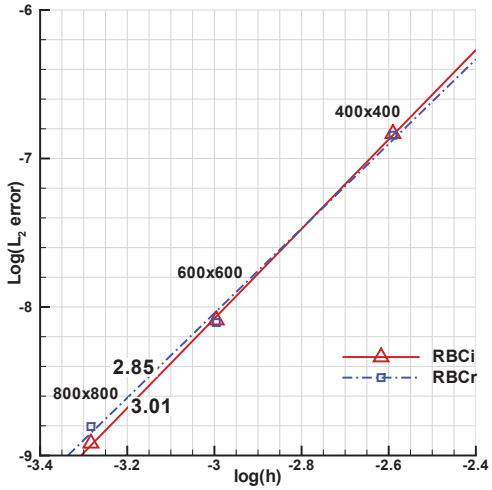


Figure IV.11: $L_2$ error on $\rho$ for shaken meshes with $\sigma = 0.05$.

For a more severly deformed grid ($\sigma = 0.1$) Fig. IV.12(a) shows that neither RBC$r$ nor RBC$i$ are third order accurate any more. Nevertheless, if we verify if they are second order accurate for this configuration by taking $\Delta t \propto h$, we find that RBC$i$ is still second order accurate, whereas RBC$r$ is less than second order (see Fig. IV.12(b)). Once again, this is in line with the theoretical analysis of Sec. IV.5.

Fig. IV.13 shows iso-lines of the density obtained on a $600 \times 600$ cell mesh with $\sigma = 0.1$ for both RBC$i$ and RBC$r$. The exact solution is also represented. It can be noticed that spurious oscillations due to mesh irregularities are produced by RBC$r$, whereas RBC$i$ provides a much smoother solution, in satisfactory with the reference.

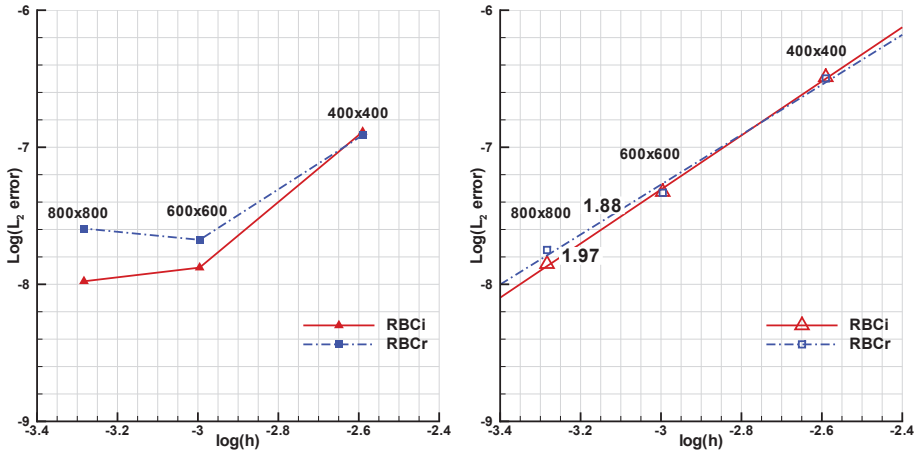


(a) Order 3 test. (b) Order 2 test.

Figure IV.12: $L_2$ error on $\rho$ for shaken meshes with $\sigma = 0.1$.

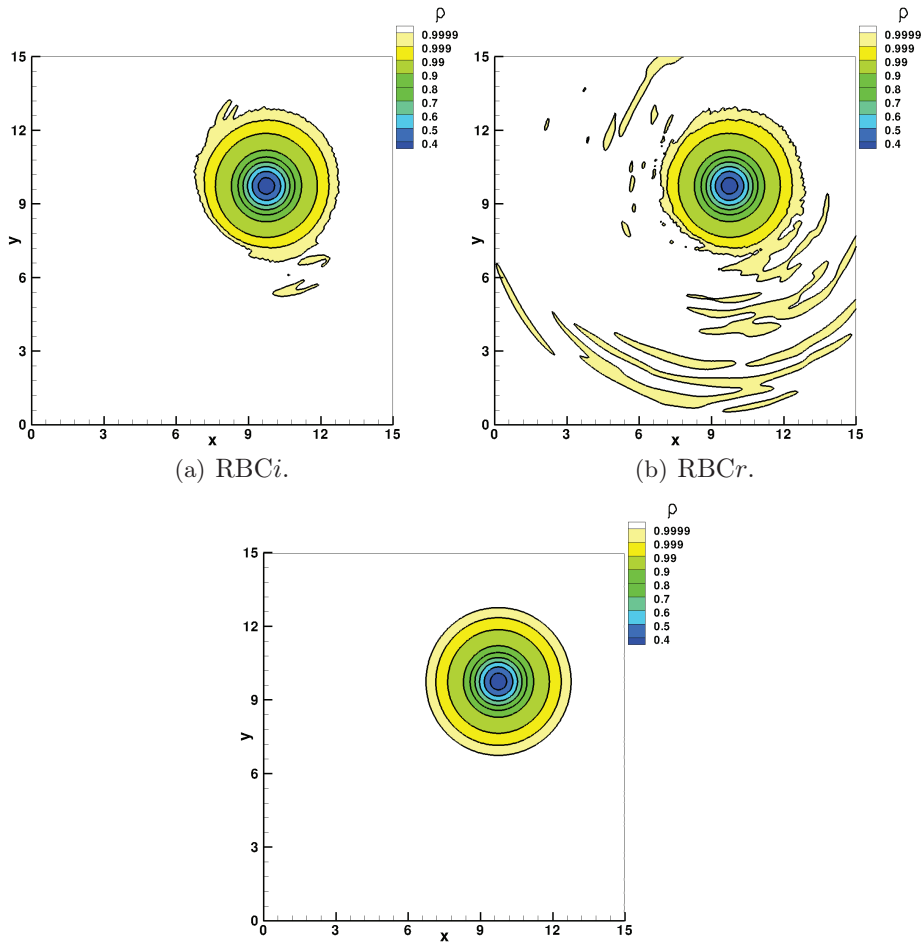


(a) RBC$i$. (b) RBC$r$.

(c) Exact solution.

Figure IV.13: Density contours of the vortex on the 600×600 mesh shaken with $\sigma = 0.1$ at $t = t_f$.

### IV.7.2 Laminar flow past a cylinder

Next, we consider an unsteady laminar flow past a two-dimensional circular cylinder at a Reynolds number of 1200 and a Mach number of 0.3. Comparing experimental and 2D computational data of the flow over a circular cylinder is complicated since this flow is driven by three-dimensional effects for a Reynolds number over 180 [43, 118, 165]. Nevertheless, it is a good test case in order to quantify the accuracy of a numerical scheme [27] for vortex-dominated viscous flows, by comparison with a reference numerical solution. The computational grid used for the third-order RBC schemes is a regular polar mesh composed by 100×168 cells. The grid points are uniformly distributed in the radial direction and clustered close to the cylinder wall in the normal direction. The external boundary is located 20 diameters far from the cylinder and the distance between the wall and the first grid point is 0.0085 times the diameter. The adimensional time step used for all the computations is $\Delta t = 3.125 \times 10^{-3}$. It is small enough to rule out numerical errors due to the time discretization. A reference computation has been carried-out on a fine mesh composed by 400×672 cells, using a nominally fifth-order accurate RBC scheme (named RBC5 [106]), and is used to evaluate the accuracy of RBC$r$ and RBC$i$.

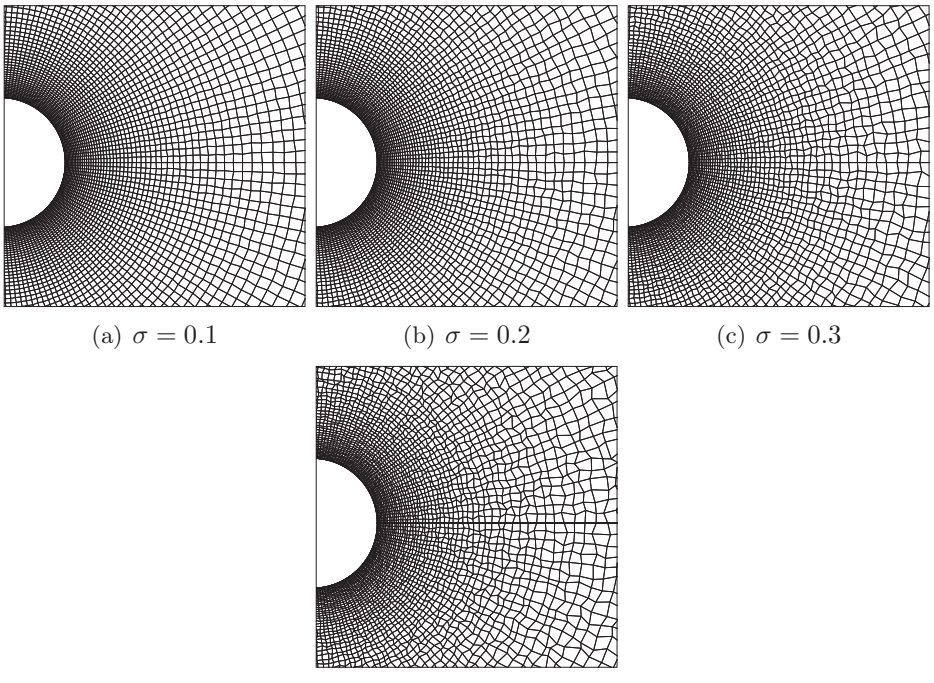

(a) $\sigma = 0.1$ (b) $\sigma = 0.2$ (c) $\sigma = 0.3$

(d) $\sigma = 0.4$

Figure IV.14: Aspect of the shaken meshes.

In addition to the regular polar mesh, a series of randomly deformed meshes is generated by shaking the nodes of the regular one by a random amount $\sigma$, going from 0. to 0.4. with a step of 0.1. Shaken grids are shown in Fig. IV.14. An overall view (isolines of the instantaneous entropy field) of the numerical solutions of RBC$r$ and RBC$i$ on the most deformed grid ($\sigma = 0.4$) is provided in Fig. IV.15. The reference solution is also represented.

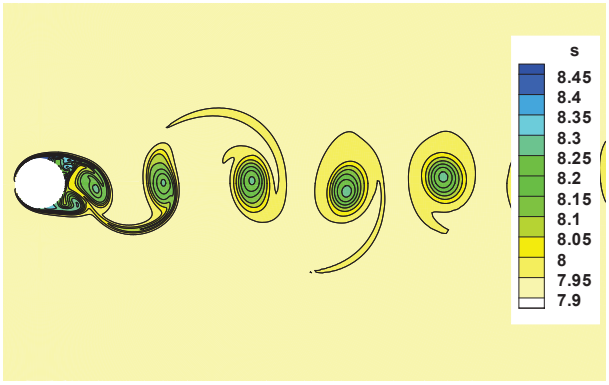


(a) RBC5, reference, 401×673 regular polar mesh

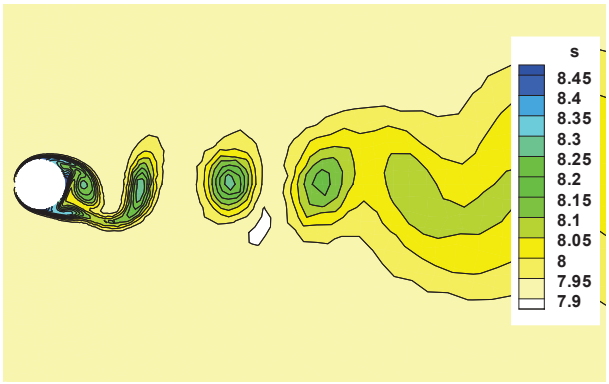


(b) RBC$i$, 100×168 shaken mesh, $\sigma = 0.4$

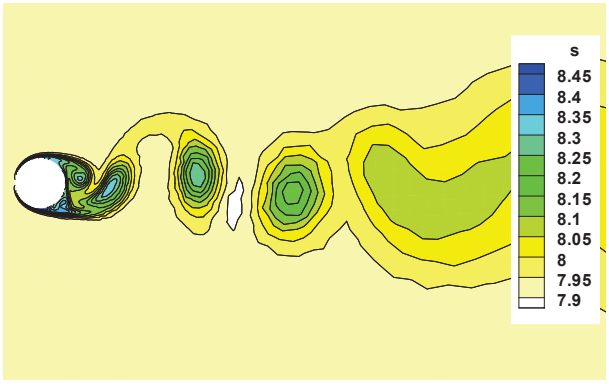


(c) RBC$r$, 100×168 shaken mesh, $\sigma = 0.4$

Figure IV.15: Snapshot of the entropy field.

Even if the vortex street is dissipated more quickly (because of the mesh coarsening and deformation), RBC$i$ provides results in somewhat closer agreement with the reference than RBC$r$. For a more quantitative comparison, we computed discrete Fourier tranforms of the unsteady vertical force acting on the cylinder for different schemes and meshes. The frequency content of the signal is essentially represented by a single mode, associated to vortex shedding. This is used to compute the Strouhal number $St$ (based on free-stream velocity and cylinder diameter) of the vortex street. The reference computation returns $St = 0.25$. Table IV.1 summarizes the results given by RBC$r$ and RBC$i$ on different meshes. RBC$i$ returns a Strouhal number equal to the reference one even on very deformed grids, whereas RBC$r$ deviates from the reference value

starting from $\sigma = 0.2$.

| | RBC$r$ | RBC$i$ |
|---|---|---|
| regular mesh | 0.25 | 0.25 |
| $\sigma = 0.1$ | 0.25 | 0.25 |
| $\sigma = 0.2$ | 0.24 | 0.25 |
| $\sigma = 0.3$ | 0.24 | 0.25 |
| $\sigma = 0.4$ | 0.23 | 0.24 |

Table IV.1: Computed Strouhal numbers on increasingly deformed grids.

Again, we conclude that for relatively academic configurations RBC$i$ provides slightly more accurate results than RBC$r$ when deformed grids are considered.

## IV.8 Chapter summary

We have presented the FV formulation of RBC schemes and a third-order finite volume Residual-Based Compact scheme, RBC$i$, has been designed for the numerical simulation of compressible flows on structured meshes. The scheme is designed to take into account mesh deformations, in such a way that it is third-order on mildly distorted structured grids and second-order on highly distorted meshes. To this purpose, suitable weighted discretisation operators, which take into account mesh deformations, are introduced. An analysis of the Fourier symbol of the proposed spatial approximation demonstrates that the resulting discretization is dissipative and then Cauchy-stable for all flow configurations. An investigation of the multidimensional modified wave number of the scheme shows that, on Cartesian grids, it is somewhat more dissipative and dispersive than its finite-difference counterpart. Specifically, the scheme dissipates more quickly ill-resolved solution modes in the transverse direction with respect to the advection velocity. This may be considered a drawback, but in practice ensure robustness on highly distorted grids, where in any case the accuracy of the straightforward finite volume extension (RBC$r$) is lost because of grid deformations, while RBC$i$ remains high-order accurate.
Numerical tests confirm the theoretical results and demonstrate the importance of using a weighted scheme formulation on very irregular meshes. For all cases, RBC$i$ is more accurate and more robust than RBC$r$ when highly deformed grids are used. This enables its application to complex flows of industrial interest, like turbomachinery flows, for which the generation of pretty smooth grids is generally a very hard task. This is demonstrated later in this manuscript by calculations of a very severe transonic flow in the high-pressure ratio VKI BRITE HP turbine stage ($cf.$ Section V).
In term of numerical cost, RBC$i$ is more expensive than RBC$r$, essentially because of the calculation of weighed operator coefficients. The CPU time of an RBC$i$ computation is roughly 1.27 times the time of an RBC$r$ computation. This is the price to pay for accuracy and robustness on irregular meshes. On the other hand, it may be expected that time savings can be made for the mesh generation task, since RBC$i$ enables high accuracy on computational grids of poor quality. In summary, present results suggest that RBCi may represent a good candidate for industrial CFD applications.
An RBC$i$ FV extension of RBC5 and RBC7 could be done in future work even if it is not straightforward and possibly too costly at high-order. An alternative to that is a multiblock approch coupled with the use of overset grid treatment: one can use RBC$i$ for body fitted meshes and higher order finite difference RBC schemes in Cartesian meshes. This is currently

being investigated in the PhD work by P.-Y. Outtier (some preliminary results are given in [121]).

In the present and preceding chapters, unsteady RBC schemes have designed and shown to be linearly stable and dissipative. Their spectral properties have been studied in detail demonstrating that RBC schemes are high-accurate. Besides, these theoretical results on RBC schemes have been validated on numerical tests. In the next Chapter, we go further in the understanding of RBC schemes behaviour by investigating the applicability of these schemes to selected unsteady compressible flows.

# Chapter V

# Application to selected unsteady compressible flows

**Contents**



## V.1 Introduction

In the present chapter, we want to go further in the understanding of RBC schemes behaviour on more realistic unsteady compressible flows. On the one hand, we look into the capabilities of RBC schemes for the computation of fine scale flow structures characteristic of turbulent flow. To this purpose, we carry out computations of the inviscid and viscous Taylor-Green Vortex case. On the other hand, we explore the feasibility of high-order RBC schemes for complex industrial flow computations. A first step to achieve this goal is the use of RBC$i$ on 2D and 3D unsteady turbomachinery as the VKI LS-59 turbine cascade and the VKI BRITE HP turbine stage respectively.

## V.2 Numerical simulation of fine scale turbulence: *the Taylor-Green Vortex*

### V.2.1 Inviscid Taylor-Green vortex

In Chapter III, the spectral properties of RBC schemes ($cf.$ Section III.9) were validated for a simple linear problem. Here, we turn to a test case well suited for the numerical investigation of the intrinsic dissipation and resolvability properties of RBC schemes for nonlinear flow

problems. Precisely, we consider the nearly incompressible, inviscid Taylor-Green vortex flow in a three-dimensional periodic domain defined as $[2\pi]^3$. The test case is a simple model for the investigation of the nonlinear transfer of kinetic energy among eddies over a range of spatial scales.

The computation is initialised with a two-dimensional, single-mode initial velocity field of the form:

$$\begin{cases} u(x,y,z,0) &= \sin(x)\cos(y)\cos(z) \\ v(x,y,z,0) &= -\cos(x)\sin(y)\cos(z) \\ w(x,y,z,0) &= 0 \end{cases} \tag{V.1}$$

and evolves to a fully three-dimensional flow characterized by small scales of motion.

To complete initialization, the preceding equations for the velocity field are supplemented with initial conditions for density and pressure:

$$\begin{cases} \rho(x,y,z,0) &= 1 \\ p(x,y,z,0) &= p_0 + \dfrac{\rho}{16}[(\cos(2z)+2)(\cos(2x)+\cos(2y))-2] \end{cases} \tag{V.2}$$

where $p_0 = 100$, so that the average Mach number in the flow field is approximately 0.08, as in [140].
As the time-evolution of the Taylor-Green vortex entails a kinetic energy cascade, the evolution of this simple flow has been used to study the effects of both viscous dissipation in Navier-Stokes dynamics and numerical dissipation in the solution of the Euler equation [32, 140].
For this inviscid and almost incompressible flow, the total kinetic energy in the computational domain is conserved for an exact solution, and it is easily seen that it remains equal to $\pi^3$. So a quantitative measure of numerical dissipation inherent in a numerical algorithm can be assessed by observing the rate of decrease of the kinetic energy from its initial value during the time-evolution of the flow. On the other hand, as the nonlinear interactions generate successively smaller scales, the enstrophy, directly related to the volume integral of the rotational kinetic energy of flow eddies –which is in its turn related to the vorticity field–, grows without bound and leads to finite time singularity. The enstrophy involves derivatives of the velocity field components, so that its computation is sensitive to the accuracy with which the small scales can be represented numerically and can be used to quantify the resolvability of a numerical scheme. Numerical dissipation significantly reduces the sharpness of the approximation of flow derivatives, and the consequent reduction of vorticity production results in a less rapid increase of the enstrophy than expected (see [140] and references cited therein for more details).
In the following, we use dissipative (in the $\chi$-criterion sense) RBC schemes of different orders to compute the Taylor-Green vortex flow on regular Cartesian grids with different resolutions. The results are compared to those of Shu *et al.* [140], obtained by using either a WENO-5 scheme or a Fourier collocation method with a sharp cut-off filter (F-SF-23N). The latter scheme is considered hereafter as a benchmark for this smooth and periodic problem, because of its spectral resolution.
Fig. V.6 illustrates the early stages of the vortex break-up process as computed by RBC5 using a grid with $128^3$ mesh cells: it provides isosurfaces of the Q criterion, Q=0, colored by the kinetic energy, $k$.

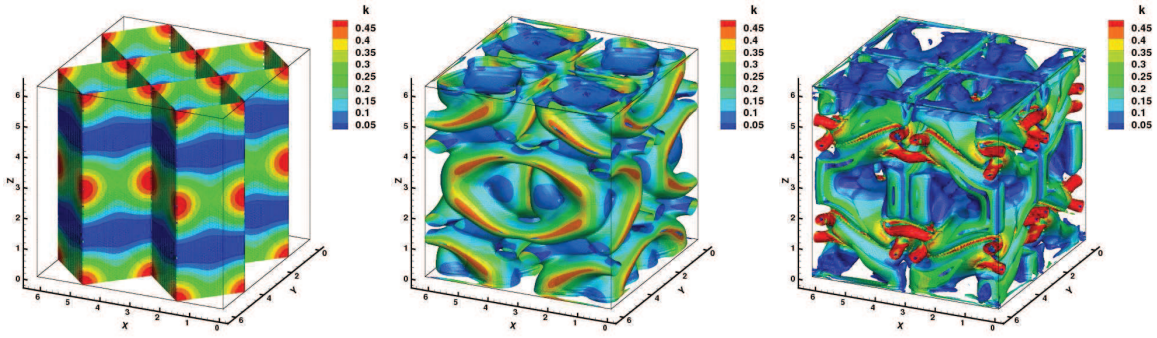


(a) $t = 0$. (b) $t = 3$. (c) $t = 5$.

Figure V.1: Iso surface Q=0 colored by $k$ (computed with RBC5 on the $128^3$ mesh). Initial phases of vortex break-up.

The vortex stretching mechanism is seen even better from Fig. V.2, which provides iso-contours of the vorticity on selected planes. At time $t = 3$ the flow displays only large structures, whereas tiny vortices and filaments are visible in the flow field at time $t = 5$.

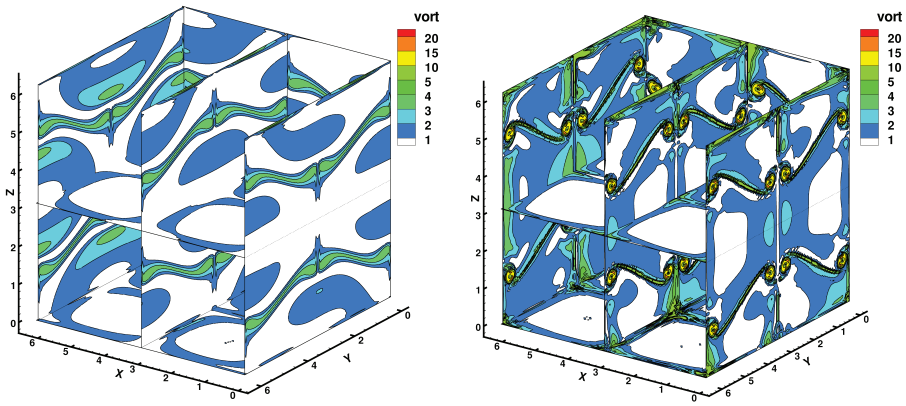


(a) $t = 3$ (b) $t = 5$

Figure V.2: Visualization of the vortex stretching through iso-contours of vorticity (computed with RBC5 on the $128^3$ mesh).

Figure V.3 shows the time history of the normalized total kinetic energy obtained for different schemes by using two grids with different resolutions. Note that the spectral scheme F-SF-23N has the property of conserving kinetic energy exactly and provides the highest rate of growth of the enstrophy. On the contrary, the WENO scheme no longer conserves energy starting from a time of approximately 1.5 on a $64^3$ mesh and a time 3 on the $128^3$ mesh. RBC schemes display intermediate behaviors between these two limits. RBC3 dissipates a bit earlier than WENO-5, buth at a slower rate, so that at time 6 it has dissipated only about 18% of the initial kinetic energy on the coarse grid and 6% on the fine grid, against 25% and 12% for WENO-5, respectively. RBC5 and RBC7 conserve the energy up to times equal to 4 and more, according to the chosen grid resolution, RBC7 being slightly more accurate than RBC5. Precisely, RBC5 loses about 4% of the initial energy on the $64^3$ grid and about 2% on the $128^3$ grid, whereas the losses are reduced to about 3% and 1.5% for RBC7, respectively.
To measure even more accurately the dissipation rate of the kinetic energy due to numerical

damping errors, we consider in Fig. V.4 the evolution of the time derivative of the total kinetic energy. This should be zero at any time for an exact solution. Once again, RBC schemes of all orders exhibit a much lower dissipation rate than WENO-5. For instance, at time $t = 6$ the dissipation rate of RBC5 is more that 2.5 times lower than that of WENO-5 on the coarse grid and, interestingly, more than 3 times lower on the finer grid, which shows that the intrinsic dissipation of RBC schemes vanishes quickly when the mesh is refined.

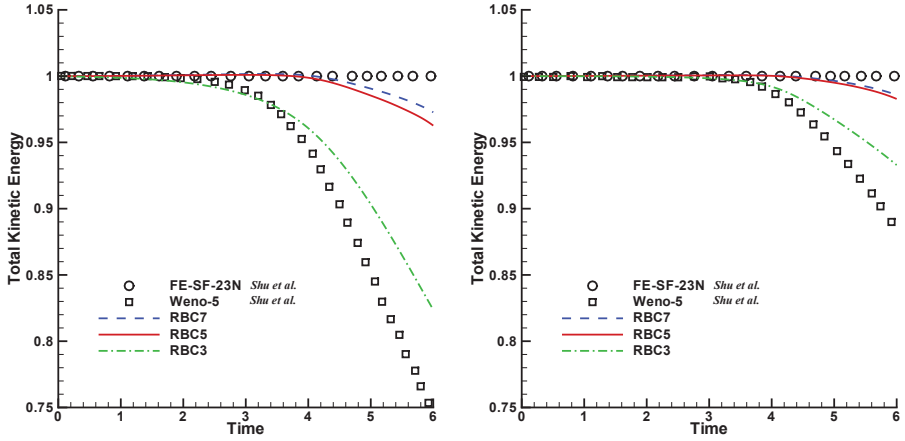


(a) $64^3$ mesh (b) $128^3$ mesh

Figure V.3: Comparison of the time evolution of the normalized total kinetic energy on a $64^3$ mesh (a) and on a $128^3$ mesh (b) with different numerical schemes.

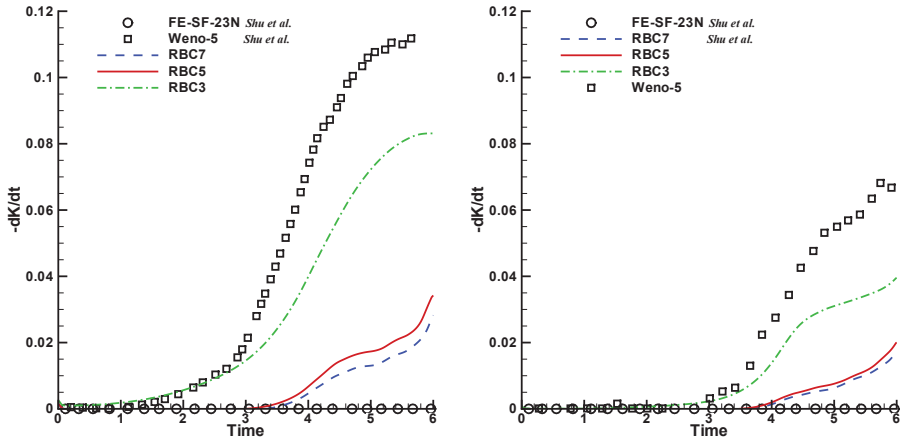


(a) $64^3$ mesh (b) $128^3$ mesh

Figure V.4: Comparison of the time evolution of the time derivative of the total kinetic energy on a $64^3$ mesh (a) and on a $128^3$ mesh (b) with different numerical schemes.

Fig. V.5 illustrates the time evolution of the flow enstrophy for the same combinations of grids and numerical schemes. The rate of increase of the enstrophy is almost the same for all schemes almost up to time 2.5 on the coarse grid and 3.5 on the finer one. As suggested in [140], this is due to the fact that at early times the vortical flow is dominated by relatively large structures that are well-captured by all of the schemes. However at later times, when the

vortex core steepens up into a high gradient, large differences among the computed values of the enstrophy appear. The largest values of the enstrophy are provided by the Fourier collocation method with the sharp-cutoff filter (F-SF-23N), followed by RBC7 and RBC5, that exhibit quite close behaviors. At later times, WENO-5 and RBC3 schemes exhibit a decrease in the rate of enstrophy production and do not produce as much vorticity as the other schemes: this is due to their higher intrisic dissipation. Nevertheless, it is noteworthy that the RBC scheme of third-order accuracy is still less dissipative than the fifth-order WENO scheme.
In the work [140], the fifth-order WENO scheme uses a global Lax-Friedrichs flux splitting [84], which computational cost in terms of number of operations per Runge-Kutta step has been estimated in [84]. Note that, based on a rough operation count, the computational cost of WENO-5 is 75% higher than the one of RBC3 space discretization, whereas it is 10% higher than those of RBC5 and RBC7. Note also that WENO results from [140] were obtained by using a third-order three-stage TVD Runge-Kutta scheme, whereas the present calculations use a second-order implicit LMM method solved by a dual-time stepping approach: this is unfavorable to RBC schemes both in terms of accuracy and efficiency and must be improved in the near future. On the other hand, the WENO-5 scheme uses a non linear approximation of convective fluxes to achieve a non-oscillatory representation of strong discontinuities, which is not the case of RBC schemes.

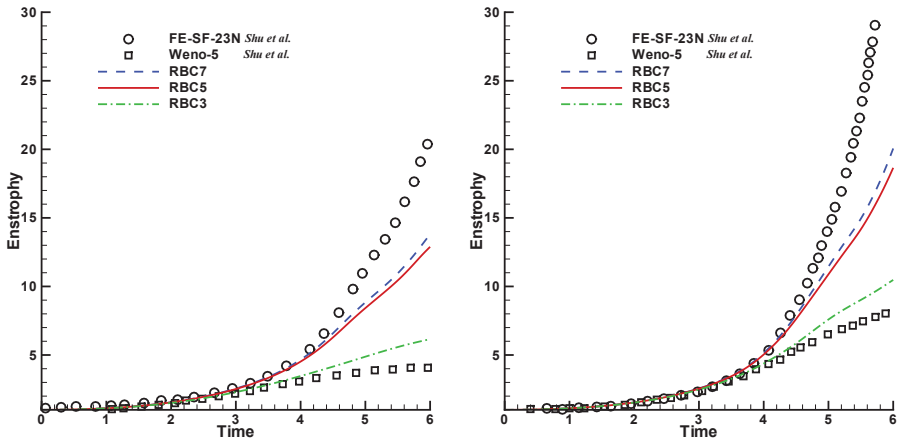


(a) $64^3$ mesh (b) $128^3$ mesh

Figure V.5: Comparison of the time evolution of the normalized total enstrophy on a $64^3$ mesh (a) and on a $128^3$ mesh (b) with different numerical schemes.

The computation of the inviscid Taylor-Green vortex flow with RBC schemes confirms numerically the interest of a well-designed RBC dissipation to resolve accurately fine scale flow structures. The high-accuracy is also demonstrated on this case since we can quantify the numerical dissipation of the schemes by means of the dissipation of the kinetic energy.

### V.2.2 Viscous Taylor-Green vortex

In the present section, we compute the viscous Taylor-Green Vortex (TGV) which is an unsteady viscous flow problem dominated by energy transfer from large to small flow scales. This problem has been proven to be an excellent testing bench to study the resolvability properties of high-order schemes in view of subsequent application to fine-scale turbulence simulations [16, 32, 53, 54, 76]. Consequently, this computation is a good prototype to scale resolving simulations.

The use of high accurate schemes is of utmost importance for numerical simulation of turbulent flows since they enable capturing flow structures from large to small scales at an acceptable computational cost.
Here, a three-dimesional vortex is set as an initial condition for a 3D-computation. Again, the computational domain is the cube $[0, 2\pi]^3$, with periodicity conditions imposed at all boundaries. Because of vortex-stretching and vortex tilting mechanisms, the vortex breaks up, giving origin to smaller and smaller structures. For finite values of the Reynolds number, the kinetic energy is transferred from larger to smaller scales and dissipated by the smallest one; the test case gives thereby a simple model of the energy cascade (Fig. V.6). The Taylor-Green vortex is a classical example of nonlinear fluid flow with kinetic energy transfert from large to small scales and is a good milestone to assess the applicability of numerical schemes to Large Eddy Simulation (LES) and has been used as a benchmark case in two workshops on high-order methods [4, 158]. Hereafter, we perform Implicit LES (ILES) where the role of the SGS model is taken by the numerical dissipation of RBC schemes.

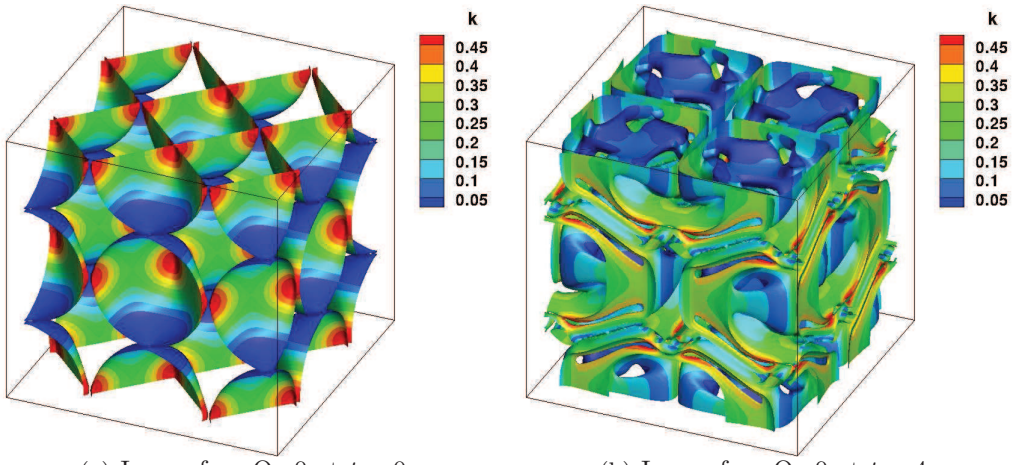


(a) Iso surface Q=0 at $t = 0$.




(b) Iso surface Q=0 at $t = 4$.

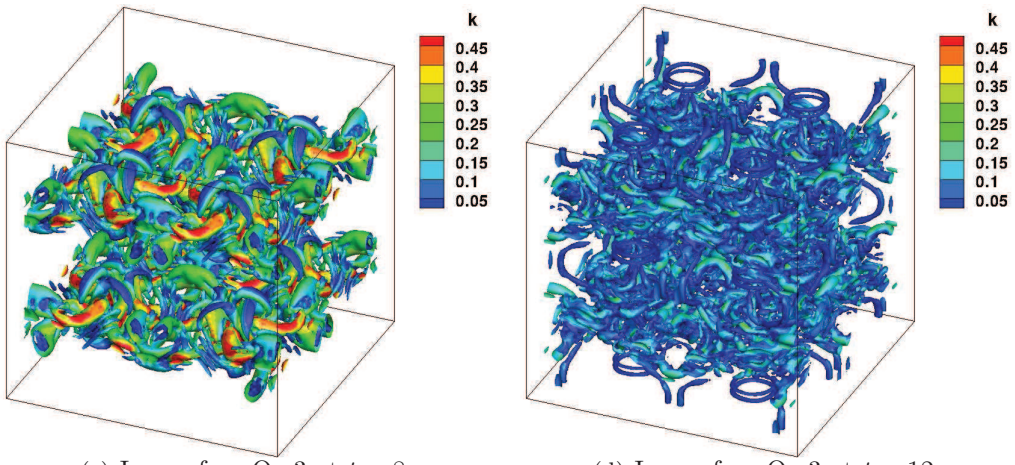


(c) Iso surface Q=3 at $t = 8$.




(d) Iso surface Q=3 at $t = 12$.

Figure V.6: Iso surface of the Q criterion colored by k (computed with RBC5 on the $128^3$ mesh). The figure show phases of the vortex break-up.

Part of the present results have been presented at an international conference [71] and an international workshop [69]. The initial conditions of the computations are again those of Eq.

(V.1) along with:

$$\begin{cases} \rho(x,y,z,0) & = 1 \\ p(x,y,z,0) & = p_0 + \dfrac{\rho}{16}(\cos(2z)+2)(\cos(2x)+\cos(2y)) \end{cases} \tag{V.3}$$

where now we choose $p_0 = 100$, a Mach number $M_0 = 0.1$, a Reynolds number $Re = 1600$ and a Prandlt number $Pr = 0.71$. For these conditions, previously computed by Brachet [32] using DNS and a spectral method, a recent DNS obtained on a $512^3$ with a pseudo-spectral code over a quite long integration time is available [4]. This solution has been shown to be converged and can be considered as a reference. The data and a detailed description of the test case are available in [4].

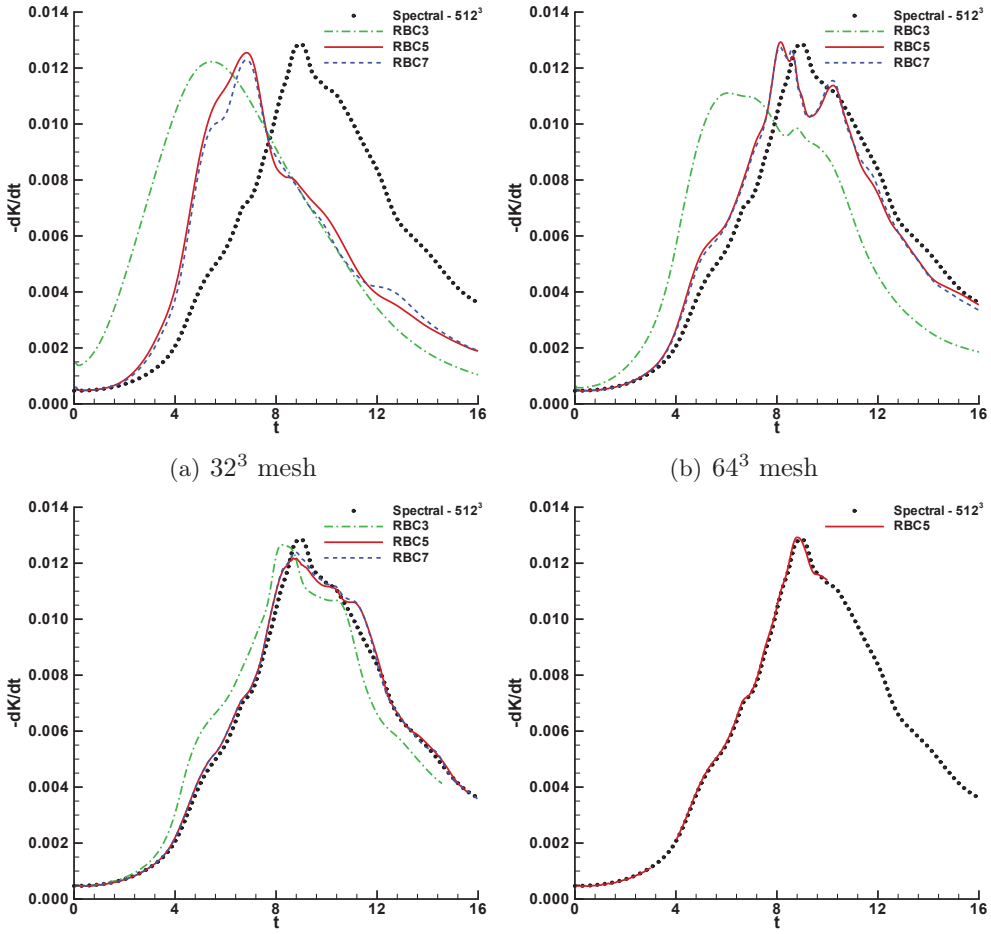


(a) $32^3$ mesh (b) $64^3$ mesh

(c) $128^3$ mesh (d) $256^3$ mesh

Figure V.7: Comparison of the time evolution of the time derivative of the total kinetic energy on a $32^3$ mesh (a), $64^3$ mesh (b), $128^3$ mesh (a) and on a $256^3$ mesh (b) with RBC schemes.

The absence of external forcing implies that the kinetic energy is only decaying during the computation. Thus, the first comparison with the the DNS is done on the time derivative of the kinetic energy integrated on the whole computational domain $-dK/dt$ (*cf.* Fig. V.7), where

$$K = \frac{1}{(2\pi)^3} \int\int\int_{[0,2\pi]^3} \frac{1}{2}\rho||\boldsymbol{u}||^2 \, dxdydz.$$

This quantity represents the kinetic energy dissipation rate. Integral quantities are more difficult to match since they are affected by numerical errors commited in the whole computational domain and not only local effects. As in the preceding inviscid case, RBC5 and RBC7 demonstrate their good resolvability, thanks to their low dissipation and dispersion errors. Even if the reference solution can not be perfectly matched on a $128^3$ mesh because of aliasing, the solutions of RBC5 and RBC7 on this mesh are yet very close to the reference one (Fig. V.7(c)). RBC5 energy dissipation rate almost matches the DNS solution on the $256^3$. The solution of RBC3 on the $128^3$ mesh is similar to the RBC5 solution on the $64^3$ mesh.

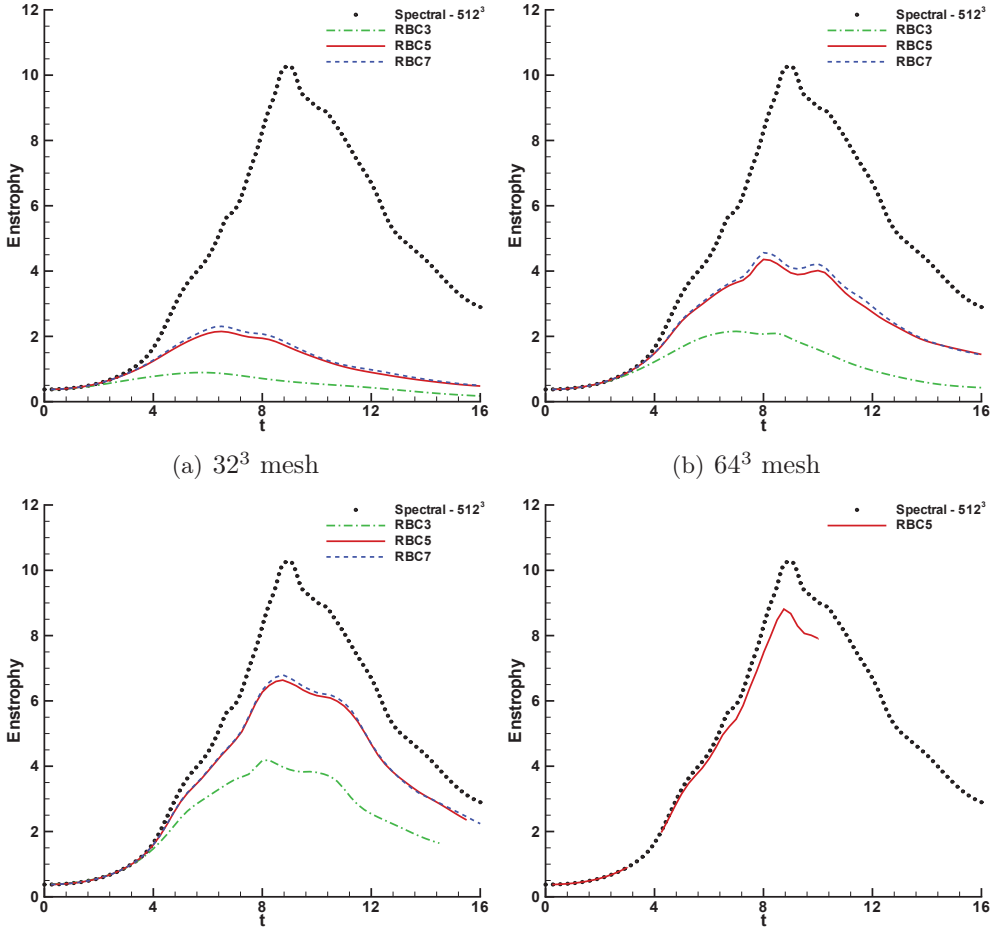


(a) $32^3$ mesh (b) $64^3$ mesh

(c) $128^3$ mesh (d) $256^3$ mesh

Figure V.8: Comparison of the time evolution of the total enstrophy on a $32^3$ mesh (a), $64^3$ mesh (b), $128^3$ mesh (a) and on a $256^3$ mesh (b) with RBC schemes.

Fig. V.8 illustrates the time evolution of the enstrophy, $\Omega$, for the same combinations of grids and numerical schemes. The total enstrophy is defined by

$$\Omega = \frac{1}{(2\pi)^3} \int\int\int_{[0,2\pi]^3} \frac{1}{2}\rho||\boldsymbol{\omega}||^2 \, dxdydz,$$

where $\boldsymbol{\omega}$ is the vorticity. This quantity is more difficult to match than the dissipation rate of the kinetic energy. The kinetic energy is indeed a second-order quantity. A given discretization can solve this field and underestimate higher-order quantities involving velocity gradient, like the

enstrophy [49]. This quantity emphasizes the difference of resolvability between RBC3, RBC5 and RBC7. Besides Figs. V.8(d) clearly shows that the computations are not converged for these scales on a $256^3$ mesh even if the dissipation rate of the kinetic energy almost matches the DNS results. The flow physic is well captured with RBC5 on a $128^3$ mesh, vortex stretching and tilding mechanisms are clearly visible (see Figures V.6(a) and V.6(b)) due to inviscid terms as well as the vortex break-up due to viscous terms (see Figures V.6(c) and V.6(d)).

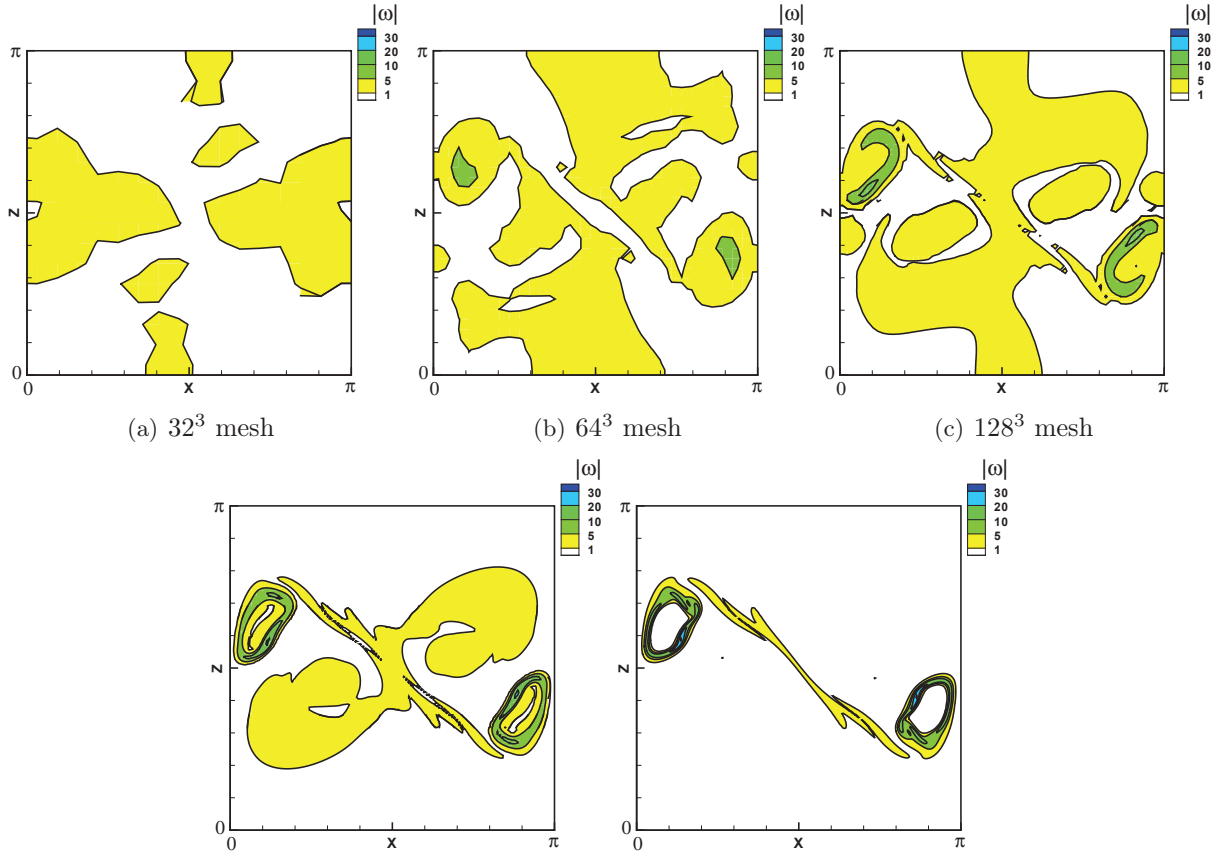


(a) $32^3$ mesh (b) $64^3$ mesh (c) $128^3$ mesh

(d) $256^3$ mesh (e) Spectral - $512^3$ mesh

Figure V.9: Iso-contours of the dimensionless vorticity norm, $|\omega|$, on a subset of the periodic face $x = -\pi$ at time $t/t_c = 8$. Comparison of the solution computed with RBC5 on the $32^3$, $64^3$, $128^3$ and $256^3$ meshes with the DNS solution.

By looking at the dimensionless vorticity norm $|\omega|$ on a subset of the plane $y = 0$ we can identify a characteristic vortical structure at time $t = 8$ (see Fig. V.9(e)). Fig. V.9 shows the grid convergence of RBC5 on this strucure. It confirms that the $32^3$ mesh is too coarse in order to capture the driving structures of the flow. Even if the $64^3$ and the $128^3$ mesh computations are not converged we can clearly distinguish and identify the investigated structure. The structure captured on the $256^3$ mesh is close to the DNS one even if the vorticity is also a quantity with high-order moment since it contains velocity gradients. Fig. V.11 provides a close-up of the comparison between this computation and the DNS confirming that the contours are really close.

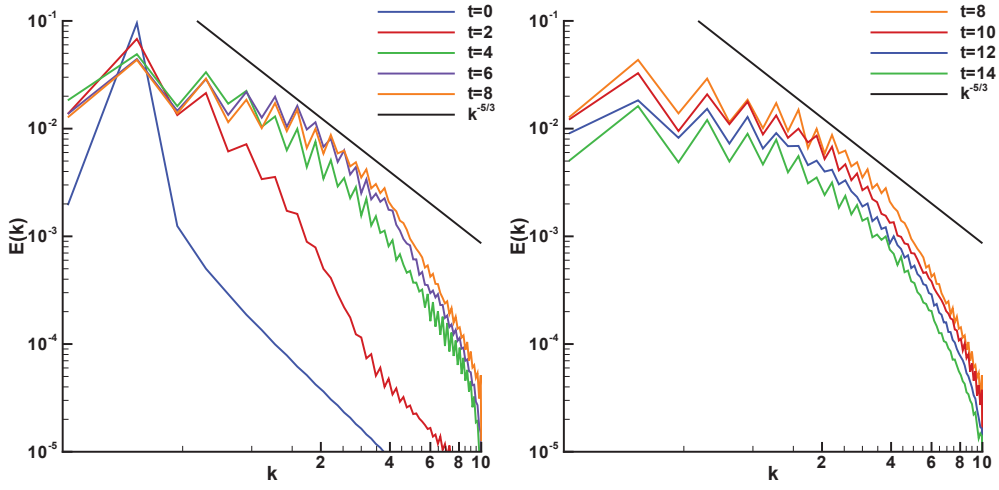


(a) RBC3, $t = 0, 2, 4, 6$ and 8




(b) RBC3, $t = 8, 10, 12$ and 14

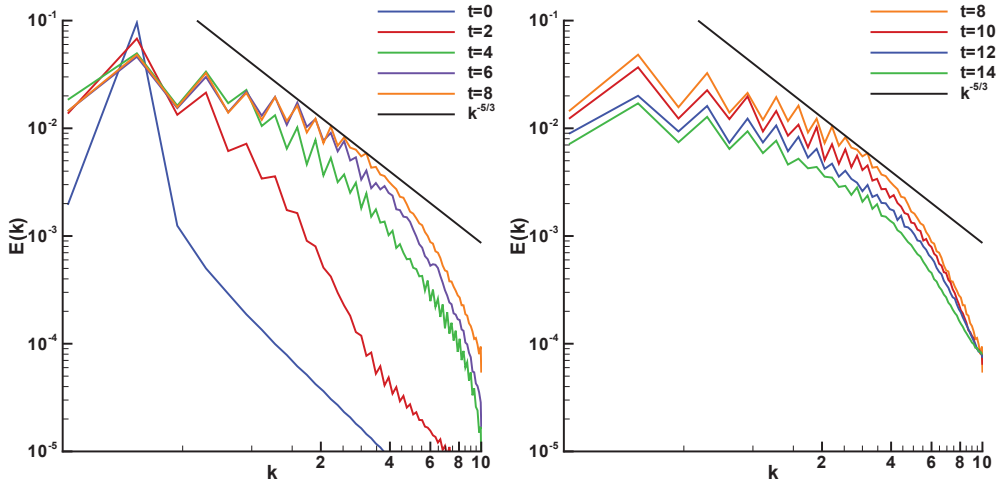


(c) RBC5, $t = 0, 2, 4, 6$ and 8




(d) RBC5, $t = 8, 10, 12$ and 14

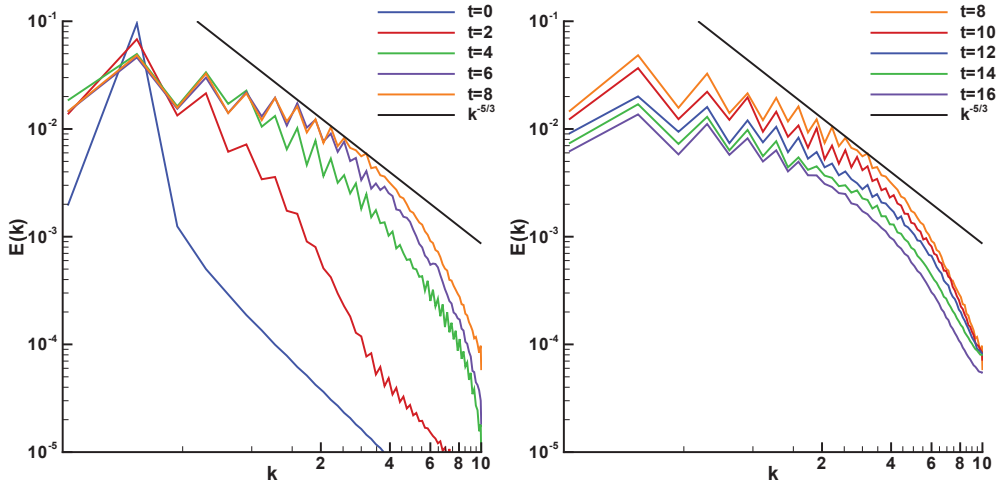


(e) RBC7, $t = 0, 2, 4, 6$ and 8




(f) RBC7, $t = 8, 10, 12, 14$ and 16

Figure V.10: Time evolution of the spectrum $E(k)$ of the solutions computed with RBC schemes on a $128^3$ mesh.

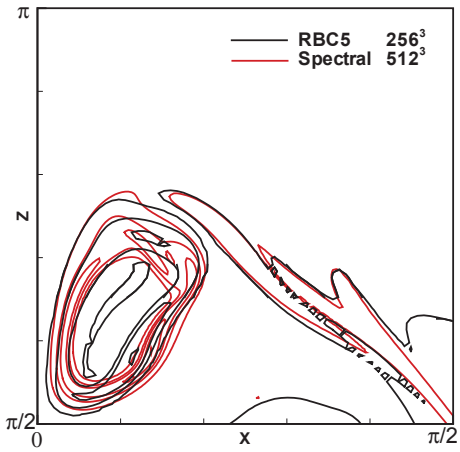


Figure V.11: Iso-contours of the dimensionless vorticity norm, $|\omega| = 1, 5, 10, 20$ and 30, on a subset of the periodic face $x = -\pi$ at time $t/t_c = 8$. Comparison of the solution computed with RBC5 on the $256^3$ meshes with the DNS solution.

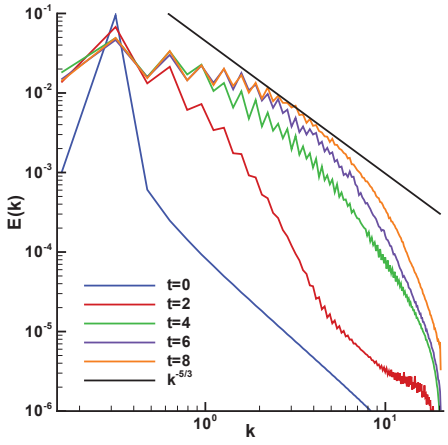


Figure V.12: Time evolution of the spectrum $E(k)$ of the solutions computed with RBC schemes on a $256^3$ mesh.

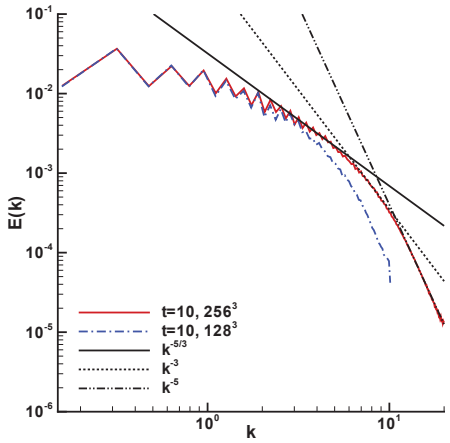


Figure V.13: Comparison of the spectrum $E(k)$ of the solution computed with RBC5 on the $256^3$ and the $128^3$ meshes at $t = 10$.

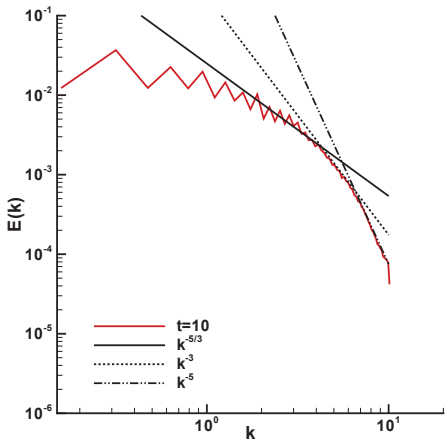


Figure V.14: Spectrum $E(k)$ of the solution computed with RBC5 on the $128^3$ mesh at $t = 10$.

Fig. V.10 provides the time evolution of the kinetic energy spectra of the solutions computed with RBC of different orders schemes on the $128^3$ mesh. These energy spectra are computed by taking the mean of the FFT (Finite Fourier Transform) done on the $3 \times 128^2$ mesh lines of the computational domain for each time of the computation represented. The range of wavenumbers is delimited on the left by the value corresponding to the domain length and on the right to the spatial discretization step. The initial spectrum is represented by a single mode. The energy of this mode is then transfered to the smaller scales. New modes are progressively generated through the vortex stretching mechanism. Fig. V.10(a), V.10(c) and V.10(e) show that all the scales present in the computation are set up at $t = 8$. From the time 8, we can distinguish the $-5/3$ slope since almost all the scales involved in this flows are set. This slope corresponds to

the inertial subrange of the energy spectrum respecting the Kolmogorov's $k^{-5/3}$ law [107, 127]. This is confirmed by the computation done with RBC5 on the $256^3$ mesh (see Fig. V.13) where the $-5/3$ slope is more identifiable at the adimensional time $t = 10$. The time $t = 10$ is chosen since it corresponds to the time where all the scales of the computation are present and no more modes are generated. This also corresponds approximately to the energy dissipation peak. At later time, no new scales are genrated and the main mecanism is represented by turbulence decay. Fauconnier *et al.*, in [53], provided the spectra of a DNS of the Taylor-Green Vortex at $Re = 3000$ confirming the presence of the $-5/3$ slope in the Taylor-Green Vortex case. These results show that even if the initial state of the Taylor-Green Vortex is highly anisotropic it verifies the local isotropy hypothesis since the Kolmogorov's $k^{-5/3}$ law is only valid under this assumption. In the present case the $-5/3$ slope has to be present on a smaller range of wave number compared to [53] since the Reynolds number is lower [134].

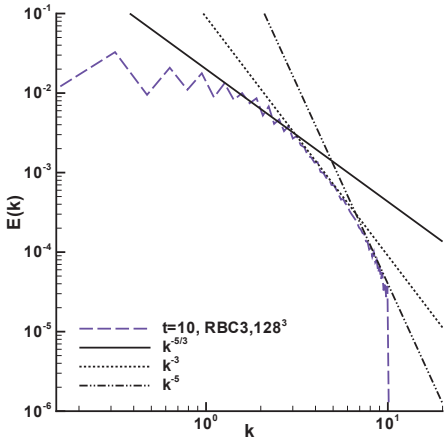


Figure V.15: Spectrum $E(k)$ of the solution computed with RBC3 on the $128^3$ mesh at $t = 10$.

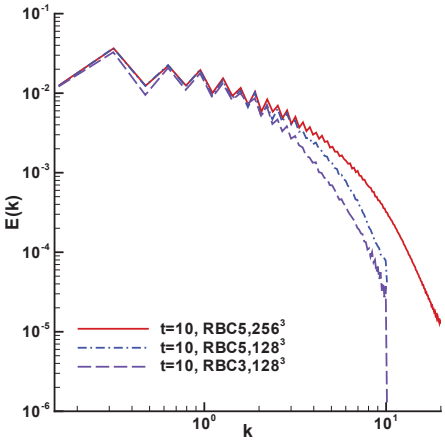


Figure V.16: Comparison of the spectrum $E(k)$ of the solutions computed with RBC3 and RBC5 on a $128^3$ mesh and RBC5 on a $256^3$ mesh at $t = 10$.

The $256^3$ computation with RBC5 is clearly not completely mesh converged since the enstrophy plot does not fit the DNS (*cf.* Fig. V.8(d)). This was expected, since we are using an LES mesh resolution. Nevertheless, the kinetic energy and its time derivative are almost converged with RBC5 on this mesh resolution (*cf.* Fig. V.7(d)). This can be explained by the fact that the kinetic energy is a second-order quantity since $E(k)$ falls rapidly for wave numbers $k$ higher than $1/\eta$, where $\eta$ is the Kolmogorov scale [49]. Here, the enstrophy is certainly underestimated since it is a higher-order moment of velocity gradient and thus is contained at smaller scales [49]. Several studies has led to this conclusion including the work of Yakhot and Sreenivasan that proposed that the finest scale that has to be resolved for a DNS are of the order of $\eta Re^{-1/4}$ [49, 168] in order to capture higer-order moments such as the enstrophy. Besides, most of the enstrophy of the turbulent fluctuant field is contained at scales of the order of the Taylor micro-scale [85].

This $256^3$ computation with RBC5 could be considered as a quasi DNS in the sense of capturing second-order moments such as the kinetic energy. Morover, the computation has been done with $256^3 \approx 1.7{\cdot}10^7$ degrees of freedom which is of the same order of $Re^{9/4} = 1600^{9/4} \approx 1.6{\cdot}10^7$. $Re^{9/4}$ corresponds to the minimum degrees of freedom needed to resolve the scales of the order of $\eta$ [168]. This is also the case in the DNS computation of Fauconnier *et al.* [53] where the number of degrees of freedom used is $384^3 = 5.6 \cdot 10^7$ which is of the same order as $Re^{9/4} = 3000^{9/4} = 6.7 \cdot 10^7$. We

have to specify that the DNS in [53] is computed with a spectral method whereas our computation is done with a finite difference method, RBC5, with good spectral properties (needing about six points per wavelentgh, *cf.* Sec. III.9).
In addition to the $-5/3$ slope, we also observe a $-3$ and a $-5$ slope in the viscous range of the computations done with RBC schemes. Figs. V.13 and V.14 show that this behavior is observable for the same scheme on different meshes and thus is not mesh dependent. Fig. V.15 shows that even for a lower order schemes, *e.g.* RBC3, we still observe this behavior. Finally, the comparison of the different spectra in Fig. V.16 show that even if RBC3 and RBC5 underestimate the kinetic energy of fine scales on the $128^3$ mesh the behavior of the RBC5 on the $256^3$ mesh seems to be mimic in the viscous range. The different slopes observed in Figs. V.13, V.14 and V.15 are investigated in detail in Fig V.17 by plotting the spectrum of $k^{5/3}E(k)$, $k^3E(k)$ and $k^5E(k)$. Even if our spectra are oscillatory we can observe a plateau in the curves corresponding to the different slopes.

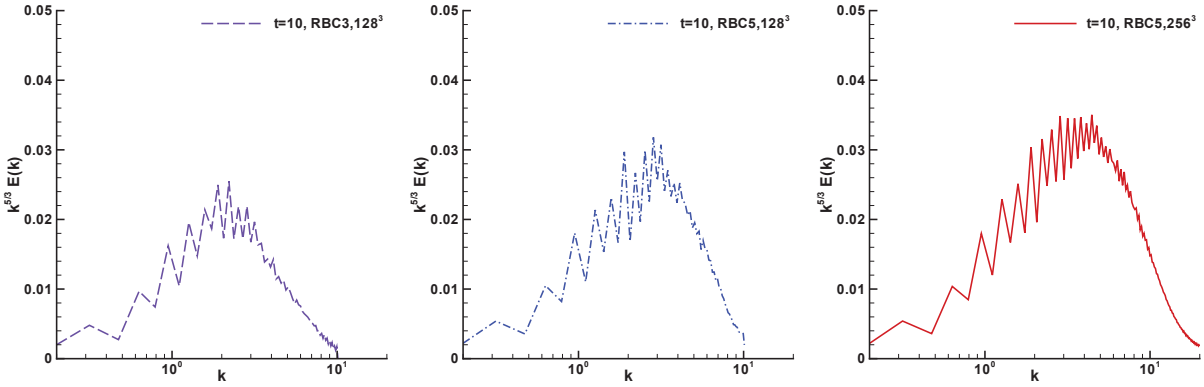


(a) $k^{5/3}E(k)$ of the solution computed with RBC3 on the $128^3$ mesh at $t = 10$.

(b) $k^{5/3}E(k)$ of the solution computed with RBC5 on the $128^3$ mesh at $t = 10$.

(c) $k^{5/3}E(k)$ of the solution computed with RBC5 on the $256^3$ mesh at $t = 10$.

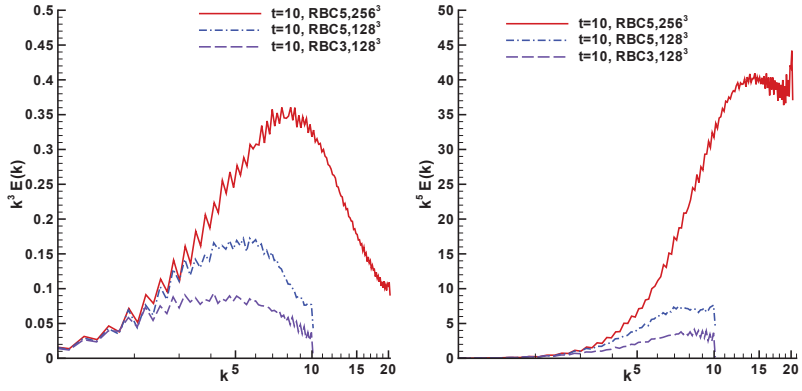


(d) $k^3E(k)$ of the solution computed with RBC3 and RBC5 on the $128^3$ mesh and RBC5 on the $256^3$ mesh at $t = 10$.

(e) $k^5E(k)$ of the solution computed with RBC3 and RBC5 on the $128^3$ mesh and RBC5 on the $256^3$ mesh at $t = 10$.

Figure V.17: Indetailed investigation of the $-5/3$, $-3$ and $-5$ slopes.

The Taylor micro-scale $\lambda$ has been defined for DNS computation by Jimenez *et al.* in [85] by

$$\lambda^2 = \frac{5\int_0^\infty E(k)dk}{\int_0^\infty k^2 E(k)dk} = \frac{5K}{\Omega}. \tag{V.4}$$

is consistent with its mono-dimensional definition [78] . This definition has been extended by Garnier *et al.* in [62] in order to compare the resolvability of several schemes. Fig. V.18 shows the time evolution of the pseudo Taylor micro-scale of our computation with RBC schemes on the different meshes. It shows that the computation with RBC5 on the $256^3$ is almost converged since it almost captures the Taylor micro-scale of the DNS. Besides it also emphasizes the mesh convergence of the schemes and the advantage of using high-order, since RBC3 results on the $128^3$ mesh are similar to the results of RBC5 on the $64^3$ mesh.

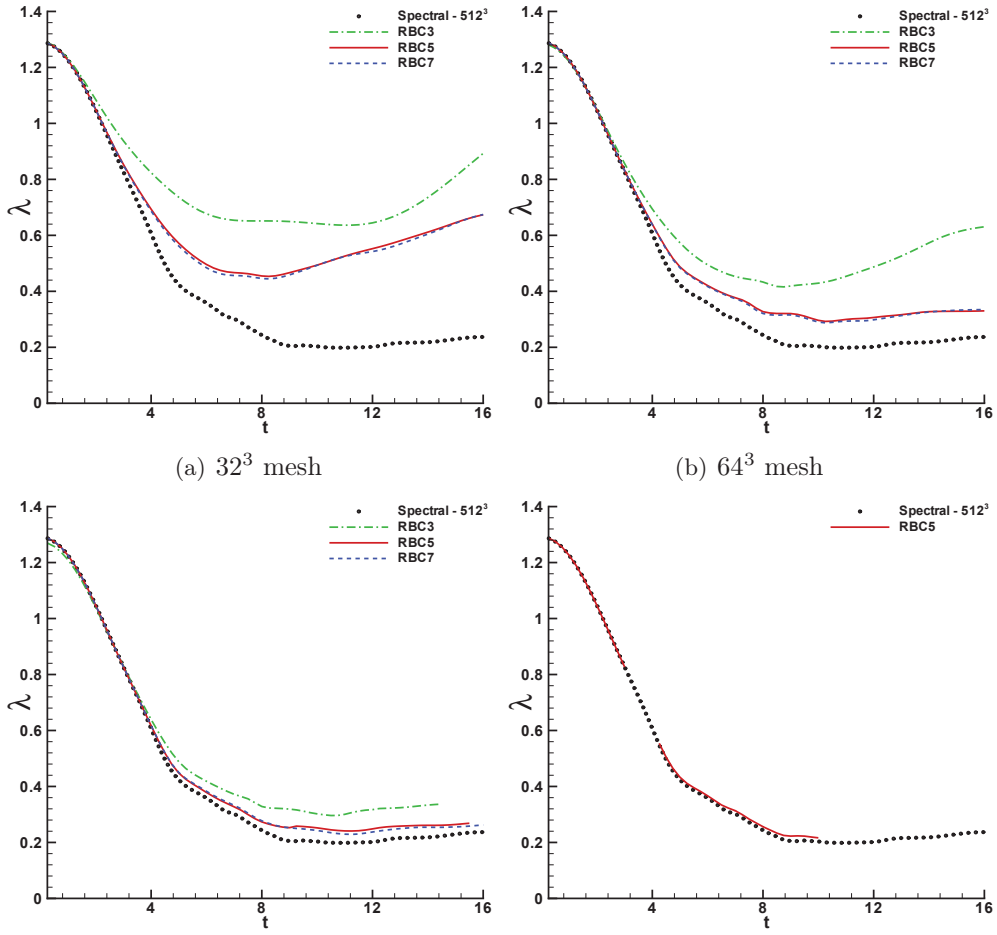


(a) $32^3$ mesh (b) $64^3$ mesh

(c) $128^3$ mesh (d) $256^3$ mesh

Figure V.18: Comparison of the time evolution of the Taylor micro-scale on a $32^3$ mesh (a), $64^3$ mesh (b), $128^3$ mesh (c) and on a $256^3$ mesh (d) with RBC schemes.

| | RBC3 | RBC5 | RBC7 |
|---|---|---|---|
| $32^3$ | $3.27\Delta$ | $2.51\Delta$ | $2.51\Delta$ |
| $64^3$ | $4.37\Delta$ | $3.02\Delta$ | $2.96\Delta$ |
| $128^3$ | $6.15\Delta$ | $5.13\Delta$ | $4.94\Delta$ |
| $256^3$ | $\times$ | $8.82\Delta$ | $\times$ |

Table V.1: Pseudo Taylor micro-scale values for RBC schemes at $t = 10$ on the $32^3$, $64^3$, $128^3$ and $256^3$ meshes with $\Delta = 2\pi/N$ ($N = 32, 64, 128, 256$).

In order to be more quantitative we compare in Table V.1 the Taylor micro-scale of different computations at time $t = 10$ in terms of the mesh spacing $\Delta = 2\pi/N$, with $N$ the number of mesh cells in one direction. It gives the number of points discretizing the Taylor micro-scale for each computation. The computation with RBC5 on the $256^3$ mesh is the only one where this number of points, 8.82, is greater than the resolvability of the scheme, 6.08 points. This results also confirms the mesh convergence of these schemes and quantify the advantage of high-order schemes.
In summary, we esteem that the preceding results are very encouraging, since they proove a good resolvabilty of RBC schemes and their capability to compute a flow with a large range of scales.

## V.3 Toward the application of RBC schemes to complex industrial flows

The application of RBC schemes to challenging industrial configurations is not straightforward. Nevertheless, a first step toward the use of these schemes in an industrial framework is the application of the third-order finite-volume RBC scheme designed in chapter IV, RBC$i$. All calculations shown in the following have been performed by using the elsA simulation software developed at ONERA [1, 33, 34]. Hereafter, we apply RBC$i$ to two increasingly realistic cases of industrial interest. The first one is a turbulent transonic flow through an isolated 2D turbine cascade, whereas the second one is a fully 3D turbine stage involving unsteady rotor/stator interaction.

### V.3.1 VKI LS-59 turbine cascade

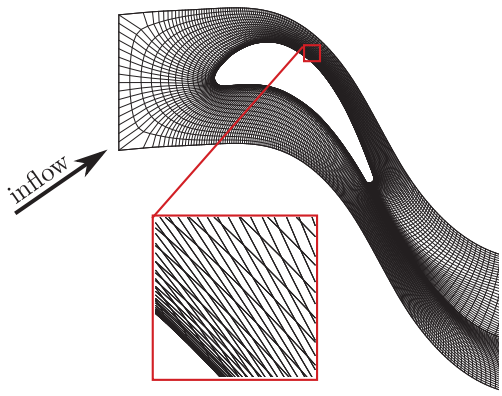


Figure V.19: VKI LS-59 turbine blade, computational grid

The VKI LS-59 is a high-loaded rotor blade with a thick, rounded trailing edge originally designed for near-sonic exit flow conditions. This rotor blade has been extensively tested in various European wind tunnels [89] and computed by several authors [14, 30, 83]. Experiments are available in a wide range of conditions, and Schlieren photographs clearly indicate the existence of vortex shedding downstream of the blade blunt trailing edge, which is responsible for an appreciable fraction of profile losses. The flow conditions considered for this study correspond to a unit exit isentropic Mach number and a Reynolds number of $7.44 \times 10^5$ based on the chord length and mean outlet velocity. The inlet flow angle is equal to 30 degrees. This choice is motivated by the fact that all numerical computations available in the literature known to the authors have been made for these conditions, for which experimental distributions of the isentropic Mach number at the wall are also available.
Unsteady two-dimensional computations are carried out using a C-grid of $384 \times 32$ cells with a conformal join along the branch cut (see Fig. V.19). The enforcing of a conformal join leads to a highly distorted mesh in the suction side region for this high-deflection blade. The unsteady computations are initialised via a preliminary steady run. For unsteady computations, the non-dimensional time step is selected in order to get approximately 30 time steps per shedding cycle. The computations are performed using the Spalart-Allmaras turbulence model.

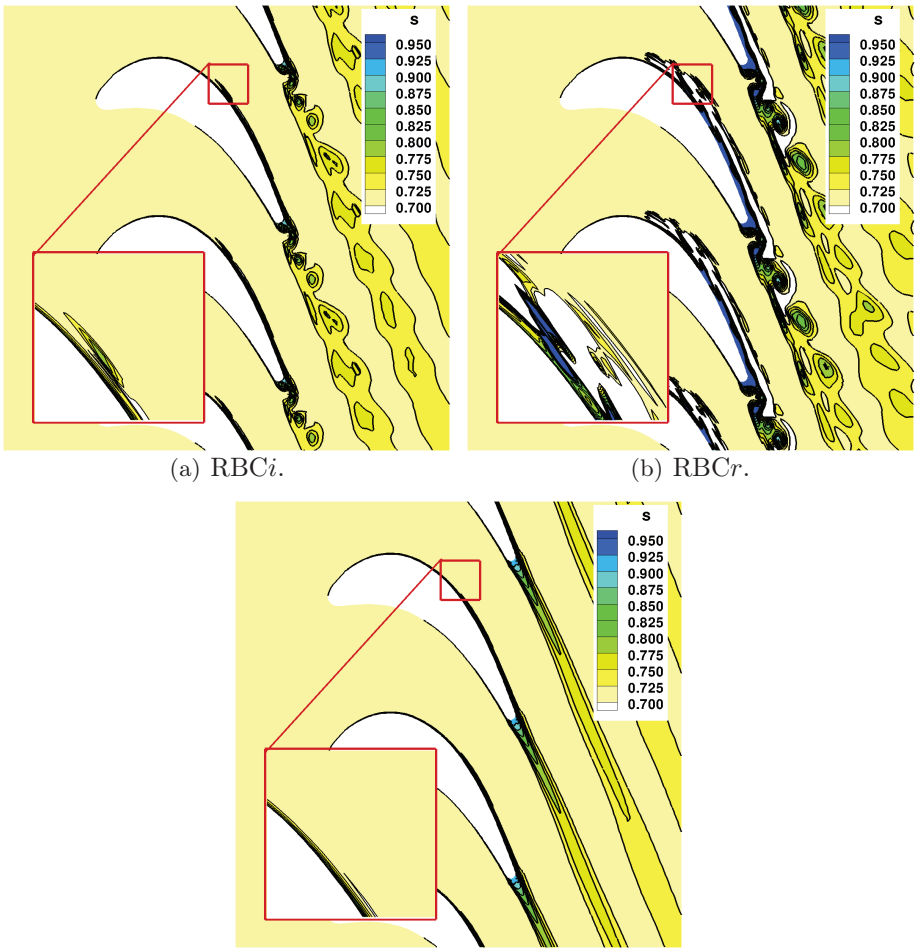


(a) RBC$i$. (b) RBC$r$.

(c) RBC2.

Figure V.20: Snapshot of the unsteady entropy field.

To investigate the importance of taking into account mesh irregularities for highly distorted grids RBC$r$ and RBC$i$ are compared with the second order RBC2. Snapshots of the unsteady entropy field computed with these three schemes are provided in Fig. V.20. Only third order schemes, RBC$r$ and RBC$i$, exhibit vortex shedding. Nevertheless, the solution of RBC$r$ exhibits non-physical features on the suction side region of the blade where the mesh is higly distorted, $cf.$ Fig. V.20(b). The solution is indeed polluted by significant spurious numerical oscillations originating from the regions of the computational domain where the grid is more severely distorted, $cf.$ Fig. V.20(b), that cannot be damped by this scheme.
Fig. V.21 provides the Fourier spectra of the blade load (tangential force acting on the blade) for RBC$i$ and RBC$r$. The computed Strouhal numbers are based on the main frequency, the isentropic outlet velocity and the thickness of the trailing edge (equal to 0.06 the axial chord for this blade). RBCi scheme returns a value of 0.24 close to the experimentally measured range [89] (0.2, 0.4), along with its harmonics. The RBC$r$ scheme returns the same Strouhal value associated to the main frequency along with a rich frequency spectrum. These additional frequencies are probably due to numerical errors introduced when mesh irregularities are not taken into account.

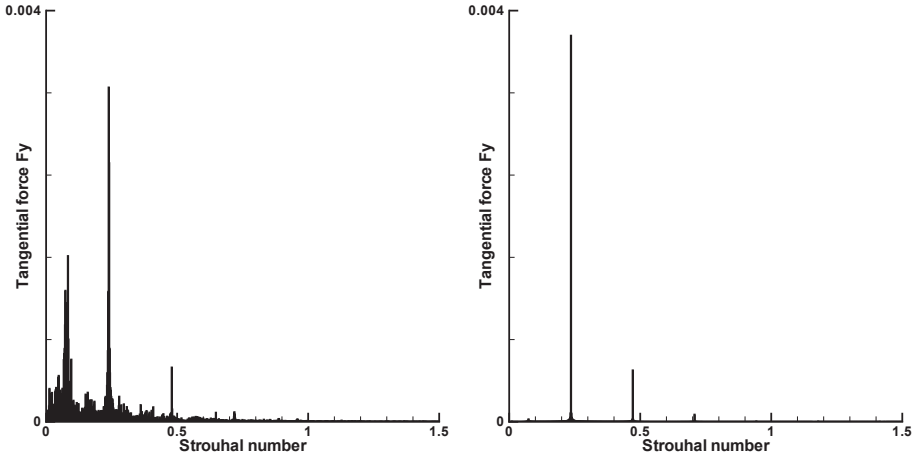


(a) RBC$r$. (b) RBC$i$.

Figure V.21: Fourier spectra of the unsteady tangential force on the blade.

Fig. V.23 displays the distributions of the isentropic Mach number at the blade's surface. The time-averaged solutions are compared to the experimental data of Kiock et al. [89]. For the second-order scheme, the time-averaged solutions can be associated to a steady solution since only the third-order schemes exhibit an unsteady solution. The rear part of the blade suction side is significantly affected by flow unsteadiness: the results of the RBCi scheme are characterised by a shock wave at the suction surface, although located more upstream than the experimental one.

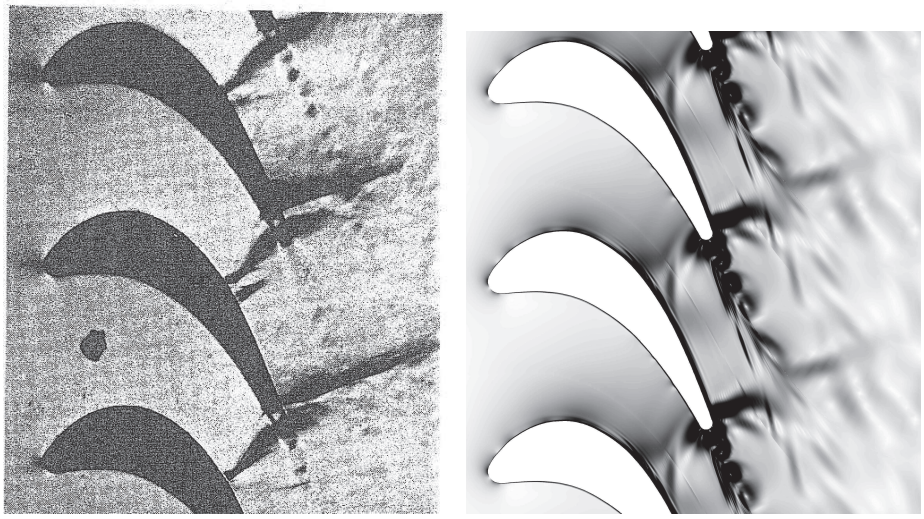

(a) Schlieren picture from [89].

(b) Snapshot of $||\nabla\rho||_2$ computed with RBC$i$.

Figure V.22: Comparison of of the aspect of RBC$i$ and experimental solutions

A snapshot of the instantaneous density gradient contours computed with RBC$i$ is provided in Fig. V.22(b). A Schlieren photograph from [89] corresponding to a slightly different exit isentropic Mach number and Reynolds number is also reported for comparison in Fig. V.22. It confirms that the RBC$i$ solution is quantitatively close to the experiment. For this reason, only the RBCi scheme is retained for the following computation.

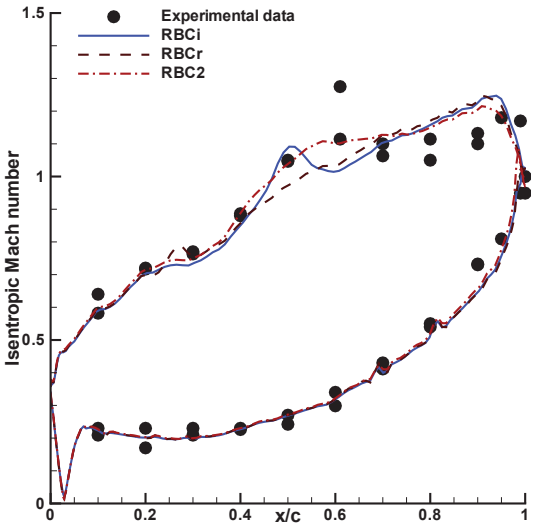


Figure V.23: Time-averaged isentropic Mach number wall distribution

### V.3.2 VKI BRITE HP turbine stage

As a final application, the RBC$i$ scheme is used to compute the BRITE HP turbine stage experimentally tested in the compression tube facility CT3 of the Von Karman Institute [46] at high vane exit Mach number (pressure ratio 5.11). This case is computed in order to demonstrate the

applicability of the proposed methodology to complex unsteady 3D cases, like a realistic turbine configuration including tip clearance.

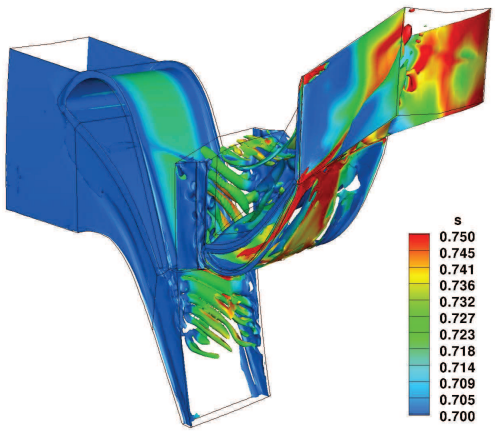


Figure V.24: Snapshot of Q criterion isosurface, Q=0.001, colored by the entropy

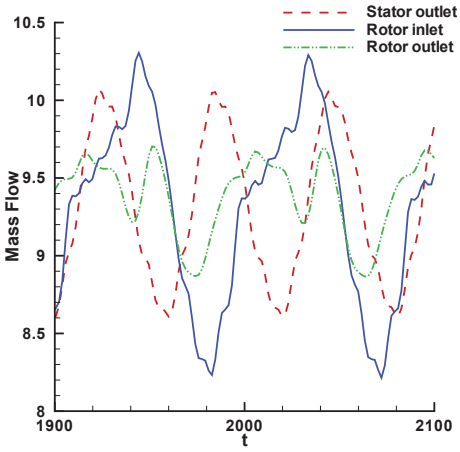


Figure V.25: Time evolution of the mass flows at stator outlet, rotor inlet and rotor outlet.

The computational grid contains approximately 3 million of points and is composed by twelve blocks: both the rotor and the stator are discretised by an O-shaped grid around the blades and three H-shaped blocks for inlet, outlet, and inter-blade regions; the tip clearance is also discretized with an O-shaped and three H-shaped grids. Unsteady computations are initialised with steady results obtained by imposing a mixing-plane inter-stage condition. The use of chorochronic periodic boundary conditions [64] allows simulating just one blade per row. The flow is modelled through the RANS equations completed by the Spalart-Allmaras transport-equation model for turbulence.

RBCi allows sharp capturing of shock waves and von Karman vortices in the blade wakes Fig. V.24 and Fig. V.27. Fig. V.24 shows a snapshot of the 3D vortex structures within the geometry with an isosurface of the Q-criterion colored by the entropy showing the 3D nature of the flow field. The complex unsteadiness of the flow with rotor/stator interaction is also captured. Fig. V.25 provides the evolution of the normalized mass flows at stator outlet, rotor inlet and rotor outlet as a function of adimensioned time. The parameters are normalized using the reference length $L_{ref} = 10^{-3}\ m$, and the speed of sound at the inlet of the stator $a_{inlet} = 416.11\ m.s^{-1}$. All these mass flows are periodic signals, the Fourier spectra of which are provided in Fig. V.26. The main frenquency at the stator outlet corresponds to the adimensioned passage frequency of rotor blades with regard to the stator, $f_{rotor} = 0.016$, with its first harmonic confirming that the rotor/stator interaction is taken into account. Similarly the main frequency observed on rotor mass flows at inlet and outlet is the adimensioned frequency of passage of stator blades with regard to the rotor, $f_{stator} = 0.011$, with its main harmonics. The high frequency peak of low magnitude at $f_{vort} = 0.116$ in the stator spectrum is likely to correspond to the vortex shedding at the trailing edge of the stator blades since it is not a multiple of blade passage frequency and its magnitude is too high. This frequency is seen by the rotor at a slightly different frequency, probably because of the chorochronic reconstruction between the rotor and the stator.

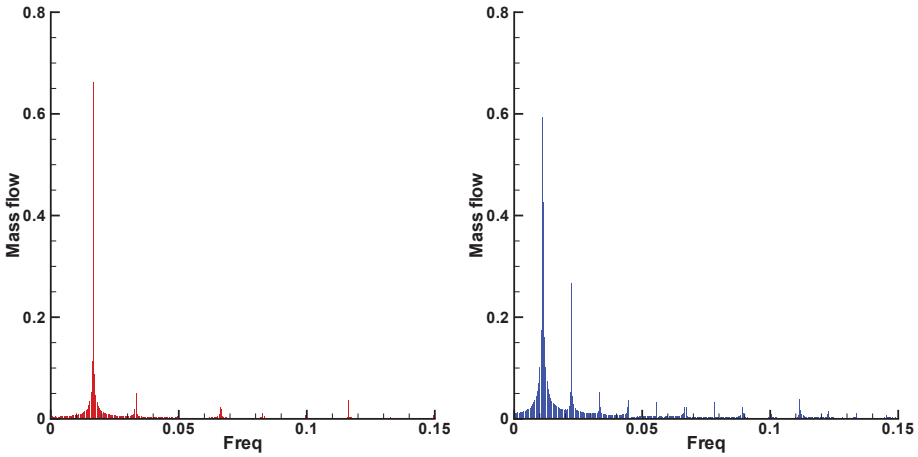


(a) Stator outlet.




(b) Rotor inlet.

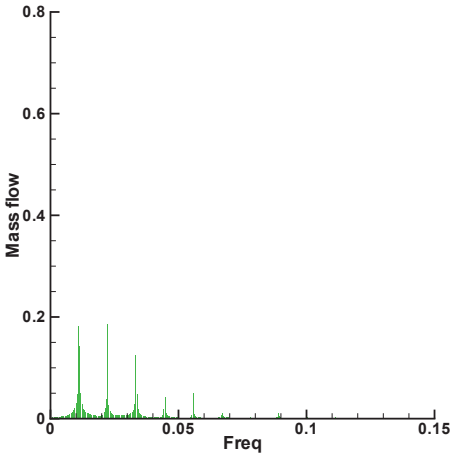


(c) Rotor outlet.

Figure V.26: Mass flow frenquency spectrum.

Fig. V.27 provides a snapshot of three slices of the configuration colored by the entropy field with isobar lines. The slices are located near the hub, at mid span of the blades and near the rotor housing. It shows that strong shocks are created at the trailing edge of the stator and rotor blades near the hub. Morover the differences between these three slices confirm that this case is highly three-dimensional with a major impact of the tip clearance on the wake of the rotor blades.

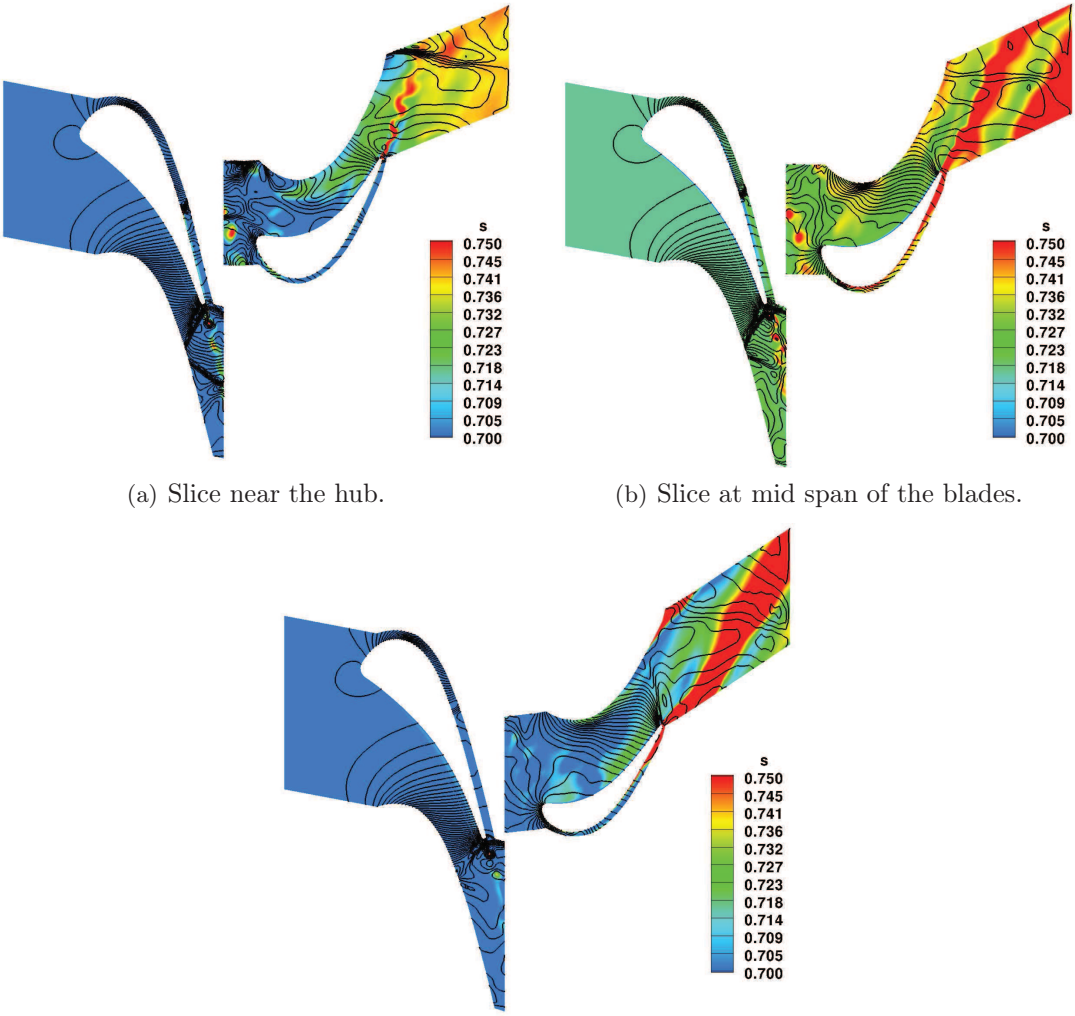


(a) Slice near the hub.

(b) Slice at mid span of the blades.

(c) Slice near the rotor housing.

Figure V.27: Snapshot of three slices colored by the entropy field with isobar lines.

## V.4 Chapter summary

In the present chapter, we went further in the understanding of RBC schemes behaviour on more realistic unsteady compressible flows. We looked into the capabilities of RBC schemes for the computation of fine scale flow structures are analysed through the computation of the inviscid and viscous Taylor-Green Vortex case. They both confirm numerically the interest of a well-designed RBC dissipation to resolve accurately fine scale flow structures. The low dissipative and dispersive errors introduced by RBC schemes make them excellent candidates for compressible turbulent flow simulations, since they combine good shock capturing (*c.f.* Sec. III.10.3) capabilities with high resolvability of fine flow structures.

Then, we went forward toward the application of RBC schemes to complex industrial flows. We used RBC$i$ on 2D and 3D unsteady turbomachinery as the VKI LS-59 turbine cascade and the VKI BRITE HP turbine stage respectively. RBC$i$ is more accurate and more robust than RBC$r$, its finite difference counterpart, when highly deformed grids are used. This enables its application to complex flows of industrial interest, like turbomachinery flows, for which the generation of

pretty smooth grids is generally a very hard task. This is demonstrated by calculations of a very severe transonic flow in the high-pressure ratio VKI BRITE HP turbine stage. The more general use of RBC schemes to industrial flows will be further investigated in future work. This will be done using a multiblock approach coupled with an overset grid technique where we can use RBC$i$ for body fitted meshes and higher order finite difference RBC schemes in Cartesian meshes.

# Chapter VI

# Conclusions and perspectives

The present work was undertaken to design and assess a family of high-order Residual-Based Compact (RBC) schemes for unsteady compressible flows with suitable dissipation properties. Specific attention was payed to the design of a numerical dissipation term ensuring stability for any flow conditions, while ensuring an accurate representation of flow structures up to mesh cutoff. This was achieved through several steps.

First of all, a comprehensive study of the dissipative properties of a general family of Residual-Based Compact schemes for 2-D and 3-D hyperbolic systems of conservation laws has been carried out. The residual-based numerical dissipation operator has been shown to be the counterpart of a high-order differential operator based on pure and mixed derivatives of even order. A general criterion (Thm. III.5.1 and III.6.1) has been established for this operator to be dissipative. Thanks to this dissipation criterion, a subset of dissipative schemes was identified from the general family. It was shown that pre-existing versions of RBC schemes for unsteady flows [73, 101], corrsponding to schemes of minimal complexity from the same family, do not always satisfy the dissipation criterion, namely for the third and seventh-order accuracy. This leads to weak instability of the fully discrete scheme. Numerical examples are used to confirm the relevancy of the proposed criterion.
Then, the dissipation and resolvability properties of RBC schemes have been quantified through a detailed analysis of their Fourier spectra for a multidimensional linear problem. The analysis of the modified wave number $\xi_\theta^*$ associated to RBC schemes of different orders proves that, for RBC schemes satifying the $\chi$-criterion, $\xi_\theta^*$ exhibit a negative imaginary part for any wave number and any choice of the CFL numbers associated to space directions. As a consequence, no solution mode can be amplified spuriously by the schemes. The modified wave number is also used to define damping and phase errors with respect to an exact transport operator. Present results confirm the $\chi$-criterion studies based on truncation error analysis and show that odd-order RBC schemes are eminently dissipative and not dispersive. For RBC schemes of higher orders (5 and 7), both dissipation and dispersion errors take very low values (less than $10^{-3}$) up to reduced wave numbers close to $\pi/2$, i.e. to the grid resolvability limit. Then, dissipation increases sharply so that higher frequencies are efficiently damped out. Moreover, thanks to their genuinely multidimensional formulation, RBC schemes conserve good dissipation and dispersion properties even for flow modes that are not aligned with the computational grid.
Numerical tests confirm the theoretical results and demonstrate the importance of a well-designed dissipation operator for numerical simulations in gas dynamics. Specifically, the present residual-based formulation ensures controlled damping of sine waves propagating along any direction with respect to the computational mesh and with any advection speed. It also allows the computation of unsteady multidimensional flows with strong shocks without any treatment for shock captur-

ing. Moreover, numerical tests for a linear advection problem confirm the theoretical results on the spectral properties of RBC schemes.

In view of computing realistic fluid flows, RBC schemes have to be extended to curvilinear meshes. Straightforward extension of RBC schemes to structured curvilinear meshes does not preserve the nominal accuracy and can lead to robustness problems. This is why a third-order finite volume Residual-Based Compact scheme for irregular structured meshes, RBC$i$, has been designed for the numerical simulation of compressible flows. This scheme takes into account mesh deformations, in such a way that it is third-order on mildly distorted structured grids and second-order on highly distorted meshes. To this purpose, suitable weighted discretisation operators are introduced. An analysis of the Fourier symbol of the proposed spatial approximation demonstrates that the resulting discretization is dissipative and then Cauchy-stable for all flow configurations. An investigation of the multidimensional modified wave number of the scheme shows that, on Cartesian grids, it is somewhat more dissipative and dispersive than its finite-difference counterpart. Specifically, the scheme dissipates more quickly ill-resolved solution modes in the transverse direction with respect to the advection velocity. This may be considered a drawback, but in practice ensures great robustness on highly distorted grids, where in any case the accuracy of the straightforward finite volume extension (RBC$r$) is lost because of grid deformations, while RBC$i$ remains high-order accurate.
Again, numerical tests confirm the theoretical results and demonstrate the importance of using a weighted scheme formulation on very irregular meshes. For all cases, RBC$i$ is more accurate and more robust than RBC$r$ when highly deformed grids are used. This enables its application to complex flows of industrial interest, like turbomachinery flows, for which the generation of pretty smooth grids is generally a very hard task. This is demonstrated by calculations of a very severe transonic flow in the high-pressure ratio VKI BRITE HP turbine stage. In term of numerical cost, RBC$i$ is more expensive than RBC$r$, essentially because of the calculation of weighed operator coefficients. On a non deforming mesh, the computational CPU time of an RBC$i$ computation is roughly 1.27 times that of an RBC$r$ computation. This is the price to pay for accuracy and robustness on irregular meshes. On the other hand, it may be expected that time savings can be made for the mesh generation task, since RBC$i$ enables high accuracy on computational grids of poor quality. In summary, present results suggest that RBCi may represent a good candidate for industrial CFD applications.

After the design and the theoretical analysis of unsteady RBC schemes, we went further in the understanding of RBC schemes behaviour on more realistic unsteady compressible flows. We looked into the capabilities of RBC schemes for the computation of fine scale flow structures through the computation of the inviscid and viscous Taylor-Green Vortex case. The results confirmed the interest of a well-designed RBC dissipation to resolve accurately fine scale flow structures. The low dissipative and dispersive errors introduced by RBC schemes make them good candidates for compressible turbulent flow simulations, since they combine good shock capturing capabilities with high resolvability of fine flow structures.
We also investigated the applicability of RBC schemes to complex industrial flows. Precisely, RBC schemes were applied to the unsteady RANS simulations of 2D and 3D turbine configurations. In both cases, the computational grids in use were highly deformed, because of the complex geometries under investigation. In such situations, taking into account mesh deformations in the very formulation of the numerical fluxes is of paramount importance to ensure robustness and to avoid the appearance of spurious oscillations, as it is observed when a straightforward extension of the numerical fluxes to curvilinear grids is used. Secondly, the numerical results show that at least third-order accuracy is required to capture the natural unsteaduness of viscous wakes

behind turbine blades. The second-order accurate RBC scheme predicts instead a steady wake.

To conclude, we have shown the advantage of high-order scheme for flows of increasing complexity. Nevertheless, some work is still required to prove the interest of higher-order methods for the numerical simulation of fluid flow of high geometrical and physical complexity, to ensure a robust behaviour of the computations, and to improve their computational efficiency. The more general use of RBC schemes to industrial flows will be further investigated in future work. An RBC$i$ FV extension of RBC5 and RBC7 could be done in future work but is not straightforward, and it is possibly very costly at high-order. An alternative to that is a multiblock approach coupled with the use of an overset grid technique such that one can use RBC$i$ for body fitted meshes and higher order finite difference RBC schemes in Cartesian meshes. Besides, there is a need for increasing the efficiency in term of computational cost of these schemes for flows governed by small time scales. In fact, the present time integration, based on the second-order backward linear multistep scheme, is not suitable for fast unsteady flow features: in this case the CFL number is limited to values of the order of 1 by physical considerations, *i.e.* by necessity of resolving correctly small time scales. Thus, performing sub-iterations to solve nonlinear systems of equations generated by such an implicit scheme (typically, at least 30 subiterations per time step are required) has a dramatic impact on computational time; on the other hand, even lower CFL numbers would be required to rule out second-order errors coming from the time integration scheme. This is not always done at present to avoid increasing further the computational cost. As a consequence, the present time integration scheme is penalizing both in terms of accuracy and efficiency. Note that this is not the case when slow unsteady flows are considered, like slow unsteadiness of the mean field in URANS: for these applications, implicit time schemes are the best choice.
To improve accuracy and efficiency for fast unsteady flow computations, a reasonable choice would be a Runge-Kutta time integration scheme. Nevertheless, direct coupling of RBC schemes with Rung-Kutta (RK) schemes would lead to the inversion of broad-band matrices at each RK stage, because of the presence of the time derivative in the RBC dissipation operator. A good option could be that of writing the dissipation at a preceding RK stage, while modifying RK coefficients to ensure the right order of accuracy in time. This kind of approach was studied by Abgrall and Ricchiuto [130] for Residual Distribution schemes.

Finally, further investigations are required to better understand the shock-capturing properties of RBC schemes. A recent analytical study [99, 100] has shown that, for steady flows, RBC schemes can provide non oscillotary shock profiles without need for limiters on the shock-capturing correction. However, further work is needed for fast unsteady flow cases. This is of particular importance in view of the application of RBC schemes to compressible turbulence. The preceding developments will ultimately allow to speed up the simulation process and improve numerical simulation capabilities over the current state-of-the-art, according to Airbus goal for "more simulation, less testing".

# Bibliography


[1] elsA. `http://elsa.onera.fr`.

[2] Europe 2020 - eu strategy for smart, sustainable and inclusive growth. `http://ec.europa.eu/europe2020`.

[3] IDIHOM. `http://www.idihom.de`.

[4] Second international workshop on high-order cfd methods. `http://www.dlr.de/as/desktopdefault.aspx/tabid-8170/13999_read-35550/`.

[5] TAU. `http://tau.dlr.de`.

[6] Flightpath 2050 europe's vision for aviation. Technical report, European commision, 2011.

[7] Saul Abarbanel and Ajay Kumar. Compact High-Order Schemes for the Euler Equations. *Journal of Scientific Computing*, 3(3):275–288, 1988.

[8] R. Abgrall. On essentially non-oscillatory schemes on unstructured meshes: Analysis and implementation. *Journal of Computational Physics*, 114(1):45–58, 1994.

[9] R. Abgrall, D. de Santis, and M. Ricchiuto. High order preserving residual distribution schemes for advection-diffusion scalar problems on arbitrary grids. *SIAM SISC*, 2013.

[10] R. Abgrall and H. Deconinck. Special issue on residual distribution schemes discontinuous galerkin schemes and adaptation. *Computers & Fluids*, 34(4-5):399–640, 2005.

[11] R. Abgrall and M. Mezine. Construction of second order accurate monotone and stable residual distribution schemes for unsteady flow problems. *Journal of Computational Physics*, 188(1):16–55, 2003.

[12] Rémi Abgrall. Residual distribution schemes: Current status and future trends. *Computers & Fluids*, 35:641–669, 2006.

[13] Rémi Abgrall, Alain Larat, M. Ricchiuto, and C. Tavé. A simple construction of very high order non-oscillatory compact schemes on unstructured meshes. *Computers & Fluids*, 38:1314–1323, August 2009.

[14] A. Arnone and R. Pacciani. Numerical investigation on wake shedding in a turbine rotor blade. *Lecture Notes in Physics*, 490:356–361, 1997.

[15] Guillaume Aubard. *Simulation des grandes echelles des instationnarites basses frequences d une interaction onde de choc / couche limite sur plaque plane*. PhD thesis, Arts et Métiers ParisTech, 2012.

[16] Guillaume Aubard, P. Stefanin-Volpiani, Xavier Gloerfelt, and J.-C. Robinet. Comparison of subgrid scale viscosity models and selective filtering strategy. *9th European Research Community on Flow, Turbulence and Combustion, ETMM9,* June 6-8, Thessaloniki, Greece, 2012.

[17] B. Aupoix. Introduction to turbulence modelling. from mixing lenth to Reynolds stress models. In *VKI Lecture series, March 22-26, 2004*, 2004.

[18] C. Bailly and C. Bogey. A family of low dispersive and low dissipatibe explicit schemes for flow and noise computations. *Journal of Computational Physics*, 194:194–214, 2004.

[19] B. S. Baldwin and H. Lomax. Thin layer approximation and algebraic model for separated turbulent flows. In *AIAA $16^{th}$ aerospace sciences meeting, Huntsville, Alabama / January 16-18, 1978*, 1978.

[20] F. Bassi, A. Crivellini, S. Rebay, and M. Savini. Discontinuous galerkin solution of the reynolds averaged navier-stokes and k-$\omega$ turbulence model equations. *Computers & Fluids*, 34:507–540, 2005.

[21] F. Bassi and S. Rebay. *GMRES discontinuous Galerkin solution of the compressible Navier-Stokes equations*, volume 11 of *Discontinuous Galerkin Methods*, pages 197–208. Springer, 1999.

[22] F. Bassi and S. Rebay. *A high-order discontinuous Galerkin method for compressible turbulent flows.* Discontinuous Galerkin Methods. Springer, 1999.

[23] F. Bassi and S. Rebay. Numerical solution of euler equations with a multi-order discontinuous finite element method. In *International Conference on Computational Fluid Dynamics, ICCFD2, Sydney, Australia, July 15-19*, 2002.

[24] F. Bassi, S. Rebay, G. Mariotti, S. Pedinotti, and M. Savini. A high-order accurate discontinuous finite element method for inviscid and viscous turbomachinery flows. In *2nd European Conference on Turbomachinery Fluid Dynamics and Thermodynamics,Antwerpen, Belgium, March 5-7, 1997*, pages 99–108, 1997.

[25] C. Benoit, G. Jeanfaivre, and E. Canonne. Synthesis of ONERA Chimera method developed in the frame of CHANCE program. In *31st European Rotorcraft Forum*, 2005.

[26] M. Berger and J. Oliger. Adaptative mesh refinement for hyperbolic partial differential equations. *Journal of Computational Physics*, 53:484–512, 1984.

[27] Hester Bijl, Mark H. Carpenter, Veer N. Vasta, and Christoper A. Kennedy. Implicit time integration schemes for unsteady compressible navier-stokes equations: laminar flow. *Journal of Computational Physics*, 179:313–329, 2002.

[28] O. J. Boelens, H. Van der Ven, B. Oskam, and A. A. Hassan. The boundary conforming discontinuous galerkin finite element approach to rotorcraft simulations. *Journal of Aircraft*, 39(5):776–785, 2002.

[29] C. Bogey, N. De Cacqueray, and C. Bailly. A shock-capturing methodology based on adaptative spatial filtering for high-order non-linear computations. *Journal of Computational Physics*, 5:1447–1465, 2009.

[30] A. Bonfiglioli, P. De Palma, G. Pascazio, and M. Napolitano. An implicit fluctuation splitting scheme for turbomachinery flows. *Journal of Turbomachinery*, 127:395–401, 2005.

[31] V. V. Borue and S. A. Orszag. Self-similar decay of three-dimensional homogeneous turbulence with hyperviscosity. *Physical Review E*, 51(2):R856–R859, 1995.

[32] M. E. Brachet, D. Meiron, S. Orszag, B. Nickel, R. Morf, and U. Frisch. The Taylor-Green vortex and fully developed turbulence. *Journal of Statistical Physics*, 34(5-6):1049–1063, 1984.

[33] L. Cambier and M. Gazaix. elsA: an efficient object-oriented solution to CFD complexity. In *40th AIAA Aerospace Science Meeting and Exhibit*, 2002.

[34] L. Cambier and J.P. Veuillot. Status of the elsA CFD software for flow simulation and multidisciplinary applications. In *48th AIAA Aerospace Science Meeting and Exhibit*, 2008.

[35] J. Chicheportchiche and X. Gloerfelt. Study of interpolation methods for high-accuracy computations on overlapping grids. *Computers & Fluids*, 68:112–133, 2012.

[36] R. F. Chisnell. The motion of a shock wave in a channel, with applications to cylindrical and spherical shock waves. *Journal of Fluid Mechanics*, 2:286–298, 1957.

[37] B. Cockburn, G. Karniadakis, and C.-W. Shu. *The development of discontinuous Galerkin methods*, volume 11 of *Discontinuous Galerkin Methods*, pages 3–50. Springer, 1999.

[38] Bernardo Cockburn, George E. Karniadakis, and Chi-Wang Shu. The develoment of discontinuous Galerkin methods. *IMA Preprint Series*, (1662), December 1999.

[39] Bernardo Cockburn and Chi-Wang Shu. Nonlinear stable compact schemes for shock calculations. *SIAM Journal of Numerical Analysis*, 31:607–627, 1994.

[40] Christophe Corre, Fabrice Falissard, and Alain Lerat. High-order residual-based compact schemes for compressible inviscid flows. *Computers & Fluids*, 36:1567–1582, 2007.

[41] Christophe Corre, Grégoire Hanss, and Alain Lerat. A residual-based compact scheme for the unsteady compressible Navier-Stokes equations. *Computers & Fluids*, 34:561–580, 2005.

[42] Christophe Corre and Alain Lerat. High-order residual-based compact schemes for advection-diffusion problems. *Computers & Fluids*, 37:505–519, 2008.

[43] Jared S. Cox, Kenneth S. Brentner, and Christopher L. Rumsey. Computation of vortex shedding and radiated sound for a circular cylinder: subcritical to transcritical reynolds numbers. *Theoretical and Computational Fluid Dynamics*, 12:233–253, 1998.

[44] G. Dahlquist. A special stability problem for linear multistep methods. *BIT*, 3:27–43, 1963.

[45] Pascal Joubert de la Motte. *Schéma à pas de temps caractéristique pour l'aérodynamique transsonique et conception aéroélastique optimale d'aile de grand allogement*. PhD thesis, Arts et Métiers ParisTech, 2007.

[46] R. Denos, T. Arts, G. Paniagua, V. Michelassi, and F. Martelli. Investigation of the unsteady rotor aerodymics in a transonic turbine stage. *Journal of turbomachinery*, 123, 2001.

[47] K. D. Devine and J. E. Flaherty. Dynamic load balancing for parallel finite element methods with adaptive h- and p-refinement. Technical Report 94-27, Rensselaer Polytechnic Institute, New York, 1994.

[48] K. D. Devine and J. E. Flaherty. Parallel adaptive hp-refinement techniques for conservation laws. *Applied Numerical Mathematics*, 20:367–386, 1996.

[49] D. A. Donzis, P. K. Yeung, and K. R. Sreenivasan. Dissipation and enstrophy in isotropic turbulence: Resolution effects ansd scaling in direct numerical simulations. *Physics of Fluids*, 20:045108, 2008.

[50] Xi Du. *Schéma d'ordre élevé basé sur le résidu pour la simulation numérique d'écoulements compressibles en maillages non-structurés*. PhD thesis, Arts et Métiers ParisTech, 2010.

[51] Xi Du, Christophe Corre, and Alain Lerat. A third-order finite-volume residual-based scheme for the 2D Euler equations on unstructured grids. *Journal of Computational Physics*, 2011.

[52] J.A. Ekaterinaris. High-order accurate, lownumerical diffusion methods for aerodynamics. *Progress in Aerospace Sciences*, 41:192–300, 2005.

[53] D. Fauconnier, C. Bogey, and E. Dick. On the performance of relaxation filtering for large-eddy simulation. *Journal of Turbulence*, 14(1):22–49, 2013.

[54] Dieter Fauconnier, Chris De Langhe, and Erik Dick. Construction of explicit and implicit dynamic finite difference schemes and application to the large-eddy simulation of the Taylor-Green vortex. *Journal of Computational Physics*, 228:8053–8084, 2009.

[55] K.J. Fidkowski and D.L. Darmofal. Adjoint-based h-p adaptive discontinuous galerkin methods for the compressible euler equations. In *47th AIAA Aerospace Sciences Meeting Including The New Horizons Forum and Aerospace Exposition, Orlando, Florida*, 2009.

[56] O. Friedrich. Weighted essentially non-oscillatory schemes for the interpolation of mean values on unstructured meshes. *Journal of Computational Physics*, 144(1):194–212, 1996.

[57] J. E. Fromm. A method for reducing dispersion in conservative difference schemes. *Journal of Computational Physics*, 3:176–189, 1968.

[58] D. Fu and Y. Ma. A high order accurate difference scheme for complex flow fields. *Journal of Computational Physics*, 134:1–15, 1997.

[59] D. V. Gaitonde and J.S. Shang. Optimized compact-difference-based finite volume schemes for linear wave phenomena. *Journal of Computational Physics*, 138:617–643, 1997.

[60] L. Gamet, F. Ducros, F. Nicoud, and T. Poinsot. Compact finite difference schemes on non-uniform meshes. application to direct numerical simulation of compressible flows. *International Journal for Numerical Methods in Fluids*, 29:159–191, 1999.

[61] E. Garnier, N. Adams, and P. Sagaut. *Large-eddy simulation for compressible flows*. Springer-Verlag, 2009.

[62] Eric Garnier, Michele Mossi, Pierre Sagaut, Pierre Comte, and Michelle Deville. On the use of shock-capturing schemes for large-eddy simulation. *Journal of Computational Physics*, 153:273–311, 1999.

[63] G. Gassner, F. Lorcher, and C.-D. Munz. A discontinuous galerkin scheme based on a space-time expansion. ii. viscous compressible flow in multi space dimensions. *Journal of Scientific Computing*, 34:260–2896, 2008.

[64] G. A. Gerolymos, G. Michon, and J. Neubauer. Analysis and application of chorochronic periodicity in turboma- chinery rotor/stator interaction computations. *Journal of Propulsion and Power*, 18:1139–1152, 2002.

[65] J. Gillyboeuf, P. Mansuy, and S. Pavsic. Two new Chimera methods : application to missile separation. In *33rd AIAA Aerospace Sciences Meeting and Exhibit*, 1995.

[66] S.K. Godunov. A finite difference method for the numerical computation of discontinuous solutions of the equations of fluid dynamics. *Mat Sbornik*, 47:271–90, 1959.

[67] Karim Grimich, Paola Cinnella, and Alain Lerat. Analysis of high-order residual-based dissipation for unsteady compressible flows. In *7th International Conference on Computational Fluid Dynamics (ICCFD)*, July 2012.

[68] Karim Grimich, Paola Cinnella, and Alain Lerat. Spectral properties of high-order residual-based compact schemes for unsteady compressible flows. *Journal of Computational Physics*, 252:142–162, 2013.

[69] Karim Grimich, Cedric Content, and Paola Cinnella. ILES computations of the Taylor Green Vortex at Re=1600. In *Second International Workshop on High-Order CFD Methods, May 27 - 28, 2013 at NH Hotel Köln City*. DLR, AIAA and AFOSR, 2013.

[70] Karim Grimich, Bertrand Michel, Paola Cinnella, and Alain Lerat. Generalized finite volume formulation of a third-order residual-based compact scheme for unsteady flow computations. *Computers & Fluids*, 2013.

[71] Karim Grimich, Pierre-Yves Outtier, Paola Cinnella, and Alain Lerat. Assessment of a fifth-order residual-based compact scheme for steady and unsteady compressible flows. In *6th European Congress on Computational Methods in Applied Sciences and Engineering, ECCOMAS 2012; Vienna; Austria; 10-14 September 2012*, pages 3111–3124, 2012.

[72] F. Haider, P. Brenner, B. Courbet, and J.-P. Croisille. Efficient implementation of high order reconstruction in finite volume methods. In *Finite Volumes for Complex Applications VI Problems & Perspectives*, volume 4, pages 553–560, 2011. Springer Proceedings in Mathematics.

[73] Grégoire Hanss. *Schémas numériques compacts basés sur le résidu en maillage irrégulier pour les équations de Navier-Stokes en compressible*. PhD thesis, Arts et Métiers ParisTech, 2002.

[74] A. Harten, B. Engquist, S. Osher, and S. Chakravarty. Uniformly high order accurate essentially non-oscillatory schemes. iii. *Journal of Computational Physics*, 71:231–303, 1987.

[75] R. Hartmann. Error estimation and adjoint based refinement for an adjoint consistent dg discretisation of the compressible euler equations. *International Journal of Computing Science and Mathematics*, 1:207–220, 2007.

[76] Stefan Hickel, Nikolaus A. Adams, and J. Andrzej Domaradzki. An adaptative local deconvolution method for implicit les. *Journal of Computational Physics*, 213:413–436, 2006.

[77] K. Hillewaert. PhD thesis, Universite Catholique de Louvain La neuve, 2012.

[78] J. O. Hinze. *Turbulence*. McGraw-Hill, New York, 1975.

[79] Richard S. Hirsh. High order accurate difference solutions of fluid mechanics problems by a compact differencing technique. *Journal of Computational Physics*, 19(1):90–109, september 1975.

[80] Hu and C.-W. Shu. Weighted essentially non-oscillatory schemes on triangular meshes. *Journal of Computational Physics*, 150:97–127, 1999.

[81] Ying Huang. *Décentrement par matrice de pas de temps caractéristique pour le calcul d'écoulements compressibles instationnaires dans les turbomachines*. PhD thesis, Arts et Métiers ParisTech, 1995.

[82] Ying Huang and Alain Lerat. Second-Order Upwinding through a Characteristic Time-Step Matrix for Compressible Flow Calculations. *Journal of Computational Physics*, 142:445–472, 1998.

[83] M. Inoue and M. Furukawa. *Numerical methods for flow calculations in turbomachines*. VKI lecture Series 1994-2006. VKI, 1994.

[84] Guang-Shan Jiang and Chi-Wang Shu. Efficient implementation of weighted eno schemes. *Journal of Computational Physics*, 126:202–228, 1996.

[85] Javier Jimenez, Alan A. Wray, Philip G. Saffman, and Robert S. Rogallo. The structure of intense vorticity in isotropic turbulence. *Journal of Fluid Mechanics*, 255:65–90, 1993.

[86] W. P. Jones and B. E. Launder. The prediction of laminarization with two equation model of turbulence. *International Journal of Heat and Mass Transfer*, 15(2):301–314, 1972.

[87] W. P. Jones and B. E. Launder. The calculation of low Reynolds-number phenomena with two-equation model of turbulence. *International Journal of Heat and Mass Transfer*, 16(6):1119–1130, 1973.

[88] R. Kannan. High order spectral volume and spectral difference methods on unstructured grids. *Graduate Theses and Dissertation*, 2008. Paper 11264.

[89] R. Kiock, F. Lehthaus, N. C. Baines, and C. H. Sieverding. The transonic flow through a plane turbine cascade as measured in four European wind tunnels. *Journal of Engineering for Gas Turbines and Power*, 108:277–285, 1986.

[90] Thibaud Kloczko. *Développement d'une méthode implicite sans matrice pour la simulation 2D-3D des écoulements compressibles et faiblement compressibles en maillages non-structurés.* PhD thesis, Arts et Métiers ParisTech, 2006.

[91] M.H. Kobayashi. On a class of padé finite volume methods. *Journal of Computational Physics*, 156:137–180, 1999.

[92] N. Kroll, H. Bieler, H. Deconinck, V. Couallier, H. Van der Ven, and K. Sorensen. *ADIGMA - A European Initiative on the Development of Adaptive Higher-Order Variational Methods for Aerospace Applications*. Notes on Numerical Fluid Mechanics and Multidisciplinary Design. Springer, 2010.

[93] Pijush K. Kundu, Ira M. Cohen, and Howard H. Hu. *Fluid Mechanics*. Academic Press, 2004.

[94] C. Lacor, S. Sminorv, and M. Baelmans. A finite volume formulation of compact central schemes on arbitrary structured meshes. *Journal of Computational Physics*, 198:535–566, 2004.

[95] J. D. Lambert. *Numerical methods for ordinary differential systems: the initial value problem*. J. Wiley edition, 1991.

[96] B. Landmann, M. Kessler, S. Wagner, and E. Kramer. A parallel discontinuous galerkin code for laminar and turbulent flows. *Computers & Fluids*, 37:427–438, 2008.

[97] Tobias Leicht and Ralf Hartmann. Error estimation and anisotropic mesh refinement for 3d aerodynamic flow simulations. *Journal of Computational Physics*, 229:7344–7360, 2010.

[98] Sanjiva K. Lele. Compact finite difference schemes with spectral-like resolution. *Journal of Computational Physics*, 103:16–42, 1992.

[99] Alain Lerat. Analysis of dicrete shock profiles of high-order compact schemes. In *EUROPEAN WORKSHOP on High Order Nonlinear Numerical Methods for Evolutionary PDEs (HONOM 2013) , March 18-22, 2013.* HONOM, 2013.

[100] Alain Lerat. Steady discrete shocks of high-order rbc schemes. *Journal of Computational Physics*, 2013. http://dx.doi.org/10.1016/j.jcp.2013.06.030.

[101] Alain Lerat, Paola Cinnella, Bertrand Michel, and Fabrice Falissard. High-order residual-based compact schemes for aerodynamics and aeroacoustics. *Computers & Fluids*, 61:31–38, 2012.

[102] Alain Lerat and Christophe Corre. A Residual-Based Compact Scheme for the Compressible Navier-Stokes Equations. *Journal of Computational Physics*, 170:642–675, 2001.

[103] Alain Lerat and Christophe Corre. Residual-based compact schemes for multidimensional hyperbolic systems of conservation laws. *Computers & Fluids*, 31:639–661, 2002.

[104] Alain Lerat and Christophe Corre. *Higher order residual-based compact schemes on structured grids*, chapter CFD-higher order discretization methods, pages 1–111. 34th Comput. Fluid Dyn. Course, von Karman Institute for Fluid Dynamics. VKI LS 2006-1, 2006.

[105] Alain Lerat, Christophe Corre, and Grégoire Hanss. *Efficient high-order schemes on non-uniform meshes for multi-dimensional compressible flows*, volume Frontiers of Computational Fluid Dynamics 2002, chapter 6, pages 89–112. World Scientific Publishing Company, 2002.

[106] Alain Lerat, Karim Grimich, and Paola Cinnella. On the design of high order residual-based dissipation for unsteady compressible flows. *Journal of Computational Physics*, 235:32–51, 2013.

[107] Marcel Lesieur. *Turbulence in fluids*, volume 84. Springer, 2008.

[108] Marcel Lesieur and Olivier Metais. New trends in large-eddy simulations of turbulence. *Annual Review of Fluid Mechanics*, 28:45–82, 1996.

[109] X.-D. Liu, S. Osher, and T. Chan. Weighted essentially non-oscillatory schemes. *Journal of Computational Physics*, 115(1):200–212, 1994.

[110] Y. Liu, M. Vinokur, and Z. J. Wang. Discontinuous spectral difference method for conservation laws on unstructured grids. *Journal of Computational Physics*, 216:780–801, 2006.

[111] Y. Liu, M. Vinokur, and Z. J. Wang. Spectral (finite) volume method for conservation laws on unstructured grids V: Extension to three-dimensional systems. *Journal of Computational Physics*, 212(2):454–472, 2006.

[112] R.W. MacCormack and A.J. Paullay. Compuational effinciency achieved by time-splitting of finite-difference operators. *AIAA Paper*, pages 72–154, 1972.

[113] R.W. MacCormack, A.W. Rizzi, and M. Inouye. *Steady supersonic flowfields with embendded subsonic regions.*, pages 424–47. Academic Press, 1976.

[114] O. Marsden, C. Bogey, and C. Bailly. High-order curvilinear simulations of flows around non-cartesian bodies. *Journal of Computational Acoustics*, 13:731–748, 2005.

[115] F. R. Menter. Two-equation eddy-viscosity turbulence models for engineering applications. *AIAA Journal*, 32(8):1598–1605, 1994.

[116] Bertrand Michel. *Contribution à la simulation numérique efficace des écoulements dans les prises d'air supersoniques.* PhD thesis, Arts et Métiers ParisTech, 2004.

[117] Bertrand Michel, Paola Cinnella, and Alain Lerat. Multiblock residual-based compact schemes for the computation of complex turbomachinery flows. *International Journal of Engineering Systems Modelling and Simulation*, 3, 2011.

[118] R. Mittal and S. Balachandar. Effect of threedimensionality on the lift and drag of nominally two dimensional cylinders. *Physics of Fluids*, 7:1841–1865, 1995.

[119] R. H. Ni. A multiple grid scheme for solving the euler equations. *AIAA Journal*, (20):1565–1571, 1981.

[120] S. A. Orszag and M. Israeli. Numerical Simulation of Viscous Incompressible Flows. *Annual Review of Fluid Mechanics*, 6:281–318, January 1974.

[121] Pierre-Yves Outtier and Paola Cinnella. Multi-block overset implementation of high-order residual-based compact schemes for compressible aerodynamics. In *EUROPEAN WORKSHOP on High Order Nonlinear Numerical Methods for Evolutionary PDEs (HONOM 2013) , March 18-22, 2013.* HONOM, 2013.

[122] Pierre-Yves Outtier, Cedric Content, Paola Cinnella, and Bertrand Michel. The high-order dynamic computational laboratory for cfd research and applications. In *21st AIAA Conference, San Diego, June 2013*, 2013.

[123] J.M.C. Pereira, M.H. Kobayashi, and J.C.F. Pereira. A fourt-order accurate finite volume compact method for incompressible navier–stokes solutions. *Journal of Computational Physics*, 167:217–243, 2001.

[124] Stephanie Peron and Christophe Benoit. Automatic off-body overset adaptive cartesian mesh method based on an octree approach. *Journal of Computational Physics*, 232:153–173, 2013.

[125] P. Persson and J. Peraire. Newton-gmres preconditioning for discontinuous galerkin discretisations of the navier-stokes equations. *Journal of Scientific Computing*, 30:2709–2733, 2008.

[126] S. Pope. *Turbulent flows*. Cambridge University Press, 2000.

[127] Stephen B. Pope. *Turbulent flows*. Cambridge University Press, 2000.

[128] A. Rezgui, P. Cinnella, and A. Lerat. Third-order finite volume schemes for euler computations on curvilinear meshes. *Computers and Fluids*, 30:875–901, 2001.

[129] Ali Rezgui. An analysis of accuracy and convergence of finite volume methods. *Computational Fluid Dynamics Journal*, 8(3):369–377, 1999.

[130] M. Ricchiuto and R. Abgrall. Explicit runge-kutta residual distribution schemes for time dependent problems: econd order case. *Computers & Fluids*, 229:5653–5691, 2010.

[131] M. Ricchiuto, N. Villedieu, R. Abgrall, and H. Deconinck. On uniformly high-order accurate residual distribution schemes for advection diffusion. *Journal of Computational Applied Mathematics*, (2):547–556, 2008.

[132] A.W. Rizzi and M. Inouye. A time-split finite-volume technique for three-dimensional blunt-body flow. *AIAA Journal*, 11:1478–85, 1973.

[133] P. L. Roe. Characteristic-based schemes for the euler equations. *Annual Review of Fluid Mechanics*, (18), 337-365.

[134] Seyed G. Saddoughi and Srinivas V. Veeravalli. Local isotropy in turbulent boundary layers at high reynolds number. *Journal of Fluid Mechanics*, 268:333–372, 1994.

[135] A. Sadiki, A. Maltsev, B. Wegner, F. Flemming, A. Kempf, and J. Janicka. Usteady methods (URANS and LES) for simulation of combustion systems. *International Journal of Thermal Sciences*, pages 760–773, 2006.

[136] Pierre Sagaut, S. Deck, and M. Terracol. *Multiscale and multiresolution approaches in turbulence*. Imperial College Press, 2006.

[137] Olivier Saunier. *Méthode d'adaptation de maillages cartésiens basée sur des schémas d'ordre élevé pour les équations d'Euler d'un fluide compressible. Application aux pales de rotor d'hélicoptère*. PhD thesis, Arts et Métiers ParisTech, 2008.

[138] Adrian Sescu, Ray Hixon, and Abdollah A. Afjeh. Multidimensional optimization of finite difference schemes for computational aeroacoustics. *Journal of Computational Physics*, 227:4563–4588, 2008.

[139] Scott E. Sherer and James N. Scott. High-order compact finite-difference methods on general overset grids. *Journal of Computational Physics*, 210:459–496, 2005.

[140] Chi-Wang Shu, Wai-Sun Don, David Gottlieb, Oleg Schilling, and Leland Jameson. Numerical convergence study of nearly incompressible, inviscid Taylor-Green vortex flow. *Journal of Scientific Computing*, 24(1), July 2005.

[141] B. R. Smith. The *k-kl* turbulence model and wall layer model for compressible flows. In *AIAA, Fluid Dynamics, Plasma Dynamics and Lasers Conference, 21 st, Seattle, WA. 1990*, 1990.

[142] P. Spalart. Reflexion on RANS modelling. Technical report, Boeing Commercial Airplanes, 2009.

[143] Y. Sun, Z. J. Wang, and Y. Liu. Spectral (finite) volume method for conservation laws on unstructured grids III: Extension to viscous flow. *Journal of Computational Physics*, 215(1):41–58, 2006.

[144] C. Tam and F. Hu. An optimized multi-dimensional interpolation scheme for computational aeroacoustics applications using overset grids. *AIAA Paper 2004-2812*, 2004.

[145] C. Tam and K. Kurbatskii. A wavenumber based extrapolation and interpolation method for use in conjunction with high-order finite difference schemes. *Journal of Computational Physics*, 157(2):588–617, 2000.

[146] Christopher K. W. Tam and Jay C. Webb. Dispersion-Relation-Preserving Finite Difference Schemes for Computational Acoustics. *Journal of Computational Physics*, 107:262–281, 1993.

[147] Ben Thornber, Andrew Mosedale, and Dimitris Drikakis. On the implicit large eddy simulations of homogeneous decaying turbulence. *Journal of Computational Physics*, 226:1902–1929, 2007.

[148] A. I. Tolstykh. *High accuracy non-centered compact difference schemes for fluid dynamics applications*. World Scientific, Singapore, 1994.

[149] Eli Turkel. Phase error and stability of second order methods for hyperbolic problems. I. *Journal of Computational Physics*, 15:226–250, 1974.

[150] M. Vinokour. An analysis of finite-difference and finite volume formulations of conservation laws. *Journal of Computational Physics*, 81:1–52, 1989.

[151] M. Visbal and D. V. Gaitonde. Compact finite difference schemes on non-uniform meshes. application to direct numerical simulation of compressible flows. *AIAA Journal*, 37:1231–1239, 1999.

[152] M. Visbal and D. V. Gaitonde. On the use of higher-order finite-difference schemes on curvilinear and deforming meshes. *Journal of Computational Physics*, 181:155–185, 2002.

[153] M. Visbal and D. Rizzetta. Large-eddy simulation on curvilinear grids using compact differencing and filtering schemes. *ASME Journal of Fluids Engineering*, 124:836–847, 2002.

[154] M. R. Visbal and D. V. Gaitonde. High-order accurate methods for complex unsteady subsonic flows. *AIAA Journal*, 37:1231–1239, 1999.

[155] Z. J. Wang. Spectral (finite) volume method for conservation laws on unstructured grids. basic formulation: Basic formulation. *Journal of Computational Physics*, 178(1):210–251, 2002.

[156] Z. J. Wang. High-order methods for the euler and navier–stokes equations on unstructured grids. *Progress in Aerospace Sciences*, 43:1–41, 2007.

[157] Z. J. Wang. High-order methods for the euler and navier–stokes equations on unstructured grids. *Progress in Aerospace Sciences*, 43:1–41, 2007.

[158] Z. J. Wang, Krzysztof Fidkowski, Remi Abgrall, Francesco Bassi, Doru Caraeni, Andrew Cary, Herman Deconinck, Ralf Hartmann, H. T. Huynh, Norbert Kroll, Georg May, Per-Olof Persson, Bram van Leer, and Miguel Visbal. High-order cfd methods: current status and perspective. *International Journal For Numerical Methods in Fluids*, (00):1–42, 2012.

[159] Z. J. Wang and Y. Liu. Spectral (finite) volume method for conservation laws on unstructured grids: II. Extension to two-dimensional scalar equation. *Journal of Computational Physics*, 179(2):665–697, 2002.

[160] Z. J. Wang and Y. Liu. Spectral (finite) volume method for conservation laws on unstructured grids III: One-dimensional systems and partition optimization. *Journal of Scientific Computing*, 20(1):137–157, 2004.

[161] Z. J. Wang, L. Zhang, and Y. Liu. Spectral (finite) volume method for conservation laws on unstructured grids IV: extension to two-dimensional systems. *Journal of Computational Physics*, 194(2):716–741, 2004.

[162] G. B. Whitham. On the propagation of shock waves through regions of non uniform area or flow. *Journal of Fluid Mechanics*, 4:337–360, 1958.

[163] David C. Wilcox. *Turbulence Modeling for CFD*. DCW industries, 2006.

[164] O. B. Wildlund. A note on unconditionally stable linear multistep methods. *BIT*, 7:65–70, 1967.

[165] C. H. K. Williamson. Vortex dynamics in the cylinder wake. *Annual Review of Fluid Mechanics*, 28:477–539, 1996.

[166] H. C. Yee. Explicit and implicit multidimensional compact high-resolution shock-capturing methods: formulation. *Journal of Computational Physics*, 131:216–232, 1997.

[167] H.C. Yee, M. Vinokur, and M.J. Djomehri. Entropy Splitting and Numerical Dissipation. *Journal of Computational Physics*, 162:33–81, Jully 2000.

[168] Victor Ykhot and Katepalli R. Sreenivasan. Anomalous scaling of structure functions and dynamic constraint on turbulence simulations. *Journal of Statistical Physics*, 121(516), 2005.

## SCHEMAS COMPACTS BASES SUR LE RESIDU D'ORDRE ELEVE POUR DES ECOULEMENTS COMPRESSIBLES INSTATIONNAIRES. Application à de la capture de fines échelles.

**RESUME :** Les solveurs de calcul en mécanique des fluides numérique (solveurs CFD) ont atteint leur maturité en termes de précision et d'efficacité de calcul. Toutefois, des progrès restent à faire pour les écoulements instationnaires surtout lorsqu'ils sont régis par de grandes structures cohérentes. Pour ces écoulements, les solveurs CFD actuels n'apportent pas de solutions assez précises à moins d'utiliser des maillages très fins. De plus, la haute précision est une caractéristique cruciale pour l'application des stratégies avancées de simulation de turbulence, comme la Simulation des Grandes Echelles (LES). Afin d'appliquer les méthodes d'ordre élevé pour les écoulements instationnaires complexes plusieurs points doivent être abordés dont la robustesse numérique et la capacité à gérer des géométries complexes. Dans cette thèse, nous étudions une famille d'approximations compactes qui offrent une grande précision non pour chaque dérivée spatiale traitée séparément mais pour le résidu r complet, c'est à dire la somme de tous les termes des équations considérées. Pour des problèmes stationnaires résolus par avancement temporelle, r est le résidu à l'état stationnaire ne comprenant que des dérivées spatiales; pour des problèmes instationnaires r comprend également la dérivée temporelle. Ce type de schémas sont appelés schémas Compacts Basés sur le Résidu (RBC). Plus précisément, nous développons des schémas RBC d'ordre élevé pour des écoulements instationnaires compressibles, et menons une étude approfondie de leurs propriétés de dissipation. Nous analysons ensuite les erreurs de dissipation et la dispersion introduites par les schémas RBC afin de quantifier leur capacité à résoudre une longueur d'onde donnée en utilisant un nombre minimal de points de maillage. Les capacités de la dissipation de RBC à drainer seulement l'énergie aux petites échelles sous-résolues sont également examinées en vue de l'application des schémas RBC pour des simulations LES implicites (ILES). Enfin, les schémas RBC sont étendus à la formulation de type volumes finis (FV) afin de gérer des géométries complexes. Une formulation FV des schémas RBC d'ordre trois préservant une précision d'ordre élevé sur des maillages irréguliers est présentée et analysée. Des applications numériques, dont la simulation d'écoulements instationnaires complexes de turbomachines régis par les équations de Navier-Stokes moyennées et des simulations ILES d'écoulements turbulents dominés par des structures cohérentes dynamiques ou en décroissance, confirment les résultats théoriques.

**Mots clés :** schéma compact basé sur le résidu, ordre élevé, instationnaire, méthode numérique.

## HIGH-ORDER RESIDUAL BASED COMPACT SCHEMES FOR UNSTEADY COMPRESSIBLE FLOWS. Application to scale resolving simulations.

**ABSTRACT :** Computational Fluid Dynamics (CFD) solvers have reached maturity in terms of solution accuracy as well as computational efficiency. However, progress remains to be done for unsteady flows especially when governed by large, coherent structures. For these flows, current CFD solvers do not provide accurate solutions unless very fine meshes are used. Moreover, high-accuracy is a crucial feature for the application of advanced turbulence simulation strategies, like Large Eddy Simulation (LES). In order to apply high-order methods to complex unsteady flows several issues needs to be addressed among which numerical robustness and the capability of handling complex geometries. In the present work, we study a family of compact approximations that provide high accuracy not for each space derivative treated apart but for the complete residual r, i.e. the sum of all of the terms in the governing equations. For steady problems solved by time marching, r is the residual at steady state and it involves space derivatives only; for unsteady problems, r also includes the time derivative. Schemes of this type are referred-to as Residual-Based Compact (RBC). Precisely, we design high-order finite difference RBC schemes for unsteady compressible flows, and provide a comprehensive study of their dissipation properties. The dissipation and dispersion errors introduced by RBC schemes are investigated to quantify their capability of resolving a given wave length using a minimal number of grid-points. The capabilities of RBC dissipation to drain energy only at small, ill-resolved scales are also discussed in view of the application of RBC schemes to implicit LES (ILES) simulations. Finally, RBC schemes are extended to the Finite Volume (FV) framework in order to handle complex geometries. A high-order accuracy preserving FV formulation of the third-order RBC scheme for general irregular grids is presented and analysed. Numerical applications, including complex Reynolds-Averaged Navier-Stokes unsteady simulation of turbomachinery flows and ILES simulations of turbulent flows dominated by coherent structure dynamics or decay, support the theoretical results.

**Keywords :** Residual-based scheme, high-order, unsteady, numerical method.

ARTS ET MÉTIERS ParisTech

ParisTech INSTITUT DES SCIENCES ET TECHNOLOGIES PARIS INSTITUTE OF TECHNOLOGY